Author:
Doan, Huan V

Title:
Synthesis, Characterisation and Applications of Novel Hierarchical Porous Materials

Synthesis, Characterisation and Applications of Novel Hierarchical Porous Materials

Huan Van Doan

A dissertation submitted to the University of Bristol in accordance with the requirements for award of the degree of Doctor of Philosophy in the Faculty of Engineering

Department of Mechanical Engineering

May 2019

Word Count: 54,357

Abstract

Porous materials such as activated carbons, zeolites and metal-organic frameworks (MOFs) have been shown to be potentially useful in drug delivery, gas separation, energy storage and catalysis. In these applications, pores or holes with different sizes and geometries play a crucial role in capture and diffusion of guest molecules. Among these materials, hierarchical porous MOFs in which micro- and/or mesoporosity is combined with macroporosity within one structure are particularly beneficial in catalytic applications. These additional large macropores can not only improve the diffusional rate and mass transfer within the MOFs but can also improve molecular accessibility to the microporous cavities which accommodate the important functional groups or active sites of the materials. In this thesis, synthetic methods, characterisation techniques, and catalytic applications of these novel hierarchical porous structures are investigated. A number of advanced techniques were used to characterise these hierarchical MOFs, such as powder X-ray diffraction (PXRD), scanning electron microscopy (SEM), and gas sorption analysis. In terms of preparation, all current synthetic methods to obtain hierarchical MOFs with macroporosity were critically reviewed. Then the thesis primarily focusses on post-synthetic acid etching and supercritical CO_2 ($scCO_2$) synthesis strategies to synthesise highly crystalline MOFs with micro/meso and macroporous structures. In the etching method, use of phosphoric acid in DMSO and MeOH was systematically investigated to prompt defect formation in prepared HKUST-1, a MOF which is prone to hydrolysis and cannot therefore be etched using standard acid exposure. As a novel finding in this thesis, geometrical interconnected macropores were formed in this MOF using this approach without compromising the bulk crystallinity. Furthermore, this additional porosity was found to be dependent both on pH and etching time. It was shown that the greater the concentration of phosphoric acid (up to pH 2.6 in this study) the more macropores in HKUST-1 were observed. Size-selective acid diffusion was considered as the primary mechanism to form the additional macropores in HKUST-1, which was in agreement with previous work using a similar approach on MIL-100(Fe). With respect to the use of supercritical fluids, as an *in situ*/direct crystallisation method, $scCO_2$ was introduced to a MOF precursor solution before the nucleation reaction was triggered, enabling a marked reduction in the volumes of organic solvents required for the synthesis. This MOF was also formed rapidly in the presence of $scCO_2$ (after 4 minutes), which is significantly faster than the crystallisation time (24 h) reported for the normal synthesis using DMSO or DMF. It was additionally shown that $scCO_2$ could be used to control the formation of HKUST-1, and importantly, we reported the presence of

macropores for the first time in this $scCO_2$-driven MOF. Etching this MOF in $scCO_2$ for over 24 h resulted in additional macroporosity which was not seen in previous reports using compressed CO_2. These findings provided a new approach by which macropores with specific performance could be introduced to traditional microporous HKUST-1 MOF. The hierarchical porous HKUST-1 MOF obtained from these two methods was catalytically tested in both gaseous and liquid- phase reactions, showing that introducing macropores into this MOF can have a myriad of advantages in facilitating interactions with the reactants and decreasing the pressure drop, resulting in increased catalytic activity. It was found that the hierarchical pore structure helped to increase the reaction conversion of styrene oxide methanolysis (by ~65% using either HKUST AE and HKUST CO_2, at 40 ^oC in 25 min) and CO oxidation (by 55% using HKUST CO_2 at 260 ^oC). These results suggest different scalable synthetic methods for preparation of materials with hierarchical porous structures, for improved molecular accessibility and diffusion for industrial catalytic applications.

Acknowledgements

Firstly, I would like to thank my PhD supervisor, Dr Valeska Ting for giving me the opportunity to study at the Centre for Sustainable Chemical Technologies (University of Bath, 2014-2016) and then the Department of Mechanical Engineering (University of Bristol, 2016-2019), and for introducing me to many great collaborators. I am especially grateful to Valeska for her constant motivation during my research and for her dedication in carefully providing feedback on my writing and presentations for conferences and competitions. It has been a privilege to learn so much from her. I additionally thank the other co-supervisors I have had during my PhD, namely: Dr Ulrich Hintermair (University of Bath), Dr Asel Sartbaeva (University of Bath) and Dr Sean Davis (University of Bristol). I want to express my particular appreciation to Uli for his supervision regarding the supercritical CO_2 experiment in which I got my first publication in this field, a success that led to four other papers during my PhD.

I would like to thank the Vietnamese Ministry of Education and Training (911 scholarship), the University of Bath (Graduate scholarship) and the University of Bristol (Queen's School scholarship) for funding to financial support me during my PhD. I am also grateful for the numerous travel bursaries I have received to attend conferences and training courses throughout my PhD, primarily from the Bristol Alumni organisation, Royal Society of Chemistry (RSC), Institute of Physics (IOP), the International Union of Pure and Applied Chemistry (IUPAC) and the International Union of Crystallography (IUCr). I am also proud to have received numerous prestigious awards and prizes such as Bristol Plus Award, RSC Materials Horizons Poster Prize and RSC Dalton Transactions Prize for my involvement in significant extra-curricular activities as well as my improvement in presentation skills during my PhD. I am so glad to have success in attending several presentation competitions and science outreach activities such as the Three-Minute Thesis and the STEM for BRITAIN competition.

I would like to thank my collaborators at the Nanyang Technological University (NTU), RMIT University, the University of Hull and Cardiff University, who have made contributions to five of my papers which are presented as main chapters in this thesis. I will always be grateful to them for their help, otherwise this work would have not been possible.

I would also like to recognise all the past and present members of the Ting group, technicians and specialists who are working in the Department of Chemistry (University of Bath), the Department of Chemical Engineering (University of Bath), the Chemical Characterisation and

Analysis Facilities (University of Bath), the Chemical Imaging Facility (University of Bristol), the Nanomaterials lab (University of Bristol) for their invaluable help with my lab work and characterisation analysis.

Furthermore, I would like to thank my past and present colleagues at the Department of Oil Refining and Petrochemistry, Hanoi University of Mining and Geology, especially Prof Pham Xuan Nui who enabled me to become the material scientist I am today. I would like to acknowledge Dr Chien D. Le (PetroVietnam) and Emeritus Professor Brian Higgins (UC Davis) who inspired me to pursue my PhD abroad.

Finally, I am eternally grateful to my incredible family for continuously supporting me in every way possible. I thank my wife and my two daughters particularly. They are always there for me, daily put up with me, and make my life an adventure.

I also want to thank anyone who reads this thesis. I sincerely hope you enjoy it.

Author's declaration

This dissertation is a collection of peer-reviewed, published or submitted journal articles as listed below. Some of the work reported in this dissertation has also been presented at conferences and competitions, as indicated in the dissemination section. I declare that the work in this dissertation was carried out in accordance with the requirements of the University's *Regulations and Code of Practice for Research Degree Programmes* and that is has not been submitted for any other academic award. Except where indicated by specific reference in the text, the work is the candidate's own work. Work done in collaboration with, or with the assistance of, others, is indicated at the start of each chapter. Any views expressed in the dissertation are those of the author.

The author was the first author of five manuscripts, with three of them having been published, and two currently under preparation.

1. **Doan, H. V.**, Prabhakaran, P., Hamzah, H. A., Petrillo, C. & Ting, V. P., 2019, 'Hierarchical metal-organic frameworks with macroporosity: synthesis, achievements, and challenges', *Nano-Micro Letters. (DOI: 10.1007/s40820-019-0286-9)*

   This manuscript is presented as Chapter 2 in this thesis.

2. **Doan, H. V.**, Sartbaeva, A., Eloi, JC., Davis, S. & Ting, V. P., 2019, 'Defective hierarchical porous copper-based metal-organic frameworks synthesised via facile acid etching strategy', *Scientific Reports. (DOI: 10.1038/s41598-019-47314-1)*

   This paper is presented as Chapter 3 in this thesis.

3. **Doan, H. V.**, Fang, Y, Yao, B, Zhili, D, White, TJ, Sartbaeva, A, Hintermair, U & Ting, V. P., 'Controlled formation of hierarchical metal-organic frameworks using CO_2 expanded solvent systems', *ACS Sustainable Chemistry & Engineering. (DOI: 10.1021/acssuschemeng.7b01429)*

   This paper is presented as Chapter 4 in this thesis.

4. **Doan, H. V.** & Ting, V. P., 2019, 'Using supercritical CO_2 in the preparation of metal-organic frameworks: investigating effects on crystallisation', *CrystEngComm (In preparation)*

   This manuscript is presented as Chapter 5 in this thesis.

5. **Doan, H. V.**, Bajaj, N. K., Sun, J., Madapusi, S., Chiang, K. & Ting, V. P., 'Novel hierarchical copper-based metal-organic frameworks for improved catalytic performance', *ChemRxiv (DOI: 10.26434/chemrxiv.9699863.v1)*

   This manuscript is presented as Chapter 6 in this thesis.

Signed:

22nd May 2019

(Revised on 5th September 2019)

Dissemination

Journal publications

Apart from the five manuscripts which are presented as chapters in this thesis, the author has also contributed to another five manuscripts (as listed below) during his PhD.

6. Pham, X. N., **Doan, H. V.**, 'Activity and stability of amino-functionalized SBA-15 immobilized 12-tungstophosphoric acid in the oxidative desulfurization of a diesel fuel model with H_2O_2', *Chemical Engineering Communications*, 2019, 206 (9), pp 1139-1151 (DOI: 10.1080/00986445.2018.1550393)
7. Pham, X. N., Nguyen, B. M., Tran, T. H. & **Doan, H. V.**, 'Synthesis of Ag-AgBr/Al-MCM-41 nanocomposite and its application in photocatalytic oxidative desulfurization of dibenzothiophene', *Advanced Powder Technology*, 2018, 29 (8), pp 1827-1837 (DOI: 10.1016/j.apt.2018.04.019)
8. Pham, X. N., Tran, D. L., Pham, T. D., Nguyen, Q. M., Thi, V. T. T., & **Doan, H. V.**, 'One-step synthesis, characterization and oxidative desulfurization of 12-tungstophosphoric heteropolyanions immobilized on amino functionalized SBA-15', *Advanced Powder Technology*, 2018, 29 (1), pp 58-65 (DOI: 10.1016/j.apt.2017.10.01)
9. Bordeneuve, H, Wales, D. J., Physick, A. J. W., **Doan, H. V.**, Ting, V. P. & Bowen, C. R., 'Understanding the AC conductivity and permittivity of trapdoor chabazites for future development of next-generation gas sensors' *Microporous and Mesoporous Materials*, 2018, 260, pp 208-216 (DOI: 10.1016/j.micromeso.2017.10.032)

Competitions

The author has participated in the following listed prestigious competitions to present the results of his PhD research to a general audience:

1. **STEM for BRITAIN** at the House of Parliament in March 2019. Only 200 out of more than 2000 candidates were selected to present their research to MPs.
2. **Three-Minute Thesis (3MT)** semi-final competition at the University of Bristol in April 2017. The author was shortlisted among 24 out of hundreds of postgraduate researchers.

Conference and workshop presentations

The author has given oral and poster presentation in the following listed international conferences and workshops, reporting some of the work mentioned throughout the thesis.

1. **Metal-organic frameworks 2018 (MOF2018)** in Auckland, New Zealand, in December 2018. Poster presentation: *Defective hierarchical porous copper-based metal-organic frameworks synthesised via facile acid etching strategy.*
2. **Emerging Material Technologies Summit (EMTS)** in Hanoi, Vietnam, in November 2018. Poster presentation: *Tailorable porous metal-organic frameworks.*
3. **85th IUVSTA Workshop on Nanoporous Materials for Green Energy Conversion and Storage** in Schloss Seggau Castle, Austria, in October 2018. Poster presentation: *Defective hierarchical porous copper-based metal-organic frameworks synthesised via facile acid etching strategy.*
4. **New directions in porous crystalline materials: Faraday Discussion** in Edinburgh, UK, in June 2017. Poster presentation: *Controlled formation of hierarchical metal-organic frameworks using CO_2 expanded solvent systems.*
5. **11th International Symposium on the Characterization of Porous Solids (COPS-XI)** in Avignon, France, in May 2017. Poster presentation: *Synthesis and characterisation of a novel porous material.*
6. **Student-led conference in sustainable development** at the University of Bristol, UK, in March 2017. Invited talk: *Porous materials in sustainability.*
7. **8th International Conference on Advanced Materials and Nanotechnology (AMN8)** in Queenstown, New Zealand, in February 2017. Poster presentation: *A hierarchical porous material synthesised in a green solvent system.*
8. **39th British Zeolite Association Meeting** at the University of Bath, UK, in March 2016. Poster presentation: *Synthesis of hierarchical metal-organic frameworks in CO_2 expanded solvent systems.*

Poster Prizes

The author has been received many notable awards for confidently and creatively presenting his research to both small and large groups, which are listed below.

1. **Poster Prize** for the presentation of *Defective macroporous metal-organic frameworks with improved catalytic performance* at the *Second Joint NSFC-RSC Symposium on Sustainable Chemistry and Processes* in York (UK) in September 2019.
2. **Materials Horizons Poster Prize** by Royal Society of Chemistry for the presentation of *Tailorable porous metal-organic frameworks* at *Emerging Material Technologies Summit* in Hanoi (Vietnam) in November 2018.
3. **Runner-up Prize** for the poster presentation of *A hierarchical porous material synthesised in a green solvent system* at the *8th International Conference on Advanced Materials and Nanotechnology (AMN8)* in Queenstown (New Zealand) in February 2017.
4. **Dalton Transactions Prize** by Royal Society of Chemistry for the best poster presentation of *Synthesis of hierarchical metal-organic frameworks in CO_2 expanded solvent systems* at the *39th British Zeolite Association (BZA) meeting* in Bath (UK) in March 2016.

The author has received the **Bristol PLUS Award** (awarded to only 700 out of 23,000 students in 2017) for his involvement in significant extra-curricular activities and skills development alongside his studies. He has also received the **Inspirational Bristol Scientist Award** (awarded to only 8 out of 12,000 postgraduate BAME students in 2019) for his excellent contributions to the university and to the wider community.

Table of Contents

List of Figures

List of Schemes

List of Tables

Acronyms

AIBN	Azobisisobutyronitrile
APTES	Aminopropyl triethoxysilane
BDC	Benzene-1,4-dicarboxylate
BET	Brunauer -Emmett-Teller
BJH	Barrett-Joyner-Halenda
BTC	Benzene-1,3,5-tricarboxylate
CA	Cellulose aerogel
CAU	Christian-Albrechts-Universität
CF	Ceramic foams
CIF	Crystallographic information file
CSD	Cambridge structural database
CTAB	Cetyltrimethylammonium bromide
CXL	CO_2-expanded liquid
DFT	Density functional theory
DLS	Dynamic light scattering
DMF	*N*,*N*-Dimethylformamide
DMOA	*N*,*N*-Dimethyloctylamine
DMSO	Dimethyl sulfoxide
DPE	1,2-di(4-pyridyl)ethylene
EDX	Energy-dispersive X-ray
ELP	Expanded liquid phase
GC	Gas chromatography
HIPE	High internal phase emulsion
HKUST	Hong Kong University of Science and Technology
HPMo	Phosphomolybdic acid hydrate
HRTEM	High-resolution transmission electron microscopy
IL	Ionic liquid
IRMOF	Isoreticular metal-organic framework
IUPAC	International Union of Pure and Applied Chemistry
KGM	Konjac glucomannan
KSC	Kenaf-stem derived macroporous carbon
MCM	Mobil Composition of Matter
MeOH	Methanol

MesoDyn	Mesodynamics
MF	Melamine foam
MFC	Mass flow controller
MIL	Materiaux de l'Institut Lavoisier
MOF	Metal-organic framework
MOFAC	MOF/aerogel composites
MW	Molecular weight
N-EtFOSA	N-ethyl perfluorooctanesulfonamide
NLDFT	Non-localized density functional theory
NOTT	Nottingham
NPC	Nitrogen-doped porous carbon
NTU	Nanyang Technological University
NU	Northwestern University
OD	Outer diameter
PAAm	Polyacrylamide
PCN	Porous coordination network
PDC	Polymer derived ceramic
PLA	Polylactic acid
POM	Polyoxometalate
PS	Polystyrene
PSD	Pore size distribution
PVA	Polyvinyl alcohol
PXRD	Powder X-ray diffraction
RT	Room temperature
SBA	Santa Barbara Amorphous
$scCO_2$	Supercritical CO_2
SCF	Supercritical fluids
SEM	Scanning electron microscopy
SNU	Seoul National University
TEA	Tetraethylamine
TEM	Transmission electron microscopy
TGA	Thermogravimetric analyser
TMEDA	Tetramethylethylene diamine
TMPPTA	Trimethylolpropane propoxylate triacrylate
TOCNF	2,2,6,6-tetramethylpiperidine-1-oxylradical-mediated oxidized cellulose nanofiber

TPU	Thermoplastic polyurethane
UiO	University of Oslo
USTA	University of Texas at San Antonio
ZIF	Zeolitic imidazolate framework
ZSM	Zeolite Socony Mobil
XPS	X-ray Photoelectron Spectroscopy

Mathematical Nomenclature

a_A	Effective area occupied by adsorbate molecule
C	BET constant
c	Concentration
d	Diameter
d_{hkl}	Interplanar spacing
E	Heat of adsorption
K	Shape factor
L	Temperature dependent constant
P	(Equilibrium) pressure
P_c	Critical pressure
P_o	Saturation pressure
S_a	Surface area of the adsorbent
T	Temperature
T_c	Critical temperature
V_a	Amount of adsorbates
V_m	Monolayer volume
w	Adsorbent mass
β*	Kamlett-Taft parameter to qualify hydrogen-bond accepting ability
π*	Kamlett-Taft parameter to qualify polarity ability
β	Integral broadening
δ	Density
θ	Scattering angle
λ	Wavelength of the incident wave
τ	Average size of the crystallites

CHAPTER ONE: INTRODUCTION

This chapter provides a brief introduction to the motivation and structure of the thesis as well as a background to the primary experimental methods used throughout the thesis.

1.1. Motivation

Metal-organic frameworks (MOFs) as a result of reticular chemistry (the chemistry of linking molecular building blocks) are open framework structures made via the self-assembly of metal clusters (or nodes) and organic linkers. The first metal-organic framework (MOF-5) with a rigid porous 3D architecture (which is synthesised from zinc ions and terephthalic acid) and high surface area (Langmuir surface area of 2900 m^2 g^{-1}) was constructed in 1999. This was reported by Omar Yaghi[1] who was inspired by previous work on linking copper ions with rod-like adiponitrile.[2] Soon after the first MOF was discovered, similar chemistry was studied by hundreds of research groups to develop new types of MOF from a variety of metal nodes and organic ligands. There were ~70,000 structures having been designed and synthesised in 2017[3] and more than 75,000 structures reported so far[4]. Among them, some are more commonly mentioned in literature such as HKUST-1 (also known as CuBTC which is synthesised from copper(II) ions and benzene-1,3,5-tricarboxylic acid[5]), UiO-66 (which is synthesised from zirconium(IV) ions and benzene-1,4-dicarboxylate[6]), MOF-74(Zn) (which is synthesised from zinc(II) ions and 2,5-dihydroxyterephthalic acid[7]) and ZIF-8 (which is synthesised from zinc(II) ions and 2-methylimidazole[8]), see Figure 1. In a growing trend, much research has been carried out to find the highest surface area that MOFs can achieve; in 2012, a record surface area of ~7,000 m^2 g^{-1} was reported for NU-110 (Figure 2).[9] The outstanding surface areas seen in MOFs have significant implications for those who are interested in gas storage and separations,[10–12] and catalysis[13,14] where voids to accommodate adsorbent molecules are essential.

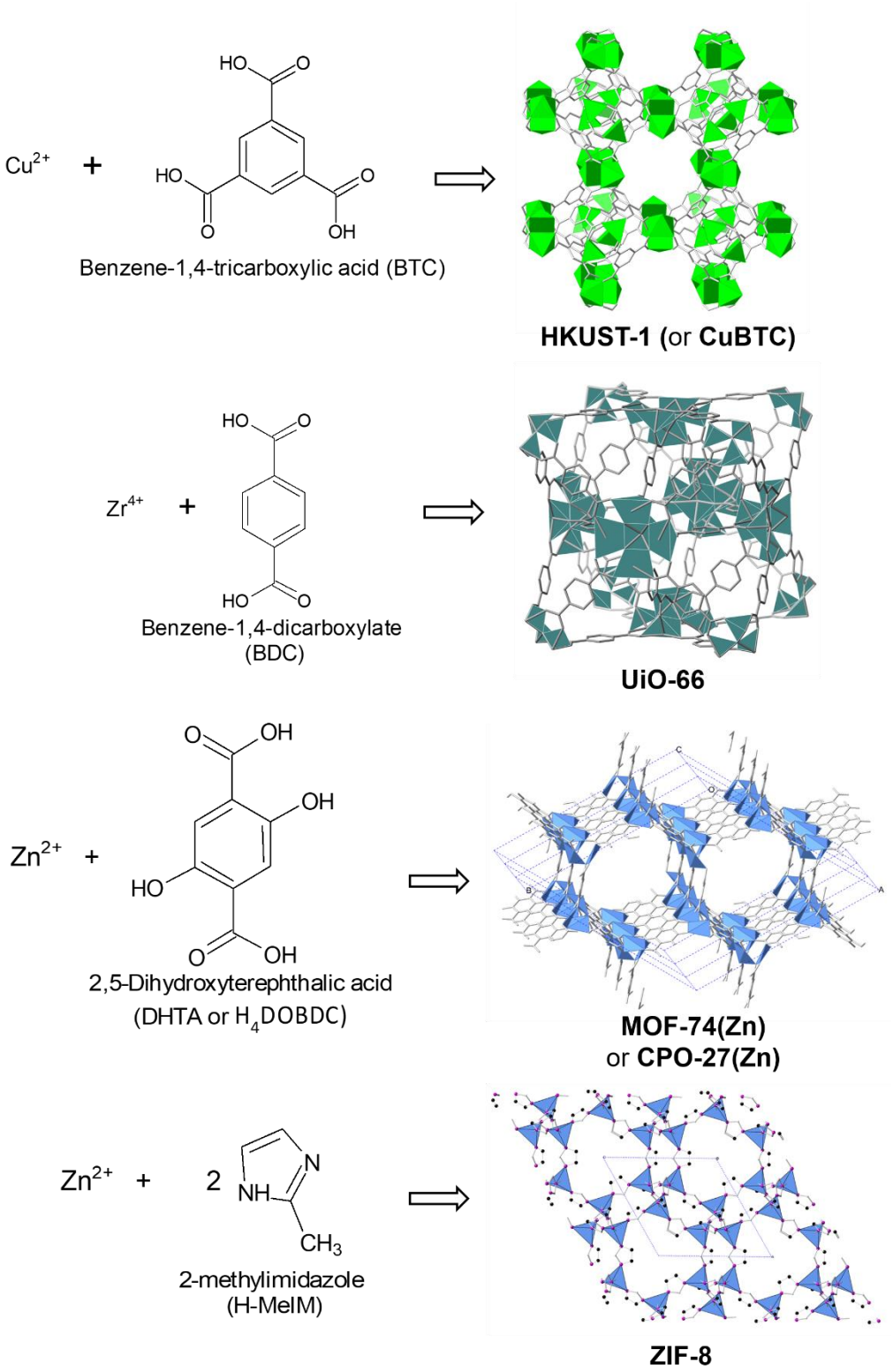

Figure 1. Some commonly studied MOF structures. From the top, HKUST-1, UiO-66, MOF-74(Zn) and ZIF-8. Copper clusters are represented by lime green octahedra, zirconium clusters are represented by dark green tetrahedra and zinc clusters are represented by blue tetrahedra. Carbon atoms are represented by grey spheres. Nitrogen atoms are represented by pink spheres. Hydrogen and oxygen atoms are omitted for clarity.

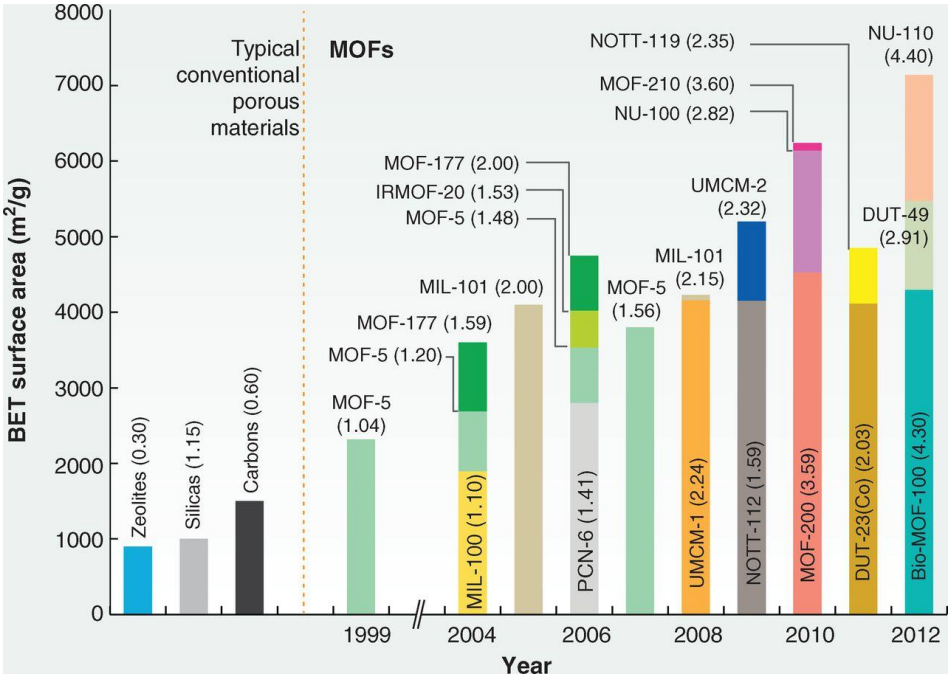

Figure 2. Progress in the synthesis of ultrahigh-porosity MOFs. BET surface areas of MOFs and typical conventional materials were estimated from gas adsorption measurements. The values in parentheses represent the pore volume (cm^3/g) of these materials. Reprinted with permission from Ref. 9. Copyright 2013 Science

Seeing that their development within last two decades, the challenge within MOF chemistry has been to considerably enlarge the pore openings (or pore apertures, see Figure 3) so that guest molecules can effectively access the structure, minimising diffusional barriers during catalysis which have been reported as a problem in other microcrystalline materials (*e.g.* zeolites[15,16]). A good example of how this can be approached is MOF-74, made of rod-like multi-metal units assembled in a hexagonal form linked by simple organic units. The pore aperture of this MOF was enlarged by increasing the length of the phenylene linker units, with the resultant mesoporous IRMOF-74XI (pore aperture 98×85 Å) displaying the largest opening of any porous crystal known.[17] There is also a growing trend to develop hierarchical porous MOFs in which mesopores (pore diameters between 2-50 nm) and macropores (pore diameters > 50 nm) are incorporated into MOF systems containing traditional micropores (pore diameters < 2 nm). This kind of hierarchical structure is of major advantage because, apart from the large apparent surface areas used to attract molecules by the van der Waals interaction (a process defined as adsorption), MOFs with these advanced structures enable molecules to reside in the framework (a process defined as absorption), leading to a combination of large gas storage capacities and diffusion rates. As opposed to simply enlarging pore apertures, introducing multiple porosity regimes into MOFs by extending ligand lengths is more difficult because of

ligand size limitations and the increased risk of pore collapse during desolvation[18]. Thus, a range of other advanced techniques have been developed to fabricate these hierarchical structures, including structural templating, gelation, defect formation, routes involving supercritical CO_2, and 3D printing.

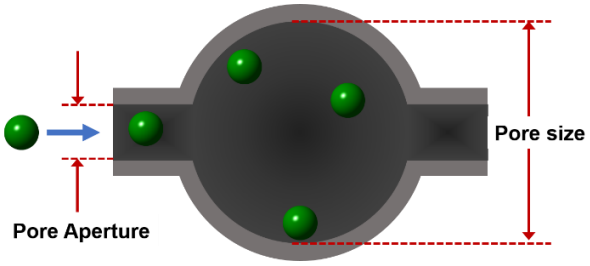

Figure 3. Pore apertures and pore sizes. Guest molecules are presented by green spheres

To further advance the practical applications of these materials, hierarchical porous MOFs with additional macropores were considered as a major focus of this research. As opposed to structural templating and gelation, which are well-known fabrication methods, two novel methods including acid etching and the use of $scCO_2$ were focused on. These structures were also tested in facilitating interactions with gaseous or liquid-phase reactants to qualify the benefits of macropores in decreasing pressure drop, which is one of the main issues hindering practical MOF application in industrial settings.

1.2. Structure of the Thesis

The aim of this thesis was to synthesise hierarchical porous MOFs with a view to demonstrating improved catalytic performance. To achieve this goal, two synthetic methods (acid etching and use of $scCO_2$) were systematically investigated. The parameters contributing to the introduction of macropores in these MOFs using these approaches were investigated and full characterisation of the materials was carried out. The resultant hierarchical structures were then tested for methanolysis of styrene oxide (as a representative for liquid phase reactions) and CO oxidation (as a representative for gas phase reactions) to examine the effect of the additional macroporosity on diffusion of different guest molecules in these hierarchical MOF structures.

The seven chapters presented in this thesis are structured as follows: after this introduction, Chapter 2 presents a review of the state of the art on current preparation techniques for metal-organic frameworks with macroporosity. This chapter summarises the achievements and challenges of all synthetic methods mentioned so far in literature to obtain macroporous metal-organic frameworks including structural templating, gelation, acid etching, use of supercritical

CO_2 ($scCO_2$) and 3D printing. Chapter 3 focuses on a post-synthetic acid etching method, in which for the first time HKUST-1 MOF with geometrical interconnected macropores was introduced. The characterisation of the materials, a systematic investigation of the added porosity as a function of pH and etching time and an exploration of the etching mechanism are presented in this chapter. Chapter 4 and Chapter 5 introduce a synthetic method involving $scCO_2$, which was investigated using a range of well-known MOFs including HKUST-1, MOF-74(Zn), ZIF-8, Zn-BTC and $[Cu_{24}(OH\text{-}m BDC)_{24}]_n$ to explore the effect of $scCO_2$ on different chemical systems. Chapter 4 presents HKUST-1 with the formation of macroporous structure in $scCO_2$. This chapter provides a complete experimental investigation into how to control the formation of HKUST-1 in the presence of $scCO_2$ as a function of reaction time and pressure. In line with the aim of this thesis, the experiments presented in this chapter were focused on producing HKUST-1 with hierarchical porous structure. In Chapter 5, to probe the generalisability of this mechanism for the introduction of additional porosity, the $scCO_2$ method was extended to other MOF systems including MOF-74(Zn), ZIF-8, Zn-BTC and $[Cu_{24}(OH\text{-}m BDC)_{24}]_n$. Little evidence of formation of macropores was observed in these systems, and the results are discussed in Chapter 5 as a comparison to the previous chapter. In Chapter 6, the HKUST-1 MOF with macropores (synthesised using both the acid etched and $scCO_2$ approaches) was tested in both liquid and gas phase reactions to determine effect of hierarchical porosity on catalytic performance. The thesis closes with a conclusion section, to reflect on the results and make suggestions for how the work could progress in the future (Chapter 7). Supplementary information for the experiments mentioned in Chapters 3, 4, 5 and 6 are provided in the Appendices (B, C, D and E, respectively).

1.3. Methodology

This section provides a summary of the solvothermal and $scCO_2$ methods which were employed to synthesise MOFs in Chapters 4 and 5. Following this, an explanation of the more commonly used characterisation techniques for testing and analysis of the prepared samples are presented. Supplementary information for these characterisation techniques are provided in the Appendix A.

1.3.1. Conventional solvothermal preparation of MOFs

In conventional synthesis, a typical MOF is synthesised by a solvothermal method in which metal and ligand ions are dissolved in a solvent to form a precursor solution containing either non-hydrogen-bonded complexes or hydrogen-bonded complexes (see Chapter 5 for

examples). This precursor solution is left for MOF crystallisation over time at a fixed temperature. Depending on the nature of hydrogen bond in the precursor solution, an antisolvent might need to be added to trigger the reaction. For example, as reported by Ameloot *et al.*,[19] HKUST-1 MOF is synthesised conventionally by dissolving copper(II) nitrate hemipentahydrate ($Cu(NO_3)_2 \times 2.5H_2O$) and benzene-1,3,5-tricarboxylic acid (trimesic acid/BTC) in DMSO to form a precursor solution (which is stabilised by hydrogen bonds between DMSO and BTC). To induce MOF formation, 100 mL methanol (as an antisolvent) is added to 10 mL of the precursor solution, heating to 40 ^oC for 24 hours with continuous stirring. Product formation is evidenced by a precipitate being formed after the reaction. The product can be isolated by centrifugation, washed with pure methanol and re-centrifuged three times. While this synthetic method is fairly straightforward to perform, copious amounts of solvents typically used in the preparation are not environmentally friendly. The formed HKUST-1 crystallites have high surface area as expected, however, using this synthesis method the micropore size in this MOF cannot be easily adapted for efficient use in particular applications.

1.3.2. Using $scCO_2$ in preparation of MOFs

Use of CO_2 for performing separations, extractions and reactions is a very promising way to reduce environmental and cost burdens in chemical companies. Although it has a bad reputation as one of the gases contributing to the greenhouse effect, when used as a solvent, CO_2 can be especially useful for certain applications with a simultaneous environmental benefit associated with reducing excessive organic solvent wastage. During the last two decades, many research groups have clearly demonstrated the advantages of a tuneable solvent composed of a compressed CO_2 dissolved in an organic compound.[20,21] By tuning the operating pressure, the generated media can be varied from neat organic solvents to a CO_2-expanded liquid (CXL) and to $scCO_2$ (where the volume of the liquid media is expanded similar to a CXL but pressure and temperature are both above the critical point of CO_2), see Figure 4. Percent volume change of the expanded media can be controlled depending on the solubility of CO_2 in liquids, to that the operating pressures and temperatures and nature of organic solvents are crucial factors, see Figure 5.[22] As for the difference of their nature, liquids can be classified into three categories, including type I solvents such as water (which are not expanded in CO_2 and do not change their properties, except acidity), type II solvents such as MeOH, DMF and DMSO (which are expanded greatly in CO_2 and have significant changes in their physical properties) and type III

solvents such as ionic liquids and crude oil (which are moderately expanded in CO_2, with some properties, such as viscosity, changing significantly while others, such as polarity, do not).[22] It can be seen that some organic solvents like MeOH and DMSO showed identical behaviours in expansion with CO_2 at low temperature (40 ^oC) but significant differences at higher temperatures (50 and 60 ^oC). The ternary system MeOH/DMSO showed decreased solubility in CO_2 because of hydrogen bonding in this system.[23]

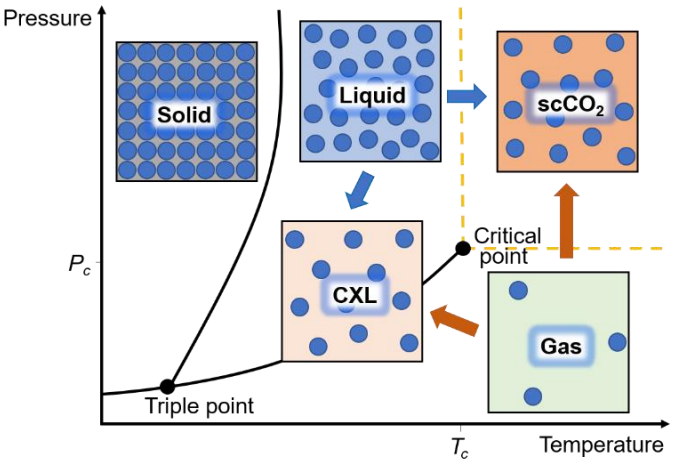

Figure 4. A phase diagram showing CO_2-expanded liquids (CXL) and $scCO_2$ formed by a mixture of gaseous CO_2 and liquid solvent

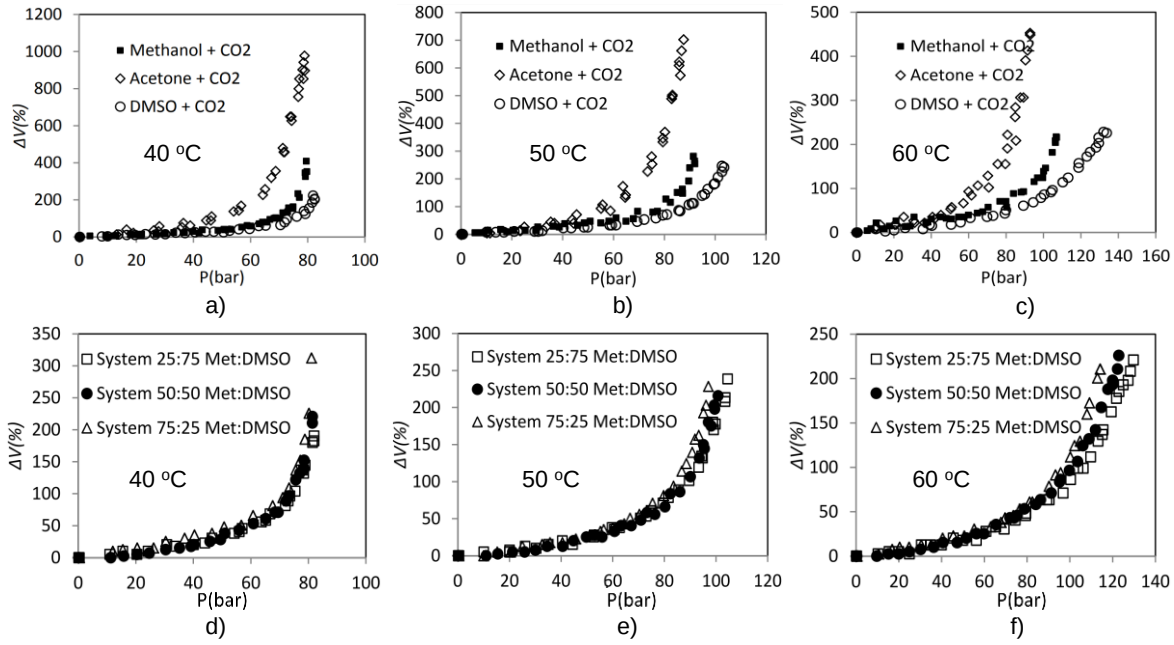

Figure 5. Percent volume change vs pressure of CO_2 for multiple solvents at 40 ^oC (a), 50 ^oC (b) and 60 ^oC (c). Percent volume change vs pressure of CO_2 for MeOH/DMSO system at 40 ^oC (d), 50 ^oC (e) and 60 ^oC (f). Reprinted with permission from Ref. 22. Copyright 2013 Chemical Engineering Transactions

As a result of the expansion, some deviations are expected to be seen in key solvent properties such as polarity,[24] hydrogen-bonding ability,[24] melting point,[25,26] transport properties,[27] conductivity[28] and acidity[29–31]. In particular, parameters in polarity and hydrogen-bond accepting/donating ability drop significantly as the CO_2 content increases; see CO_2-expanded methanol (MeOH)[24] (Figure 6) for example. It was shown that diffusivities of solutes such as benzene and pyridine in CXL, however, increase as a function of the CO_2 pressure.[27] Viscosity and surface tension of liquids have shown to be significantly reduced upon CO_2 introduction.[32–34] As expected, increased ion mobility in compressed CO_2 can result in an increase of solvent conductivity. This has been confirmed by Umecky *et al.*[28] who showed the correlation between the electrical conductivity in CO_2-expanded [C(4)*mim*]PF_6 and CO_2 pressure. Solvent acidity has also been demonstrated to be lowered by dissolving CO_2. Toews *et al.*[29] have shown that the pH of water in the presence of CO_2 drops to 2.84 at 71 bar and 40 °C (*i.e.* in the presence of supercritical CO_2). The author also showed that this pH value did not significantly change upon further increase of CO_2 pressure. Enhanced acidity was also observed by Hunter *et al.*[30] and West *el al.*[31] who took an advantage of this effect to use high-temperature water and alcohols with CO_2 in acid-catalysed reactions.

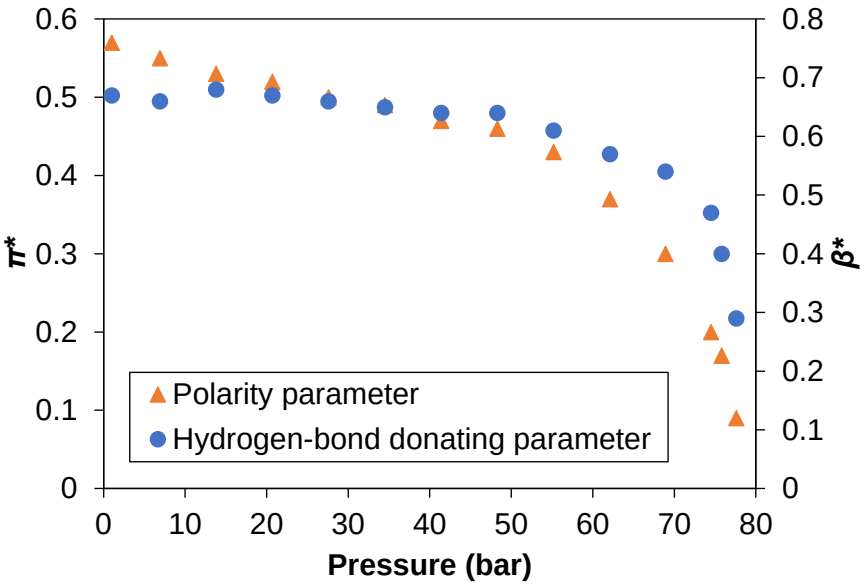

Figure 6. Experimental π and β* values for MeOH/CO_2 binary mixtures using 4-nitroanisole as the solvatochromic probes at 40 °C, showing an increase in CO_2 pressure leads to a decrease in the polarity (quantified by Kamlett-Taft π* parameter[35]) and hydrogen-bond donating ability (quantified by Kamlett-Taft β* parameter[35]) of the MeOH/CO_2. Reproduced from Table 3 in Ref. 24 with permission. Copyright 2005 The Journal of Supercritical Fluids*

Due to the enhanced mass transfer, the reduced surface tension and viscosity, CXL and $scCO_2$ have been considered as promising solvents in material synthesis and processing.[21,36,37] CO_2 has been shown to serve as an antisolvent by decreasing the density of the solvent phase to trigger precipitation.[38] This can be achieved by simply bubbling the organic solvent with $scCO_2$ to achieve solvent expansion (termed the gas antisolvent method, GAS[39]), spraying the solution into the $scCO_2$ (called precipitation with compressed antisolvent, PCA[40]) or depressurising quickly the expanded solvent to lower rapidly the temperature for the compound to crystallise (termed depressurisation of an expanded liquid organic solution, DELOS[41,42]). CO_2 was also used for depositing nanoparticles into high aspect ratio nanostructures. An example of this application was demonstrated by McLeod *et al.* who have utilised CO_2 for narrowing the size distribution of nanoparticles through pressure-tuneable CXL.[43,44] As CO_2 can lower the polarity, a solvent in this gas can have switchable polarity or fluorophilicity. This is particularly useful for one-step syntheses in which the reaction is performed in polar solvents, but the solvent extraction is optimised in non-polar solvents.[45,46] Interestingly, some porous materials such as hydrogels and MOFs, once formed, can be dried in $scCO_2$ without the pore collapse common with other solvent removal methods.[47]

In the studies presented in Chapter 4 and 5 of this thesis, $scCO_2$ was used as an antisolvent for MOF formation. In a typical experiment, by using a pump, $scCO_2$ was introduced into a glass vial containing MOF stock solution (a co-solvent might need to be added in, see Chapter 4 as an example), heating at 40 ^oC under stirring with CO_2 pressure and reaction times varied for investigating optimal conditions, see Figure 7. High pressure view-cell experiments were carried out in a 20 mL stainless steel vessel with opposing windows of single crystal sapphire (Figure 8) to observe MOF precipitation under $scCO_2$ pressure.

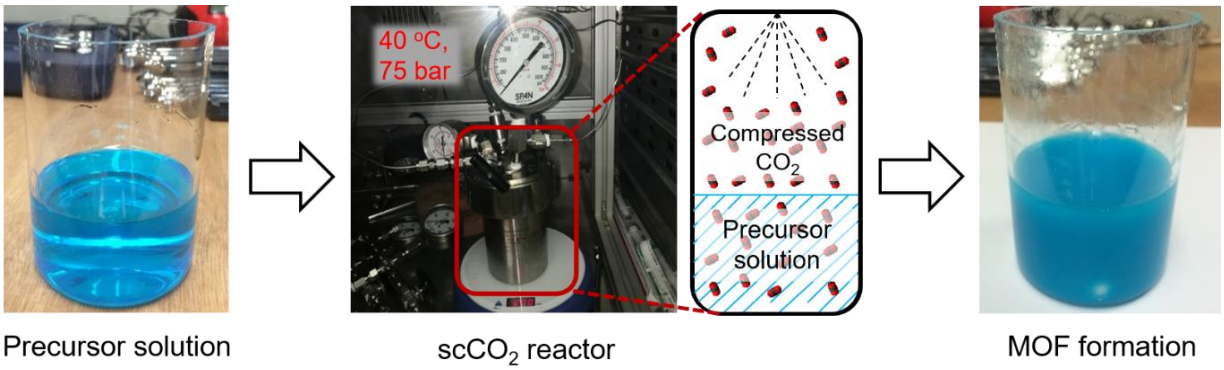

Figure 7. Use of supercritical CO_2 to synthesise MOFs, showing that MOF precipitation occurred during CO_2 introduction

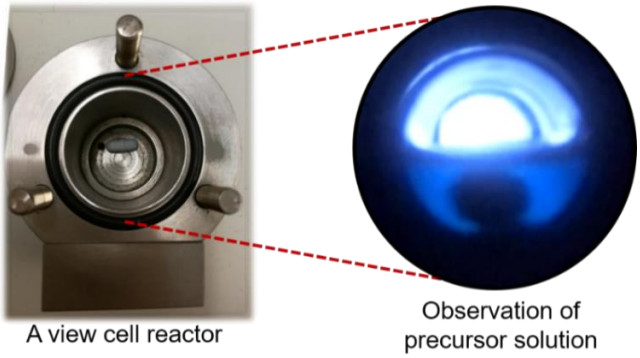

Figure 8. Observation of MOF formation under $scCO_2$ pressure in a view cell reactor

All products were dried further by continuous-flow $scCO_2$ extraction. As a general procedure, a sample of 0.1-0.3 g solid is placed in 2 cm dialysis tubing (cellulose, 1000 MW cut-off), sealed with copper wire and then placed into stainless steel high-pressure tubing (0.5 inch diameter, 10 cm length) with a 50 µm particulate filter at the outlet. The sample is subjected to continuous $scCO_2$ extraction at 40 ^oC and 120 bar (δ = 0.69 g mL^{-1}) with 2 g CO_2 min^{-1} over 18 hours using a custom-built supercritical fluid (SCF) continuous flow rig similar to that previously described.[48] The plug flow reactor is then depressurised at 10 bar min^{-1}, the solid sample recovered by carefully removing the dialysis tube and analysed immediately.

1.3.3. Powder X-ray diffraction

Powder X-ray diffraction (PXRD) data analysis throughout this thesis was used primarily for phase identification, with some additional investigation of the crystallite size of prepared samples. The technique is performed by diffraction of periodic and long-range X-ray radiation scattered from an X-ray tube at specific angles onto a densely packed sample in flat plate geometry and recorded by a detector, as shown in Figure 9a.

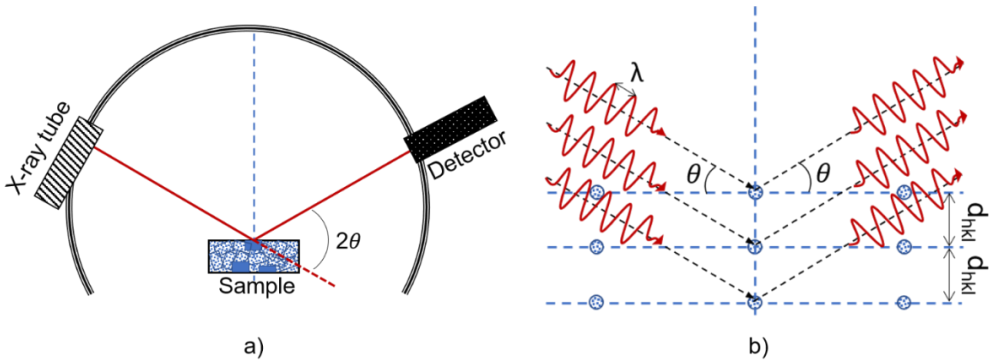

Figure 9. PXRD technique represented by a schematic diagram of the experimental PXRD geometry (a) and a schematic depicting Bragg's law (b)

All MOF samples studied in this thesis are considered as crystals where the atoms are arranged in a periodic array and in a specific order depending on the crystal structures of the materials. The scattering of X-rays from these atoms produces a unique diffraction pattern, which contains information on the crystal structure. Observed diffraction peaks with Miller indices (*hkl*) can be related to different planes of atoms and are used to analyse the atomic structure and microstructure of a sample. The scattering angle where a diffraction peak is produced can be calculated by Bragg's law (see Equation 1.1).

$$\lambda = 2d_{hkl}sin\theta \qquad \text{(Equation 1.1)}$$

where d_{hkl} is the interplanar spacing, θ is the scattering angle and λ is the wavelength of the incident wave (see Figure 9b). In the BRUKER AXS D8-Advance diffractometer, Cu *K*α was chosen as a source of X-ray radiation with the wavelength fixed at 1.5418 Å, which is similar to the distance between atoms. In this thesis, phase identification of prepared samples was determined by the position and relative intensity of diffraction peaks to compare experimental data to the simulated patterns generated from a crystallographic information file (cif) of the reference crystal structure.

The average crystallite size of nanoparticles can be quantified by peak broadening using the Scherrer equation, see Equation 1.2. To achieve this, the contribution of peak width from the instrument needs to be identified by using a calibration curve. Typically, the broader the peak observed in the PXRD pattern, the smaller the crystal size that was in the sample (see PXRD results of UiO-66 in Appendix C2.4 as an example).

$$\tau = \frac{K\lambda}{\beta cos\theta} \qquad \text{(Equation 1.2)}$$

where τ is the average size of the crystallites, *K* is a shape factor which has a typical value of about 0.9, β is the line broadening at half the maximum peak intensity.

In a typical experiment, PXRD analyses were performed on a BRUKER AXS D8-Advance instrument with Vantec-1 detector using Cu Kα (λ = 1.5418 Å) as the source of X-ray radiation, in flat plate geometry, spinner speed 15 rpm, at room temperature. The two theta range, between 2 and 60 degrees was used with a 0.02 degree interval for collection and 20 minute scans.

1.3.4. Gas sorption analysis

As key features of MOF materials, surface area and pore size distribution are two common textural characteristics which were examined throughout this thesis. In most cases when MOFs

are applied in liquid or gas phase catalysis, the reaction occurs at the interface between phases, where the surface area of a solid is the primary property used to estimate the chemical kinetics of a particular reaction. Increasing the surface areas of catalysts can increase the rate of chemical reactions as reagents have greater accessibility to the active sites of the material.[49–51] Surface area of a material is normally affected by the particle size, particle morphology, surface texturing and porosity. Typically, breaking down a large particle into smaller ones increases the total surface area. For example, the surface area of one cubic particle can increase 4 times after being divided into 64 smaller pieces (see Figure 10). Texturing is also a factor affecting surface area. For example, MOF-74(Zn) after etching in supercritical CO_2 has a rough surface (observed from SEM results), resulting in an increased surface area in comparison to the smoothly faced sample before etching, see the results and discussion in Chapter 5 of this thesis.

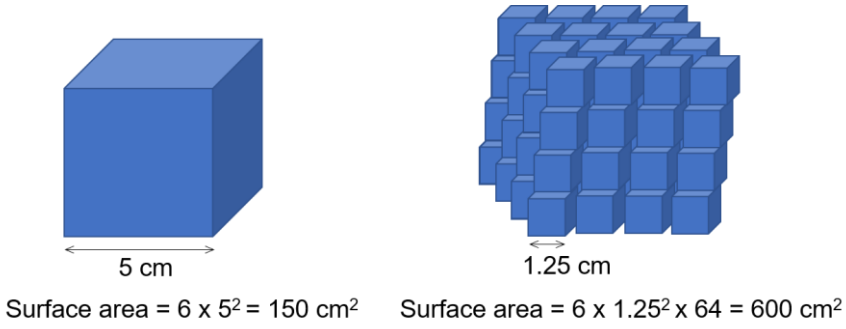

Figure 10. Illustration of one particle having increased surface area after being broken down into smaller pieces

Surface area and pore size distribution can be estimated using various techniques such as scanning electron microscopy,[52] small angle X-ray scattering,[53] and Monte Carlo simulation,[54,55] however, gas adsorption is considered the most direct and reliable technique[56]. In the latter method, gas molecules collide with a solid surface and adsorb for a period of time until the solid is covered or the pores are filled. Assumed by Langmuir in 1916, a monomolecular layer is formed on an energetically uniform surface by non-interaction adsorbed molecules, surface area of the adsorbent S_a can be measured from the amount of adsorbate V_a at a given pressure P using Equations 1.3 and 1.4.[57] This method is appropriate for calculating high surface areas in materials with very narrow micropores, however, deviates significantly in many cases such as materials with rough inhomogeneous surfaces which have multiple site-types available for adsorption (Langmuir method is more appropriate for monolayer adsorption). As an advance on the Langmuir treatment, the BET (Brunauer-Emmett-Teller) method equates rate of condensation onto an already adsorbed layer to the rate

of evaporation in multilayer adsorption, which is more likely to take place in meso- and macropores.[58] In this method, monolayer volume V_m is calculated from the slope $(C-1)/V_mC$ and intercept $1/V_mC$ of the BET plot using the BET equation (see Equation 1.5 and 1.6), then surface area S_a is calculated using Equation 1.4. The BET method is widely used to report the surface area in most materials.

$$V_a = \frac{V_m LP}{1+LP} \quad \text{(Equation 1.3)}$$

$$a = \frac{V_m}{w}\frac{6.023\times10^{23}}{22400}a_A \quad \text{(Equation 1.4)}$$

$$\frac{P}{V_a(P_o-P)} = \frac{1}{V_mC} + \frac{(C-1)}{V_mC}\frac{P}{P_o} \quad \text{(Equation 1.5)}$$

$$C = \exp\left(\frac{E_1-E_C}{RT}\right) \quad \text{(Equation 1.6)}$$

where L is a temperature dependent constant, P and P_o are the equilibrium and the saturation pressure of adsorbates at the temperature of adsorption, C is the BET constant, E_1 is the heat of adsorption for the first layer, E_C is the heat of adsorption for the second and higher layers and is equal to the heat of condensation, w is adsorbent mass under analysis and a_A is effective area occupied by adsorbate molecule. In BET theory, surface area is generally measured by plotting the amount of adsorbed gases against relative pressure (p/p^o) between 0.05 and 0.3. For surface area measurements of HKUST-1 samples in Chapter 3, 4 and 6, an optimised range of relative pressure suggested by Rouquerol is necessary to obtain positive C value for the BET calculation[59].

An adsorption isotherm describes the relationship between the amount of gas molecules adsorbed by a material and the relative pressure at constant temperature, and is used to study the adsorption process. The correlation between adsorption isotherms (using the experimental 77 K N_2 isotherm of HKUST-1 as an example) and gas behaviour on a solid surface is illustrated in Figure 11. Gas adsorption begins by exposing the sample to a low pressure of the adsorptive gas, which causes an increase of adsorbate density at the adsorbent surface. In the next step, gas molecules can form a monolayer (Langmuir theory) or can stack, where the heat of adsorption and heat of condensation need to be considered (BET theory) before surface area is measured, using the corresponding equations. Note that the two steps in the isotherm represent different micropore sizes in the HKUST-1 sample. As the pressure rises, additional gas molecules adsorb to form multilayer coverage (BET theory), giving information of mesopores in the material. A further increase in the gas pressure will cause complete coverage

of the sample and fill all the pores (if the pores are not too large), providing further pore size data and total pore volume.

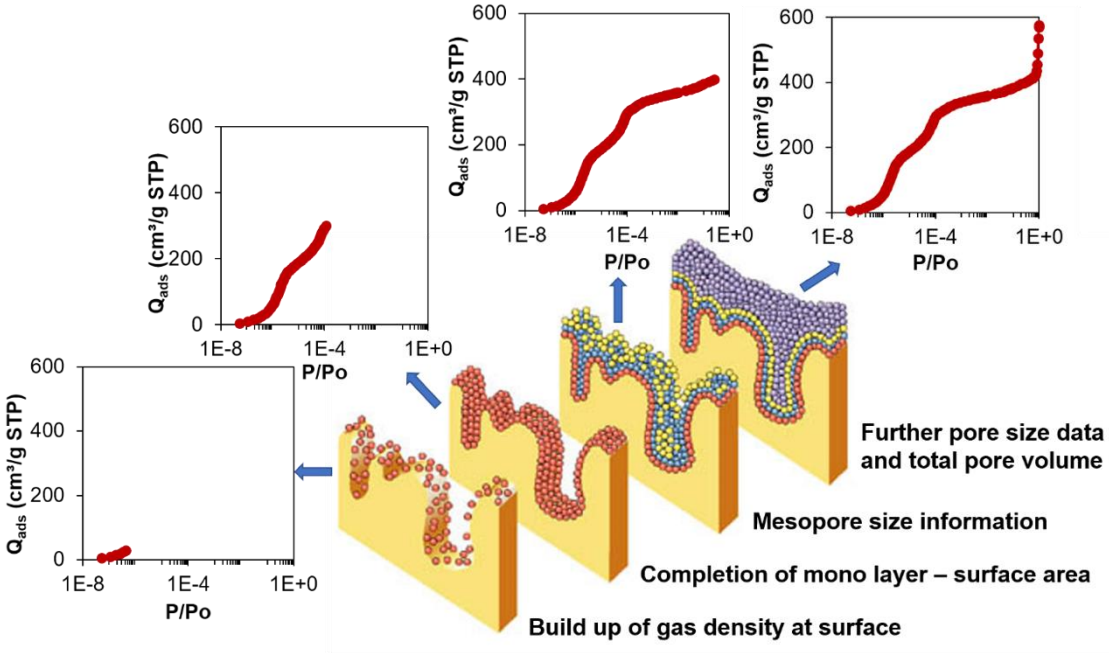

Figure 11. The correlation between gas sorption isotherm (experimental 77 K N_2 isotherm of HKUST-1 was used as an example) and gas behaviour on the solid surface. This figure was adapted from the image in Ref. 59.

Following updated IUPAC classifications,[60] adsorption isotherms can be grouped into six characteristic types which are used to identify particular pore structures, see Figure 12. A steep uptake at very low relative pressure in a type I isotherm is the result of enhanced interactions between adsorbents and adsorbates in narrow micropores (pore width ≤ 1 nm in type I(a) isotherms or ≤ 2.5 nm in type I(b) isotherms). Langmuir theory can be applied in this case to measure surface area. The shape of type II isotherms is due to unrestricted monolayer-multilayer adsorption in nonporous or macroporous materials at high relative pressure. The knee point in this graph (point B) represents the completion of monolayer coverage and the beginning of multilayer adsorption. In type II isotherms, this point is less distinctive, with a reversed curvature indicating that adsorbent-adsorbate interactions become relatively weak. The adsorbed molecules are bunched around the most favourable sites on the surface and the adsorbed multilayer appears to increase and remains finite at the saturation pressure. Adsorption on mesoporous solids produces type IV and V isotherms, in which the initial parts are similar to monolayer-multilayer adsorption in the type II and III isotherms, respectively. The final stages are typical saturation plateaus associated with capillary condensation taking place in mesopores. In a type IV isotherm, the adsorption and desorption processes can be

accompanied by a hysteresis loop (IVa) or are completely reversible (IVb) depending on the mesopore size and geometry. Monolayer-multilayer adsorption on nonporous solids can be represented by stepwise type VI isotherms with the step-height associated to the monolayer capacity for each adsorbed layer.

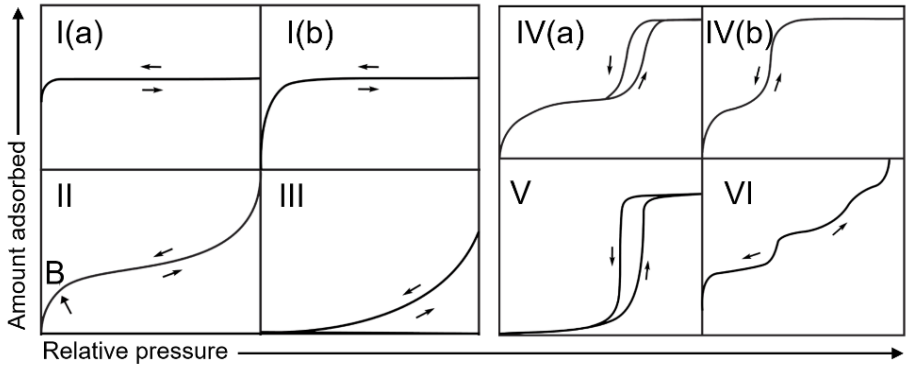

Figure 12. Updated IUPAC classifications of adsorption isotherms. Reprinted with permission from Ref. 60. Copyright 2015 Pure and Applied Chemistry

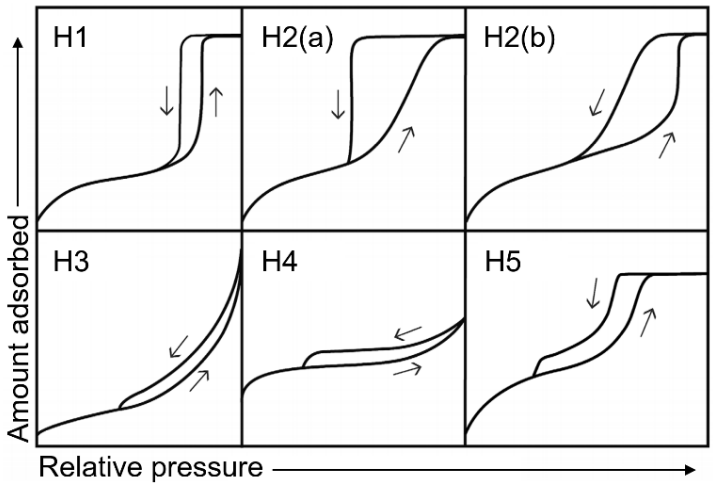

Figure 13. Updated IUPAC classifications of hysteresis loops. Reprinted with permission from Ref. 60. Copyright 2015 Pure and Applied Chemistry

In pore size measurements, the adsorption isotherm is followed by reducing the pressure to prompt desorption. In most cases when monolayer-multilayer adsorption is associated with capillary condensation, adsorption and desorption processes in isotherms can produce many different shapes of hysteresis loops (Figure 13), which are used to predict pore structure and adsorption mechanism at high relative pressure (usually at *P/Po* ~0.4-0.5 for nitrogen at 77 K). In general, the less sharp the pore condensation step, the wider the pore size distribution. The steep loop in type H1 is attributed to delayed condensation on the adsorption branch, which is found in well-defined and narrow cylindrical mesopore networks. The big loop in type H2 is

produced by disordered pores due to blocking or percolation. The difference in pore neck widths can result in H2(a) loops (small pore necks) and H2(b) loops (large pore necks). Type H3 is produced by slit-shaped pores in non-rigid aggregates of plate-like particles. This hysteresis loop is also for macropore networks which are not completely filled by the adsorbate during pore condensation. Type H4 is produced by narrow slit micropores, which are common in zeolites and activated carbons. Type H5 also possesses a sharp stepped desorption branch as seen in H2(b) and H3 but with a distinctive shape that is attributed to open or semi-open mesopores in solid adsorbents.

Pore size and volume of micro- and mesoporous materials (up to 300 nm diameter) can be analysed from gas sorption using various calculation methods such as Horvath-Kawazoe (HK), non-linear density functional theory (NLDFT) and Barrett-Joyner-Halenda (BJH) methods. For mesoporous materials, BJH is likely the most appropriate method because it is able to derive multiple layers adsorbed on solid surface and additional condensation into central capillary region in mesopores.

In a typical experiment, gas sorption isotherms are determined using nitrogen sorption at 77 K with a Micromeritics 3-Flex volumetric gas sorption analysis system. Samples (~100 mg) are degassed at 120 °C under dynamic high vacuum (10^{-6} mbar) over at least 6 hours before analysis to remove moistures and contaminants. The total pore volume is taken at the end of the filling of the pore. Surface area is determined by the BET method according to British Standards,[61] with relative pressure (P/P_o) selected considering the Rouquerol consistency criterion between values of 0 and 0.3.

1.3.5. Scanning electron microscopy

Scanning electron microscopy (SEM) is a high-resolution imaging technique that uses a focused beam of electrons to study external morphology, surface topography and chemical composition of various materials. In this thesis, SEM analysis was used (in conjunction with gas sorption) to identify additional macropores and surface features of prepared MOF samples under extreme magnification. In a typical SEM set-up (see Figure 14), electrons are generated from a heated tungsten wire in an electron gun and accelerated down the column. A condenser lens, apertures, and an objective lens are used to manipulate the size and the focus of the electron beam. Accelerated electrons in this beam produce vast amounts of kinetic energy (ranging from 0.2 keV to 40 keV) which is transformed into signals after interacting with the

sample. Unlike transmission electron microscopy (TEM), which detects electrons passing through a thin sample, SEM detects backscattered (from deeper regions) and secondary electrons (from surface regions), as a result of inelastic interactions between the electron beam and the sample.

In this thesis, scanning electron microscopy (SEM) analysis was typically perfomed on a JSM-IT300 (JEOL, Japan) at 5 kV with a 10.8 mm working distance and magnifications from 350 to 40,000 times. The samples were sputtered with a thin layer of silver (10 nm) and imaged with a secondary electron detector. Elemental composition in the samples is analysed by energy-dispersive X-ray (EDX) technique. In this thesis, EDX data was collected on HKUST-1 samples used for catalytic testing (in Chapter 6) using an Oxford INCA X-ray analyser attached to the microscope.

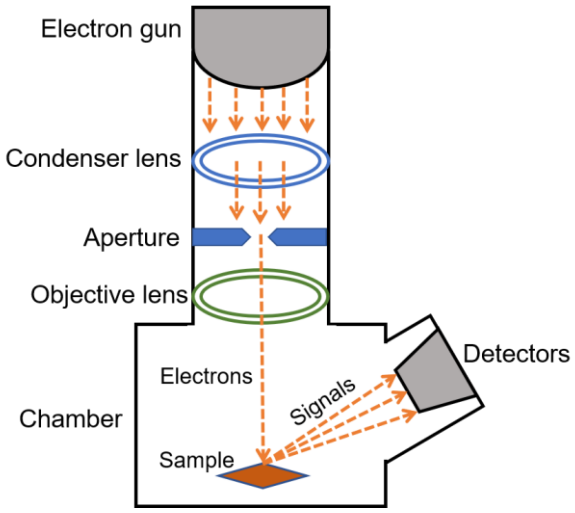

Figure 14. Diagram of typical SEM experimental geometry

CHAPTER TWO: HIERARCHICAL METAL-ORGANIC FRAMEWORKS WITH MACROPOROSITY: SYNTHESIS, ACHIEVEMENTS, AND CHALLENGES

In this chapter, the most recent research into the preparation of hierarchical MOFs with macroporosity is presented. MOFs are typically microporous, containing pores of less than 2 nm in diameter, which means that gas- and liquid-phase interactions may be limited by low rates of diffusion or high pressure drop (*i.e.* a high pressure differential between inlet and outlet, which may be a result of hindered gas- or liquid- flow through a catalytic bed). This can be overcome by the introduction of larger pores or hierarchical porosity to improve molecular accessibility. To do this, all new state-of-the-art synthetic methods including use of structural templating agents, gelation, defect formation, routes involving supercritical CO_2 and 3D printing are discussed. These approaches could lead to improved molecular accessibility and diffusion and should impact on a range of applications of these materials including catalysis and drug delivery.

This chapter appeared as a review paper published to *Nano-Micro Letters* journal (DOI: 10.1007/s40820-019-0286-9), with the author of this thesis as the first author. The author confirms that he did the majority of the work for this review, including defining the scope and structure, preparation of a first draft (with extra contributions by other co-authors in the subsequent versions are stated as below), revising the penultimate version and leading on the submission. Additional contributions were made by co-authors on the paper, including Harina Amer Hamzah, who provided extra comments and corrections on a review of macroporous MOFs synthesised using structural templating (Section 2.2.1), Prasanth Karikkethu Prabhakaran who provided extra comments and corrections on a review of macroporous MOFs synthesised via defect formation (Section 2.2.2), Chiara Petrillo who provided extra comments and corrections on a review of macroporous MOFs synthesised via 3D printing (Section 2.2.4) and Valeska P. Ting who provided feedback, comments and corrections throughout the review paper.

Abstract

Introduction of multiple pore size regimes into metal-organic frameworks (MOFs) to form hierarchical porous structures can lead to improved performance of the material in various applications. In many cases, where interactions with bulky molecules are involved, enlarging the pore sizes of typically microporous MOF adsorbents or MOF catalysts is crucial for enhancing both mass transfer and molecular accessibility. In this review, we examine the range of synthetic strategies which have been reported thus far to prepare hierarchical MOFs or MOF composites with added macroporosity. These fabrication techniques can be either pre- or post-synthetic and include use of hard or soft structural templating agents, defect formation, routes involving supercritical CO_2, and 3D printing. We also discuss potential applications and some of the challenges involved with current techniques, which must be addressed if any of these approaches are to be taken forward for industrial applications.

2.1. Introduction

The interactions of gases and liquids with porous materials have been a great source of inspiration for scientists tackling problems related to gas separation,[62–65] energy storage,[66–69] drug delivery[70–73] and catalysis[74–77]. Pores can be discrete or can form complete pathways or channels from one surface to another and play a crucial role in gas adsorption and fluid dynamics.[78] Depending on the size of these pores or channels, these materials can be classified as microporous (pore diameters of less than 2 nm), mesoporous (pore diameters between 2 and 50 nm) or macroporous (diameters above 50 nm).[79] There has been a recent trend towards the development of new porous materials incorporating pores with different size regimes to form hierarchical systems with interconnected pores and entirely new properties for desired applications. While the concept of introducing meso- and macropores into microporous materials has been extensively investigated in zeolitic porous systems,[80–82] development of metal-organic frameworks (MOFs) with open framework structures comprised of metal nodes and organic ligands has seen a rapid expansion of research interest last two decades. Advances in synthetic chemistry have reported numerous MOF structures (~70,000 structures reported in 2017[3] and just above 75,000 structures reported so far[4]) with potential use in gas storage,[10–12] gas separation,[83–86] catalysis,[13,14] carbon dioxide capture[87–89] and as semiconductor materials[90,91]. As the vast majority of MOF materials are microporous, great interest has developed in the creation of multiple porosities in these materials. While a number of excellent

reviews on hierarchical MOFs have recently been published,[92,93] the focus of these articles has been primarily on MOFs containing micro- and mesoporosity. The current review emphasises the recent achievements in the development of specifically macroporous MOF structures which, though important, are under-represented in the MOF field. Macropores are desirable in hierarchical porous materials to enable faster molecular diffusion and mass transfer, which is especially important for applications involving large molecules, viscous solutions or applications involving high throughput with low pressure gradients.

The benefits of a hierarchical structure for catalytic applications have been well-established in analogous inorganic systems. For example, hierarchical meso-macroporous structures in high internal phase emulsion (HIPE) templated halloysite nanotubes have been shown to have greatly improved catalytic activity for the conversion of cellulose to 5-hydroxymethylfurfural due to the catalyst's increased permeability and mass transfer efficiency.[94] Similarly, the macroporous nature of the support in hierarchical flower-like TiO_2 superstructures helps in facilitating more efficient photo-degradation of bulky dye molecules such as methyl orange.[95] The degradation of Rhodamine B under visible light irradiation using hierarchical core–shell Fe_3O_4/WO_3 was tested by Xi *et al.*, showing that the combination of mesoporous and macroporous regions enhances the photocatalytic activity with almost 100% decomposition achieved after 90 min compared to <20% and 50% for the iron(iii) oxide core and tungsten(vi) oxide respectively.[96] In addition, the large voids between the Fe_3O_4 and WO_3 in the hierarchical structure were deemed to synergistically reduce the recombination rate of photogenerated electron–hole pairs, further improving the photocatalytic degradation. The importance of pore size in catalysis was further illustrated by Feng and co-workers[97] using a hierarchical MOF composite comprised of PCN-222 (also known as MOF-545) and ZIF-8 to achieve size-selective catalysis. The PCN-222(Fe)@ZIF-8 composite was exposed to two molecules sensitive to oxidation by PCN-222, namely *o*-phenylenediamine (*o*-PDA) (0.5 x 0.5 nm) and 2,2′- azino-bis(3-ethylbenzothiazoline-6-sulfonic acid) (ABTS) (0.7 x 1.6 nm). Whilst PCN-222 successfully catalysed the transformation of *o*-PDA, the catalysis of the larger ABTS molecule was hindered due to constricted diffusion through the small pore-size window of ZIF-8. Thus, considering the importance of hierarchical structure in these inorganic systems, the ability to fabricate hierarchical MOF structures with macroporosity may be of great importance when considering future practical applications.

The nature of the porosity in a material can be determined by various characterisation techniques, which can be generally grouped into use of fluid penetration, scattering and

imaging. Fluid penetration techniques involve the filling of pores with a liquid or a gas, to obtain information on the pore sizes and volumes. For MOFs, (conventionally microporous materials), gas sorption (generally with nitrogen at 77 K up to 1 bar) is the most common characterisation method to establish the specific surface area, pore volume and pore size distributions. To obtain this information, the gas sorption isotherms are modelled using standard and widely accepted approaches such as the Brunauer–Emmett–Teller (BET) method for calculating surface area,[98] density functional theory (DFT) or the Horvath-Kawazoe (H-K) method for calculation of the pore size distribution in the micropore region, and the Barrett-Joyner-Halenda (BJH) for mesopore distribution.[99,100] However, nitrogen sorption at 77 K will typically not provide information on macropores larger than 100 nm.[99] For materials containing pores in the mesopore and macropore range (~4 nm – 60 μm), an alternative method is mercury intrusion porosimetry, which uses non-wetting mercury to penetrate the pores under pressure.[99,101] While this method can produce a macroporous size distribution in robust porous materials, it has the disadvantages of using a toxic compound (mercury) for the characterisation, cannot be used on soft or deformable structures and (unlike gas sorption) is destructive to the sample.

Scattering techniques, which involve bombarding the sample with, for example, X-rays, neutrons or electrons to obtain a pattern, and can be non-destructive while still enabling characterisation of the porosity. While powder X-ray diffraction (PXRD) and single crystal X-ray diffraction (SXD) are commonly used to study the microstructures of crystalline porous materials, small angle X-ray scattering (SAXS) can be used to probe the variations of scattering length density which occur over distances exceeding typical interatomic spacings to determine larger particle or pore sizes. Hence, SAXS can be used to calculate pore size distributions in porous materials (1- 100 nm range), and can be used for both crystalline or non-crystalline materials, and for materials having regular (but perhaps non-crystalline or disordered) porosity.[102] Both neutron and X-ray scattering can be used to provide information on the pore dimensions in a bulk sample, and, unlike fluid penetration, which can only give information on interconnected pores that are accessible to penetration by the fluid (“open”) porosity, can provide information on isolated, or “closed” pores in the material. However, for scattering techniques to be used for characterisation of porosity, there needs to be appropriate scattering length contrast between the pores and the surrounding material, which can be difficult in the case of X-ray scattering from MOFs, where the voids are often filled with air and the materials contain predominantly light organic materials such as C or H. Increasing the contrast may be

achieved by the filling of the pores with a suitable contrast agent,[103] which may have the undesirable effect of distorting the pores, for example, in the case of flexible MOFs, or where there is a soft, compliant matrix, such as a hydrogel. In cases where the scattering length density contrast is too small for X-rays, small angle neutron scattering (SANS) can be used.[104] As neutron scattering length varies independent of atomic number) even light atoms such as hydrogen and carbon can be easily distinguished using neutrons,[105] but the need for a neutron source means this is a far less widely-used technique.

As can be seen throughout the literature, imaging is by far the most common technique to visualise the macropores appearing in MOFs due to widespread accessibility of the technique and ease of use. Microscopy can provide valuable insight into the shape and spatial distribution of pores. For small macropores, (*e.g.* below 10 micron) scanning electron microscopy (SEM) and transmission electron microscopy (TEM) can be used to image porosity, and can be performed in a very straightforward way on a very small amount of sample. However, these imaging methods are not bulk techniques (with SEM in particular being restricted to definition of surface features), and can only sample a small number of particles and therefore may not be representative of the bulk porosity. For imaging of larger macropores (from a few tens of microns to millimetres in size), optical microscopy can be useful, but cannot not provide information on the connectivity or tortuosity of the interior pore network in monolithic structures. The ability of X-rays to penetrate light materials can be used in X-ray computed tomography (CT), whereby a series of 2D images of a material are computationally compiled and reassembled to obtain a 3D image.[106] X-ray CT can thus be used to image large pores in monolithic structures, though the resolution of such techniques is currently limited to a few tens of microns.[106] X-ray CT can thus be used to image large pores in monolithic structures, though the resolution of such techniques is currently limited to a few tens of microns.[106] Therefore, as will be shown in this review, due to the complexity of such materials, a combination of several techniques may be needed obtain a full description of the macroporosity in hierarchical MOF structures.

The routes to formation of such complex structures are equally varied. In terms of approaches to increase pore dimensions in MOFs using synthetic chemistry, the typical methods used in MOF synthesis to produce mesopores (such as extending ligand lengths or enlarging building blocks) are of limited use in the creation of much larger macropores. This is due to the difficulties in stabilising these pores against collapse upon desolvation during activation.[18] Hence, the formation of macroporosity (rather than mesoporosity) in MOFs necessitates the

use of very different fabrication approaches. In this review, we focus on the synthetic strategies and challenges of creating MOFs with hierarchical pore structures containing macropores to provide readers with a wider scope of the strategies available for fabrication of hierarchical macroporous MOFs.

We have grouped the macroporous MOF structures that have been studied together under four broad approaches, which are presented in order of most commonly-reported method to least reported as follows: macroporous MOFs synthesised via structural templating, defect formation, use of compressed or supercritical CO_2 ($scCO_2$), and via 3D printing routes (as summarised in Figure 15 and Table 1).

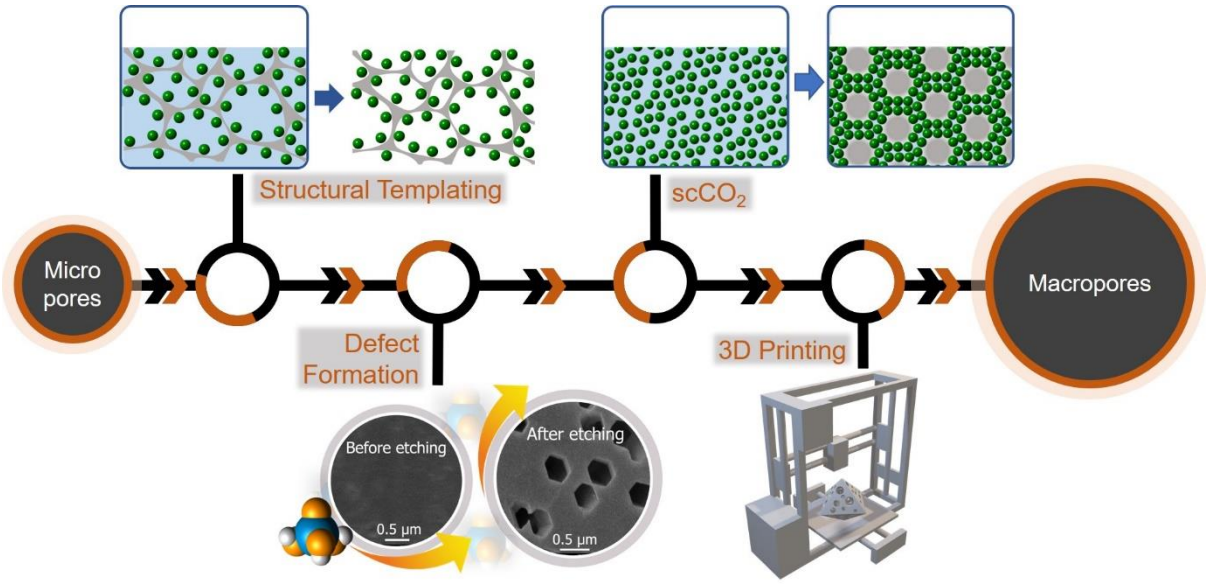

Figure 15. Schematic representation of synthetic methods for hierarchical MOFs with macroporosity. Aggregated clusters of MOFs are represented by green spheres.

Broadly speaking, structural templating involves use of a template containing macroporous voids to produce a macroporous composite structure by directly growing the crystalline MOF either on or around a template. The template can be "hard" (*e.g.* a foam or porous monolith) or "soft" template (*e.g.* a gel or emulsion) and can be retained or removed after templating.

Defect formation describes the disruption of the periodic crystalline structure of the MOF *e.g.* by incorporating a bulky ligand during synthesis which introduces a porous defect or by selective removal of sites to produce pores *e.g.* via post-synthetic acid etching of MOF single crystals.

Compressed or supercritical CO_2 has been used extensively for the removal of solvents and soft templates to produce porous aerogel structures, but when used in expanded solvent systems,

$scCO_2$ has recently been shown useful for producing macroporous voids during MOF synthesis.

Finally, the recent use of 3D Printing combines MOFs with binders to create MOF-based inks capable of forming hierarchical monoliths on deposition. This represents a new method with potential to enable the construction of hierarchical monoliths with complex geometries.

Most of these methods can be employed either using MOF precursor solutions (termed "direct synthesis") or using pre-formed MOFs (post-synthetic treatment), as seen in Table 1. This review also describes strategies involving $scCO_2$ which were originally used to activate MOFs,[47] yet can be tailored to create macroporous structures via an *in situ* method.

Table 1. A summary of preparation techniques, crystallisation routes and templates for the formation of hierarchical MOFs with macroporosity.

Preparation techniques	**Macropore formation route**	**Templates, substrates, modulators or reagents used**	**MOFs prepared using these methods**	**References**
Hard structural templating	Direct synthesis	Macroporous carbon derived from kenaf stem, polymer derived ceramic (PDC) foam, oxide-bonded silicon carbide and alumina (Al_2O_3), ceramic foams (CF), copper foam	HKUST-1, CAU-10, UiO-66(Zr), MOF-5	112, 115, 117, 119
	Post-synthetic treatment	Nickel foam	MIL-101(Cr)	113
Soft structural templating	Direct synthesis	Cellulose solution, konjac glucomannan, graphene-oxide, melamine foam (MF), three-dimensional polystyrene (PS), *N*,*N*-dimethyloctylamine (DMOA), polyacrylamide (PAAm)	ZIF-8, ZIF-9, ZIF-12, PCN-224, HKUST-1	122, 123, 127, 128, 129, 130, 131
	Post-synthetic treatment	Melamine sponge	ZIF-67	125
Defect formation	Direct synthesis (linker modulation)	Alkyl chains, monocarboxylic acids	MOF-5, UiO-66	145, 146
	Post-synthetic treatment (acid etching)	Phenolic acid, cyanuric chloride and tetraethylamine (TEA), phosphoric acid,	ZIF-8, IRMOF-3, MIL-	147, 148, 149, 151 152

		hydroquinone, H_3BO_3 and NaCl	101(Fe), HKUST-1	
Use of compressed or supercritical CO_2	Post-synthetic treatment ($scCO_2$ drying)	Emulsion	HKUST-1, AlBTC, AlBDC	162, 164
	Direct synthesis (expanded solvent)	N-EtFOSA/TMGT solution, DMF, DMSO/MeOH	Zn-BTC, HKUST-1, Co-BTC	167, 168, 170, 174
3D printing	Post-synthetic incorporation	Polyvinyl alcohol (PVA), trimethylolpropane propoxylate triacrylate (TMPPTA), polylactic acid (PLA)	MOF-74(Ni), UTSA-16(Co), UiO-66, ZIF-8	199, 200, 201
	Direct synthesis	Anionic 2,2,6,6-tetramethylpiperidine-1-oxylradical-mediated oxidised cellulose nanofibers (TOCNFs)	ZIF-8 and MIL-100(Fe)	202

2.2. Preparation techniques for hierarchical MOFs with macroporosity

2.2.1 Macroporous MOFs synthesised using structural templating

The most common approach to the introduction of macropores into an intrinsically microporous MOF is via use of structural templating to form a hierarchical structure. As demonstrated for a multitude of other porous materials systems, the macroscopic shape and the pore size of the resulting hierarchical structures can be well controlled through judicious choice of template.[107–111] The resulting hierarchical porous MOF structures could potentially exhibit improved properties such as more rapid molecular diffusion compared to the respective non-hierarchical MOFs, better mechanical or thermochemical stability, or immobilisation of nanoparticulates. Thus, they are preferentially used in some applications that require easy integration and regeneration *e.g.* for adsorbent systems[112,113] or exceptional mass transfer *e.g.* for catalyst supports[114].

The macroporous MOF structures deriving from the template approach can be divided into two main categories; ones where the template remains in the final MOF structure, forming a

composite material or ones where the template is sacrificial and is removed to obtain a macroporous structure in the pure MOF (often called a MOF aerogel or a foam). Template types can be broadly grouped into "hard" and "soft". Hard templates may be carbons,[115] ceramics,[112,114,116–118] and metals[113,119–121]) and are typically in the form of monoliths, porous membranes or foams.[113,115,122] As it is difficult to remove hard templates, the majority of these templates act as supports, resulting in macroporous composite MOF structures.

Hard structural templating

As an example of direct MOF synthesis on a hard template to obtain a hierarchical structure with macropores, Xie and co-workers grew HKUST-1 MOF crystals on three-dimensional kenaf stem-derived macroporous carbons (3D-KSCs), forming a composite material with a macroporous structure.[115] In this work, it was shown that a large number of smooth-faced octahedral HKUST-1 crystallites with maintained morphology were formed on the surface and inner walls of the macroporous 3D-KSC template (Figure 16a and b), with the amount of HKUST-1 loaded onto this template increasing with increased reaction time. The as-obtained composites were tested for electrochemical sensing of glucose, showing very promising activity with a relatively wide linear range (15.84 μM - 5.62 mM), low limit of detection (4.8 μM) and a high sensitivity (28.67 $\mu A mM^{-1} cm^{-2}$). The excellent electrocatalytic activity was attributed to the presence of macropores in the hierarchical structure which lead to improved mass transfer.

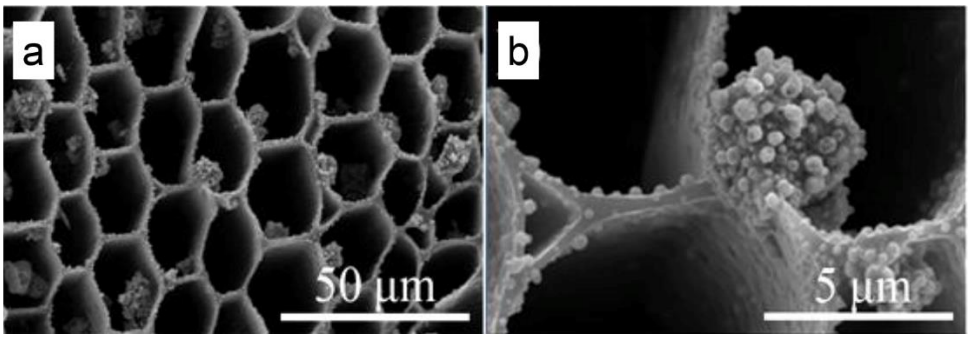

Figure 16. SEM images of HKUST-1/3D-KSCs$_{800}$ at different magnifications, showing the growth of microporous HKUST-1 crystals on the 3D-KSCs$_{800}$ macroporous template. Reprinted with permission from Ref. 115. Copyright 2018 Journal of Alloys and Compounds.

Using a similar hard template, Sandra *et al.*[112] synthesised a series of silicoboron carbonitride (Si/B/C/N) polymer derived ceramic (PDC) foams with micro/macroporosity using silicon and carbon high internal phase emulsions (HIPE) as *exo*-templates and boron modified polycarbosilazane as an organosilicon precursor. HKUST-1 was impregnated by growing the

MOF inside the macropores of the PDC to form Si/B/C/N@MOF composite foams, thus allowing faster and more efficient uptake and release kinetics, in particular for CO_2 capture.

Direct synthesis of MOFs on hard templates has also been shown by Betke *et al.*[117] and is readily adaptable to a variety of MOF types, with a range of macroporous MOF@ceramic foam composite materials being formed by growing MOFs such as HKUST-1, CAU-10, MIL-101(Cr) and UiO-66(Zr) on macroporous oxide-bonded silicon carbide (ob-SiC) and alumina ceramic foams (CF). In these cases, where the MOFs were being tested for use in sorptive heat pump/heat storage applications, the macroporous ceramic structure not only had benefits for the mass transfer and adsorption/desorption kinetics (which had the effect of decreasing cycling times), but also enhanced heat transfer in comparison to the powdered MOF, increasing the potential for adsorptive cooling in this application. The surface properties of the CF were modified by silanisation using aminopropyl triethoxysilane/terephthaloyl chloride treatment prior to the MOF crystallisation to obtain a thick homogeneous MOF coating on the surface. The thickness of the MOF on the surface was also shown to be influenced by an alumina sol coating on the cellular CF support before silanisation, as supported by the SEM images of HKUST-1 on the surface without (Figure 17a and c) and with (Figure 17b and d) alumina sol coating. The coating thickness of HKUST-1 crystals ranged between 112 µm and 264 µm for the ob-SiC based composites and between 36 µm and 151 µm for the HKUST-1@alumina composites.

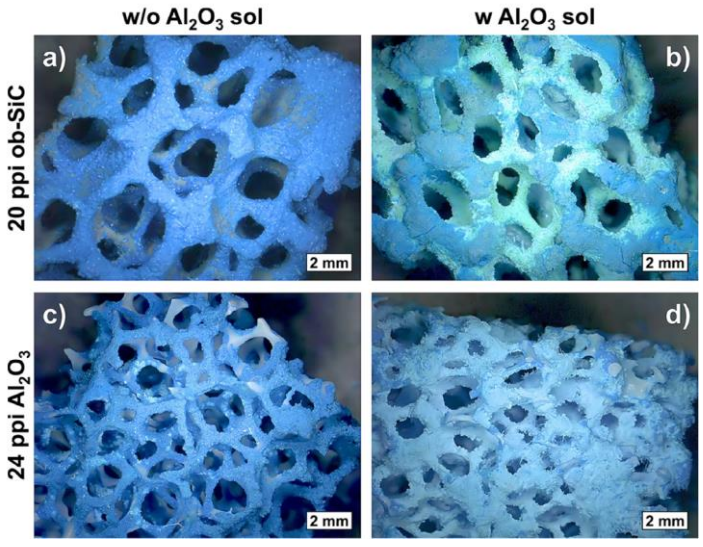

Figure 17. SEM images of HKUST-1 coatings on ob-SiC and Al_2O_3 ceramic foams without (a and c) and with preliminary alumina sol coating (b and d). The HKUST-1 coating layers on the ob-SiC composites are thicker than those on Al_2O_3 composites. Reprinted with permission from Ref. 117. Copyright 2017 Microporous and Mesoporous Materials.

Similarly, Li *et al.* reported a facile synthesis of hierarchical porous MOF-5 structure using a copper foam as a template, for removal of volatile sulphides from plant sources.[119] The MOF composite was prepared by solution impregnation of zinc nitrate and terephthalic acid into a pre-treated copper foam. The macroporous MOF monolith was tested for the extraction of volatile organic sulphur compounds with detection values of 6.0–54.6 μg g^{-1}.The extraction process could be replicated at least 200 times, indicating that the formation of the macroporous composite structure may have been beneficial for the stability of MOF-5, which is widely recognised for being prone to hydrolysis, particularly in humid environments.

While the direct crystallisation of MOFs onto a macroporous template is the most commonly used method, in addition to the direct synthesis and growth approaches discussed above, a microporous MOF can also be endowed with a macroporous structure by combining a macroporous substrate with a pre-formed MOF. For example, Ren *et al.* prepared MIL-101(Cr) powders and immobilised the nanocrystals on a macroporous nickel (Ni) foam via spray coating.[113] The PXRD pattern of the MIL-101/Ni foam composite showed peaks which correspond to both MIL-101 powders and Ni foam (Figure 18a). The incorporation of the MOF crystals on the Ni foam was further evidenced by SEM, in which the porosity of the Ni foam was reduced by the presence of multi-layered MIL-101 powders on its surface (Figure 18b).

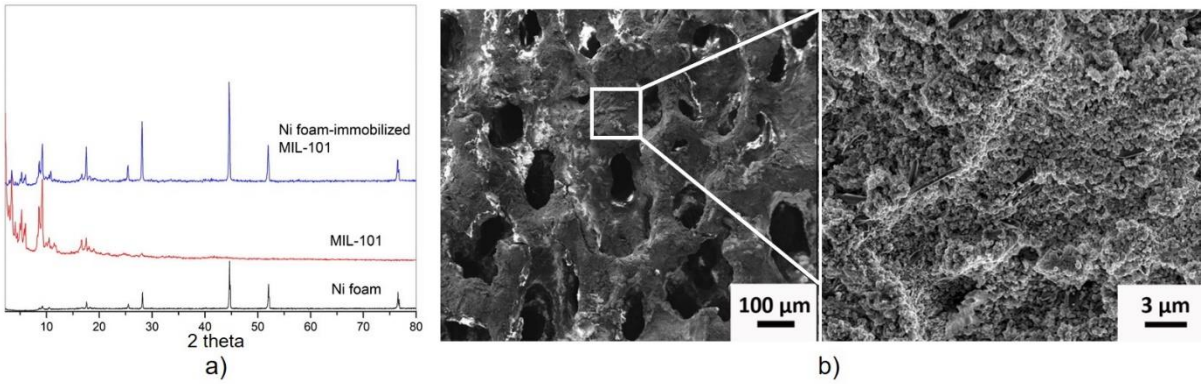

Figure 18. a) The PXRD patterns of Ni foam-immobilised MIL-101(Cr) (blue) showing the presence of peaks which correspond to both Ni foam (black) and MIL-101(Cr) nanocrystals (red). b) SEM images of Ni foam-immobilised MIL-101(Cr) showing the presence of multi-layered MIL-101(Cr) nanocrystals on the macroporous Ni foam. Reprinted with permission from Ref. 113. Copyright 2015 Journal of Alloys and Compounds.

The MIL-101/Ni foam composite was tested for hydrogen storage and the composite with 81 wt.% loading of MIL-101(Cr) nanocrystals exhibited a hydrogen adsorption capacity similar to pure MIL-101(Cr) powders. Although an increase in hydrogen uptake was not observed, the

immobilisation of MIL-101(Cr) powders onto a macrostructural support provides a facile method to process MOF powders and immobilise the nanoparticulates for applications in practical systems.

Soft structural templating

In situations where flexibility of the porous support is desired, soft macroporous templates are sometimes advantageous. Soft templates can include surfactants,[123] polymers,[124–126] gels and emulsions. Flexible macroporous composite materials were developed by Bo *et al.*, who reported a facile method for the direct synthesis of a cellulose hybrid aerogel of ZIF-8 (ZIF-8@CA) in which zinc cations were dispersed in a cellulose solution before prompting nucleation reaction with 2-methylimidazole to form the MOF as illustrated by the schematic in Figure 19.[127] ZIF-type materials are favoured candidates because of their high water stability which is crucial for gel formation without losing the original crystallinity. As shown in the inset of Figure 19, the resulting hybrid material retained the original ZIF-8 particle size (20-40 nm) with hierarchical porous structures (pore size between 10 and 100 μm). Cr(VI) sorption was performed on this sample, showing a greatly improved uptake in the composite material when compared with a single component. A similar synthetic method was applied to the synthesis of ZIF-9 and ZIF-12 on CA (Figure 20a and b, respectively),[128] which showed macropores with improved catalytic performance in p-nitrophenol degradation (90% in 1 h). Preparation of a ZIF aerogel via a one-pot strategy was further explored using various templates such as biodegradable konjac glucomannan by deacetylation[129] and graphene-oxide,[130] and resulted in structures with outstanding photoelectric, mechanical and thermal properties.

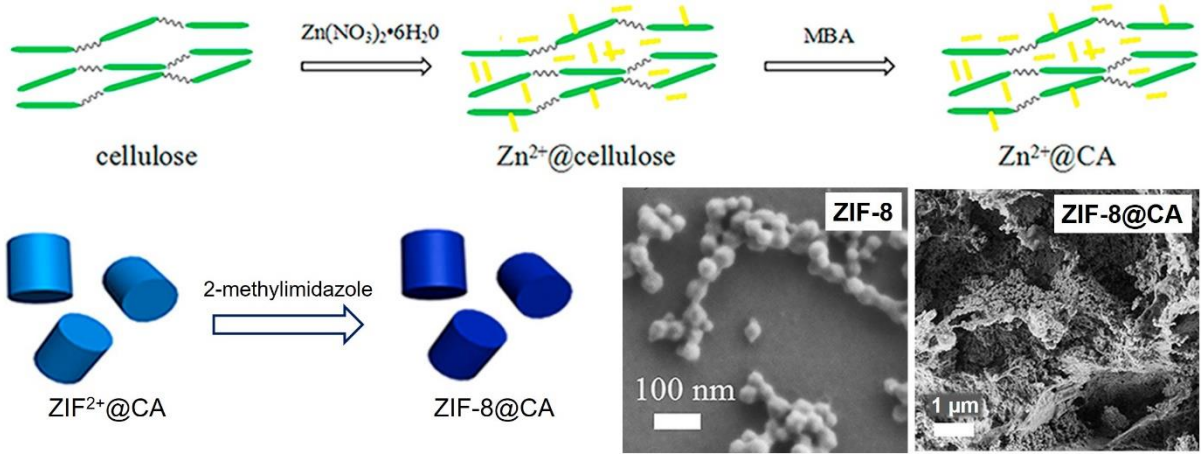

Figure 19. Schematic illustrations showing the preparation of ZIF-8@CA and the resulting SEM images. Reprinted with permission from Ref. 127. Copyright 2018 Journal of Solid State Chemistry.

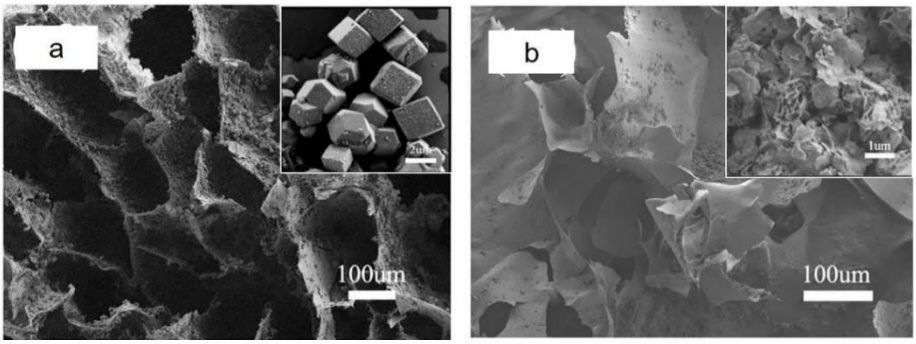

Figure 20. SEM images of ZIF-9@CA and pure ZIF-9 inset (a); and ZIF-12@CA and pure ZIF-12 inset (b). Reprinted with permission from Ref. 128. Copyright 2018 Chemical Engineering Journal.

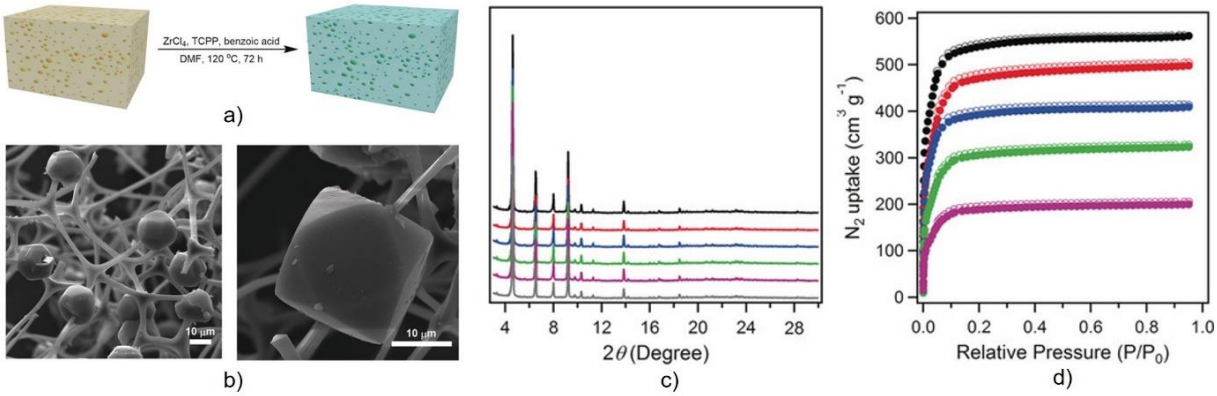

Figure 21. a) The procedure for the preparation of PCN-224 decorated melamine foam composites. b) FE-SEM images of PCN-224(Fe)/MF composite depicting the melamine foam network homogeneously decorated with PCN-224(Fe) microcrystals. c) The high similarities between the PXRD patterns of PCN-224(Fe) (grey) and PCN-224(Fe)$_{50\%}$/MF (purple), PCN-224(Fe)$_{100\%}$/MF (green), PCN-224(Fe)$_{150\%}$/MF (blue), PCN-224(Fe)$_{200\%}$/MF (red) and PCN-224(Fe)$_{325\%}$/MF (black) indicating the structural stability of the MOF composites. d) N_2 sorption isotherms of PCN-224(Fe)$_{50\%}$/MF (purple), PCN-224(Fe)$_{100\%}$/MF (green), PCN-224(Fe)$_{150\%}$/MF (blue), PCN-224(Fe)$_{200\%}$/MF (red), and PCN-224(Fe)$_{325\%}$/MF (black). The BET surface areas increased with the increasing loading amount of PCN-224(Fe) in the composites. Reprinted with permission from Ref. 131. Copyright 2018 Angewandte Chemie International Edition.

Another example of using soft structural templates in direct synthesis was given by Huang *et al.*,[131] who reported a series of porous coordination network (PCN) MOFs that were integrated into a macroporous monolithic melamine foam (MF) using a one-pot synthesis (Figure 21a and b), hierarchical porosity, and a flexible and elastic texture, which may be favourable for

heterogeneous catalysis. Additionally, the BET surface areas were found to increase with the loading amount of PCN-224(Fe) in the composites (1704 – 1623 m^2 g^{-1}) (Figure 21d). The positive effect of the macroporous structure on the application of these samples was confirmed in the highly-efficient catalytic epoxidation of unsaturated cholesteryl esters. The 2 mol% of PCN-224(Ru)200%/MF showed an excellent yield (92%) of the corresponding epoxide after 36 h, compared to a yield of 56% using normal PCN-224(Ru) and 0% conversion using a control of pure melamine foam.the corresponding epoxide after 36 h, compared to a yield of 56% using normal PCN-224(Ru) and 0% conversion using a control of pure melamine foam.

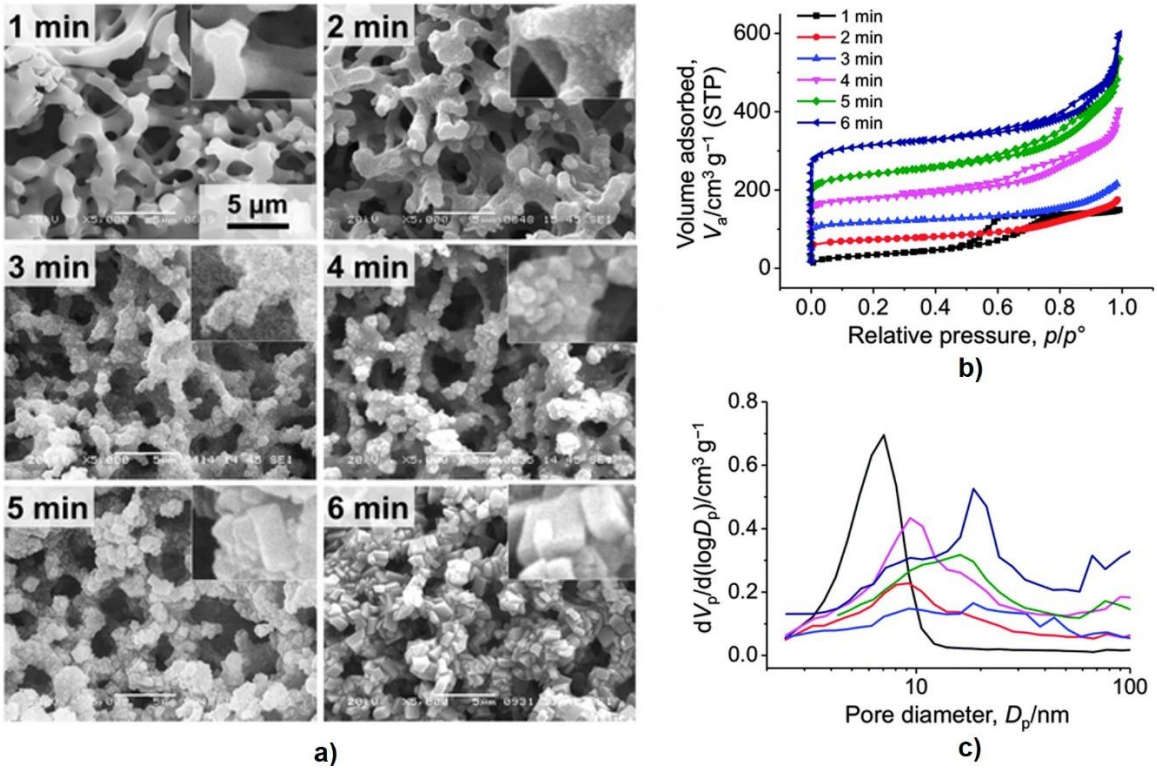

Figure 22. a) SEM images of the conversion of Cu-06 to HKUST-1 with 1-minute time intervals, showing the growth of polyhedral crystallites with the preservation of the co-continuous macroporous gel structure. All the images are in the identical magnification. N_2 sorption isotherms (b) and BJH pore size distributions (c) with respect to increased immersion times. The BET surface areas and pore sizes increased with immersion times. Reprinted with permission from Ref. 132. Copyright 2015 Royal Society of Chemistry.

Moitra *et al.* developed an innovative protocol for the direct synthesis of a macroporous monolithic HKUST-1 composite by conversion of $Cu(OH)_2$-based networks in a polyacrylamide (PAAm) gel.[132] The presence of PAAm in the original (oxy)hydroxide network supported the scaffold of $Cu(OH)_2$ by chelating the copper ions with the N-groups in the amide, resulting in gelation and producing a co-continuous network which was converted to HKUST-

1 through coordination by H_3BTC. The macropore size within the aggregated particles could be controlled by changing the amount of PAAm from 0.3 to 1 g, or by varying the immersion time in H_3BTC from between 3 and 6 min (Figure 22a). In addition, enhancements in N_2 uptake (Figure 22b) and pore size (Figure 22c) were reported with increased immersion times. The resulting HKUST-1 monolith showed high crystallinity, a high surface area of 1,315 $m^2 g^{-1}$ and good mechanical properties (stress values at catastrophic failure of 1.5 MPa), which is promising for possible applications to continuous flow reactors.

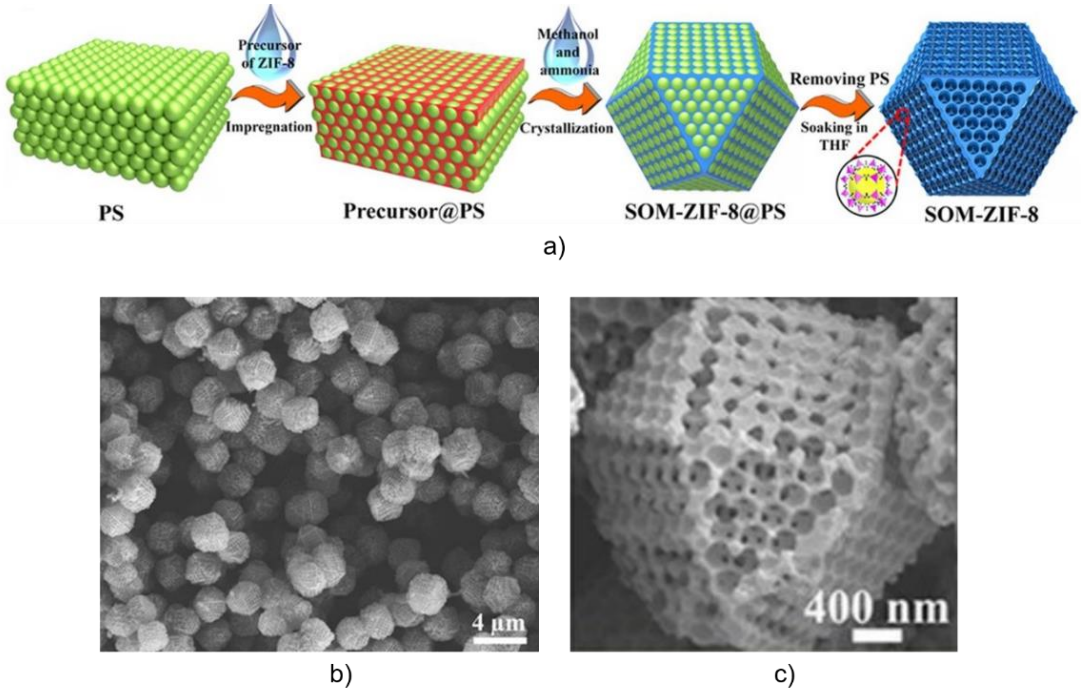

Figure 23. a) Schematic diagram of SOM-ZIF-8 synthesis. SEM images of SOM-ZIF-8 (b) and an isolated crystal of SOM-ZIF-8 (c) showing the tetrakaidecahedron morphology. Reprinted with permission from Ref. 122. Copyright 2018 Science.

Soft templates are often beneficial where facile template removal is desired. As an example of where a polymer has been used as a sacrificial soft template to form a macroporous MOF, a hierarchical SOM-ZIF-8 MOF was formed by impregnating ZIF-8 precursors into the interstices of three-dimensional polystyrene (PS) spheres in a mixture of methanol/ammonia (Figure 23a).[122] SEM confirmed that ZIF-8 single crystals were uniformly grown around the PS template and the overall network displayed a tetrakaidecahedron morphology (Figure 23b and c). The macroporous framework could be accessed by dissolving the PS template in THF, and subsequently activated via removal. The presence of macropores in the MOF was confirmed by mercury intrusion porosimetry and the size of the macropores could be modified (80 – 470 nm) by changing the diameter of the polystyrene templates. Furthermore, Shen *et al.*

reported that single crystal growth is governed by the solvent system and the crystal size could be tuned by modifying the ratio of the methanol/ammonia mixture.

Xi *et al.* reported the soft-templated synthesis of a HKUST-1 framework that contains micro-, meso- and macropores,[123] formed by a mixture of a hydroxy double salt (Zn and Cu based) with an ethanolic solution of *N*,*N*-dimethyloctylamine (DMOA) and benzenetricarboxylic acid (H_3BTC) at room temperature. The DMOA surfactant was employed as a sacrificial template to direct the formation of meso- and macropores whereas the hydroxy double salt accelerated crystal nucleation. The role of DMOA as a template was demonstrated by mesodynamics simulation in which the introduction of DMOA into the reaction mixture resulted in the formation of supramolecular micelles. Subsequently, the MOF precursors were self-assembled on the surface of the template micelles, which led to the formation of the hierarchical porous HKUST-1 upon the removal of DMOA template. SEM revealed the hierarchical nature of this MOF whereby continuous pore voids were formed between the nanoparticles. TEM further confirmed the abundance of mesopores and macropores (pore sizes of 40–100 nm) in the final product. Due to the presence of macropores which contribute to high molecular diffusion, the hierarchical MOF exhibited a high toluene storage capacity (646 mg g^{-1} at 298 K), representing a 25 wt.% increase compared to that for the non-hierarchical HKUST-1 (516 mg g^{-1}).[133] This value is also much higher than other microporous MOFs and zeolites.[134–136] The preparation of this hierarchical MOF can be expanded to other MOF systems such as ZIF-8 and the degree of porosity can also be tuned by adjusting the amount and type of surfactant used.

In addition to direct synthesis, it may also be the case that preformed MOFs can be deposited onto a macroporous soft template. For example, Lin *et al.* used a surfactant-assisted dip coating method to similar effect, to synthesise a three dimensional hierarchically porous ZIF-67/melamine sponge composite (as illustrated by the schematic of Figure 24a and b).[125] The ZIF nanocrystals were dip-coated on the surface of a surfactant modified melamine sponge by immersing it in ZIF-67 suspension while stirring for 3 hours. The self-assembly of MOF crystals on the modified melamine sponge occurs via electrostatic attractions and possibly π–π stacking interactions. The SEM image (Figure 24c and d) showed that the clean, smooth surface of the melamine sponge became roughened by the ZIF-67 coating. Four types of surfactants were used for the modification of the melamine sponge including anionic sodium dodecyl benzene sulfonate (SDBS), cationic cetyltrimethylammonium bromide (CTAB), non-ionic hydrophobic sorbitan monooleate (denoted as SPAN-80) and non-ionic hydrophilic Triton X-100 to study the effect of surfactant properties on the ZIF-67 loading. It was found

that increasing the concentration of CTAB and Triton X-100 did not increase the ZIF-67 loading. However, an increase in ZIF-67 loading was observed when the melamine sponge was modified by SDBS and SPAN-80. According to zeta potential measurements, in the testing pH range, Triton X-100 was found to be neutral, ZIF-67 and CTAB displayed positive surface charges, and SDBS and SPAN showed negative surface charges. The increase in ZIF-67 loading with SDBS and SPAN surfactants was attributed to the electrostatic attraction between the positively surface charged ZIF-67 and negatively surface charged SBDS and SPAN. This approach to synthesising the ZIF-67/melamine sponges could be further used to fabricate various shapes such as fibres or membranes and can be used as adsorbents for the removal of toxic large molecule pollutants like malachite green dye.

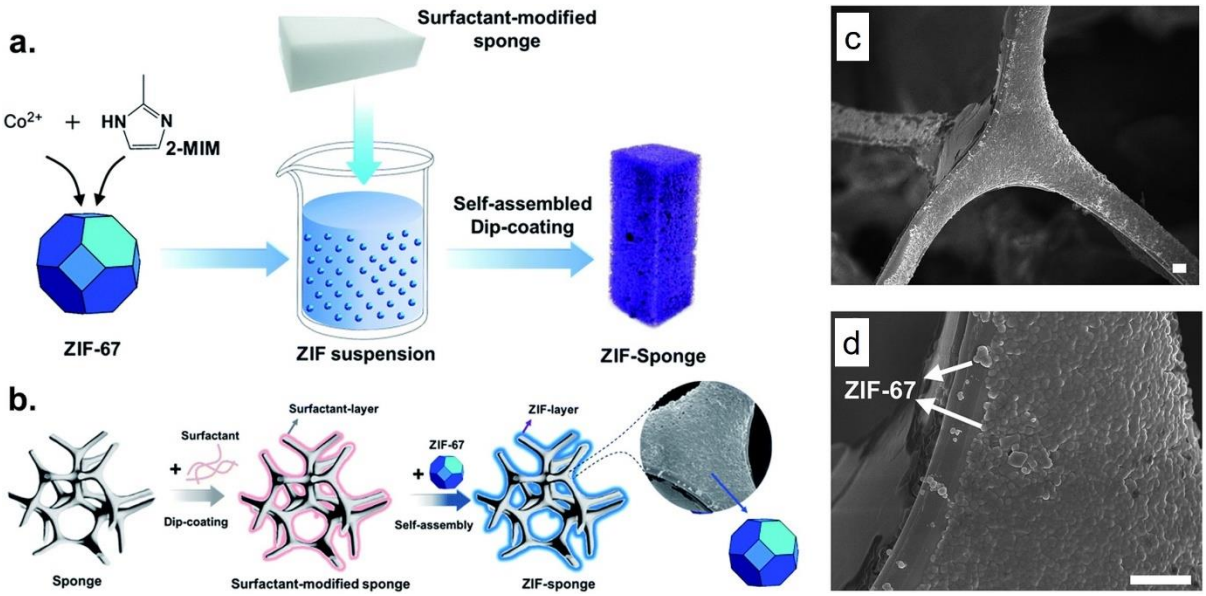

Figure 24. a and b) Schematic illustrations showing the preparation of ZIF–sponge, showing surfactant-assisted dip-coating self-assembling process (a) and surface-modification of the sponge skeleton first with a surfactant and then ZIF-67(b). c and d) SEM images of ZIF–sponge prepared with the assistance of SDBS under different magnifications (the scale bar is 2 μm), showing ZIF nanocrystals were dip-coated on the surface of melamine sponge. Reprinted with permission from Ref. 125. Copyright 2015 Royal Society of Chemistry.

The use of structural templating agents remains the most established method in the formation of macroporous MOFs due to the wide range of templates and templating agents that can be employed using this technique. Based on the examples given thus far, the resulting hierarchical structures generally adopt the shape of the templating agents. It was also shown that these templates could be introduced either in the reaction solution during MOF synthesis or in the precursor solution where the prepared MOFs were dispersed. The final materials could be

obtained as MOF-based composites with the template retained or as pure MOF superstructures without the template. When the templating agents are incorporated in the final MOF structures, in addition to the immobilisation of the MOF crystals, they may also contribute to improved mechanical and thermochemical stability of the MOF composites. In the case of MOFs with sacrificial templates, washing processes to remove the templates are required, which in some cases (such as coordination polymer frameworks, silicates and MCM-41) can be detrimental to the stability of the pore structures.[137–140] Furthermore, incomplete removal can lead to occlusion of the pores and therefore loss of functionality for gas sorption/catalytic reactions. In terms of potential uses, the MOFs formed via this method have been utilised in various applications which range from catalytic applications, heat and mass transfer to extraction of volatile compounds.

2.2.2. Macroporous MOFs synthesised via defect formation

From the point of view of sustainable processing, the ability to form macroporosity in the absence of sacrificial templates or scaffolds would be preferable. An alternative successful strategy to obtain hierarchical porous MOFs without using templates is through direct introduction of defects into microporous structures. This process could be carried out using either *in situ* synthetic methods (*e.g.* using linker modulation) or using post-synthetic treatment (*e.g.* via acid etching). Linker modulation methods predominantly produce mesoporous defects in microporous MOFs. Yuan *et al.* demonstrated linker labilisation to introduce mesoporosity in microporous MOFs. Using this method, a pro-labile organic linker was used for the synthesis of PCN-160 MOF and the defect in the preformed MOF was introduced by splitting this pro-labile linker into removable monocarboxylate moieties under acidic conditions which improved their gas adsorption and catalytic properties.[141] Similarly, Kim *et al.* created mesoporous defects in microporous HKUST-1 using an acetic acid fragmented linker co-assembly method. A small amount of acetic acid removed the BTC linker to create mesoporous defects. On increasing the amount of acetic acid, metal clusters in MOF were removed, which resulted in interconnected defect sites and mesoporous channels inside the MOF, which enhanced the methane storage capacity in the defective MOF [142]. These methods have been employed extensively in numerous studies to functionalise meso- and macropores with straightforward synthetic procedures and a number of effective mechanisms have been demonstrated,[143,144] but there have been additional reports of the use of similar methods for production of macroporous structures.

Examples of macroporous materials formed by *in situ* linker modulation methods include the introduction of bulky aliphatic chains to MOF linkers in MOF-5 to result in sponge-like or pomegranate-like crystallite structures[145] and the use of alkyl chains as modulators for macropore formation in UiO-66. In the case of the hierarchical macroporous MOF-5 structures, the formation of either the sponge-like (spng-MOF-5) or pomegranate-like (png-MOF-5) structures were the result of incorporating different proportions of the linkers containing bulky void-forming alkyl chain (50% and 30% incorporation, respectively). The modulators were shown by gas sorption to prompt formation of additional mesoporosity and macroporosity into MOF-5, which influenced the CO_2 uptake properties of the different structures. However, the additional beneficial effects of having such an interconnected macroporous structure which was evidenced from the SEM, would have been more obvious if a bulkier adsorbent than CO_2 had been employed. In the case of the defective UiO-66 synthesised by a modulator-induced defect-formation strategy described by Cai *et al.*,[146] Zr^{4+} ions reacted with less than stoichiometric amounts of BDC^{2-} linkers and COO^- ions in monocarboxylic acids as a modulator to pre-coordinate Zr-oxo clusters. The alkyl chain on the modulators then linked these clusters to create large voids during synthesis (Scheme 1).

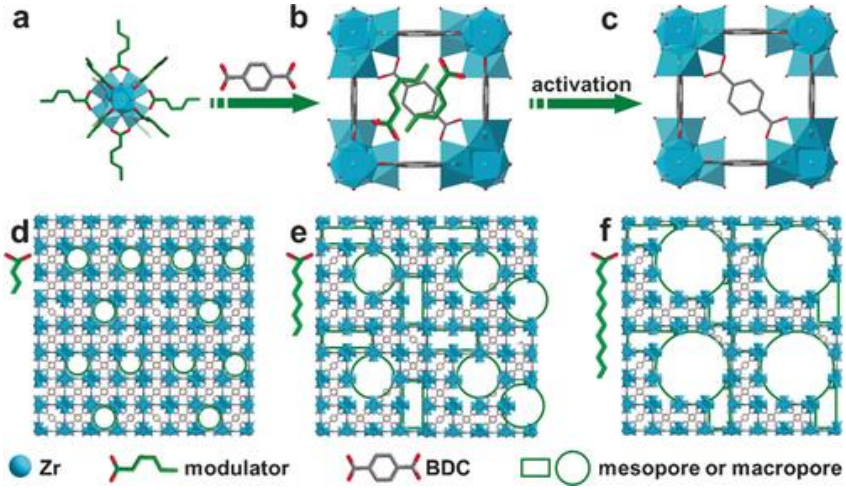

Scheme 1. Schematic illustration of the synthesis of HP-MOFs with adjustable porosity using UiO-66 as an example. Reprinted with permission from Ref. 146. Copyright 2017 Angewandte Chemie International Edition.

The pore sizes were tuneable by changing the molar ratio of Zr to H_2BDC and alkyl chain length. The ability to transport large molecules through the defect structure was demonstrated using the catalytic methanolysis of styrene oxide, indicating that the hierarchical porous UiO-66 with additional large mesopores exhibited superior catalytic activity when compared to the normal MOF. It was foreseen by the authors that macropores could be obtained with further

investigation of the alkyl chain length in the modulator. However, they noted that the high pK_a values of elongated alkyl chains could decrease the solubility and coordination ability of the modulator with Zr-oxo clusters, which might result in adverse effects such as pore shrinkage.

An alternative approach for synthesis of defective MOFs with macropores is via the post-synthetic etching of prepared microporous MOFs. This can be done either by an acid etching mechanism whereby selected acid molecules diffuse through the MOF structure, forming large voids over time, or by synergistic etching where bulky acid molecules modify and protect the MOF surface to obtain the holey materials.

Koo *et al.*[147] investigated a size selective acid diffusion method for the post synthetic treatment of MIL-100 (Fe) using phosphoric acid (d = 0.61 nm) as the etching agent. During the etching process phosphoric acid could specifically diffuse through the hexagonal windows (d = 0.89 nm) but not through the pentagonal windows (d = 0.49 nm) of MIL-101(Fe) to form macropores in the framework, preserving the microporous nature by selective removal of metal nodes and BTC linkers. The framework crystallinity and morphology of the MOF crystals were well maintained even after post-synthetic treatment. Note that this process cannot be achieved by employing smaller acids such as HCl (d = 0.34 nm) using the same manner. This is simply because the small cages could also be attacked during etching, leading to complete collapse of the MOF structure. This etching method seems to be effective for the creation of hierarchical porous MOFs with tuneable pore sizes. However, as mentioned in the literature,[147] these approaches are only applicable for highly water-stable MOFs.

A similar idea was developed by Ahmed *et al.* with their report on solvothermal post-synthetic modification of microporous HKUST-1 (Figure 25a).[148] By etching prepared HKUST-1 in weakly acidic hydroquinone (pK_a = 9.85 in water) at 150 ˚C for 16 h, macroporous channels with pore sizes ranging from 500 nm to 10 μm ((via Hg intrusion porosimetry – see Figure 25c and d) were observed within HKUST-1 microparticles while retaining the structure of the large crystallites and high surface area. The etching process was further investigated at 120 ºC and 180 ºC for 16 h, and 150 ºC for 72 h, showing that the degree of macropore formation was dependant on reaction time and temperature. By using ICP analysis of HKUST-1 on the etching solution, it was found that Cu(II) ions were selectively removed from the framework when using a hydroquinone solution. This was also confirmed by a slight distortion in the single crystal XRD patterns, likely caused by Cu deposits generated during the modification process. Other reagents (including H_3BO_3 and NaCl) were also tested in this process. Etching HKUST-1 in H_3BO_3 and NaCl resulted in the formation of large etched holes at the centre of the particles

(Figure 26a and b), yielding additional macropores in this MOF. Diffusion of acid molecules within the MOF particles was considered as the main mechanism, which can be also used to explain why edges of these etched MOFs are unaffected. The synthesised macroporous HKUST-1 crystals were then successfully used to separate styrene and ethyl benzene when packed into a high performance liquid chromatography (HPLC) column.

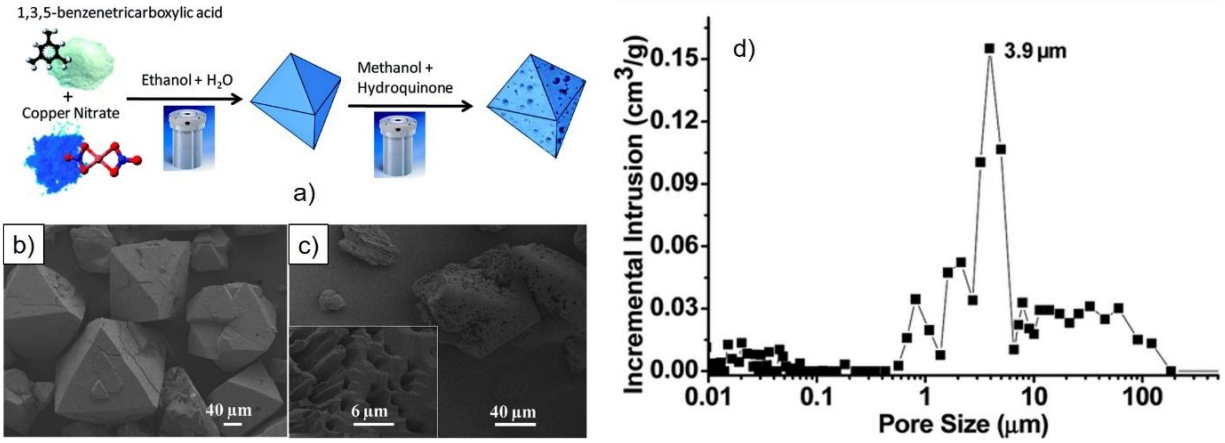

Figure 25. a) Schematic representation for the preparation of HKUST-1 particles and the subsequent modification to produce macroporous HKUST-1 particles. b) SEM image of HKUST-1 microparticles prepared by solvothermal synthesis with water–ethanol (1 : 1 v/v). c) SEM image of modified HKUST-1 particle with hydroquinone at 150 °C for 16 h, showing the macroporous microparticles. d) Macropore size distribution as measured by Hg intrusion porosimetry, with an intrusion pore volume 2.65 cm^3 g^{-1}, for the modified HKUST-1 particles. Reprinted with permission from Ref. 148. Copyright 2014 Royal Society of Chemistry.

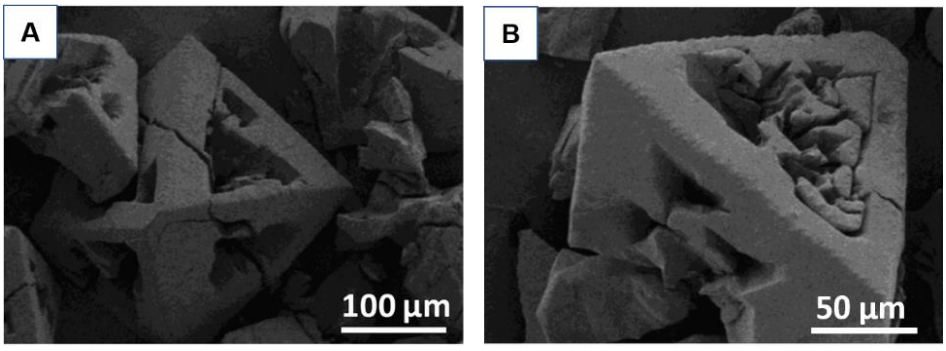

Figure 26. SEM images of HKUST-1 particles modified by different reagents other than hydroquinone in 50 µl boric acid aqueous solution at 150 ˚C for 16 (a) and in 50 µl NaCl aqueous solution at 150 ˚C for 16 h (b), showing some large etched holes were formed from the centre of the particles. Reprinted with permission from Ref. 148. Copyright 2014 Royal Society of Chemistry.

Prompted by the size-selective acid diffusion mechanism, a defective HKUST-1 was synthesised by Doan *et al.* using a phosphoric acid etching agent (Figure 27a).[149] The mechanism of macropore formation was explained by the disassembly of 1 copper cluster and the paddle wheel linkers in the framework of HKUST-1 by phosphoric acid (Figure 27b). The degradation problem of HKUST-1 in water was effectively solved by employing DMSO and methanol as dilute solvents. More interestingly, a range of interconnected highly geometrical macropores were observed with the extent of porosity being tailorable by controlling time and pH in these systems (Figure 27c-e). It can be anticipated that the macropores in these MOFs would improve the diffusion and accessibility of bulky molecules to active sites in catalysis, as was shown to be the case of defective UiO-66 which showed improved catalytic performance in Lewis acid catalysed reactions.[150]

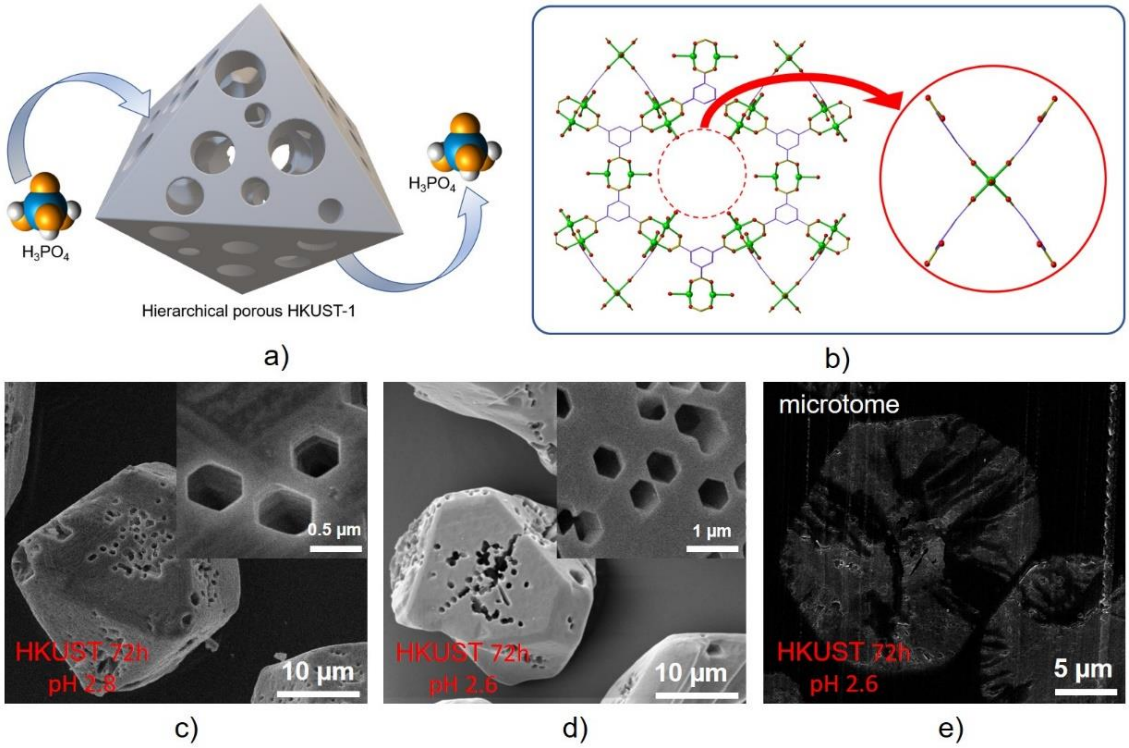

Figure 27. a and b) Schematic representation of etching process for HKUST-1 using phosphoric acid, showing phosphoric acid diffuses into HKUST-1 to form a hierarchical porous structure (a) and the disassembly of a cluster and 4 linkers (b). c-e) SEM images of HKUST-1 etching in phosphoric acid using DMSO and MeOH as dilute solvents at pH 2.8 (c) and pH 2.6 (d and e), showing interconnected geometrical macropores after etching. Reprinted with permission from Ref. 149.

As an extension on the idea of size-selective acid etching, another post-synthetic process, termed "synergistic etching and surface functionalisation", was reported by Hu *et al.*[151] In this

study, weak bulky phenolic acids such as gallic acid and tannic acid were used to provide free protons that penetrated into the MOF crystals to form a hollow structure. Interestingly, these acids with large molecular sizes simultaneously blocked the exposed surface of ZIF-8, leading to the preservation of the parent crystalline framework of MOF in the outer shell. Yoo *et al.* reported that by etching IRMOF-3 with cyanuric chloride and tetraethylamine (TEA), protons released from the modification can create a mesoporous structure or even macro-scale defects if the etching process proceeds further.[152] In this case, TEA was used as a proton scavenger to prevent the complete dissolution of IRMOF-3 in cyanuric chloride, thus preserving the MOF crystallinity.

From the above examples, it can be seen that it is possible for the defective MOFs resulting from these approaches to possess well-defined crystal structures and preserve their external morphology after acid etching. Whilst water unstable MOFs were considered as limited candidates in some etching mechanisms, this could be solved by varying the dilute solvents employed. The nature of the interactions of various solvents with MOF frameworks therefore needs to be well understood to generate a method applicable to different MOF systems. Acid etching approaches for the preparation of hierarchical macroporosity in MOFs are a comparatively facile procedure compared to templating methods, as they can be carried out as a post-synthetic step on larger samples of MOFs. However, judicious choice of the etching agent and etching conditions is essential to obtain controllable macroporosity in MOFs without the loss of crystallinity or complete dissolution of the crystalline structure.

2.2.3. Macroporous MOFs synthesised using compressed or supercritical carbon dioxide

Compressed or supercritical carbon dioxide has been widely applied to a range of MOF processing steps including crystallisation,[153–155] impregnation,[156] dispersion,[157] drying[158] and activation[159,160]. Formation of highly porous materials will generally benefit the use of supercritical drying (typically supercritical carbon dioxide), with the low viscosity and high diffusivity of supercritical fluids being recognised as being especially vital for activation of large pores, to avoid pore collapse in MOFs during solvent removal.[161] An alternative approach for generating microporous structures in MOFs, as opposed to depositing a MOF on a porous support which has then to be removed, is to directly form microporous MOFs into an aerogel, establishing free-standing monoliths with added macroporosity. The resulting MOF monolithic aerogels are more practically used as catalysts and catalyst supports themselves without

restrictions in mass transport and catalyst recovery as would be the case for normal nanocrystalline MOF powders. Drying with $scCO_2$ has been illustrated as a key post treatment step for synthesis of macroporous MOF/aerogel composites (MOFAC) in the absence of a polymer template. In this synthesis, a prepared MOF may be added into an emulsion to form a stable network, before drying by $scCO_2$ to obtain an aerogel. Recently, a strategy to synthesise HKUST-1 MOF-stabilised high internal phase emulsions (HIPE) at the oil-water interface was described by Zhang *et al.*[162] After removing the liquids with supercritical CO_2 (Figure 28a), the as-assembled MOF aerogel presented a macroporous structure with an outstanding volume expansion and low density of 0.015 g cm^{-3} (Figure 28e-g) compared to 0.350 g cm^{-3} in commercial HKUST-1[163], the macropore size could be easily tuned by changing the initial oil volume fraction of the emulsion structures without the need for single-use sacrificial polymer templates (Figure 28b-d).

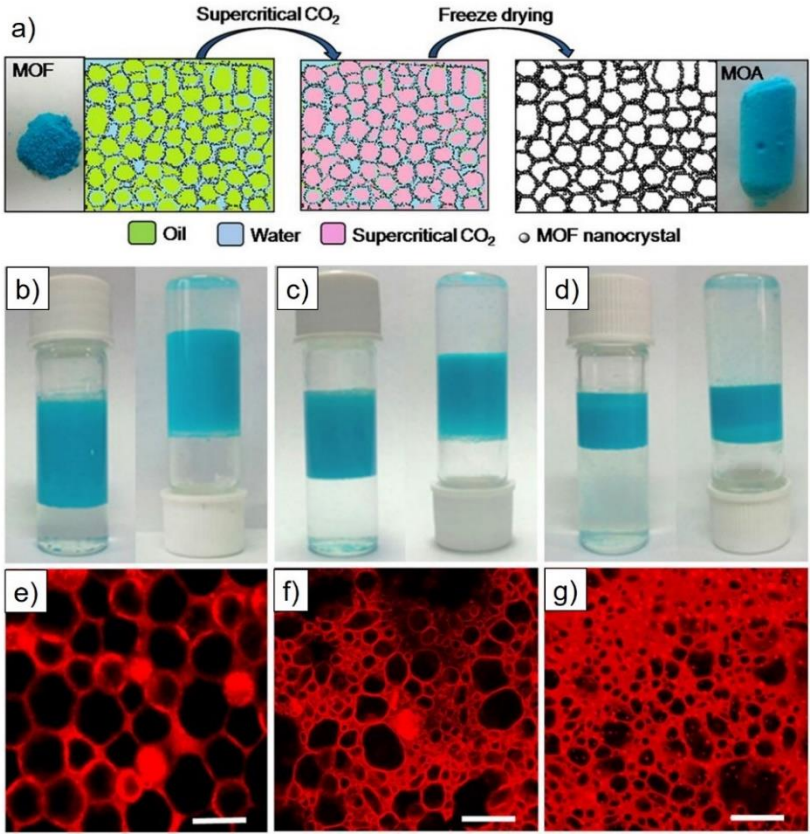

Figure 28. a Diagram illustrating the MOF-stabilized HIPE and derivation of MOA from HIPE. b-d Photographs of the emulsions stabilised by $Cu_3(BTC)_2$ with the initial diethyl ether volume fractions of 0.57, 0.43 and 0.29, respectively, demonstrating ability to tune pore size in HIPEs. e-g The corresponding confocal laser scanning microscopy images of the above HIPEs (HIPE-1, HIPE-2 and HIPE-3, respectively). Scale bars, 20 μm. Reprinted with permission from Zhang et al.[162]*. Copyright CC BY-NC-SA 4.0.*

Similarily, Li *et al.* reported a two-step gelation of MOF nanoparicles, in which AlBTC and AlBDC gels with different metal-to-ligand ratios and concentrations were formed before exchanging the pore liquid with CO_2(l) under subcritical extraction to produce aerogels (Al-MOAs), resulting in meso-/macroporous aerogel scaffolds.[164] It can be seen that this method heavily relies on the use of supercritical CO_2 to avoid the collapse of porous networks, and hence requires specialised high-pressure equipment for solvent removal. These MOF aerogel composites can be produced as free-standing monolithic porous solids which can be easily formed into desired shapes for numerous applications.[165,166] The formation of monolithic structures holds significant advantages over the powdered materials, including ease of handling, immobilisation of particulates and improved robustness and mechanical properties.

In addition to its use for aerogel formation, compressed or supercritical carbon dioxide has been recently investigated as an unconventional solvent for direct MOF synthesis. By varying CO_2 pressure in the reactor, particle sizes and porosity can be controlled, which is not possible using conventional solvothermal synthesis. These substantial benefits are reasons why using this alternative solvent in MOF synthesis can be preferred even though a high pressure is required.

As an early demonstration of this synthetic strategy, Peng *et al.* described a CO_2–ionic liquid interfacial templating route for the synthesis of hollow Zn-based MOF polyhedral.[167] By varying the pressure of gaseous CO_2 from 10 to 63 bar in a solution of *N*-ethyl perfluorooctylsulfonamide/*N*,*N*,*N*′,*N*′-tetramethylguanidinium trifluoroacetate (*N*-EtFOSA/TMGT), tetrahedron-like particles were formed as CO_2 bubbles generated (Figure 29a). It was also seen that at high pressure, the MOF tetrahedroids possessed a hollow structure with inner cores evidenced by SEM (Figure 29b), TEM (Figure 29c) and gas sorption. The formation of this structure was explained by the selective assembly of metal nodes and organic linkers at the bubble interfaces during the crystallisation. This MOF was then tested in the reaction of propylene oxide and CO_2 to produce propylene carbonate, indicating an increase in conversion from 20.1% to 97.4% with the presence of the hollow structure.

At the same time, Peng *et al.* also reported a method using CO_2 to form an expanded solvent to synthesise HKUST-1 (Figure 30a-f).[168] It is noticeable that large mesopores (up to 30 nm) with pore wall diameters of around 10 nm could be formed within this MOF by increasing pressure to 66 bar at 30 ^{o}C for 3 h (Figure 30g), resulting in improved performance in catalysed reactions with benzyl alcohol oxidation. The mesocellular formation of this MOF with large mesopores and thin mesopore walls[168] in CO_2-expanded liquids was explained by the assembly

of HKUST-1 nanosized framework building blocks in expanded liquid volumes at CO_2 pressure. Whilst the formation of larger mesopores was favoured by higher CO_2 pressures, this study was limited to introducing CO_2 at 66 bar and 30 ^oC, and the maximum pore sizes witnessed were ~ 30 nm. It can be anticipated that these mesopores need to be further enlarged in some cases to obtain macropores which more significantly enhance the transportation of reactants, intermediates, and products in heterogeneous catalysis applications.

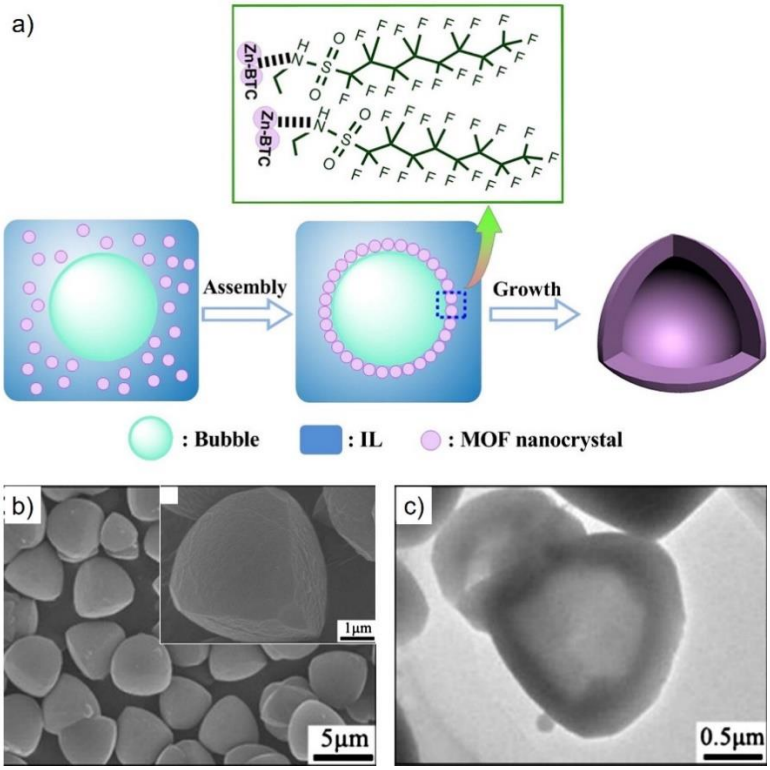

Figure 29. a) Schematic illustration for the formation of hollow Zn–BTC tetrahedroids via a CO_2–IL interfacial templating route. SEM (b) and TEM (c) images of the hollow tetrahedron-like Zn–BTC microparticles. The N-EtFOSA concentration is 2.0 wt% based on IL and the CO_2 pressure is 6.3 MPa. Reprinted with permission from Ref. 167. Copyright 2014 Journal of Colloid and Interface Science.

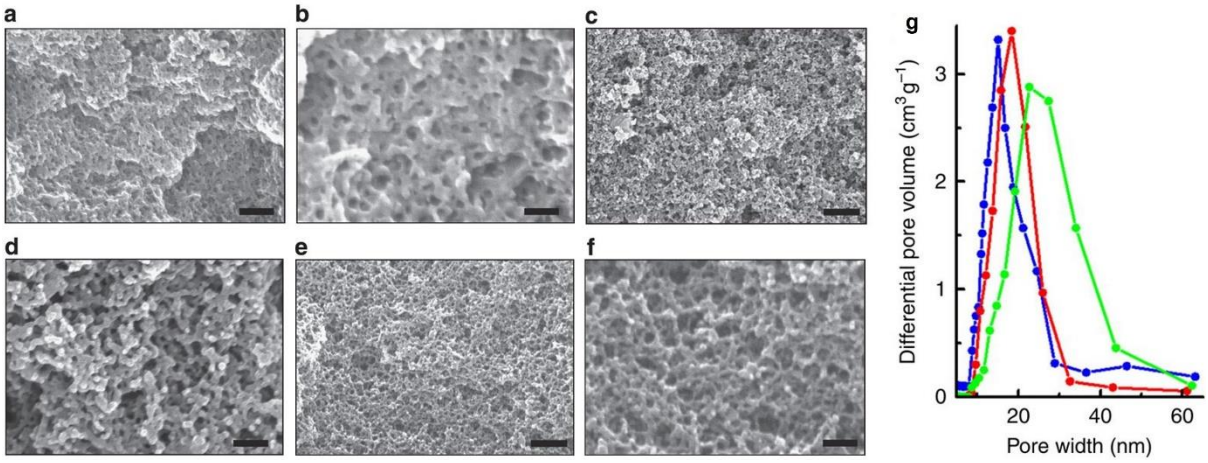

Figure 30. a-f) SEM images of HKUST-1 synthesised in CO_2-expanded DMF at 2.0 (a,b), 4.5 (c,d) and 6.6 (e,f) MPa. Scale bars, 150, 50, 500, 150, 500 and 150 nm for a–f, respectively. g) The mesopore size distribution curves for the $Cu_3(BTC)_2$ synthesised in CO_2-expanded DMF at 2.0 MPa (blue curves), 4.5 MPa (red curves) and 6.6 MPa (green curves). Reprinted with permission from Peng et al.[168]. Copyright CC BY-NC-SA 4.0.

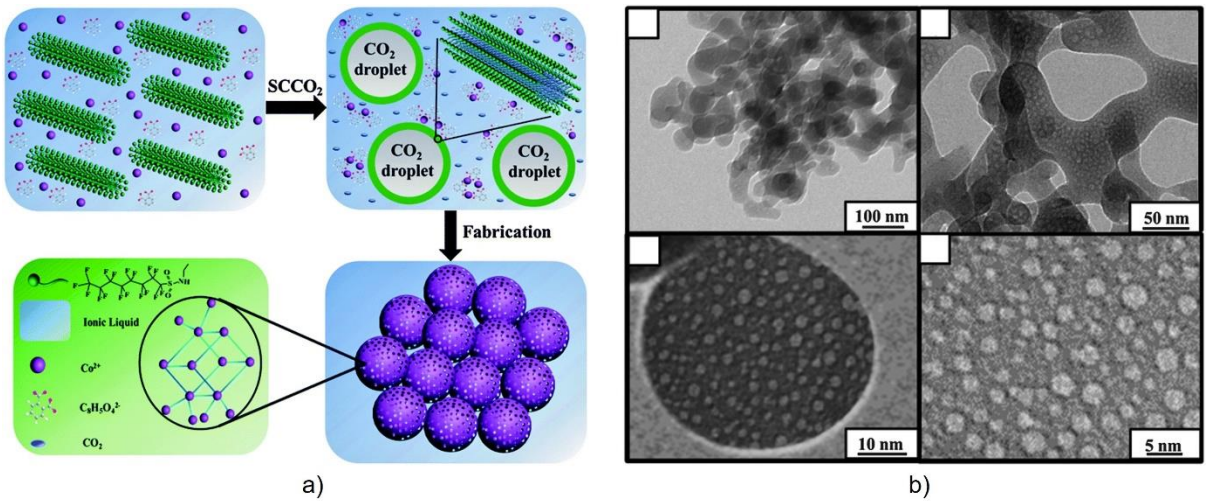

Figure 31. a) Schematic illustration for the formation of the mesoporous Co-MOF in an IL/SC CO_2/surfactant emulsion system. b) TEM images of the Co-MOF synthesised in an IL/SC CO_2/surfactant emulsion system at 16 MPa and 80 °C for 48 h. Reprinted with permission from Ref. 169. Copyright 2015 Royal Society of Chemistry.

Utilisation of $scCO_2$ in binary solvent systems comprising an ionic liquid (IL) was also reported for the synthesis of mesoporous zinc and cobalt MOFs (Figure 31a).[169,170] In these studies, $scCO_2$ not only established the pattern of the MOF nanospheres but also swelled the IL micelles to form long-range ordered mesopores which could be tuned easily by changing the CO_2 pressure. Remarkably, in the case of Co-MOF,[169] a series of interconnected macropores could

also be seen with a worm-like morphology (Figure 31b). Note that these MOF syntheses were investigated at supercritical conditions of CO_2 (160 bar, 80 ^oC) and for extended reaction times (48 h) which differ from conditions chosen in Peng's research introduced previously. The extreme reaction conditions in CO_2 have also been employed in the synthesis of 1D, 2D and 3D MOFs by reactive crystallisation in the absence of or using lower volumes of solvents.[171–173]

By tuning the conditions used in previous studies, Doan *et al.* demonstrated the synthesis of HKUST-1 using supercritical carbon dioxide as a pressure-tuneable antisolvent to induce MOF crystallisation from the resulting single phase expanded liquid (Figure 32a).[174] Interestingly, this methodology allowed control over nucleation and growth kinetics, and also introduced a range of larger macropores into these typically microporous materials leading to so-called "hierarchical" porous materials (Figure 32b). The ability to control the expansion of the solvent by control of the density of CO_2 permits access to new structures and material morphologies not accessible by traditional methods. SEM and TEM images of the materials showed that crystallites were of the order of ~100 nm to microns in size, with interconnected macropores ranging from ~50-200 nm in diameter (Figure 32c). A view-cell experiment (allowing direct observation of the reactants under high pressure $scCO_2$) showed that HKUST-1 could be formed within a few minutes rather than the 18 hours required for the conventional synthesis.[175] In addition, due to the expansion in volume with CO_2 pressure, the amount of solvent required was greatly reduced in comparison to the conventional synthesis.

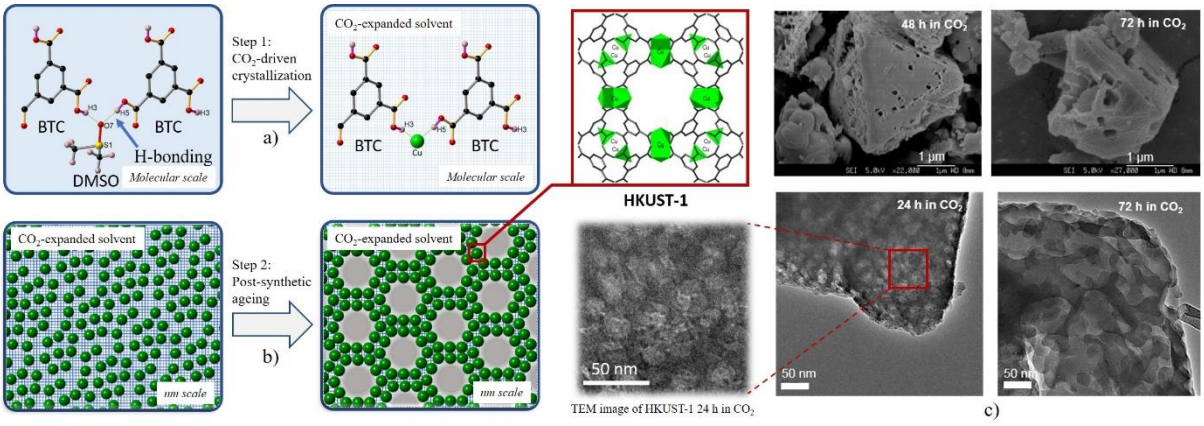

Figure 32. Schematic illustration for HKUST-1 crystallisation (a) and meso/macropore formation (b) in the CO_2-expanded solvent. c SEM images (top) and TEM images (bottom) of HKUST-1 synthesised using $scCO_2$ at 75 bar, 40 ^oC for more than 24 h, showing introduction of interconnected macropores. Reprinted with permission from Doan et al.[174]*. Copyright CC BY-NC-SA 4.0.*

The latest research demonstrates that MOFs with macropores can be synthesised using supercritical CO_2. These findings suggest an intelligent method to obtain this structure without using templates. It is anticipated that this process may be applicable to other MOF systems. Note that in the case of HKUST-1 metal-ligand coordination forces between Cu^{2+} and BTC^{3-} in DMSO dominated the MOF aggregation process, resulting in a precursor solution.[19] It was found that the nucleation was only triggered when the introduction of CO_2 and a small amount of methanol served to disrupt the H-bonding in the stock solution. Due to critical conditions of CO_2 applied in this method (T_c and P_c of CO_2 are 31.1 ^oC and 73.9 bar, respectively[176]), a high pressure reactor needed to be employed. Also, low temperature synthesis at 40 ^oC was found to be more favourable, which is not easy to achieve for most MOFs. Another challenge in this synthetic strategy is carrying out the experiment in *in situ* characterisation to understand the mechanism of the macropore formation during CO_2 pressurisation.

2.2.4. Macroporous MOFs synthesised via 3D printing

The formation of macropores in MOFs by the acid etching and $scCO_2$ methods detailed above have been shown to be beneficial for catalytic applications, but, with the exception of the MOF aerogels, most still result in MOF materials consisting of small crystallites, rather than controllable monolithic structures. As discussed in the preceding sections, a key barrier to the implementation of MOFs in industry is their lack of processability owing to their general insolubility and inherently powdered form. Whilst a variety of methods have been attempted to transform MOF powders into appropriate monolithic forms, such as pressing powders into pellets,[177] melting them to form glasses,[178–180] or forming MOF coatings on monolithic supports (such as those mentioned in Section 2.2.1),[181] typically such techniques result in reduced MOF surface area.

Over the past few decades, 3D printing, also known as additive manufacture or robocasting technology, has been developed and applied successfully to fabricate monoliths with controlled 3D shapes by careful placement of material in space. Currently, printing methods are not limited to utilising inks comprised of plastics for art exhibitions, and may also employ inks comprised of ceramics, metals, graphene additives, and even stimuli responsive hydrogel composites[182] for prototyping and industrial applications.[183–185] Recently, there has been a growing number of research papers on developing tailored porous biomedical scaffolds,[186] membranes,[187–189] carbons,[190] zeolites,[191–193] aminosilicate adsorbents[194] and heterogeneous

catalytic systems[195] by taking advantage of this technique.

In comparison to other processing techniques for making microporous MOFs such as solvothermal and microemulsions, 3D printing promises multiple advantages such as high reproducibility of complex geometries, low cost, scalability, and efficiency. Furthermore, with regards to MOFs specifically, the printing of a MOF composite would represent major advantages over alternative methods of monolith formation, which generally involve the deposition of MOFs onto non-flexible substrates like metals and require complicated techniques for precise MOF positioning.[196,197] Additionally, a further benefit is the formation of a printed monolith has potential to enable additional porosity to be implemented depending on the additives employed in the ink. Hence, 3D printed monoliths not only offer an implementable contact medium for MOFs, but also enable an increased pore size distribution to be attained compared to parent MOF powders. In addition, polymers with a variety of unique attributes, such as softness, thermal and chemical stability, and optoelectrical properties that can be integrated with MOFs to make hybrids with sophisticated architectures.[198] With numerous potential applications, 3D-printed MOFs have been prepared successfully, though only recently, and therefore have been studied to a limited extent.

The first report in which MOF based inks were developed and printed to give monoliths was described by Thakka et al, and employed MOF-74(Ni) and UTSA-16(Co).[199] In this study, pre-prepared MOF powders and bentonite clay (as a binder and rheological modifier) were dissolved in ethanol to obtain a homogeneous solution. This solution was then combined with a mixture of polyvinyl alcohol (PVA) and deionised water to form an extrudable paste, before loading into a 3D-printer to create a MOF-based object with desired shapes, as illustrated in Figure 33a. The obtained 3D-printed MOF monoliths (at 80 and 85 wt.% loadings) retained the physical properties and mechanical integrity of their powder counterparts, and also displayed crystallinity akin to their parent MOF crystal structures. While physical properties were retained, the surface area of the 3D-printed MOF composites was reduced by a maximum of 38 % (from 1180 to 737 m^2/g), owing to the inclusion of bentonite clay and PVA additives. The key challenge underlined by the work of Thakka *et al.* was the effect of ink rheology on the resulting printed structures, the cross-sectional areas of which are displayed in Figure 33. Differences in wall thicknesses and channel sizes were attributed to the viscosity of the prepared MOF pastes, with the less viscous UTSA-16(Co) paste resulting in the expansion of layers on deposition. Nevertheless, the printed MOF monoliths displayed CO_2 capacities

similar to their MOF powder counterparts with stable performance and faster adsorption kinetics than that of the corresponding powder (by 15 mins).

According to Semino and co-workers, the general method developed by Thakka *et al.* for the production of hierarchical MOF monoliths is likely governed by the polymer it is embedded in: firstly by the partial blocking of MOF pores by flexible polymers (giving smaller pore sizes), and secondly by the formation of voids within the polymer matrix itself.[200] The influence of polymer characteristics on the fabrication of hierarchical MOF monoliths by 3D printing was in fact investigated by Evans *et al.* in 2018.[200] In this study, high loadings of powdered ZIF-8 (up to 50 wt.%) were incorporated into a matrix of either polylactic acid (PLA) or thermoplastic polyurethane, representing rigid and flexible polymer matrices, respectively, to produce a filament feedstock for 3D printing. It was revealed that the rigidity of the PLA chains limited their re-organisation around ZIF-8 crystals during extrusion, resulting in various void sizes (micro-, meso-, and macro-voids) and hence giving a hierarchical MOF monolith with preserved MOF crystallinity. Unfortunately, employment of the flexible polymer matrix resulted in almost complete pore occlusion, as concluded from the low specific surface area of the monolith (68 $m^2 g^{-1}$ at 50% MOF loading).

Recently, Young *et al.* highlighted a practical solution to the problem of pore occlusion in MOF composite monoliths by 3D-printing UiO-66 in combination with a mixture of flexible acrylates which exhibited low thermal stability (<100 ^oC).[201] As expected, the printed UiO-66 monoliths were non-porous (owing to blockage by flexible acrylate chains), however, on heating to 100 ^oC the polymer matrix degraded to recover porosity and reveal UiO-66 sites. Interestingly, although the treated composite displayed physisorption behaviour characteristic of microporous UiO-66, the presence of small mesopores were also identified. This work, carried out by Young *et al.*, promises a method to embed MOFs within 3D printed monoliths and later expose crystals as required for production of structures with hierarchical porosity. Furthermore, UiO-66 was found to behave as a rheological modifier itself, avoiding the need for additives such as the bentonite clay employed in earlier studies.

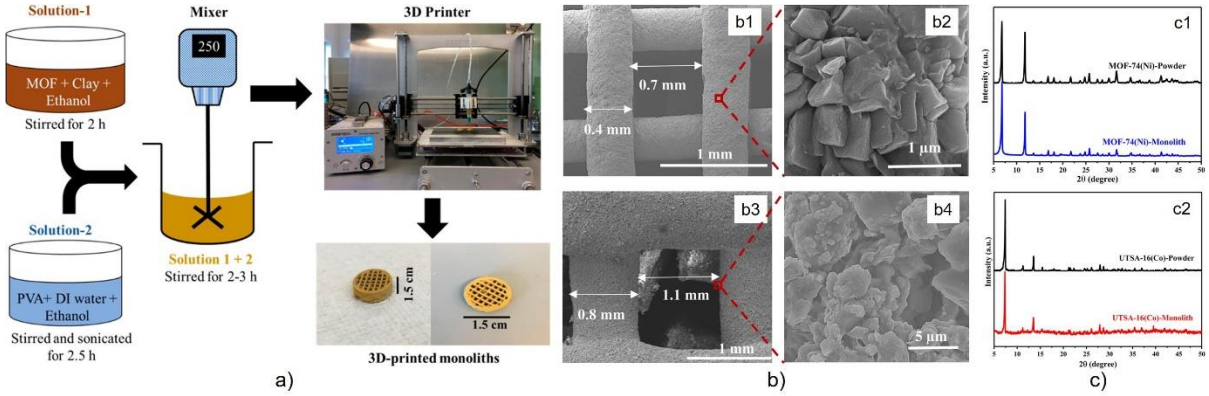

Figure 33. a) Schematic of the 3D-printed MOF monolith preparation procedure. b) SEM images of 3D-printed MOF-74(Ni) (b1 and b2) and 3D-printed UTSA-16(Co) (b3 and b4), showing uniform distribution of MOF crystals and with large voids. c) PXRD patterns of 3D-printed MOF-74(Ni) (c1) and 3D-printed UTSA-16(Co) (c2) with their powder counterparts, showing crystallinity retained for both MOF-74(Ni) and UTSA-16(Co) MOFs after they were extruded into the monolith form. Reprinted with permission from Ref. 199. Copyright 2017 Applied Materials and Interfaces.

Whilst the most commonly employed methods to prepare printable MOF inks combine synthesised MOFs and additives (such as binders and plasticisers) in ethanol, a novel one-pot room temperature approach using water as a solvent was carried out by Sultan *et al.*[202] The printable ink was formulated by *in situ* growth of ZIF-8 and MIL-100(Fe) MOFs onto anionic 2,2,6,6-tetramethylpiperidine-1-oxylradical-mediated oxidised cellulose nanofibers (TOCNFs) prior to combination with a sodium alginate binder and calcium chloride crosslinker. Introducing MOFs into cellulose resulted in increased pore volume and surface area of the composite material compared to unmodified TOCNF. In contrast, the cellulose (with high aspect ratio, negative zeta potential and good mechanical performance) provided benefits to MOFs by offering high printability and versatility of the hybrid inks. The printed scaffolds (Figure 34a-d) possessed a large pore size (1 mm), useful for drug delivery applications, as the large pores would aid in infiltration of biological fluids into the support. In addition, the 3D-printed composite was found to be stimuli-responsive (pH-dependent) regarding the release of curcumin and methylene blue, indicating that the printed MOF monoliths produced using a simple and inexpensive printer could potentially be used in biomedical applications.

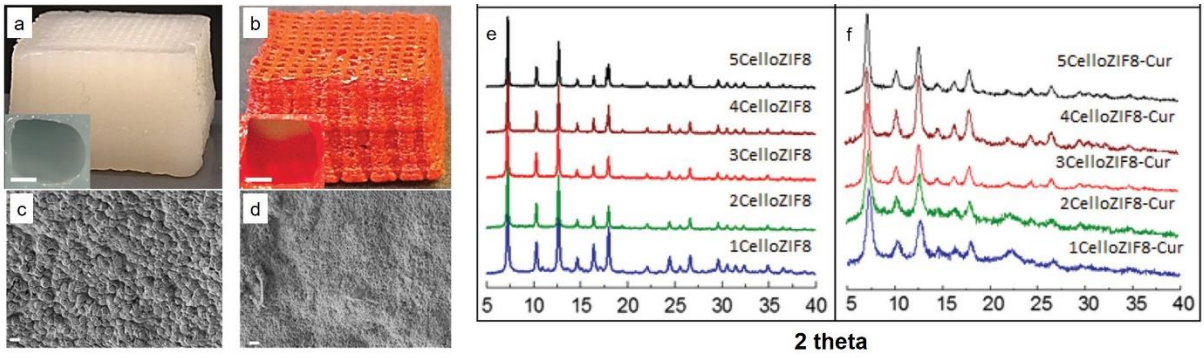

Figure 34. Photos of 3D printed scaffolds: 4CelloZIF8 (a) and 4CelloZIF8-Cur (b). Insets are images representing the pores, with the scale bar representing 0.5 mm. SEM images of scaffold 4CelloZIF8 (c) and scaffold 4CelloZIF8-Cur (d). Scale bar = 1 µm. PXRD patterns of CelloZIF8 hybrids using different ZIF-8 (e) and different ZIF-8 loadings while keeping Hmim:Zn to 35:1 and curcumin to 30 mg (f), showing that the crystallinity and the framework are maintained with different curcumin and Zn loadings. Reprinted with permission from Ref. 202. Copyright 2019 Advanced Functional Materials.

Recent developments in the fabrication of 3D-printed MOFs have been successful in both providing a monolith suited for practical applications, as well as adding hierarchical porosity into MOF based materials. Although 3D printing of MOF monoliths has predominantly required high processing temperatures (up to 230 ^{o}C) or ultraviolet curing,[203,204] the recent work described by Sultan and co-workers demonstrates the feasibility of room temperature synthesis. However, it should be noted that this technique may not be suited to a variety of MOFs which are unstable in air, since the layer-by-layer printing process may necessitate air-exposure for extended periods (15-120 h). For example, Kreider and co-workers[205,206] observed the degradation of water-sensitive MOF-5 during blending of the printable ink with the MOF powder and attributed this to ambient humidity. Interestingly though, irrespective of the observed MOF degradation, the resulting monolith was capable of adsorbing more H_2 than the pure polymer counterpart, demonstrating the viability for H_2 storage using 3D printed MOFs even in humid conditions.

Overall, the ability to tailor both the MOF and binding matrix could render extensive applications viable, from providing photonic platforms to biomedical testing and catalysis. Whilst the precise placement of materials in 3D printing renders more complex macroscale structures achievable, it should be noted that fine control on the micron - nanoscale could be challenging in terms of accurately controlling the size of macropores which form inherently during ink deposition. However, as 3D printing methods become more established, it is

anticipated that finer control over macropore sizes will be achievable. Finally, since significant research attention has taken steps towards employing MOFs in biomolecule encapsulation for controlled drug delivery and in biological applications, where macroporosity would be beneficial for facilitating mass transfer of biological fluids, it may be useful to consider the biodegradability of MOFs in low pH environments.[207,208] To this end, future work could explore the development of ink matrices which could protect embedded MOFs from such degradation.

2.3. Conclusions

In this review, a range of current achievements and challenges of creating hierarchical pore structures with additional macropores have been discussed. Introduction of macroporosity has been demonstrated to lead to improvements in mass transfer and catalytic activity, and reductions in pressure drop over traditional powdered or nanocrystalline MOFs. Templating and gelation stand out as the most popular routes towards obtaining macroporous MOFs with numerous studies reported on these methods so far. Most macropores were formed within composite materials in which the interaction between MOFs and other substrates need to be carefully investigated. The stability of the MOFs used in these methods remains a major challenge. In some cases, macroporous MOFs have been shown to form stand-alone aerogel monoliths, however, carefully controlled drying techniques are required to remove the gel without collapsing pore networks. While defect formation and selective acid etching has resulted in some impressive macroporous MOF crystal structures, studies of macroporous MOFs formed via acid etching are limited, due to the instability of most MOFs under acidic conditions. However, the discovery that large geometrical pores within HKUST-1 could be achieved by acid etching indicates that with further investigation of the synthetic conditions and further understanding of the etching mechanisms, the approach to the formation of such macropores in MOF crystallites may be more widely applied.

Use of supercritical or compressed CO_2 is well-known in MOF synthesis and post-synthetic treatment, but the use of supercritical CO_2 routes for formation of additional macropores was demonstrated through use of longer reaction times and higher pressures 3D printing, on the other hand, is a very new but promising technique which shows promise for generalised use in MOF preparation, allowing a very high MOFs loading to be incorporated into scaffolds (~85 wt.%). The high reproducibility, fabrication of complex geometries and controlled pore

structures of these MOFs have potential to open up new applications for MOF materials in biomedical fields. The range of fabrication approaches presented here indicates the vast variety of different macroporous structures that can be achieved using functional MOF materials. Further development of this toolbox will surely give materials scientists greater flexibility in tailoring the porosity and structure of their MOF materials toward particular functions and should help to accelerate the use of MOFs in practical applications.

CHAPTER THREE: DEFECTIVE HIERARCHICAL POROUS COPPER-BASED METAL-ORGANIC FRAMEWORKS SYNTHESISED VIA FACILE ACID ETCHING STRATEGY

In this chapter, a post-synthetic acid etching strategy is presented to synthesise MOFs with macroporosity. Acid etching, as presented in Chapter 2, is a potentially simple and scalable approach to producing macroporosity, but as many MOFs are prone to hydrolysis including archetypical and high surface area materials such as MOF-5, HKUST-1 and SNU-80, limitations in the water stability of a large number of MOFs mean that the simplest acid etching approaches are often not suitable. In this chapter, a size-selective acid etching approach using phosphoric acid, DMSO and methanol is developed for MOFs that are unstable in water, using HKUST-1 as an example system. A systematic chemical and structural investigation using electron microscopy, gas sorption and X-ray diffraction analysis revealed that varying the time and pH of the etching process resulted in the formation of interconnected hexagonal macropores in this MOF while the bulk crystallinity was retained. This chapter appeared as a manuscript which has been published in *Scientific Reports* (DOI: 10.1038/s41598-019-47314-1), with the author of this thesis as the first author. The author confirms that he carried out all synthesis experiments, PXRD, SEM, gas sorption experiments, data analysis and prepared the manuscript. Additional work was contributed by Jean-Charles Eloi (University of Bristol), who provided a training on using SEM and helped with the microtome experiment. Sean Davis (University of Bristol), Asel Sartbaeva (University of Bath) and Valeska P. Ting provided feedback and comments on the manuscript.

Abstract

Introducing hierarchical pore structure to microporous materials such as metal-organic frameworks (MOFs) can be beneficial for reactions where the rate of reaction is limited by low rates of diffusion or high pressure drop. This advantageous pore structure can be obtained by defect formation, mostly via post-synthetic acid etching, which has been studied extensively on water-stable MOFs. Here we show that a water-unstable HKUST-1 MOF can also be modified in a corresponding manner by using phosphoric acid as a size-selective etching agent and a mixture of dimethyl sulfoxide and methanol as a dilute solvent. Interestingly, we demonstrate that the etching process which is time- and acidity- dependent, can result in formation of defective HKUST-1 with extra interconnected hexagonal macropores without compromising on the bulk crystallinity. These findings suggest an intelligent scalable synthetic method for formation of hierarchical porosity in MOFs that are prone to hydrolysis, for improved molecular accessibility and diffusion for catalysis.

3.1. Introduction

Metal-organic frameworks (MOFs) are a new class of crystalline porous solids which can be self-assembled from an abundance of inorganic ions/clusters and a variety of organic linkers/ligands, thus possessing tailorable chemical and structural characteristics. According to the Cambridge Structural Database (CSD), more than 70,000 MOF structures have been designed and synthesised so far.[3] This figure is far higher than the number of reported zeolites which is limited to 64 natural structures and about 240 synthesised structures.[209] Due to the functional flexibility of their structures, MOFs possess exceptional properties such as apparent surface areas[9] up to 7,000 $m^2 g^{-1}$ (compared to the maximum reported values of ~1,000 $m^2 g^{-1}$ for zeolites and 3,500 $m^2 g^{-1}$ for activated carbons[18,210]) and the highest porosity (3.60 $cm^3 g^{-1}$)[211] yet achieved for any porous material.[212] These unique properties lead to MOFs being trialled in various energy and environmentally relevant applications such as gas storage,[10–12] gas separation,[83–86] catalysis,[13,14] carbon dioxide capture[87–89] and as semiconductors.[90,91] Due to the enormous number of MOF entries dispersed throughout the literature and their potential for application, there is growing research effort focussed on the large-scale synthesis and practical application of novel MOF structures. Promising new approaches have focussed on novel synthetic methods such as supercritical fluid processing to reduce the environmental impacts associated with solvothermal synthesis[37,174,213] or mechanochemical synthesis to scale

up the production of MOFs.[214] Other recent research strategies have involved tailoring porosity of conventional MOF-based structures to form hierarchically-structured porous materials,[82,174,215,216] to fabricate materials based on MOFs that can be tailored for use in numerous areas such as environmental remediation[28], catalysis,[29] energy,[219] health,[220] or in electronic devices and chemical sensors.[221]

Among these new synthetic approaches, the development of advanced hierarchical porous MOFs made of interconnected pores spanning different length scales ranging from micro-, to meso- and macroporosity (referring to pore diameters of <2 nm, 2-50 nm and >50 nm, respectively) has attracted considerable current interest. Introduction of larger meso- and macropores into traditionally microporous MOFs is desirable for facilitating diffusional processes, thereby increasing the rate of reaction for diffusion-limited or mass-transfer limited processes.[76,215] Numerous methods to synthesise these types of hierarchical porous MOFs have been developed, including template-assisted routes (*e.g.* dual surfactant templating methods[216,222] and CO_2-ionic liquid interfacial templating routes[167]), template-free routes (*e.g.* facile self-assembly processes[223] and use of CO_2-expanded solvents[168,174]), spontaneous formation (via linker labilisation[141] and metal-ligand fragmentation[142,224,225]) and post-treatment (acid etching[151,226] and emulsion templating[162]).

While other methods require lengthy synthetic procedures to functionalise meso/macropores in hierarchical porous MOFs, acid etching stands out as the simplest method to create mesoporous defects and to engineer large voids via controlled acid etching. Recently, a process called size-selective acid diffusion was investigated and explained by Koo *et al.*[147] By observing the etching process and the mesopore transformation of MIL-100(Fe), phosphoric acid with an appropriate size (d = 0.61 nm) was indicated to selectively diffuse into the 3D tetrahedral channel of MIL-100(Fe) through the hexagonal windows (d = 0.89 nm) rather than pentagonal windows (d = 0.49 nm) of the MOF. After gradual etching at 70 ^{o}C, the metal nodes and the benzene-1,3,5-tricarboxylic acid (BTC) linkers near this channel were disassembled, leading to the creation of large cages while maintaining the majority of the microporous cages, to preserve the crystallinity and external morphology. This is simply because the acid molecules are unable to diffuse through and provide the etching effect on the small microporous channels. With the smaller acids, for example HCl (d = 0.34 nm), MIL-100(Fe) collapsed after etching because the small cages were also attacked, in contrast to the size-selective acid diffusion approach. A similar size-selective controlled etching process, termed "synergistic etching and surface functionalisation", was reported by Hu *et al.*[151] on a ZIF-8

MOF. In that research, weak bulky phenolic acids such as gallic acid and tannic acid were used to provide free protons that penetrating into the MOF crystals to form a hollow structure. Interestingly, these acids with large molecular size simultaneously blocked the exposed surface of ZIF-8, leading to the preservation of the parent crystalline framework of MOF in the outer shell. Typically, such use of acid etching to tune pore size in those processes is only applicable for highly water-stable MOFs. As the stability of MOFs is a recognised impediment to their industrial applicability and a large number of MOFs are not stable in water,[227,228] the generalisation of this inventive acid etching method remains a significant challenge.

Inspired by recent reports where phosphoric acid could be used to tailor porosity via selective acid etching, we report an innovative method to create hierarchical porous structure in water-unstable MOFs which has not been examined so far. Here, we used the archetypical HKUST-1 (Cu-BTC) MOF as a model. This study sought to investigate to what extent porosity may be tailorable by controlling the degree of acid etching in these systems.

3.2. Materials and Methods

All chemicals used in this study were purchased from commercial suppliers without further purification (see Appendix B Table S1). A commercial HKUST-1 (also known as Basolite C 300, copper benzene-1,3,5-tricarboxylate or Cu-BTC and referred here as normal HKUST) was sourced from Sigma-Aldrich and was subjected to acid etching, as follows. To test the effect of pH on the etching process, 50 mL DMSO and 50 mL methanol were mixed and magnetically stirred at room temperature for 10 minutes to obtain a stock solution (SS) with pH = 6.4. Subsequently, different amounts of 90% phosphoric acid (0.2 mL, 0.6 mL and 1 mL) were added to 20 mL of the stock solution, with continuous stirring at room temperature for another 10 minutes. The acidities of these solutions were recorded by a calibrated Jenway 3510 pH meter with an accuracy of ±0.003. More information of using a pH meter to measure acidity of solution can be found in Appendix B. The stock solution containing 1 mL phosphoric acid is subsequently referred to as SSH. To increase the pH, 20 mL of SS was acidified by addition of 0.2 mL, 0.6 mL and 1 mL of SSH, with vigorous stirring before measuring pH (see Table 2). In the etching process, 20 mL of the prepared solution with different pH from 2.6 to 6.4 was added to 50 mL centrifuge tubes containing 200 mg of normal HKUST, and was agitated strongly before being placed in an oven at 40 ^{o}C for 72 h. To evaluate the effect of etching time, the same amount of normal HKUST was soaked in 20 mL SSH at 40 ^{o}C for 1 h, 3 h, 5 h,

24 h, 48 h, 72 h and 240 h. The details of the HKUST-1 acid etching process are summarised in Appendix B Figure S4. After etching, the solid was isolated by centrifugation (10,000 rpm for 10 minutes), washed with pure methanol, re-centrifuged and re-washed three times and dried at 60 ^{o}C overnight. The dried samples in the centrifuge tubes were weighed before and after etching to record the weight loss with respect to the starting dry weight.

Table 2. Preparation of stock solutions (a mixture of phosphoric acid, DMSO and methanol) with different pH for testing HKUST in acid etching.

	Stock solution (SS)	**SS + 1 mL H_3PO_4 (SSH)**	**SS + 0.6 mL H_3PO_4**	**SS + 0.2 mL H_3PO_4**	**SS + 1 mL SSH**	**SS + 0.6 mL SSH**	**SS + 0.2 mL SSH**
pH	6.4	2.6	2.8	3.1	3.6	4.0	4.5

The etched HKUST MOFs were characterised by powder X-ray diffraction (PXRD) on a BRUKER AXS D8-Advance instrument (Cu Kα radiation, λ = 1.5418 Å, in flat plate geometry) to check the crystallinity and phase, thermogravimetric analysis (TGA) at 5 ^{o}C min^{-1} ramp rate in air to determine changes in the metal-linker ratios with etching, nitrogen sorption analysis at 77 K using a Micrometrics 3 Flex (degassing at 120 ^{o}C under dynamic high vacuum over 6 hours using at least 100 mg of sample) to measure BET surface area and pore size distribution and scanning electron microscopy (SEM) using a JSM-IT300 instrument with a secondary electron detector (coating the samples with 10 nm silver) to investigate crystal morphology and macroporosity. In addition, a representative HKUST single crystal etched in pH 2.6 for 72 h was embedded in an epoxy resin, cured at 60 °C for 12 h, and sectioned using an ultra-microtome to image its internal structure. The microtomed block was coated with a thin layer of silver (10 nm) and imaged with SEM at 5 kV using a back-scattered electron detector to reveal the pore connectivity. HKUST samples were dissolved in 0.1 mL deuterium chloride (DCl, 99 atom% D) and 3 mL anhydrous dimethyl sulfoxide-d_6 (DMSO-d_6, 99 atom% D) before being tested by ^{31}P nuclear magnetic resonance (NMR). Further details of these experiments are provided in Appendix C1.

3.3. Results and discussion

Prior to etching, HKUST-1 was assessed for water stability at 40 ^{o}C to avoid unexpected degradation while controlling the degree of acid etching on HKUST-1. This was of importance

for obtaining a defective hierarchical porous HKUST-1 while retaining the MOF microstructure. To investigate the degradation of HKUST-1 in water, 50 mg of normal HKUST-1 was immersed in 50 mL of distilled water for different lengths of time (from 1 to 72 h) at 40 ^{o}C without stirring. PXRD results of these samples show that HKUST-1 immersed in water for 1, 3 and 5 hours partially maintained its original crystallinity with the preservation of peaks at 7 and 12 degrees 2θ. However, after 24 h, this MOF started to noticeably change in structure with the absence of the peaks at 7 and 12 degrees 2θ and an obvious split in the peak at 10 degrees 2θ (Figure 35). Note that peaks at 14, 17 and 27 degrees 2θ retained their positions in all samples, so the assumption of changes in unit cell parameter in the samples immersed in water for periods greater than 24 h can be disregarded. This result is consistent with what was shown in the literature[229] where HKUST-1 was reported to be stable in relative humidity up to 90% at temperature up to 50 ^{o}C and for 6 hours. Disappearance of the characteristic diffraction peaks in PXRD results show that changing the concentration of the acid solution by using serial dilution in water (which was shown to be a very promising method for control of the degree of etching in MIL-100(Fe) from 2 to 12 hours in 40 mM of H_3PO_4[147]) would not be applicable to HKUST-1. In fact, HKUST-1 samples etched in a mixture of phosphoric acid and water at different concentration and time showed poor crystallinity and very low surface area (below 34 m^2 g^{-1}), in comparison to normal HKUST-1 (more than 2,200 m^2 g^{-1}) (Appendix B Figure S7, Table S3 and Table S2).

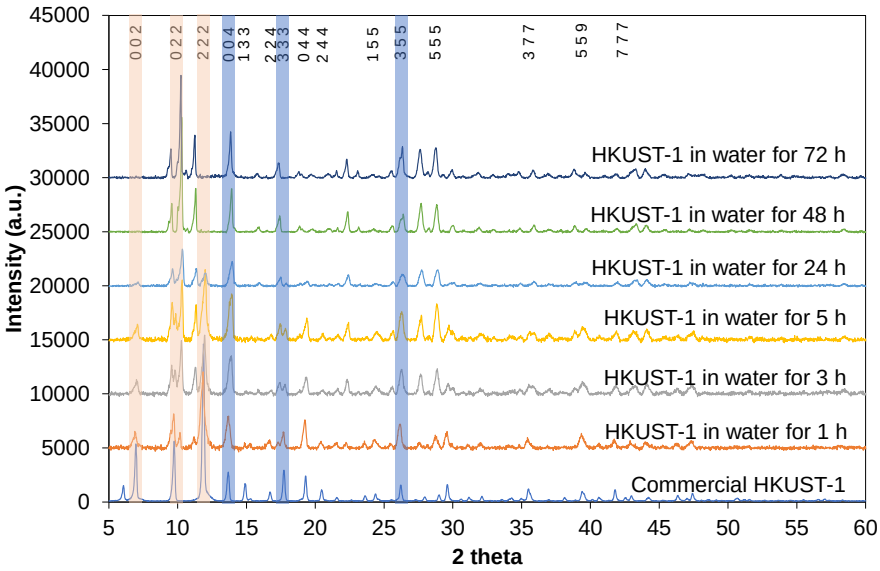

Figure 35. PXRD results of HKUST-1 immersed in water from 1 to 72 hours. Key peaks that remained the same are highlighted in light blue. Key peaks that changed or disappeared are highlighted in light orange. PXRD spectra are offset in intensity, for clarity.

It has been shown that HKUST-1 can be synthesised from a stable precursor solution formed by a mixture of trimesic acid, copper nitrate and DMSO[19]. Recently, we also reported a novel method to synthesise HKUST-1 using supercritical CO_2 to dramatically reduce the amount of MeOH needed to trigger the HKUST-1 nucleation reaction inside the precursor solution[174]. These results suggested that HKUST-1 would be stable in a mixture of DMSO and MeOH, indicating that this could be used to vary the concentration of the acid solution and control the degree of etching in HKUST-1. Indeed, the overall crystallinity of HKUST-1 remained unchanged with up to 10 days etching and up to an acidity of pH 2.6, which is confirmed by the series of PXRD results shown in Figure 36a and b. Note that the decrease in the intensity of the peak at 5.8 degrees 2θ is because of different amounts of moisture adsorbed in the samples during XRD preparation. This was demonstrated by comparing XRD patterns of two simulated HKUST MOFs in hydrated and dehydrated form. It can be seen that the peak at 5.8 degrees 2θ significantly decreased after removing all oxygen atoms of water molecules coordinated with copper in simulated dehydrated HKUST-1 structure (see Appendix B Figure S8).

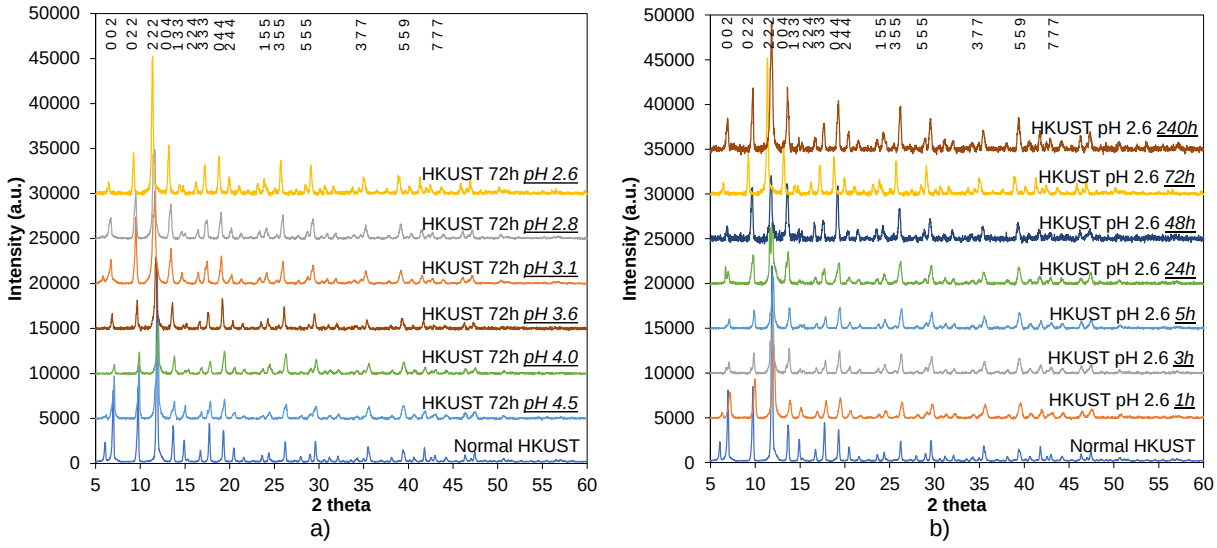

Figure 36. PXRD results of HKUST-1 etching in phosphoric acid using DMSO and MeOH as dilute solvents at different concentrations (a) and times (b). PXRD spectra are offset in intensity, for clarity.

To investigate the mass change after acid etching, the dry weights of the HKUST samples in centrifuge tubes were recorded before exposure to phosphoric acid and after washing with methanol 3 times to remove excess acid and drying the solid in an oven overnight at 60 ^{o}C. The acid etching of the HKUST-1 at pH 2.6 for 72 h was repeated 5 times at the same conditions

to test reproducibility and to estimate experimental errors which could be caused by sample loss during the decanting of the solvents, drying or weighing. The deviation in the measured dry weights shows that the error bars in the measured weights for this experiment are about ±1.5 mg – equipvalent to ~6.2% (Table S5 in Appendix B), which was deemed reliable enough to initially investigate the etching process and compare between samples etched for different times and with different acid concentrations. Figure 37 shows that when etching at pH 2.6 for 72 h, the dried sample lost 24 wt.%. The weight loss decreased when pH increased from 2.8 to 6.4, meaning that the lower the phosphoric acid concentration, the less weight loss (and presumably the less etching) was seen in the sample. When the pH was fixed at 2.6 and the etching time was varied from 1 h to 240 h, a reverse trend was observed. The weight loss of samples etched for short periods (1, 3 and 5 h) was between 13 and 18 wt.%, and for longer periods of exposure to the acid (24, 48 and 72 h) the weight loss observed was between 22 and 24 wt.%. The highest figure was seen in the sample etched for 240 h, reaching 42 wt.% loss after etching in acid. From these results, it can be predicted that the degree of etching depends on both concentration and time.

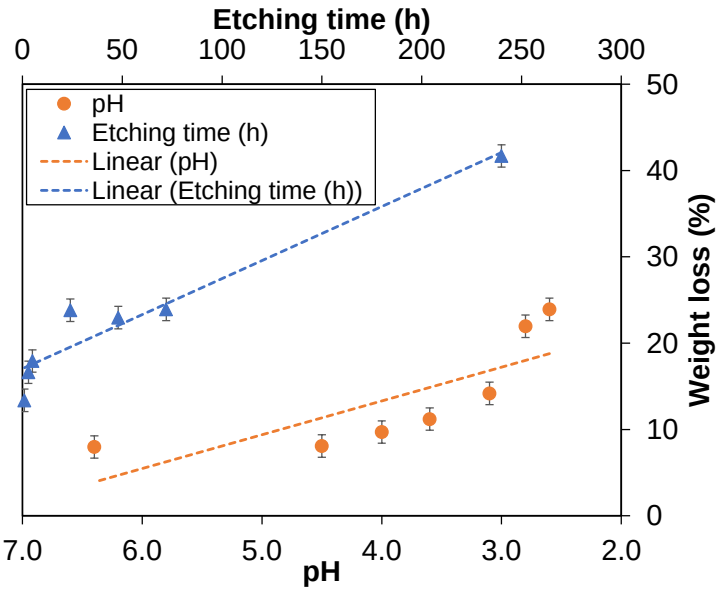

Figure 37. Weight loss of HKUST-1 etching in phosphoric acid using DMSO and MeOH as dilute solvents at different concentrations and times. The dotted lines are linear fits, intended as guides to the eye.

Samples were examined by SEM to investigate the effects of etching on crystal morphology and surface structure. The untreated HKUST crystals were faceted and typically up to 40 microns in diameter (Figure 38a). These features were retained on exposure to the pH 6.4 DMSO/MeOH stock solution (Figure 38b). There was no discernible etching by the SS of the

exposed crystal faces (see insets Figure 38a and b). In contrast, for the samples etched in phosphoric acid for a constant etching time of 72 h using DMSO and MeOH as dilute solvents at different acidities ranging between 2.6 and 4.5 (Figure 38c-h), it can be seen that at less acidic conditions (pH at 3.6 and above) there was no appearance of macropores in these samples even though some features witnessed on the surface of HKUST 72h pH 3.6 show some minor etching effects which can be evidenced in the SEM images in Figure 38c and e.

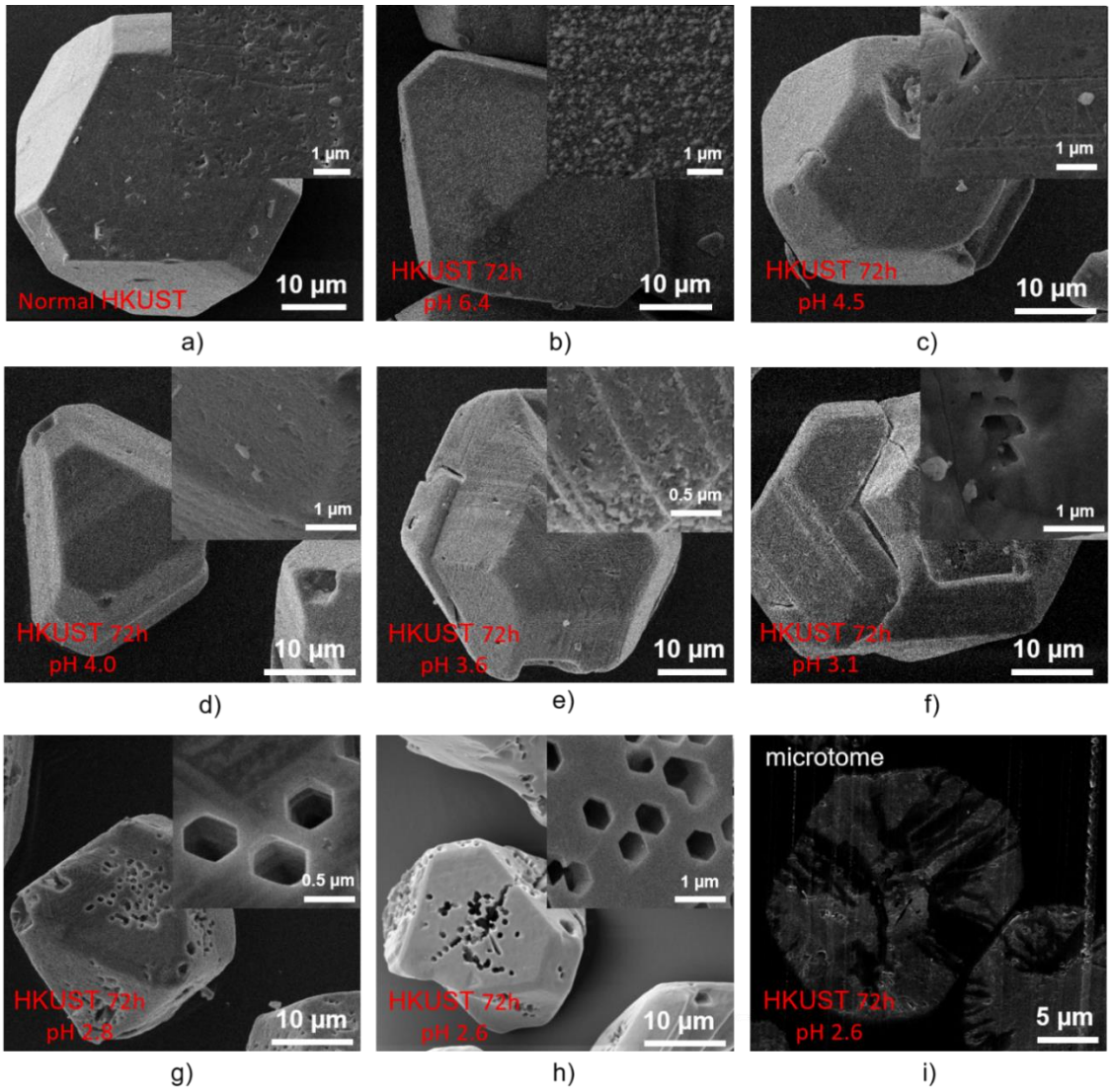

Figure 38. SEM images of HKUST-1 etching in phosphoric acid using DMSO and MeOH as dilute solvents at different concentrations.

At higher concentrations of phosphoric acid in DMSO and MeOH, interestingly, a number of large hexagonal pores with an approximate diameter size of 0.5 µm can be observed. The number of these newly-introduced holes seemed to increase while increasing the acid concentration. Surprisingly, the regular, well-ordered hexagonal shape of these holes in

HKUST-1 has not been reported even though this MOF is a favoured candidate for study of porosity tailoring and surface functionalisation. The sample etching only in DMSO and MeOH (pH = 6.4) in 72 h do not result in any noticeable changes on the surface (Figure 38b), indicating that phosphoric acid played a critical role in creating these hexagonal holes.

To show the inner connectivity of these holes, the sample that was etched at acidity of pH 2.6 over 72 h was carefully sectioned using a microtome and observed again under the SEM. Interestingly, the etching in phosphoric acid using DMSO and MeOH as dilute solvents not only generated hexagonal macropores while preserving the HKUST-1 microstructure and external crystal morphology but also prompted formation of a connected interior pore network between these holes (Figure 38i), which might be very useful to improve molecular diffusion in catalytic processes. Note that the possibility of mechanical cracking on cutting through the resin-embedded crystal can be disregarded because there was no clear evidence of this in the SEM (the HKUST-1 octahedron was still maintained).

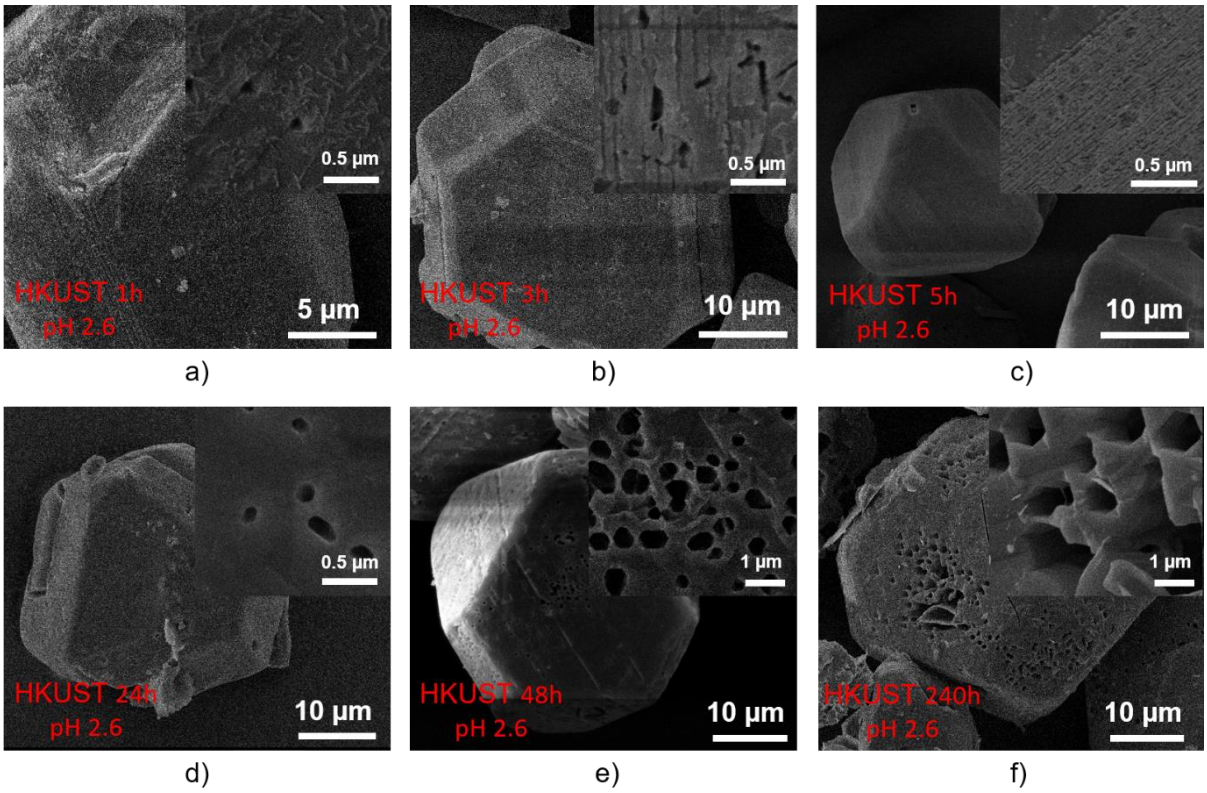

Figure 39. SEM images of HKUST-1 etching in phosphoric acid using DMSO and MeOH as dilute solvents at different times.

In order to examine the effect of etching time on creation of these macropores in HKUST-1, the acidity was maintained at 2.6 (1 mL H_3PO_4 in 10 mL DMSO and 10 mL MeOH) and the etching time was varied from 1 hour to 240 hours (Figure 39a-f). Small holes with some

triangle-shaped geometrical edge features appeared on the surface of the sample etching for 1 hour (Figure 39a), which may suggest the direction of creating hexagonal pores observed previously in the sample etching in 72 hours (Figure 38h). It is also notable that the large hexagonal pores did not appear when using a shorter etching time (up to 5 hours; Figure 39a-c) but appeared when increasing etching time to 24 hours and above (Figure 39d-f). These results are consistent with the non-linear time-dependent porosity generation with supercritical CO_2 exposure time we reported previously.[174] The number of these hexagonal holes in the sample etched over 240 h (Figure 39f) is obviously higher than those in the samples etched over 24 h (Figure 39d), 48 h (Figure 39e) and 72 h (Figure 38h). It can also be seen that the crystal morphology of the original HKUST-1 samples was still preserved (compared with Figure 38a) with an octahedral shape and a crystal size of 15-20 µm.

The surface areas and total pore volumes of each of the samples were examined by using N_2 sorption at 77 K. In the isotherm data shown in Figure 40, all etched samples possess the typical microporous isotherms with two steps clearly observed in the low relative pressure region (P/P_o below than 10^{-3}). This adsorption isotherm is to be expected in normal HKUST-1 which has larger primary pores (d = 0.83 nm) and smaller secondary pores (d = 0.51 nm). This result confirms that the micropore structure within the samples was maintained after etching, in contrast to the distinct loss of microporosity when etching HKUST-1 in phosphoric acid using water as the key solvent (see Appendix B Table S3 and Table S2).

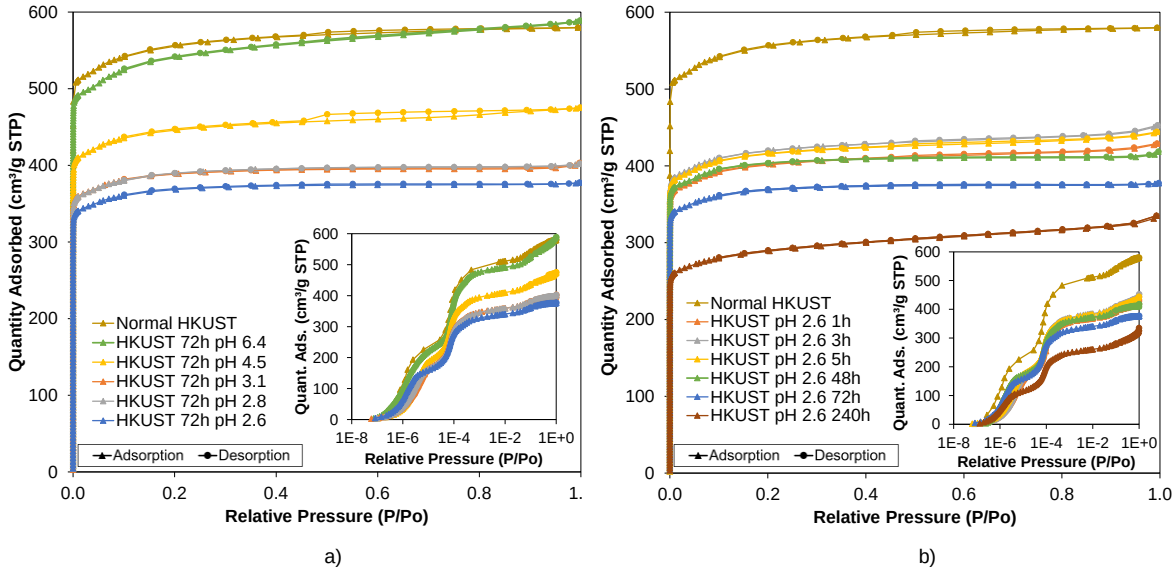

Figure 40. Nitrogen isotherms of HKUST-1 etching in phosphoric acid using DMSO and MeOH as dilute solvents at different concentrations (a) and times (b). The full isotherms in logarithmic scale in the blown-up sections show 2-stepped adsorption in the samples, which correspond to two different micropores preserved after etching.

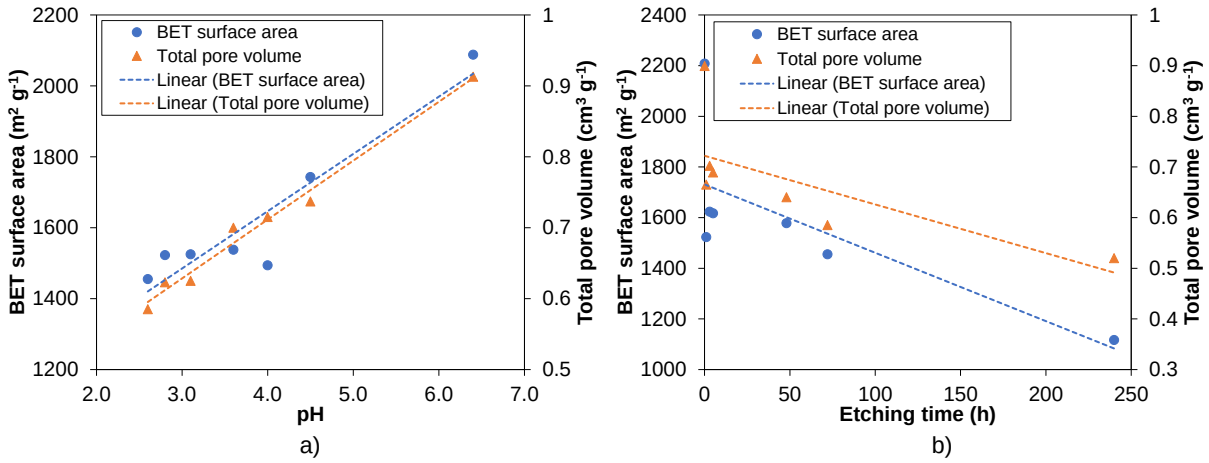

Figure 41. Gas sorption results of HKUST-1 etching in phosphoric acid using DMSO and MeOH as dilute solvents at different concentrations (a) and times (b). The dotted lines are linear fits, intended as guides to the eye.

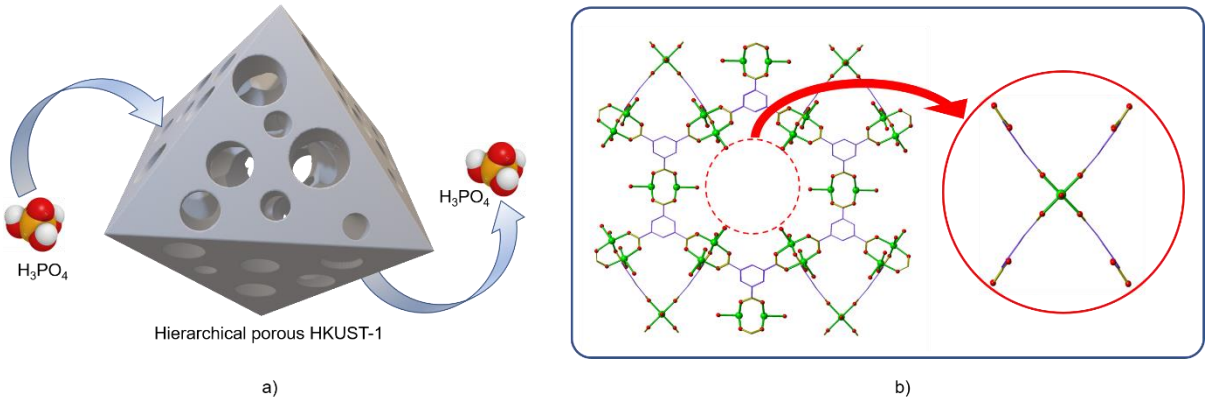

Figure 42. Etching process for HKUST-1 using phosphoric acid. a) Phosphoric acid diffuses into HKUST-1 to form a hierarchical porous structure. b) The disassembly of a cluster and 4 linkers.

The disassembly of 1 copper cluster and 4 linkers (paddlewheels) was considered the main reason of defect formation in HKUST-1.[142,225] This defect formation was confirmed by TGA, which indicated by proportionally lower weight loss over the region between 250 °C and 300 °C for the etched acid- samples (see Figure S10 in Appendix B). ^{31}P NMR additionally confirmed the defect formation did not result in coordination of PO_4^{3-} in the MOF structure (Figure S5 in Appendix B). This cluster disassembly mechanism can be used to explain the formation of large hexagonal cages, which would be, in turn, more susceptible to selective acid etching in HKUST-1 using H_3PO_4 (Figure 42b). Removal of some secondary building units can also be used to explain the lower BET surface areas after HKUST-1 acid etching (Figure 41). The longer the HKUST-1 was exposed to etching in H_3PO_4, a greater number of clusters and linkers in the tetrahedral channel were disassembled, resulting in a greater number of large

hexagonal voids being observed. Remarkably, the overall crystallinity was still preserved due to the maintained structural integrity formed by the majority of secondary building units in the small cages which were not easily accessible by the acid and therefore not affected by the selective acid etching.

3.4. Conclusion

In this study, an innovative approach to acid etching was systematically investigated on a MOF (HKUST-1) that is known not to be stable in water. It is demonstrated that the extent of etching on this MOF depends on both pH and etching time. Geometrical pores were observed on HKUST-1 MOF immersed in phosphoric acid, DMSO and methanol at pH less than 2.8 for more than 24 h. It is predicted that by using phosphoric acid with a size-selective diameter (d = 0.61 nm), the diffusion process occurs preferably in larger pores (d = 0.83 nm) rather than in smaller pores (d = 0.51 nm) of HKUST-1, resulting in the interconnected macropores appearing over longer etching times and higher acid concentrations while the overall crystallinity, morphology and microporosity of this MOF was still preserved. The tailorable hierarchical pore structure obtained by this method would be promising for the use of MOF catalysts, to speed up reactions of bulky molecules where the rate of reaction is limited by low diffusion process or high pressure drop.

CHAPTER FOUR: CONTROLLED FORMATION OF HIERARCHICAL METAL-ORGANIC FRAMEWORKS USING CO_2 EXPANDED SOLVENT SYSTEMS

Methods involving $scCO_2$ synthesis of hierarchical MOFs are introduced in this chapter. HKUST-1 MOF, used as the model MOF for the post treatment via acid etching strategy, is used here also. The use of $scCO_2$ allowed rapid synthesis of HKUST-1, as well as a reduction in the amounts of conventional solvents required for synthesis. Interestingly, this method could be used to control macroporosity in the resulting MOF. This chapter provides a detailed study of the effect of CO_2 pressurisation on the synthesis, resulting in important differences in the structures of the resultant crystallites. The ability to form materials with hierarchical porosity influences their ability to perform useful functions in catalysis and gas storage, indicating that this low-solvent approach could be a facile route to introducing useful hierarchical porosity into these MOF systems.

This chapter appeared as a paper published in *ACS Sustainable Chemistry and Engineering* (DOI: 10.1021/acssuschemeng.7b01429), with the author of this thesis as the first author. The author confirms that he carried out all synthetic experiments, PXRD, SEM, DLS, gas sorption experiments, data analysis and prepared the manuscript. Additional contributions were made by Yanan Fang (Nanyang Technological University), Bingqing Yao (Nanyang Technological University) and Dong Zhili (Nanyang Technological University) who helped with the TEM experiment. Timothy J. White (Nanyang Technological University), Asel Sartbaeva (University of Bath), Ulrich Hintermair (University of Bath) and Valeska P. Ting provided feedback and comments on the manuscript.

Abstract

It is shown that a crystalline metal-organic framework (HKUST-1) can be rapidly synthesised from DMSO/MeOH solution with greatly reduced amounts of organic solvents using a supercritical CO_2 ($scCO_2$) solvent expansion technique. The precursor solution is stable for months under ambient conditions, and CO_2-driven MOF crystallisation is achieved under mild conditions (40˚C, 40-100 bar) with excellent reproducibility. As the degree of liquid phase expansion drives MOF nucleation and growth, the crystallite size and overall yield can be tuned by adjusting the CO_2 pressure. Furthermore, scanning electron microscopy (SEM), high-resolution transmission electron microscopy (HRTEM) and gas sorption analyses showed that in the presence of $scCO_2$, HKUST-1 crystallites with a hierarchical pore structure are generated through a post-crystallisation etching process. These findings demonstrate that $scCO_2$ is a time and material efficient route to MOF synthesis with a high level of control over the crystallisation process for accessing tailored material properties.

4.1. Introduction

Porous materials are attracting considerable attention for numerous applications because of their ability to interact with molecules, not only at their surfaces, but also within the internal cavities. An interesting class of materials which have a wide range of surface areas and porosity are the metal-organic frameworks (MOF), which are extended coordination polymers built from metal ions/metal clusters and organic linkers. These architectures are of interest due to their permanent porosity and flexible linking of metal-cluster nodes and organic ligands, leading to high porosity, chemical stability and thermal resistance.[9,230] The metal-containing units in MOFs, also called secondary building units (SBUs), are rigid squares, tetrahedra or octahedra that self-assemble to form designed topologies, creating permanent porosity. The ability to systematically vary the size and nature of MOF tunnels and cavities makes them promising candidates for applications in gas separation and storage, and catalysis.[12,86,87,231–235]

One of the most stable nanoporous MOFs is copper trimesate (CuBTC) $\{Cu_3[(O_2C)_3C_6H_3]_2(H_2O)_3\}_n$ also known as HKUST-1 or MOF-199. This material, first reported in 1999 by Chui *et al.*,[5] has a cubic 3D framework where the most abundant pore size diameter is 11 Å. HKUST-1 can be synthesised by dissolving $Cu(NO_3)_2$ and trimesic acid (benzene-1,3,5-tricarboxylic acid, BTC) in DMF with a molar ratio Cu/BTC/DMF of 1 : 1 : 90,[236] whereupon nucleation proceeds rapidly after 30 min with the formation of a light-blue

solid. This is exceptional for solvothermal MOF synthesis, which normally require reaction times of several hours to days. Under basic conditions precipitation occurred during precursor solutions mixing, however, the solids formed were ill-defined, amorphous and showed neither the morphology nor the composition of the desired MOF.[237,238] Subsequently, a refined method using DMSO instead of DMF or DEF without additional base prevented premature precipitation, resulting in a very stable HKUST-1 precursor solution even at concentrations as high as 0.5 mol L^{-1}.[19] Addition of a several fold excess of methanol then triggered MOF crystallisation within 10 minutes at room temperature, yielding HKUST-1 with 2 microns octahedral crystals of uniform size.[239]

While appropriate on laboratory scale, the use of large amounts of organic solvents, many of which are volatile, harmful and flammable, is detrimental to the environment and expensive at large scale. Therefore, alternative methods for synthesizing porous MOFs have been investigated, mainly focused on non-conventional solvents including supercritical fluids (SCFs),[240,241] ionic liquids[242] and fluorinated solvents.[170] More recently, "zero-solvent" approaches using solid-phase[243] and gas-phase[244] syntheses have been developed. Although requiring high pressure, SCFs reduce not only the quantities of solvents needed, but also the energy and time required for separation of the SCF from the porous product, because the traditional multiple exchange, filtration and drying steps are unnecessary.[168] In addition, due to their low surface tension and capillary forces, removal of the SCF solvent minimizes pore collapse during purification, which can be significant for highly porous materials.[21] This feature has long been exploited for the post-synthetic purification of aerogels[21,245] and ultra-high surface area MOFs,[18] but somewhat surprisingly, SCF MOF synthesis and purification have rarely been combined so far.

In a separate line of research, the development of tailor-made porous materials exhibiting so-called hierarchical pore structures has attracted considerable current interest.[246,247] These intriguing materials combine micro-, meso- and macro-porosity within one structure, which not only enhances the total surface area, but also facilitates diffusional processes within the solid, thereby improving catalytic activity.[76]

Inspired by recent work, where HKUST-1 synthesised from $Cu(OAc)_2$ with BTC and NEt_3 in DMF diluted with liquid CO_2 showed modified pore sizes,[168] this study sought to investigate how MOF crystallisation may be controlled by CO_2-induced solvent expansion. Specifically, the influence of the mixed media on the product structure was examined. To assess the intrinsic porosity, the materials were subjected to post-synthetic continuous-flow $scCO_2$ extraction.

4.2. Experimental methods

All chemicals were sourced from commercial suppliers and used without further purification (Appendix C Table S6). The general synthesis procedure of HKUST-1 is summarised in Figure S12. Conventional HKUST-1 was prepared following Ameloot *et al.*[19] with a 20-fold scale up. First, a stock solution was made by dissolving 24.52 g copper(II) nitrate hemipentahydrate ($Cu(NO_3)_2 \times 2.5H_2O$) (10.54 mmol) and 11.66 g benzene-1,3,5-tricarboxylic acid (trimesic acid/BTC) (5.54 mmol) in 100 mL DMSO. This deep blue solution was stable over at least 6 weeks at ambient conditions (Appendix C Figure S13a and b). To induce HKUST-1 formation, 10 mL of the stock solution was magnetically stirred at 200 rpm in a glass beaker, 100 mL methanol was added in one portion, and the sample heated to 40 °C for 1 hour with continuous stirring. The HKUST-1 crystallisation reaction is shown in Scheme 2. Product formation was evidenced by a pale turquoise precipitate being formed within 10 minutes. The product was isolated by centrifugation (3000 rpm for 20 minutes), washed with pure methanol and re-centrifuged three times. The clear, colourless solvent was finally decanted and the product dried in air at room temperature to yield 436 mg of a deep blue microcrystalline powder (8.6 wt.% yield).

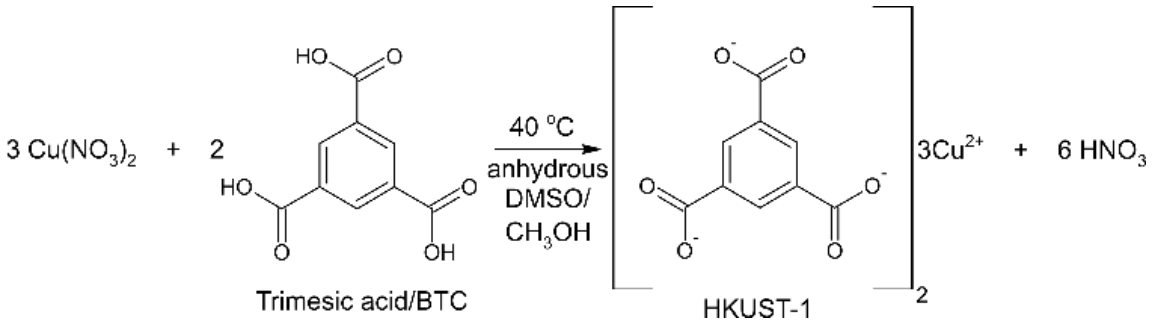

Scheme 2. HKUST-1 crystallisation reaction.

For experiments using CO_2 instead of methanol, 40 mL of the stock solution were added to a glass vial containing 40 mL of methanol, which did not lead to colour change or precipitation. The vial was placed inside a stainless steel high-pressure vessel (V = 250 mL), stirred with a magnetic bar at 200 rpm, heated to 40 °C and pressurised with CO_2 at a flowrate of 5 g min^{-1}. The vessel was then sealed and left stirring at 40 °C. Reaction times ranged from 1 to 72 hours and pressures between 40 and 90 bar (Appendix C Table S7). High pressure view-cell experiments were carried out in a 20 mL stainless steel vessel with opposing windows of single crystal sapphire using 1.5 mL of DMSO stock solution combined with 1.5 mL methanol under otherwise identical conditions.

All products were dried further by continuous-flow $scCO_2$ extraction. A sample of 0.1-0.3 g solid was placed in 2 cm dialysis tubing (cellulose, 1000 MW cut-off), sealed with copper wire (Appendix C Figure S13d), and then placed into stainless steel high-pressure tubing (0.5 inch diameter, 10 cm length) with a 50 µm particulate filter at the outlet. The sample was subjected to continuous $scCO_2$ extraction at 40 ^oC and 120 bar (δ = 0.69 g/mL) with 2 g CO_2 min^{-1} over 18 hours using a custom-built SCF continuous flow rig similar to that previously described.[48] The plug flow reactor was then depressurised at 10 bar min^{-1}, the sample recovered and analysed immediately. After drying, the sample colour had changed from dark to light blue (Figure S13f and g), with a weight loss of 6-10%.

To investigate the potential solubility and post-synthetic modification of crystalline HKUST-1 in methanol and DMSO, 0.1 g of conventionally synthesised HKUST-1 was added to a mixture of 40 mL methanol and 40 mL DMSO, and stirred magnetically at 200 rpm and 40 ^oC for 48 hours (Appendix C Figure S13c).

The porous MOFs were characterised by powder X-ray diffraction (PXRD), gas sorption analysis, scanning electron microscopy (SEM), high-resolution transmission electron microscopy (HRTEM), and dynamic light scattering (DLS). Details of these experiments are provided in the Appendix C1.

4.3. Results

4.3.1. Using CO_2 as anti-solvent for HKUST-1 synthesis

As reported previously, HKUST-1 nucleation from DMSO can be promoted by either evaporating at 373 K over 24 hours or by adding methanol as an anti-solvent to prompt nucleation. The latter method requiring 50 times excess methanol[239] is challenging in large scale batch-wise synthesis, thus we investigated the amount of anti-solvent required by systematically varying methanol addition (1:1, 2:1, 4:1, 6:1, 8:1 and 10:1 by volume) while monitoring HKUST-1 formation (Figure 43a). It was found that a 4-fold excess of methanol is the minimum to induce nucleation within 1 hour, with higher yields obtained with more MeOH. In common with the pure DMSO precursor solution, 1:1 mixtures of DMSO and MeOH failed to produce any solid even after 6 weeks at room temperature. Thus, the possibility of inducing HKUST-1 formation from neat DMSO and 1:1 DMSO/MeOH solutions by expansion with CO_2 was investigated. Many liquid organic compounds (including DMSO and MeOH) form so-called type II solvent mixtures of high mutual solubility with compressed CO_2 in the near-

critical region (*i.e.* around p_c, but above T_c), see section 1.3.2.[20] The dissolution of large amounts of CO_2 leads to volumetric expansion of the solvent (up to 10 times the initial volume), and these expanded liquid phases (ELPs) show a range of interesting (tuneable) physico-chemical properties.[248] In case of DMSO, the decrease in polarity and disruption of the stabilizing hydrogen bonding interactions that prevent premature HKUST-1 formation[249,250] in the absence of an anti-solvent were expected to be the trigger for CO_2 induced MOF crystallisation. Note that the HKUST-1 precursor solution was stabilised by strong O-H···O hydrogen bonds, forming a two-dimensional supramolecular network within each layer (see Figure S14). The donor groups are the hydroxyls of the trimesic acid molecules, while the acceptors are the carbonyl or the sulfoxide O atoms.[249]

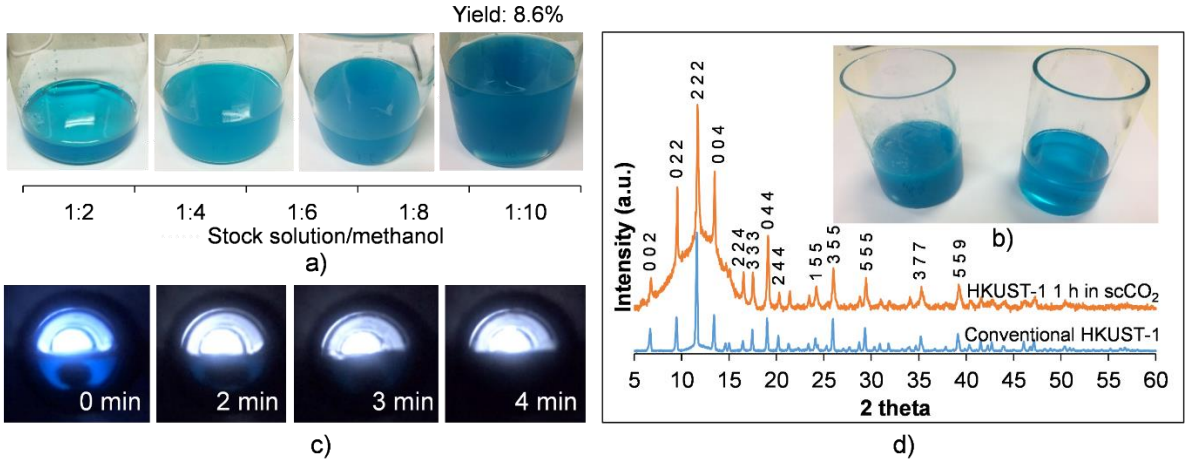

Figure 43. HKUST-1 formation driven by solvent expansion with CO_2. a) Conventional HKUST-1 synthesis with different ratios of DMSO to methanol. b) Precursor solution as 1:1 mixture of DMSO/MeOH after 72 hours at 40 °C in air (right) and after exposure to 75 bar CO_2 (right). c) Observation of HKUST-1 synthesised with 65 bar CO_2 in a view cell. d) PXRD diffraction peaks of HKUST-1 synthesised by conventional MeOH excess method compared to using CO_2 induced solvent expansion.

It was found that HKUST-1 formation could not be induced by expanding pure DMSO precursor solutions with 90 bar CO_2 for 72 hours at 40°C. However, pressurizing the equally stable 1:1 DMSO/MeOH mixture with CO_2 at 40 °C resulted in a blue precipitate in yields of 4-9% (depending on conditions; see below) that did not re-dissolve upon depressurisation. PXRD showed the solid to be pure HKUST-1 (Figure 43d), and SEM revealed octahedral crystallites ~2 µm in size, similar to conventional synthesis using >10-fold excess of MeOH (Figure 46a). This confirms that MOFs can be synthesised by CO_2 induced solvent expansion using greatly reduced amounts of organic solvent. As the solubility of CO_2 in DMSO and

MeOH is very similar,[23] leading to a comparable decreases in polarity when expanded with CO_2,[251] it is concluded that H-bonding disruption must be the effective driving force for CO_2-induced HKUST-1 crystallisation from DMSO/MeOH mixtures.

When the reaction was followed in a high-pressure view cell at 40 ^oC, a precipitate was observed within 2 minutes after introducing 65 bar of CO_2 to the reactor, and a fully opaque mixture was obtained after 4 minutes (Figure 43c). Thus, CO_2 driven HKUST-1 crystallisation from DMSO solution is faster than with excess MeOH, yet produces phase-pure crystalline material, distinct from the use of DMF and/or additional bases.

4.3.2. Effect of CO_2 pressure on HKUST-1 yields and particle sizes

To investigate how the CO_2 content in the expanded liquid phase affects HKUST-1 formation, the CO_2 pressure applied was varied from 40-90 bar while temperature, reaction time and flowrate were held constant (40 ^oC, 24 h and 5 g min^{-1}). Longer reaction times were chosen for these experiments to ensure that equilibrium was established. Figure 44c shows that up to 60 bar CO_2 the yield of HKUST-1 increased to levels obtained with an excess of organic anti-solvent. At higher pressures the yields decreased again, an observation ascribed to a decrease in pH with increasing pressure, which progressively destabilizes the product. This is supported by the known sensitivity of HKUST-1 to acidic media[246,247] and our observation of post-synthetic etching effects described below.

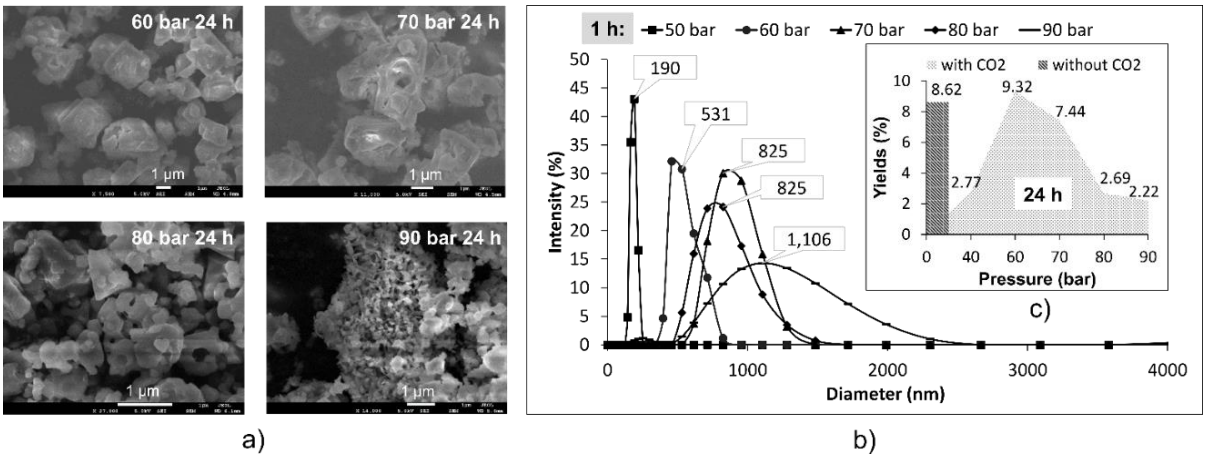

Figure 44. Effect of CO_2 pressure on particle sizes and yields. a) SEM images of HKUST-1 synthesised with different CO_2 pressures at 40 ^oC after 24 h. b) Particle size distribution of HKUST-1 synthesised with different CO_2 pressures at 40 ^oC after 1 h. c) Yields of HKUST-1 formation synthesised with different CO_2 pressures at 40 ^oC after 24 h.

SEM showed that up to 70 bar CO_2, the particle sizes obtained were comparable to the conventionally synthesised material, but at higher pressures smaller particles with ill-defined shapes formed, despite retaining their crystallinity (Figure 44a). Lowering the pressurisation rate from 5 g min^{-1} to 0.1 g min^{-1} for 75 bar CO_2 gave similar yields and crystallite sizes (Appendix C Table S7), indicating that the amount of CO_2 added is the dominant factor in the crystallisation process, rather than its rate of addition.

To gain deeper insight into how CO_2 pressure affects crystallite nucleation and growth, particle size distributions were analysed by dynamic light scattering (DLS) after one hour reaction time (Figure 44b). Under these conditions, applying 40 bar of CO_2 produced insignificant amounts of HKUST-1. However, at 50 bar and above, the DLS results showed a direct relationship between pressure and average particle size, with dispersity increasing substantially at higher pressure. This behaviour suggests more rapid nucleation at higher pressures, likely due to the larger amounts of anti-solvent added. These results demonstrate that particle sizes and dispersity can easily be controlled over a wide range simply by varying the CO_2 pressure applied (if the temperature is kept above T_c to avoid condensation).

4.3.3. Effect of CO_2 exposure on HKUST-1 porosity

To confirm the production of porous HKUST-1 crystallites and assess the influence of CO_2 on their mesostructure, nitrogen adsorption/desorption analysis at 77 K was performed following $scCO_2$ extraction of the isolated materials. The samples synthesised by CO_2-induced solvent expansion showed the typical microporous isotherms expected of HKUST-1, with total pore volumes >0.5 cm^3 g^{-1} and BET surface areas >1000 m^2 g^{-1} (Appendix C Figure S4). Interestingly, when comparing different reaction times under otherwise identical conditions, a small but consistent decrease in both surface areas and pore volumes the longer the samples had been left in the CO_2 expanded DMSO/MeOH solvent mixture is seen (Table 3). Analysis of the N_2 adsorption/desorption isotherms shows this to originate from a greater proportion of macropores which contribute less to surface area than micropores (Figure S16), which can also be seen in the SEM and TEM analyses. Figure 46b-f shows the change in morphology over time, with faceted macroporous crystallites and mesopores appearing in the samples left for 24 h (Figure 46d and Appendix C Figure S17a). The number of mesopores increased with longer exposure to CO_2; after 72 h the microstructure consisted of a finely divided network of macro- and mesopores (Figure 46f and Appendix C Figure S19a). For 24 h and 72 h, the nature of the

porosity was further confirmed by HRTEM (Figure 46j and k, Appendix C Figure S17b and Figure S19b). All samples produced PXRD patterns characteristic of HKUST-1 (Appendix C Figure S15), confirming the MOF framework was preserved.

Table 3. BET surface areas and total pore volumes of HKUST-1 samples precipitated with different anti-solvents at varying reaction times (all at 40˚C, all $scCO_2$ extracted prior to analysis).

	HKUST-1 MeOH 1h	**HKUST-1 MeOH 48h**	**HKUST-1 70 bar CO_2 1h**	**HKUST-1 70 bar CO_2 24 h**	**HKUST-1 70 bar CO_2 48 h**	**HKUST-1 70 bar CO_2 72 h**
Surface area (m^2 g^{-1})	2032 ± 2	1789 ± 2	1616 ± 3	1693 ± 2	1409 ± 2	1220 ± 1
Total pore volume (cm^3 g^{-1})	0.811	1.405	0.592	0.794	0.666	0.545

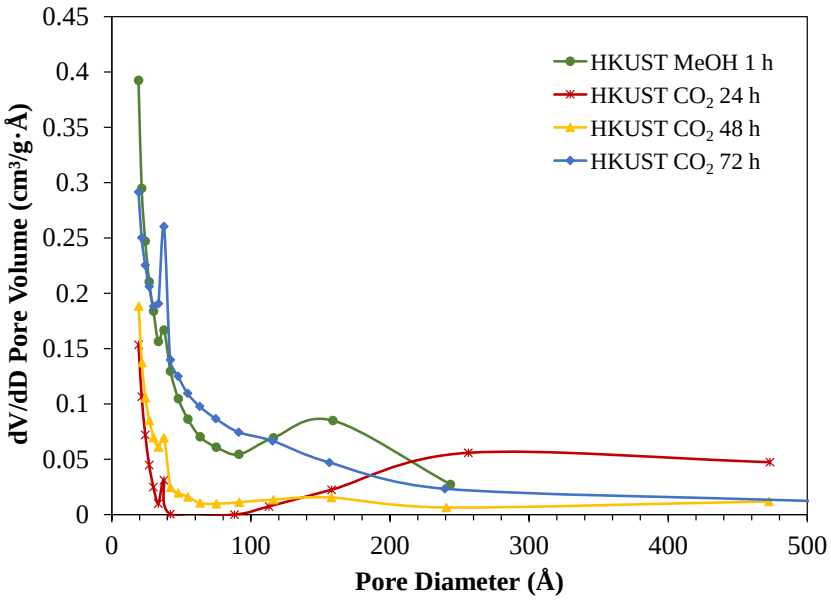

Figure 45. The mesopore size distribution curves for HKUST-1 samples precipitated with different anti-solvents at varying reaction times (all at 40˚C, all $scCO_2$ extracted prior to analysis).

Analysis of the differential pores size distributions (Figure 45) revealed that all samples precipitated from base-free 1:1 DMSO/MeOH solution, either with a 10-fold excess of MeOH or with 70 bar CO_2, showed the characteristically high, intrinsic microporosity of HKUST-1. Consistent with the SEM analyses, samples synthesised via CO_2 expansion of the DMSO/MeOH precursor solution show added macroporosity. These results differ from Peng's data[168] that showed almost exclusive mesoporosity for HKUST-1 synthesised from DMF/NEt_3 precursor solutions which alone form non-porous, amorphous solids, but addition of liquid CO_2 allows macroporous HKUST-1 to crystallize from the solvent mixture.

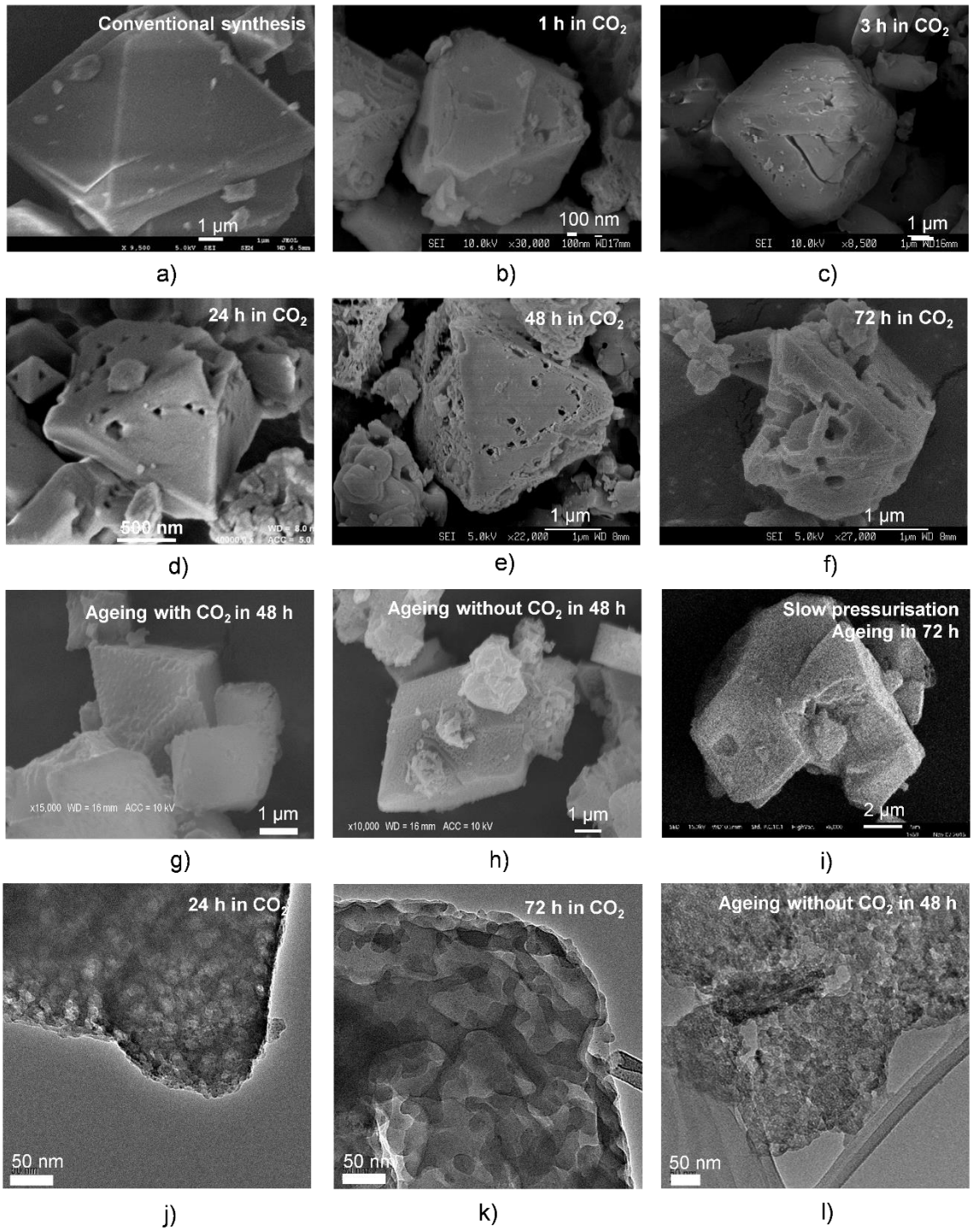

Figure 46. SEM and HRTEM images of HKUST-1 synthesised in different conditions. a) HKUST-1 synthesised by a conventional method. b-f) HKUST-1 synthesised with CO_2 at 75 bar over 1, 3, 24, 48 and 72 hours respectively. g) HKUST-1 ageing in methanol, DMSO and CO_2 over 48 hours. h) HKUST-1 ageing in methanol and DMSO over 48 hours. i) HKUST-1 synthesised with CO_2 at 75 bar slow pressurisation. j) and k) HRTEM images of HKUST-1 synthesised in 24 and 72 hours. l) HRTEM image of HKUST-1 ageing in methanol and DMSO over 48 hours.

To test for post-synthetic ageing effects in conventionally synthesised HKUST-1 material we left samples in 1:1 DMSO/MeOH for 48 h at 40 ˚C without added CO_2. PXRD and SEM analyses showed that both the crystallinity (Appendix C Figure S15) and microstructure (Figure 46h) were preserved in this case, although there is some evidence of surface roughening by HRTEM (Figure 46l) and the BET surface area is slightly reduced (Table 3). Considering the much more pronounced effect of HKUST-1 ageing in the CO_2 expanded DMSO/MeOH mixtures it can be concluded that, in line with the observation of lower yields at higher pressures discussed above (Figure 44), the additional acidity introduced by CO_2 accelerates post-synthetic ageing that leads to increased levels of macroporosity in the MOF crystallites. This observation, which to the best of our knowledge has not been previously described for a MOF,[*] represents another experimental variable of the CO_2 expansion method for MOF crystallisation that allows fine-tuning the properties of the resulting material. The possibility of adding larger pores and channels to a crystalline MOF without compromising its intrinsic highly microporous structure offers exciting prospects for applications in any process that may be limited by diffusional resistance to its internal surface. Importantly, crystallite size and porosity may be adjusted independently by the appropriate choice of CO_2 pressure and reaction time respectively, allowing high levels of process control that may be challenging using conventional protocols.

4.4. Conclusion

It has been demonstrated that crystalline, porous HKUST-1 can be synthesised using CO_2-induced solvent expansion as an alternative to adding copious amounts of organic solvents. HKUST-1 crystallisation is triggered by the application of CO_2 to a stable 1:1 DMSO/MeOH precursor solution that does not form any precipitate in the absence of CO_2. Rapid nucleation and HKUST-1 crystallisation occur under 50-90 bar CO_2 at 40 ˚C to achieve yields comparable to conventional anti-solvent methods. This low-solvent route to MOF synthesis may find wider use and lead to greener MOF production with reduced environmental impact. Significantly, the CO_2 expansion technique allows tight control over crystallite size by adjustment of CO_2 pressure, and post-synthetic ageing accelerated by the presence of CO_2 to create additional porosity. As this added meso- and macro-porosity is interconnected with the intrinsic

[*] A similar change of morphology over time (in the absence of CO_2) has very recently been observed for the Zn-based zeolitic imidazolate framework ZIF-8.[172]

microporosity of the MOF, a truly hierarchical pore architecture was obtained that could prove beneficial for applications in gas separation and catalysis.

CHAPTER FIVE: USING SUPERCRITICAL CO_2 IN THE PREPARATION OF METAL-ORGANIC FRAMEWORKS: INVESTIGATING EFFECTS ON CRYSTALLISATION

The $scCO_2$ method, which was successfully utilised on HKUST-1 MOF, was extended to other MOF systems including MOF-74(Zn), UiO-66, Zn-BTC (in DMSO) and $[Cu_{24}(OH\text{-}mBDC)_{24}]_n$ to probe the generalisability of this mechanism for the introduction of additional porosity. In this chapter, it was proven that the effectiveness of $scCO_2$ to create hierarchical porous structures depends on the MOF chemistry, in which the nature of solvents, ligands and metals in the precursor solution need to be considered. This chapter appeared as a draft which is about to be submitted to *CrystEngComm*. The author confirms that he carried out all MOF preparation experiments, PXRD, SEM, gas sorption experiments, data analysis and prepared the manuscript. Additional contributions were made by Valeska P. Ting, who provided feedback and comments on the manuscript.

Abstract

Supercritical CO_2 ($scCO_2$) has been used extensively in the removal of solvents from gels or polymers, to produce highly porous materials. They have shown some promise in the preparation of metal-organic frameworks (MOFs) with a goal of achieving permanent additional meso- and macropores (forming so-called hierarchical structures) in these materials. Here, we have applied this process to a range of MOFs including MOF-74(Zn), Zn-BTC, UiO-66 and $[Cu_{24}(OH\text{-}m BDC)_{24}]_n$ to explore the effect of $scCO_2$ on different chemical systems. It was shown that $scCO_2$ can have an effect on crystallinity, crystal size and morphology, however, there was no evidence of additional meso- or macroporosity in these MOFs. These findings provide new information on the effects of introducing $scCO_2$ into the synthesis of a broad range of different MOFs, and provides information to direct further application of $scCO_2$ as an approach for morphological control.

5.1. Introduction

Supercritical fluids (SCFs) are fluids under conditions where both temperature and pressure are maintained beyond the critical point of the pure substance. In the SCF regime, chemical and physical properties undergo remarkable changes, allowing changes in solvent polarity, liquid-like densities, gas-like viscosities and compressibility, reduced surface tension and increased diffusivities. As a result, mass transfer behaviour in SCFs can be greatly enhanced, allowing the SCF to easily penetrate solid matrices and dissolve a wide range of compounds.

Thus, SCFs have been widely used in industry, for example in food technology (*e.g.* for extraction of vitamin E from natural sources,[252,253] decaffeination of coffee[254] and removal of alcohol from wine and beer,[255,256]), as a "green" solvent in dry cleaning of textiles[257]. More recently, they have been applied in the synthesis and processing of porous materials[21,36,37]. Some substances commonly used in the form of SCFs include nitrous oxide, ethylene, propylene, propane, n-heptane, ethanol and ammonia but supercritical CO_2 ($scCO_2$) is the most common[258] because of its low critical point (T_c and P_c of CO_2 are 31.1 ^oC and 73.9 bar, respectively[176]), and its non-toxic, non-flammable and inexpensive nature. Use of $scCO_2$ has been extensively studied as a way to incorporate stable permanent porosity in materials during various processing steps including crystallisation,[153–155] impregnation,[156] dispersion,[157] drying[158] and activation[159,160].

The study of porous materials, which can be either ordered structures (including zeolites, metal-organic frameworks (MOFs) and silicates), or disordered materials (including activated carbons, ceramics, metals and polymers), has been listed among the fastest growing research areas of recent years. In this field, MOFs, normally microporous or mesoporous crystallites constructed by the coordination of transition-metal nodes and organic linkers, have emerged as enabling materials for a wide variety of potential applications, showing promise for gas storage,[10–12] gas separation,[83–86] catalysis,[13,14] carbon dioxide capture[87–89] and as semiconductors[90,91]. Due to the high interest in these materials, various synthetic methods have been developed beyond the conventional solvothermal approaches which are a straightforward way to achieve highly crystalline materials but have the potential to use large amounts of organic solvents. In addition, there has been a recent trend towards creation of multiple porosities (so-called hierarchical pore structures) in these materials,[92,259] leading to the development of a number of innovative synthetic strategies including macrostructural templating,[112,114,116–118] gelation,[127,128,132,260] acid etching,[146–148,151] use of supercritical CO_2[167,168,171–173] and three-dimensional (3D) printing[199,201,202,261].

Using supercritical carbon dioxide during the synthesis has been shown to be successful in introducing additional porosity to traditionally microporous or mesoporous MOFs.[154,155,174] Unlike other methods such as templating or gelation, using $scCO_2$ can preclude the use of additional purification or activation steps to obtain hierarchical structures without pore collapse. It has been reported that introducing $scCO_2$ into a system containing organic or ionic liquids to obtain a switchable solvent[168] or binary solvent,[169,170] resulted in additional mesoporosity in MOFs. Interestingly, it has been shown that particle sizes and porosity can be tuned by varying CO_2 pressure during synthesis, or by using $scCO_2$ to acid etch post synthetically which introduces a further method for producing hierarchical porous MOFs with improved diffusion rates in catalytic applications.

However, the mechanism for the introduction of the larger pores in the MOF crystallites via $scCO_2$ synthesis is not well understood. It was thought that the expanded liquid volume at CO_2 pressure resulted in the mesocellular formation of building blocks before the frameworks were assembled.[168] However, by changing to hydrogen-bonded complexes (using DMSO instead of DMF to form a precursor solution in HKUST preparation), Doan *et al.* reported that the MOF was actually formed before additional macropores were driven by $scCO_2$. The latter synthesis can be related to the etching mechanism which was further studied using different acidic agents.[147–149] In addition, a method involving $scCO_2$ has been reported which has the

advantages of triggering or enhancing the nucleation rate from a MOF stock solution,[174] while simultaneously reducing the amount of co-solvent required to trigger the reaction. Here, we report the results of a range of investigations into the use of $scCO_2$ in different MOF syntheses (see Figure 47), to provide insights which could improve the generality of such approaches.

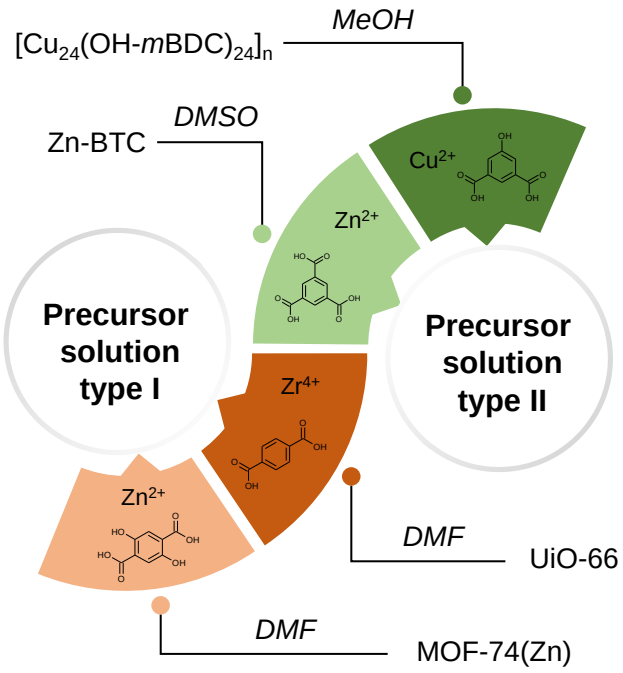

Figure 47. Schematic representation of synthetic methods for different MOFs. Precursor solutions where MOFs were formed without adding antisolvents are referred to as "precursor solutions type I" and precursor solutions where MOFs crystallised only if an antisolvent was added are referred to as "precursor solutions type II"

In this study, the $scCO_2$ synthetic method which was successfully employed in HKUST-1[168,174] and Zn-BTC (in DMF)[167] was further examined using a range of other MOF systems including MOF-74(Zn), UiO-66, Zn-BTC (in DMSO) and $[Cu_{24}(OH\text{-}m BDC)_{24}]_n$. These MOFs were examined to see the effect of $scCO_2$ on the creation of meso- and macropores. Zn-BTC was chosen as an example of a HKUST-1 MOF analogue that could not be typically synthesised using the mixture of DMSO and MeOH which was reported previously as a crucial factor to obtain additional macropores from expanded solvent systems,[161] even though this MOF was shown to be a successful candidate for $scCO_2$ templating.[167] $[Cu_{24}(OH\text{-}m BDC)_{24}]_n$ was selected as an example of a MOF which shares the same copper paddlewheel and similar ligands to the HKUST-1 MOF used in previous $scCO_2$ synthetic studies,[59] but having a benzene derivative

with two instead of three carboxylic acid groups. MOF-74(Zn) was also synthesised with $scCO_2$ in the same manner as reported in the literature,[174] in order to investigate the behaviour of CO_2 towards different solvent systems. UiO-66 was chosen as an example of a well-known MOF that is not easily synthesised at 40 °C, to see if the crystallisation could be triggered in the presence of $scCO_2$. In the syntheses of MOF-74(Zn), UiO-66, Zn-BTC and $[Cu_{24}(OH\text{-}m BDC)_{24}]_n$, $scCO_2$ was introduced to precursor solutions where either MOFs were formed without adding antisolvents (hereafter referred to as "precursor solution type I") or MOFs crystallised only if an antisolvent was added (hereafter referred to as "precursor solution type II"). Introducing $scCO_2$ to these different solutions was carried out to help to understand the role of this supercritical fluid in MOF formation.

As will be seen, employing $scCO_2$ in these systems had a variety of effects on the crystallisation of these MOFs. The results of this study can be used to build up an understanding of the behaviour of $scCO_2$ in different solvents on MOF crystallisation.

5.2. Materials and Methods

All reagents were purchased from commercial sources and used without further purification. Due to constraints on CO_2 pressure, MOF synthesis at low temperature was preferred. In this study, 40 °C was chosen as the synthesis temperature for MOF-74(Zn), UiO-66 (see Appendix D2.4), Zn-BTC and $[Cu_{24}(OH\text{-}m BDC)_{24}]_n$. The conventional syntheses of these materials were also reported to allow comparison with the $scCO_2$ method.

5.2.1. Synthesis of MOFs by conventional methods

Synthesis of MOF-74(Zn)

MOF-74(Zn) (*i.e* $Zn_2(DOBDC)$, where DOBDC is 2,5-dioxido-1,4-benzenedicarboxylate) was synthesised at low temperature following the method reported by Yaghi *et al.*[262] Typically, 0.24 g 2,5-dihydroxyterephthalic acid (H_4DOBDC, 2.4 mmol) and 0.69 g $Zn(OAc)_2{\cdot}2H_2O$ (6.24 mmol) were dissolved in 40 mL of DMF in a 200 mL glass vial, stirring magnetically for 30 mins until a clear solution formed. This vial was sealed with parafilm before being placed in an oven for crystallisation at 40 °C for 24 h. The product was separated by filtration and repeatedly washed with methanol, before drying at room temperature to obtain 0.69 g MOF-74 solid (giving a yield of 34.0% based on Zn). The reaction scheme for formation of this MOF at low temperature is shown in Scheme 3.

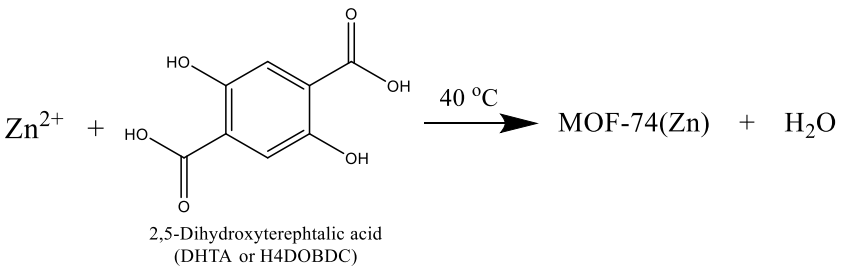

Scheme 3. Synthesis of MOF-74(Zn)

Synthesis of [Cu_{24}(OH-mBDC)$_{24}$]$_n$

The synthesis of [Cu_{24}(OH-*m*BDC)$_{24}$]$_n$ was informed by the procedure reported for synthesis of copper-based cuboctahedron metal-organic polyhedra by Lee *et al.*[263]. The synthesis of this MOF is illustrated in Scheme 2. Typically, 40 mL of 1.46 g OH-*m*BDC MeOH was mixed with 120 mL of 1.60 g Cu(OAc)$_2$.H$_2$O MeOH (MeOH was used as a solvent in this system) to form a stock solution. No precipitation occurred after 10 days. After that, 12.5 mL *N,N'*-dimethylacetamide and 7.5 mL of MeOH were added to 80 mL of the stock solution, stirring at 200 rpm at 40 °C for 3 days. The blue solid was separated by filtration, repeatedly washed with methanol, yielding 1.9 g of solid after drying at room temperature.

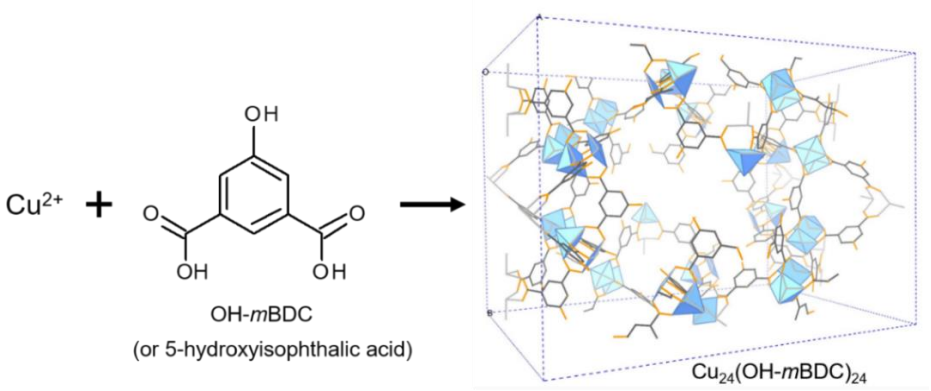

Scheme 4. Synthesis of [Cu_{24}(OH-mBDC)$_{24}$]$_n$ (copper clusters represented as blue polyhedra, C-C bonds are represented as dark grey sticks, C-O bonds are represented as orange sticks; all hydrogen atoms are omitted for clarity)

5.2.2. Synthesis of MOFs using supercritical CO_2 ($scCO_2$)

In the $scCO_2$ routes, MOF precursor solutions (a mixture of metal salt and acid linker dissolved in a solvent) were produced with the same concentrations as the conventional methods above and were placed in a 200 mL glass vial, then sealed inside a 250 mL cylindrical steel reactor pressure vessel, magnetically stirrer at 200 rpm and heated to 40 °C in an oven. The vessel was

connected to a $scCO_2$ rig equipped with a flow controllable liquid pump. The vessel was pressurised to 75 bar at a flowrate of 5 g min^{-1}, keeping the reaction time the same as for the normal synthesis, *i.e.* without $scCO_2$. After reaction, the reactor was depressurised slowly to atmospheric pressure. The resulting solution was centrifuged (10,000 rpm for 10 minutes), washed with methanol 3 times, and dried in air at room temperature to obtain a solid product.

5.3. Results and Discussion

This study focuses on some well-known MOFs, namely: MOF-74(Zn), UiO-66, Zn-BTC and $[Cu_{24}(OH\text{-}mBDC)_{24}]_n$ (see Table 4). Synthetic procedures of the well-known MOFs mentioned above with and without $scCO_2$ are given in either the Materials and Methods (section 5.2) or in the Appendix D (section D2). In the conventional method in the absence of $scCO_2$, MOF-74(Zn) was synthesised using DMF and taken to the crystallisation step without the use of antisolvents. Using $scCO_2$ in these MOF syntheses was expected to form the same meso- and macroporous structures as seen in HKUST-1 and Zn-BTC reported by Peng *et al*[167,168]. $[Cu_{24}(OH\text{-}mBDC)_{24}]_n$ with similar structural composition to HKUST-1 was synthesised in MeOH in which a precursor solution of OH-*m*BDC and $Cu(OAc)_2$ was formed. Results of these syntheses are further discussed below.

Table 4. Summary of MOFs synthesised by conventional methods

MOFs	Metal nodes	Linkers	Solvents	Temperature
MOF-74(Zn)	Zn	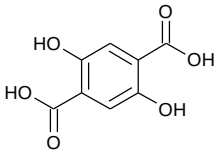	In DMF, MOF was formed without adding antisolvents	RT
$[Cu_{24}(OH\text{-}mBDC)_{24}]_n$	Cu	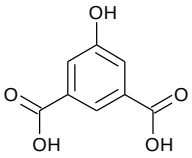	In MeOH, MOF was not formed without adding antisolvents	RT
Zn-BTC (see Appendix D)	Zn	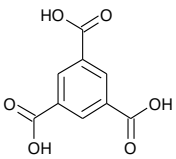	In DMF, MOF was formed without adding antisolvents. In DMSO, MOF was not formed without adding antisolvents	100 °C
UiO-66 (see Appendix D)	Zr	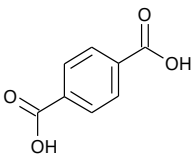	In DMF, MOF was not formed without adding antisolvents	120 °C

The use of DMSO in BTC to form hydrogen-bonded complexes as reported in the HKUST-1 synthesis[174] was extended to the Zn-BTC. However, this method did not seem to be successful for this MOF, with no precipitation occurring from the stock solution after adding up to ten times the volume of MeOH and introducing $scCO_2$ into the system after 3 days. This might be due to the metal-ligand coordination forces between Zn and BTC not being able to overcome the H-bonding, even in the presence of CO_2-expanded MeOH as an antisolvent at 40 ^oC. In the synthesis of UiO-66, 40 ^oC was chosen as the technical preferable temperature for the $scCO_2$ method. However, the MOF synthesised at this temperature shows poor crystallinity with broader PXRD peaks than conventional UiO-66. Syntheses of Zn-BTC (in DMSO) and UiO-66 are described and further discussed in Appendix D.

5.3.1. Using $scCO_2$ in precursor solution type I

In MOF-74(Zn) synthesis

MOF-74(Zn) was synthesised via the methods given in the Materials and Methods section, enabling comparison of the MOFs synthesised without CO_2 (here called "normal MOF-74(Zn)") to the MOF synthesised with $scCO_2$ (here called "MOF-74(Zn) in $scCO_2$"). As seen in Figure 48, normal MOF-74(Zn) samples show a similar powder X-ray diffraction (PXRD) pattern to simulated MOF-74(Zn) with all the main peaks at 7, 12, 22, 25 and 32 degrees 2θ preserved, confirming that this MOF can be successfully synthesised at low temperature (40 ^oC) in addition to the higher temperatures of 110 ^oC or 100 ^oC as reported by others[264,265]. The PXRD pattern of MOF-74(Zn) in $scCO_2$ is almost identical to the normal MOF-74(Zn) sample (see Figure 48), showing that the $scCO_2$ did not overly affect the MOF crystal structure during the synthesis. Yields in both syntheses are also comparable (0.70 g in normal and 0.73 g in $scCO_2$). SEM analysis of these samples revealed that the typical morphology of normal MOF-74(Zn) is octahedral with smooth crystal faces, while MOF-74(Zn) in $scCO_2$ shows a similar morphology but with very rough faces (Figure 49), which might be due to an acidic etching effect of the CO_2 at 75 bar and 40 ^oC for 72 h. Etching processes of MOFs in different solvents such as cyanuric chloride, tetraethylamine (TEA), hydroquinone, H_3BO_3, NaCl, and tetramethylethylene diamine (TMEDA) have been investigated recently, which resulted in remarkable effects such as interconnected geometrical macropores and etched hole features.[148,149,152]

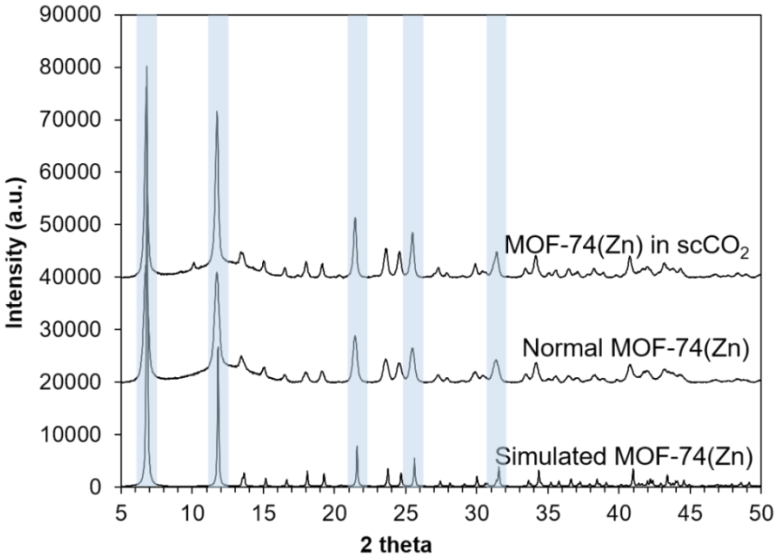

Figure 48. PXRD results of normal MOF-74(Zn) and MOF-74(Zn) in $scCO_2$

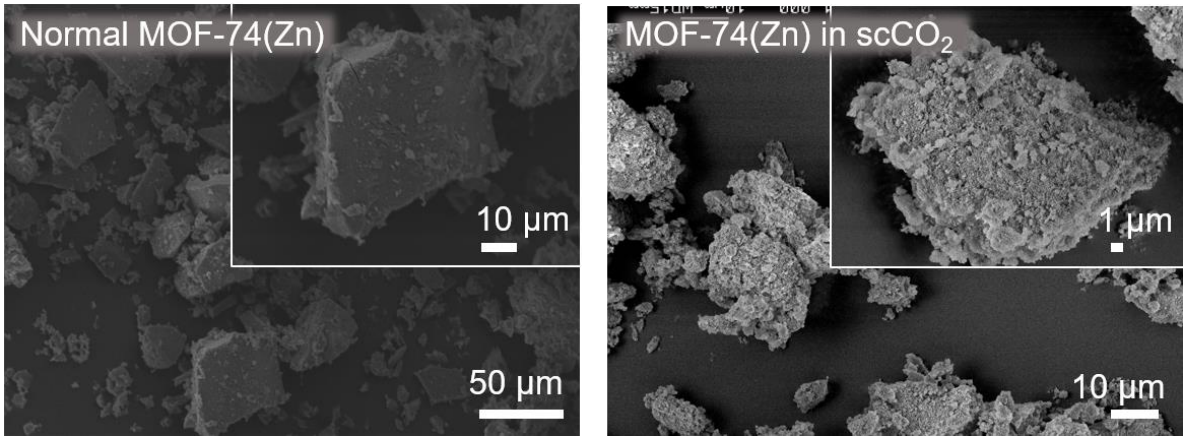

Figure 49. SEM results of normal MOF-74(Zn) and MOF-74(Zn) in $scCO_2$. The main peaks which are preserved (compared to simulated MOF-74(Zn)[7]) are marked by light blue, confirming that this MOF can be successfully synthesised at 40 °C

Gas sorption experiments were carried out on these samples to investigate the etching effect on the micro/mesoporosity. The surface area observed in the normal MOF-74(Zn) in this study (BET surface area of normal MOF-74(Zn) is 201 $m^2 g^{-1}$, see Figure 50a) was lower than those reported in the literature, and the type III isotherm indicated a lower level of microporosity.[266] This may be due to incomplete solvent removal as solvent removal was achieved through $scCO_2$ depressurisation rather than the lengthy high temperature activation used in previous studies.[266] However, it should be noted that the $scCO_2$ route also provides additional features on the surface of the sample (presumably due to an etching effect), which had the effect of increasing the BET surface area of this MOF compared to the normal MOF-74(Zn) synthesised at low temperature (BET surface area of MOF-74(Zn) in $scCO_2$ is 352 $m^2 g^{-1}$, see Figure 50a).

The pore size distributions obtained from gas sorption isotherms using the BJH method, however, do not show any significant differences between these two samples, meaning that there were no additional meso- and macropores formed in MOF-74(Zn) through exposure to $scCO_2$, indicating that addition of $scCO_2$ during this MOF synthesis did not help to enlarge the pores as was the case for HKUST-1.[168,174] This might due to the differences in chemistry of these MOFs. In HKUST-1, a precursor solution was formed by the domination of H-bonding formed by the BTC^{3-} linker and DMSO. The aggregation and self-assembly process for formation of this MOF was only triggered when CO_2-expanded MeOH was introduced.

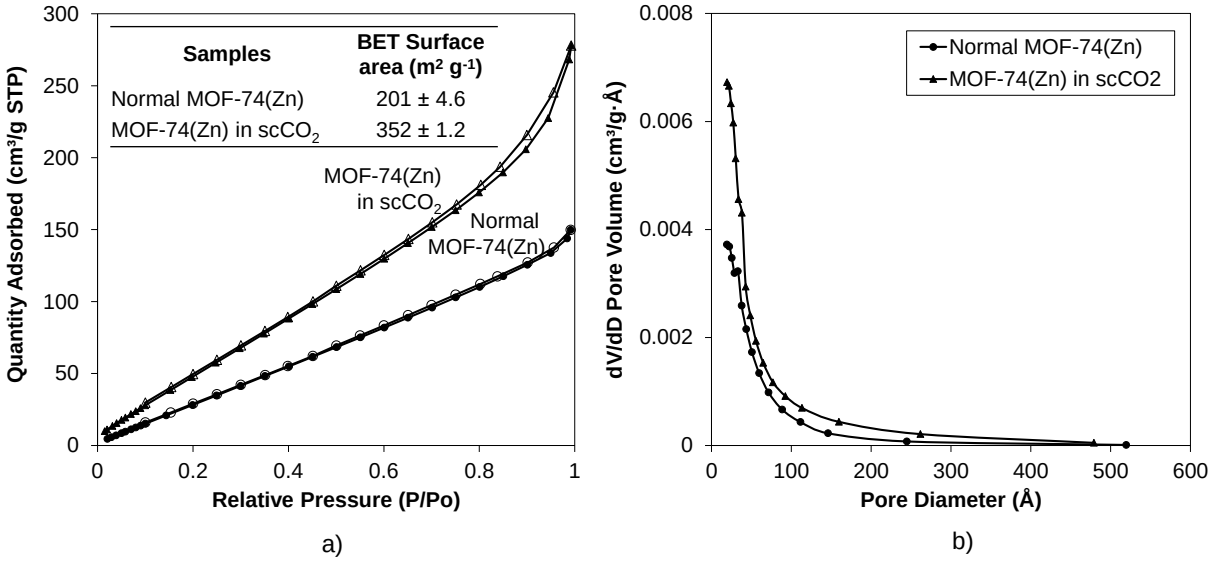

Figure 50. Gas sorption results of normal MOF-74(Zn) and MOF-74(Zn) in $scCO_2$. a) N_2 isotherm at 77 K and BET surface area shows that MOF-74(Zn) in $scCO_2$ has improved gas uptake capacity compared to normal MOF-74(Zn). Filled markers are adsorbed N_2 and unfilled markers are desorbed N_2. b) Pore size distribution by BJH method shows no additional mesopores in the MOF-74(Zn) synthesised using $scCO_2$

5.3.2. Using $scCO_2$ in precursor solution type II

In $[Cu_{24}(OH\text{-}mBDC)_{24}]_n$ synthesis

The composition of $[Cu_{24}(OH\text{-}mBDC)_{24}]_n$ is very similar to HKUST-1, containing the same $Cu_2(COO)_4$ paddlewheel as a metal node but using an OH-*m*BDC organic linker with two instead of three carboxylic acid groups as in benzene-1,3,5-tricarboxylic acid. In addition, it was shown that the metal nodes and linkers in this MOF remained unreacted in MeOH for up to 10 days, resulting in a stable precursor solution as with other MOF syntheses[19,239].

Stable precursors of this sort are promising for investigation of the effect of $scCO_2$ on this MOF because the aggregation can happen at the same time that the solvent is expanded. Indeed, in comparing the two $[Cu_{24}(OH\text{-}m BDC)_{24}]_n$ samples synthesised from the same starting materials and at the same temperature but with and without $scCO_2$ pressure (*i.e.* at 0 and 75 bar), some distortion occurred in the sample treated with $scCO_2$, as evidenced by differences in the intensities and shapes of the PXRD peaks at 7, 14 and 18 degree 2θ (see Figure 51a). In the SEM images of these two samples (Figure 51b), it can be seen that they have identical morphologies with crystal facets similar to the HKUST-1 octahedron.

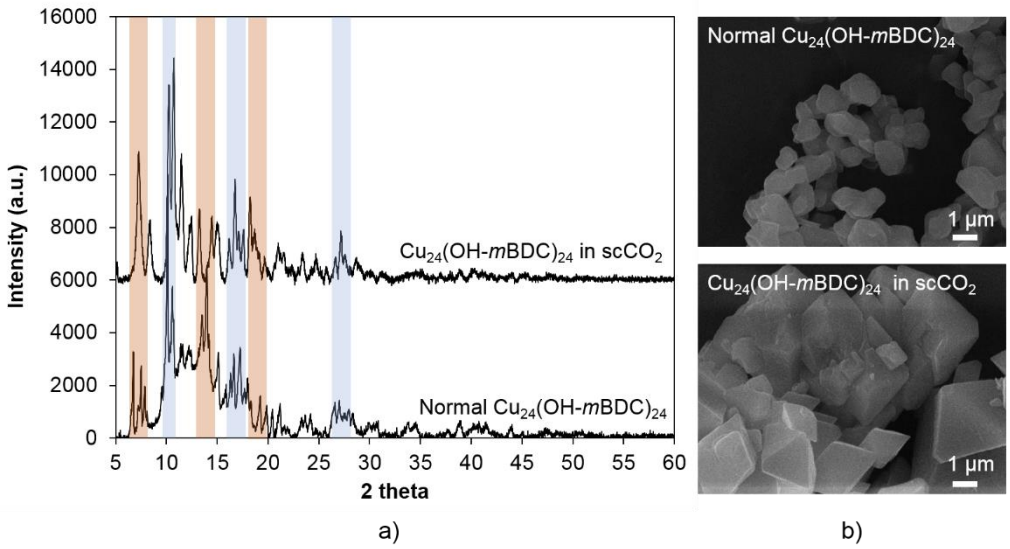

Figure 51. a) PXRD results of normal $[Cu_{24}(OH\text{-}mBDC)_{24}]_n$ and $[Cu_{24}(OH\text{-}mBDC)_{24}]_n$ in $scCO_2$. Peaks which are retained are marked by light blue, while peaks which are changed are marked by light purple. b) SEM results of normal $[Cu_{24}(OH\text{-}mBDC)_{24}]_n$ and $[Cu_{24}(OH\text{-}mBDC)_{24}]_n$ in $scCO_2$, showing that these samples have identical morphology but increased crystal size and do not appear to have additional meso- and macropores.

The crystallite size of the samples produced in $scCO_2$ is remarkably larger than the normal sample (~2 µm compared to ~1 µm), indicating the $scCO_2$ affected the growth rates of this MOF. Significantly, there was no evidence of additional meso- and macropores appearing in these samples, even though $scCO_2$ was shown to successfully introduce a large number of macropores in HKUST-1[168,174]. This might be due to the difference between MeOH (in $[Cu_{24}(OH\text{-}m BDC)_{24}]_n$ synthesis) and DMSO (used in the HKUST-1 synthesis[6]) interacting with the starting materials during the formation of precursor solutions. The CO_2-expanded MeOH used in HKUST-1 synthesis had the effect of disrupting the H-bonding between DMSO and the BTC^{3-} linker, while in the $[Cu_{24}(OH\text{-}m BDC)_{24}]_n$ synthesis, the $scCO_2$ could have

simply interrupted the reaction between Cu(II) and OH-*m*BDC when *N,N'*-dimethylacetamide was introduced. Dissolving 1.6 g $Cu(OAc)_2.H_2O$ and 1.5 g OH-*m*BDC in 100 mL DMSO resulted in precipitation after 2 hours (see Appendix D Figure S21), showing that the precursor solution in this MOF was formed by a different chemical route to that of HKUST-1.

The results of the syntheses of MOF-74(Zn), UiO-66, Zn-BTC (in DMSO) and $[Cu_{24}(OH\text{-}mBDC)_{24}]_n$ are summarised in Table 5.

Table 5. A summary of the results from both precursor solutions type I and II in the synthesis of MOFs in the presence of $scCO_2$

Precursor	MOFs	Solvents	Temperature	Formation in $scCO_2$
Type I	MOF-74(Zn)	DMF	40 °C	Product formed. Crystallinity and morphology preserved. Surface texture changed. Surface area increased.
	UiO-66	DMF	40 °C	Same as without $scCO_2$ at 40 °C but with crystal size smaller than conventional UiO-66
Type II	$[Cu_{24}(OH\text{-}mBDC)_{24}]_n$	MeOH	40 °C	Product formed. Crystallinity slightly changed. Morphology preserved. Crystal size increased.
	Zn-BTC (in DMSO)	DMSO	40 °C	Product not formed.

5.4. Conclusions

In this study, $scCO_2$ was introduced in different precursor complexes to synthesise various MOF systems. There was substantial evidence that $scCO_2$ had an effect on surface texturing and crystal growth in these MOF syntheses. MOF-74(Zn) was formed in $scCO_2$ and precursor solution type I, showing some changes in surface texture and surface area. $[Cu_{24}(OH\text{-}mBDC)_{24}]_n$ with increased crystal size was also formed in $scCO_2$ and precursor solution type II, indicating the growth rates of this MOF increased in the CO_2-expanded solvent system. However, there was no evidence showing that additional porosity appeared in these MOFs in $scCO_2$. Zn-BTC (in DMSO) and UiO-66 were formed but contained smaller crystallites in the $scCO_2$ case. While $scCO_2$ indeed showed some positive effects on synthesis of Zn-BTC and HKUST-1 in introducing additional porosity, the mechanism of these effects needs to be further studied to extend the method to other MOF systems.

CHAPTER SIX: NOVEL HIERARCHICAL COPPER-BASED METAL-ORGANIC FRAMEWORKS FOR IMPROVED CATALYTIC PERFORMANCE

To qualify the benefits of hierarchical porous structures in improving molecular accessibility and diffusion in catalytic applications, HKUST-1 MOF with the microporous structures reported in Chapter 3 (as a result of acid etching) and Chapter 4 (from the $scCO_2$ synthesis) were employed as catalysts in both liquid and gas phase reactions. Due to more accessible macropore structures, hierarchical porous HKUST-1 are kinetically superior catalysts than normal HKUST-1 in both cases. This chapter appeared as a paper submitted as a preprint in *ChemRxiv (DOI: 10.26434/chemrxiv.9699863.v1)*, with the author of this thesis as the first author. The author confirms that he carried out all synthetic experiments, PXRD, SEM, gas sorption experiments, the CO oxidation testing, data analysis and prepared the manuscript. Additional contributions were made by Samuel Pattisson (Cardiff University) who helped in carrying out the methanolysis experiment and Ken Chiang (RMIT) who helped in carrying out the CO oxidation experiment. Srinivasan Madapusi (RMIT), Stuart Taylor (Cardiff University) and Valeska P. Ting provided feedback and comments on the manuscript.

Abstract

Introducing additional meso- or macroporosity into traditionally microporous metal-organic frameworks (MOFs) is a very promising way to improve the catalytic performance of these materials, mostly due to the resultant reductions of diffusional barriers during liquid-phase or gas-phase reactions. Here we show that HKUST-1 can be successfully synthesised either via post treatment (etching prepared HKUST-1 sample in phosphoric acid, here called HKUST AE) or *in situ* crystallisation (exposure the MOF precursor solution to supercritical CO_2, here called HKUST CO_2) to produce hierarchical porous structures that are highly beneficial for catalysis. These hierarchical MOFs were characterised by powder X-ray diffraction (PXRD), scanning electron microscopy (SEM) and gas sorption to confirm the preservation of the microscopic structure and the appearance of macropores in the crystallites. More importantly, the advantages of introducing these hierarchical porous structures into this MOF for improving the diffusion accessibility of reagents to the catalytic site in the sample in liquid- and gas-phase reactions were quantified for the first time. It was found that the hierarchical pore structure helped to increase the reaction conversion of styrene oxide methanolysis (by ~65% using either HKUST AE and HKUST CO_2, at 40 ^oC in 25 min) and CO oxidation (by 55% using HKUST CO_2 at 260 ^oC). These findings demonstrate the advantages of using hierarchical porous MOFs in catalysis.

6.1. Introduction

Over the past decade, significant efforts have been made to produce hierarchical porous materials which contain multiple porosities with a well-chosen selection of micropores (diameter < 2 nm), mesopores (diameter between 2 and 50 nm) and macropores (diameter > 50 nm, according to the IUPAC classification[79]). These hierarchical pore structures offer an effective strategy for minimising diffusional barriers, thus potentially enhancing mass transport during catalytic reactions of bulky molecules. In some cases, the incorporated meso- and macropores can be usefully employed to improve accessibility of reagents into active sites dispersed in the micropores, hence improving the kinetics of such reactions. The approach of using hierarchical pore structures in catalytic applications has been well-developed in zeolites,[15,16,267,268] porous polymers,[269] porous silicas[270,271] and in metal nanoparticulate systems[272].

Potentially becoming the newest candidate in the aforementioned list, hierarchically porous metal-organic frameworks (MOFs), which are typically microporous materials comprised of organic struts and metal joints, can also be used as catalysts. The challenges associated with MOFs for scaled catalytic applications is that these materials are generally limited in their stability at high temperatures (typically decomposing at temperatures above 300 ^{o}C) or at high relative humidity. Despite their limitations, MOFs show many advantageous properties, such as exceptionally high surface areas (up to 7,000 m^2 g^{-1})[18], large internal porosity (up to 3.60 cm^3 g^{-1})[211] and functional structure flexibility over other porous materials. These advantages have prompted a large number of studies concerning the use of MOF-based materials in catalysis, such as in the upgrading of biofuels using Pd/NPC-ZIF-8,[273] Knoevenagel condensation-hydrogenation on Pd/Cz-MOF-253-800,[274] CO oxidation on CuO/CeO_2-UiO-66,[275] Fischer-Tropsch on Fe-BTC,[276] photodegradation on Fe_3O_4@HKUST-1[277] and hydrogen production using Fe-MIL-101[278]. This has led to a growing interest in the modification of MOF structures to enhance catalysis, with such approaches as formation of defective MOFs,[141,146,279–281] surface synergistically etched MOFs,[151] hollow structured MOFs[147,167,282] and core-shell structured MOFs,[283] producing some promising results. For example, Wang *et al.* used a HKUST-1@TiO_2 core-shell structure with photogenerated holes to effectively accumulate electrons on the surface of TiO_2, hence improving the photocatalytic isopropanol oxidation performance.[284] Peng *et al.* described the synthesis of a hollow Zn-BTC polyhedron via a CO_2–ionic liquid interfacial templating route[167] for enhancing the mass flow in the reaction of propylene oxide catalysed by Zn-BTC using n-Bu_4NBr as a promoter. The same author also tested the use of mesoporous HKUST-1 synthesised using supercritical CO_2 in benzyl alcohol oxidation.[168] The mesoporous MOF was shown to improve the diffusion of substrates and products, thus allowing the reaction to proceed more efficiently than when using HKUST-1 synthesised using solvothermal methods. Vermoortele *et al.* demonstrated a defective UiO-66 with a large number of open sites which was shown to enhance the catalytic performance of the parent MOF in Lewis acid catalysed reactions.[150] Recently, Liu *et al.* reported a method for synthesising HKUST-1 with controllable particle size using citric acid as a modulator and dimethylacetamide as a cosolvent.[285] By tuning synthetic conditions such as the amount of acid and reaction time, a range of large pores with diameters between 30 and 100 nm could be formed, while the intrinsic microporous HKUST-1 structure was maintained. The resultant hierarchical porous sample was loaded with phosphomolybdic acid hydrate (HPMo) as a catalytic guest species and tested for the methanolysis of styrene oxide, showing an enhanced catalytic performance (99.6% in reaction conversion using hierarchical HKUST-1 at 40 ^{o}C in

20 min compared to ~50% using normal HKUST-1). Advantages of the facile mass transport originating from its hierarchical porous nature in this reaction were also confirmed in hierarchical porous UiO-66[146] and FeBTC[286]. These results are evidence that MOFs with hierarchically porous structures are very promising when employed in catalysis.

Looking back to typical microporous MOFs, among the thousands of candidates that have been reported so far, HKUST-1, which is formed from an assembly of copper nodes and 1,3,5-benzenetricarboxylic acid (trimesic acid) linkers, is one of the most commonly reported MOFs for use in catalysis. This is because this MOF possesses Lewis acid sites (provided by coordinatively unsaturated copper[287]) and can further encapsulate Brønsted acidic guest molecules (*e.g.*, polyoxometalates, POMs)[288]. Also, in comparison to platinum-group metals, copper is classified as a cheap and relatively abundant metal but still effective for a range of catalytic reactions. Besides the methanolysis of styrene oxide, which has been mentioned previously, the catalytic performance of HKUST-1 was also demonstrated in the Knoevenagel condensation of different aldehydes and active methylene compounds, investigated by Opanasenko *et al.*[289] This study showed that HKUST-1 provided high reaction yields at a relatively low reaction temperature (80 ^{o}C) at which zeolites were not active. This MOF was also examined critically in CO oxidation, to examine the effect of activation temperature on the catalytic performance,[290,291] as well as being employed as a support for various nanoparticles, which were introduced into HKUST-1 to improve the catalytic activity of this MOF[292–294].

As reported previously, HKUST-1 MOF with additional macroporosity can be synthesised either via post treatment or *in situ* crystallisation methods.[149,174] These studies introduced to the scientific community new methods for forming a popular MOF but with an added hierarchical porous structure. However, these unusual structures have not been tested in any applications thus far. In this study, we synthesised the hierarchical porous HKUST-1 via acid etching and through use of scCO_2 at the optimal conditions mentioned in the literature (here called simply "HKUST AE" and "HKUST CO_2", respectively). These MOFs were then tested for catalysis in both liquid- and gas-phase reactions and compared to commercial HKUST-1 in an effort to quantify the advantages of the macropores in this application.

6.2. Experimental methods

6.2.1. Sample synthesis and characterisation

In this experiment, three HKUST-1 MOFs, including HKUST-1 purchased from Sigma Aldrich ("normal HKUST"), HKUST-1 etched in phosphoric acid ("HKUST AE") and HKUST-1 synthesised in supercritical CO_2 ("HKUST CO_2"), were tested for catalytic performance in liquid phase reactions (here methanolysis of styrene oxide was chosen as a model reaction) and gas phase reactions (where CO oxidation was chosen as an example reaction). HKUST AE and HKUST CO_2 were synthesised following our previous work using the optimal conditions (in H_3PO_4/MeOH/DMSO pH 2.6, 40 ^oC, 72 h for HKUST AE and in scCO_2 40 ^oC, 75 bar, 72 h for HKUST CO_2) to obtain a high proportion of macropores.[149,174] The specific synthetic procedures are described in more detail in the Appendix E1. The samples were characterised by powder X-ray diffraction (PXRD), scanning electron microscopy (SEM), energy-dispersive X-ray spectroscopy (EDX), thermogravimetric analysis (TGA) and gas sorption analysis to confirm phase purity and to allow comparison of key structural and chemical parameters. Details of these experiments are given in the Appendix E2.

6.2.2. Encapsulation of phosphomolybdic acid hydrate on HKUST-1 MOFs for the methanolysis of styrene oxide

Inspired by previous findings on the methanolysis of styrene oxide reaction,[146,285] phosphomolybdic acid hydrate (HPMo) was chosen as the catalytic guest species to be immobilised within the pores of the hierarchical porous platform. To achieve this, 30 mg of each MOF sample was soaked in 18 mL of ethanol containing 135 mg HPMo and sonicated at room temperature for 18 h. After encapsulation of the HPMo, the solid MOF was isolated by centrifugation (8,000 rpm for 5 minutes), washed with pure ethanol, re-centrifuged and re-washed three times and dried at 60 ^oC overnight. The resultant catalysts were denoted as HPMo/Normal HKUST, HPMo/HKUST AE and HPMo/HKUST CO_2, depending on the particular MOF structure used as the platform in the preparation. Elemental composition of these samples was obtained by EDX to determine %Mo loading, with details and results given in the Appendix E3.1.

6.2.3. Testing hierarchical porous HKUST-1 on the liquid phase methanolysis of styrene oxide

Prior to the testing, 2.0 mg of each HPMo/MOF sample was loaded into a round bottomed flask (5 mL) and activated in a vacuum oven at 85 °C for 2 h. Styrene oxide (25 mmol) in methanol (1.5 mL) was added to the flask and the reaction was started by immersing into an oil bath at 40 °C. The methanolysis reaction of styrene oxide is given in Scheme 5. The reaction mixture was stirred at 1200 rpm and sampled after 0, 5, 10, 15, 20 and 25 min using nitrobenzene (15 µL) as an internal standard. The reaction carried out at the same conditions without catalyst was referred to the blank sample.

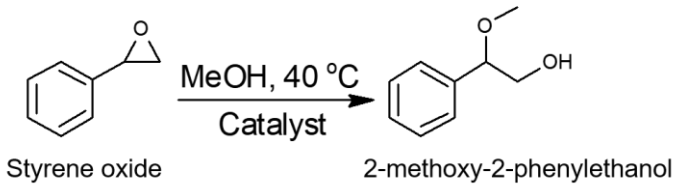

Scheme 5. Methanolysis of styrene oxide with methanol in the presence of HPMo encapsulated in HKUST-1 as an acid catalyst to produce 2-methoxy-2-phenylethanol

Quantification of reactants and products was conducted using an Agilent 7820A Gas Chromatograph (GC) equipped with a CP-wax-52 column and calibrated using bought analytical standards. The only observed product in all reactions was the target 2-methoxy-2-phenylethanol, see GC data of HKUST AE sample (1200 rpm, 25 min) in the Appendix E3.3 as an example. The reaction conversion was calculated from GC data using Equation 6.1. Crystallinities of the samples after the reaction were tested by PXRD with details and results given in Appendix E3.4.

$$Conversion_{Styrene\ oxide}(\%) = \frac{[Total\ Products]}{[Styrene\ oxide]_0} \times 100 \qquad \text{(Equation 6.1)}$$

6.2.4. Thermal activation of HKUST-1 MOFs for CO oxidation

As proven in previous studies,[290,291] catalytic activity of HKUST-1 on CO oxidation depends on the number of unsaturated coordination sites which are normally occupied by water and solvent molecules. It was also shown that by thermal activation of HKUST-1 with pure gases (Ar, H_2, O_2 or CO) the coordinated molecules can be removed, exposing metal sites for the reaction.[290] Here, normal HKUST and HKUST CO_2 were pre-degassed in the oven at 120 °C overnight to reduce the moisture content that might coordinate to the secondary building units.

Then 500 mg of the sample was loaded into a 1/4" OD tubular reactor made of stainless steel with sufficient quartz wool held at both ends to maintain a constant position and length (1 cm) of the catalyst packed bed. The reactor was inserted in a programmable electric furnace that provided heating for the catalytic reaction. Before the reaction, the sample was further degassed at 150 ^{o}C under vacuum overnight to remove pre-adsorbed impurities in the sample. This degassing step was assisted by applying vacuum downstream to the catalyst bed. The sample was then activated in a flow of 1% CO/Ar (25 mL min^{-1}) at 220 ^{o}C for 3 hours. The online GC (PerkinElmer Clarus 580 GC-TCD with 30 m plot alumina column) was used to monitor and confirm the absence of the CO_2 product after the activation. As a control, normal HKUST and HKUST CO_2 samples without encapsulation were tested in CO oxidation experiments after activation.

6.2.5. Testing hierarchical porous HKUST-1 on gas phase CO oxidation

The CO oxidation was performed in the gas phase with a packed bed of solid MOF sample in a tubular reactor. The reactor assembly and gas system are shown in Figure 52. Mass flow controllers (MFCs) were used to control the flow rate of 20% O_2/N_2 (synthetic air) and 1% CO/Ar in all experiments.

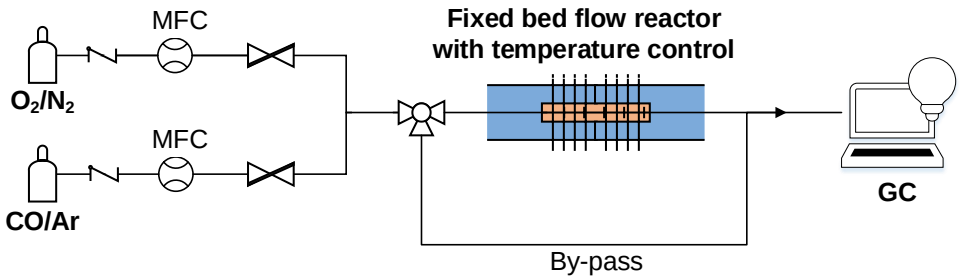

Figure 52. CO oxidation system.

Prior to the reaction, the activated catalyst was isolated while a steady flow of a 1% CO/Ar (25 mL min^{-1}) and 20% O_2/N_2 (25 mL min^{-1}) gas mixture was established in the by-pass line. Once a constant composition was achieved, the gas mixture was brought into contact with the catalyst. As it had been previously reported that there is no activity on HKUST-1 at temperatures below 220 ^{o}C in the same conditions,[292] the reaction was tested at temperatures between 220 and 280 ^{o}C. In all experiments, the gas composition was recorded using GC and the conversion was calculated using Equation 6.2, in which $[CO]_0$ and $[CO]_t$ are the concentration of CO before and after the reaction, respectively. Samples after reaction were tested for crystallinity using PXRD, see Appendix E Figure S33.

$$Conversion_{CO}(\%) = \frac{[CO]_0 - [CO]_t}{[CO]_0} \times 100 \qquad \text{(Equation 6.2)}$$

6.3. Results and Discussion

6.3.1. Characterisation of normal HKUST, HKUST AE and HKUST CO_2

Prior to the catalytic testing, the crystallinity of normal HKUST-1, HKUST-1 etched in phosphoric acid (HKUST AE) and HKUST-1 synthesised in $scCO_2$ (HKUST CO_2) were analysed by using PXRD. In Figure 53, it can be seen that the commercial HKUST-1 sample and the two modified samples were all highly crystalline and had almost identical XRD patterns, with all main peaks at 7, 10, 12, 18 and 27 degrees 2θ retained.

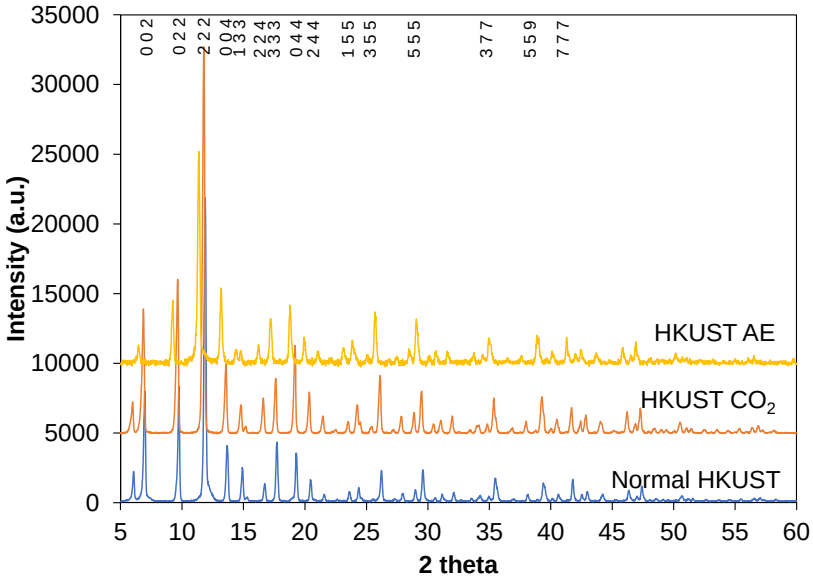

Figure 53. XRD results of normal HKUST, HKUST AE and HKUST CO_2. PXRD spectra are offset in intensity, for clarity.

From the SEM images, it can be seen that normal HKUST-1 crystallites are generally smooth-faced octahedra with a size of ~30-70 µm (Figure 54a, b, and c).[295] In the phosphoric acid etched HKUST-1 sample, there are a considerable large number of hexagonal macropores with a diameter of ~0.5 µm (Figure 54e and f). These pores can be seen in archetypal HKUST AE particles (Figure 54d), demonstrating that phosphoric acid diffused efficiently in DMSO and methanol over 72 hours without compromising the external morphology. In contrast, the regular morphology of the single HKUST-1 crystals was not maintained when synthesised via the $scCO_2$ route, as can be seen in Figure 54g. This might due to the effect of CO_2 pressure during the MOF crystallisation. At higher magnification, macropores with a diameter of ~200

nm can be observed in this sample (Figure 54h and i), which was likely to be due to the formation of HKUST-1 in CO_2-expanded DMSO/methanol solvent. This was consistent with the findings in our previous paper, in which the extent of macropores in this MOF (depending on both reaction time and pressure) was thoroughly investigated.[174] The emergence of these large pores in addition to the intrinsic micropores in HKUST AE and HKUST CO_2 can provide enormous benefits to improve the accessibility and diffusion of guest molecules within the pores, hence potentially enhancing the catalytic performance. Note that particle size of HKUST CO_2 is significantly smaller than the commercial sample (~1-3 μm particles in HKUST CO_2 compared to ~30-70 μm in normal HKUST). It can be assumed that by having smaller crystallites, the exposed external surface area of the HKUST CO_2 would be greater, therefore increasing the reaction rate.

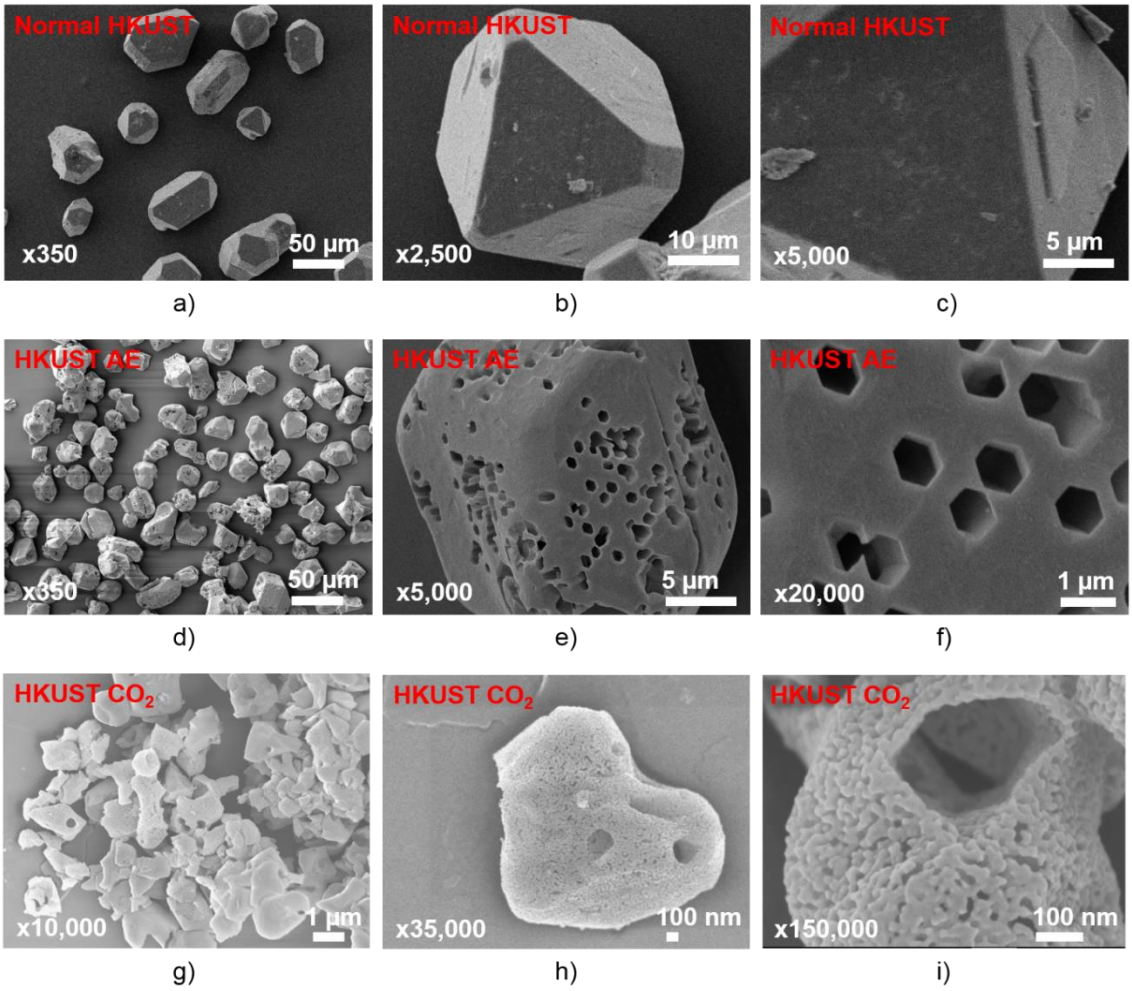

Figure 54. SEM images in different magnifications of normal HKUST (a, b and c), HKUST AE, from acid etching (d, e and f) and HKUST CO_2 synthesised in scCO_2 (g, h and i).

From the gas sorption results with N_2 at 77 K (Figure 55a), it can be seen that all samples have high surface area (~2,200 m^2 g^{-1} in normal HKUST, ~1280 m^2 g^{-1} in HKUST AE and ~1,220 m^2 g^{-1} in HKUST CO_2). These values are very promising for catalysis, compared to other commercial catalysts such as Pt/Al_2O_3 (334 m^2 g^{-1})[296], ZSM-5 (443 m^2 g^{-1})[297] or SBA-15 (~500 m^2 g^{-1})[298]. The similarity of the two-stepped N_2 sorption isotherm shown on a logarithmic scale in normal HKUST, HKUST AE and HKUST CO_2 in Figure 55b evidenced that these samples have very similar microporous structures (as confirmed by PXRD, above). It can therefore be assumed that these MOF samples are chemically identical and differ only in particle size and morphology, allowing a comparison of the effects of diffusion on catalytic activity. It is noteworthy that the measured BET surface area of HKUST AE and HKUST CO_2 was lower than the normal HKUST due to the existence of macropores (rather than purely micropores, which contribute more heavily to surface areas) in this MOF. Such a decrease in surface area was also found in other defective MOFs with meso- and macropores.[299]

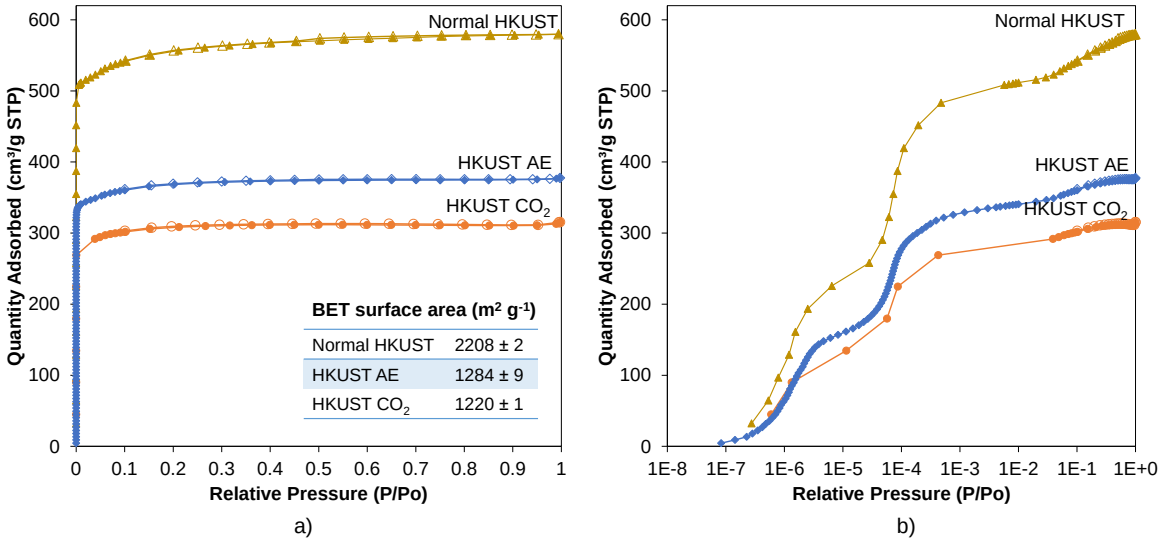

Figure 55. Nitrogen isotherm at 77 K of normal HKUST, HKUST AE and HKUST CO_2. a) Linear scale. b) Logarithmic scale. The adsorption branch of the nitrogen isotherms is represented by filled markers and desorption is represented by unfilled markers. All samples have typical type I isotherm with two-stepped sorption representing the two distinct sizes of micropores in HKUST-1

The CO_2 uptake of normal HKUST and HKUST CO_2 were also assessed at 273 K (see Appendix E Figure S31), which shows that these MOFs have nearly identical sorption ability towards CO_2. This indicates that the amounts of CO_2 formed after CO oxidation and then retained by adsorption in the two MOFs are almost identical and can therefore be regarded as a constant in this experiment.

6.3.2. Testing HKUST AE and HKUST CO_2 samples in methanolysis of styrene oxide

As suggested in previous studies, Lewis acid sites, which are present in HKUST-1,[287] can function as an active site for the ring opening of styrene oxide,[286] however, reactions on these MOFs did not prove to be particularly efficient (*e.g.* a large amount of catalyst or a long reaction time was required[146,300–302]). Indeed, as presented in Figure 56, normal HKUST demonstrated no activity up to 25 min reaction at 40 °C and 1200 rpm, which is the same as a blank sample. To increase the reaction rate, all samples were impregnated with HPMo, which was shown to be an efficient Brønsted site for these kind of reactions.[303] In this study, 18 mL of ethanol containing 135 mg HPMo was used to impregnate the samples (30 mg each) with Mo under the same conditions, resulting in very similar %Mo loadings in each HKUST-1 samples (see EDX results in Appendix E3.1).

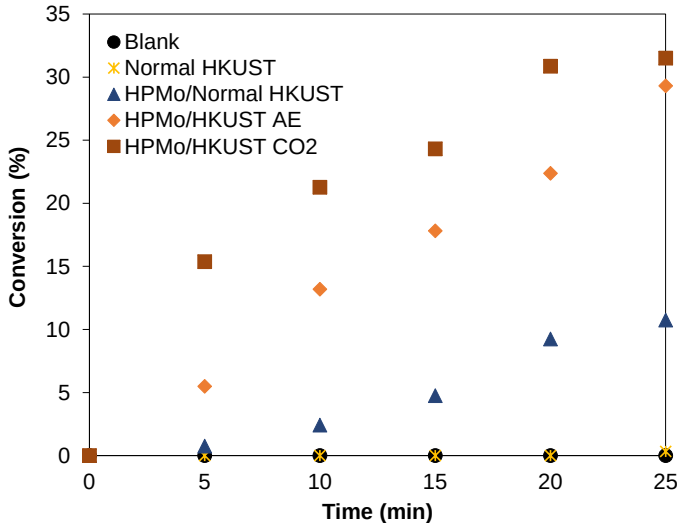

Figure 56. Catalytic activity of normal HKUST, HKUST AE and HKUST CO_2 in methanolysis of styrene oxide.

After impregnation, it can be seen that all samples showed increased activities over the 25 minutes, even though the overall surface areas of the hierarchical porous platforms were shown to be smaller than normal HKUST (see Figure 55). Comparing the encapsulated HMPo samples, it can be seen that ~30% styrene oxide reacted using the HPMo/HKUST AE and HPMo/HKUST CO_2 catalysts at 25 min, compared to ~10% in HPMo/normal HKUST. These results show that HKUST AE and HKUST CO_2 are kinetically better catalysts than normal HKUST, which might be due to more accessible macropore structures in these materials. The used samples (*i.e.* HPMo/HKUST AE and HPMo/HKUST CO_2 catalysts after the reaction) were tested by PXRD, confirming that the crystallinities were maintained, see Appendix E Figure S29.

6.3.3. Testing HKUST CO_2 sample in CO oxidation

Prior to the CO oxidation, normal HKUST and HKUST CO_2 were activated with a flow of 1% CO/Ar at 220 ^oC, which aimed to remove coordinated water molecules and to enhance the chemisorption of CO molecules on the exposed metal sites in the MOF.[291] Szanyi *et al.*[304] showed that Cu(I) centres in HKUST-1 can readily be generated after a thermal treatment of this MOF with CO (with the highest concentration of Cu(I) sites annealing at 200 ^oC. The Cu(II)/Cu(I) interchange after CO oxidation might be used to explain the mechanism of this CO oxidation reaction at this temperature. In this study, both samples started to show CO oxidation activity once the temperature reached 220 ^oC and the rate of CO oxidation increased rapidly with increased temperature. It was also observed that CO was fully converted to CO_2 at 280 ^oC with normal HKUST and at 260 ^oC with HKUST CO_2. The results from normal HKUST are in good agreement with those in the literature.[292] In comparing these two MOFs, it can be seen that HKUST CO_2 maintained higher activity than normal HKUST between 220 and 260 ^oC (see Figure 57a, where the conversion of CO increased by 55% at 260 ^oC), demonstrating that CO molecules could access the open copper sites in HKUST CO_2 more efficiently than in normal HKUST at these temperatures. Note that HKUST CO_2 sample has decreased surface area (Figure 55) and slightly lowered amounts of copper (see EDX results in Appendix E Figure S30 and Table S10) than normal HKUST, which should have compromised the activity. However, the higher conversion of the HKUST CO_2 might due to the existence of the macropores in this material which was proven previously in SEM (see Figure 54). To gain confirmation of this effect, each reaction temperature was held for one hour and the CO conversion was recorded 4 times by the online GC. As can be seen in Figure 57b, the higher activity of HKUST CO_2 can be seen for all temperatures studied. The lower activity of normal HKUST with some minor decreases in CO conversion at 220 ^oC over time might due to the purely microporous nature combined with the larger particle size of this MOF, which reduces the accessibility of CO to the active sites as well as the removal of the CO_2 product. Use of HKUST CO_2 was limited to a maximum temperature of 280 ^oC due to the degradation at this temperature. Indeed, the sample which was used for CO oxidation at 280 ^oC did not maintain the crystallinity as in normal HKUST (see Appendix E Figure S33a and b). TGA results showed that this sample started to decompose at ~280 ^oC compared to 300 ^oC for normal HKUST (see Appendix E Figure S34). In a good agreement with other reported studies,[305,306] the decreased particle size is considered to be a reason for the lowered thermal stability in this sample.

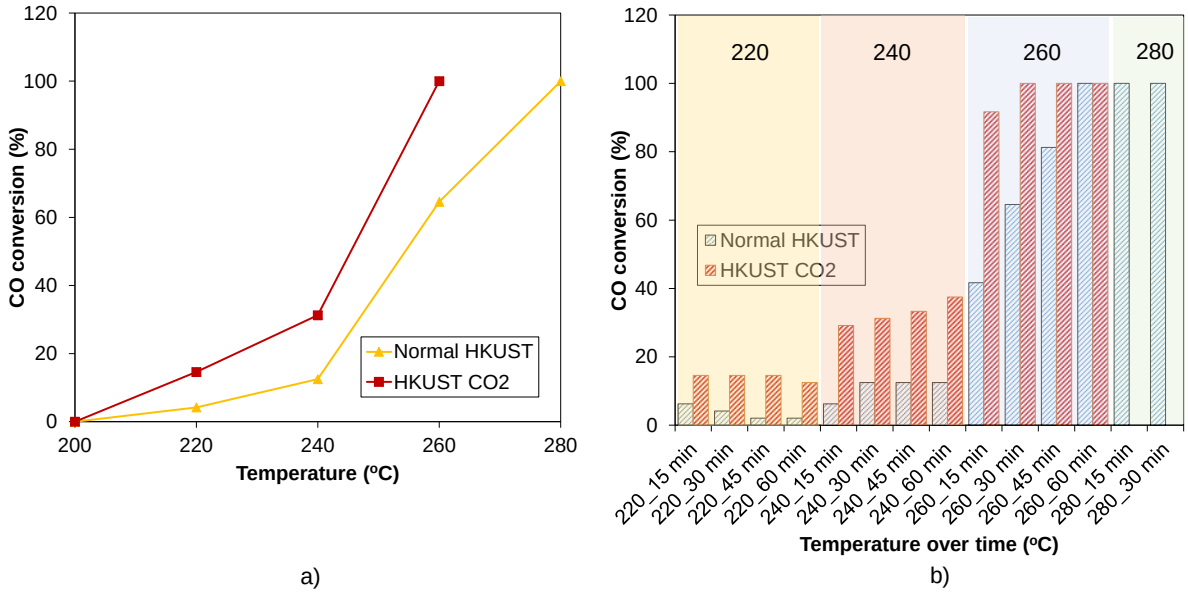

a) b)

Figure 57. Catalytic activity of normal HKUST and HKUST CO_2 in CO oxidation. a) CO conversion (%) with temperature. b) CO conversion (%) with temperature over time (4 measurements per temperature).

It can be seen that macroporous structures in HKUST-1 MOF produce a greater improvement in the catalytic performance of liquid phase reactions, when compared to gas phase reactions (~65% compared to 55%). This result evidences that macropores may be beneficial in overcoming the diffusional limitations which are more prevalent in liquid-phase reactions than in the gas phase, and have a greater effect on reactions where bulky molecules are involved.

6.4. Conclusion

In this study, two hierarchical porous HKUST-1 MOFs were tested for catalytic activity in methanolysis of styrene oxide and CO oxidation to investigate the effect of introducing macropores in both liquid and gas phases on the reaction rate. It was demonstrated that the conversion of the liquid phase reaction using the HKUST AE and the HKUST CO_2 samples increases dramatically in comparison to normal HKUST (by ~65% at 40 ºC in 25 min for methanolysis of styrene oxide). In the case of CO oxidation, the hierarchical pore structure in HKUST CO_2 indeed improved the reagent diffusion and accessibility to the copper sites, which was considered to be the main reason for the observed increase in reaction conversion (by 55% in CO oxidation). This result evidences the success of acid etching and use of $scCO_2$ methods in synthesising hierarchical porous HKUST-1, as a way of substantially improving the performance of this MOF. These synthetic methods can be applied to other MOF systems that are active in a greater variety of catalytic applications, to improve rates of reaction.

CHAPTER SEVEN: CONCLUDING REMARKS

This chapter provides a short summary of the new findings and conclusions made throughout the thesis. By reflecting on results, broad recommendations are put forward for how the work could be advanced in the future.

The principal aim of this work was to synthesise hierarchical porous MOFs with enhanced catalytic performance. Working towards this goal, two preparation methods (acid etching and use of $scCO_2$), a number of characterisation techniques (such as PXRD, SEM and gas sorption) and two catalysed reactions (methanolysis of styrene oxide as a representative for liquid phase reactions and CO oxidation as a representative for gas phase reactions) were carried out and discussed throughout this thesis. Some main conclusions drawn from this work are listed below.

Introduction of macroporosity has been demonstrated to lead to improvements in mass transfer and catalytic activity, and reductions in pressure drop over traditional powdered or nanocrystalline materials. These macropores can also improve molecular accessibility of reagents to the microporous cavities which accommodate important functional groups or active sites, enhancing the catalytic performance of the materials. The advantages of macropores in catalytic applications have been well-demonstrated for zeolites and metal oxides. For MOFs as microporous crystallites (which are purposely designed to possess high surface areas), introducing additional meso- and macropores to form hierarchical structures without compromising the micropores and the crystallinity which give them their high surface areas, is becoming the subject of much research. While mesopores can be created via numerous methods such as ligand exchange and use of surfactants, further expanding these to the macropore regime remains a challenge due to the post-synthetic activation methods needed to obtain accessible pores.

As shown in this thesis, the main techniques reported for fabrication of macroporous materials can be described using four general approaches: use of structural templating, defect formation, use of CO_2 and 3D printing. Templating stands out as the most popular route towards obtaining macroporous MOFs with numerous studies reported so far, due to the ease of structural control and the ease with which this method can be adapted for use with a range of MOFs. Deposition of MOFs onto hard macroporous templates and the formation of MOF composites via direct synthesis onto a porous template often do not require significant deviation from the synthetic conditions identified for the MOF itself and may offer an additional advantage in improving mechanical and thermochemical stability and providing immobilisation of nanocrystalline MOF materials. This may improve the outlook for MOFs to be used in industrial catalysis, for example, in alkylation and fluid catalytic cracking in oil refining processes involving bulky hydrocarbons (C15-C16), where harsh conditions require higher catalyst stability. In addition, the use of a hard template means that the active MOF material may only constitute a small

proportion of the overall composite by weight, which may be advantageous in the case of more expensive MOF materials. In post-treatment synthetic methods, pre-formed MOFs can be immobilised on macroporous templates such as foams and sponges using dip-coating methods to form the composites. The stability of the MOFs used in this method remains a major challenge due to a long exposure time to the high humidity conditions during the immobilisation process, though this may be addressed through careful choice of solvents. In addition, in these macroporous composite structures, the MOF materials must be suitably bonded to the surface (*e.g.* via functionalisation of the template surface) to avoid being washed off over time.

If, rather than rigid composites, flexible composites or pure macroporous MOF structures are required, soft macroporous templates such as polymers, emulsions or gels can be used. Polymer templates can allow for more pliable macroporous structures, while the use of emulsions or gels may allow for easier removal after templating. Use of sacrificial soft templates can result in macroporous stand-alone aerogel monoliths which can lead to easier and safer materials handling for particular applications, however, careful template removal is required to avoid incomplete removal (which could lead to loss of porosity) or collapse of pore networks.

Defect formation can be implemented via direct synthesis using linker modulation techniques or post-synthetic acid etching of prepared MOFs in low pH environments. The former has been widely reported for synthesis of mesoporous MOFs with defects as active adsorption and reaction sites for enhanced catalytic activity and gas storage, with linker modulation now being explored for introduction of larger macroporous voids. Defect formation via acid etching can overcome the limitation of the need for extended ligands and can potentially create macropores via size-selective diffusion processes. In fact, various etching agents such as hydroquinone, boric acid and phosphoric acid have been studied so far to synthesise some impressive macroporous MOF crystal structures. While this method remains challenging due to the instability of most MOFs under acidic conditions, there have been promising recent developments, such as the discovery that careful selection of solvents can allow large geometrical pores within HKUST to be achieved by acid etching, and that the use of synergistic etching to protect surfaces can be used to control etching. These examples indicate that with further investigation of the synthetic conditions and further understanding of the etching mechanisms, this simple approach to the formation of such macropores in MOF crystallites may be more widely applied.

Utilising supercritical or compressed CO_2 in MOF preparation can address some key challenges noted in previous methods including pore collapse during solvent removal steps when using soft structural templating. In fact, this method is well-known in MOF synthesis and post-synthetic treatment and has showed some promising results in creating open macroporous aerogel structures. Further adapting the synthetic conditions (*e.g.* longer reaction times and higher pressures), the use of supercritical CO_2 routes was shown to be able to form additional macropores in the direct synthesis of MOFs. In HKUST-1 synthesis, this method was also demonstrated to quickly trigger the reaction with a lowered amount of solvent, and as an added advantage, due to the insolubility of supercritical CO_2 in stock solutions, the multiple purification steps required in conventional synthetic methods could be curtailed. Particle sizes and porosity of this MOF can be tuneable via tight control over etching time. This route offers substantial benefits in HKUST-1 preparation compared to conventional solvothermal method. However, the mechanisms of the macroporous HKUST-1 formation need to be fully understood, before generalising this strategy to other MOF systems.

3D printing is a very new fabrication technique which shows promise for generalised use in MOF preparation, allowing a very high MOF loading to be incorporated into porous printed structures (~85 wt.%). The high reproducibility, fabrication of complex geometries and controlled pore structures of these MOFs have potential to open up new applications for MOF materials in biomedical fields. This method, however, relies on the ability to incorporate MOFs and MOF precursors into inks capable of being printed into stable structures without compromising on the nanoscale structure of the MOF. Enabling higher resolution (sub-mm) printing is also an area for future development, to enable greater control over the macrostructure, for example in biomedical applications such as tailored drug delivery or where the size-selective diffusion of proteins to oxidation sites within MOFs facilitates biocatalysis.

As shown by many of the studies mentioned in Chapter 2, macroporous MOF structures can show enhanced performance in adsorptive and catalytic applications due to the improved mass transfer and molecular accessibility. It can be predicted that more research will be carried out to produce more useful composites of functional MOFs coordinated with macroporous substrates using reproducible and sustainable synthetic approaches. The range of fabrication approaches presented here indicates the vast variety of different macroporous structures that can be achieved using functional MOF materials. The ability to include structural macroporosity should help to accelerate the practical application of MOFs in such varied fields

as large molecule adsorption and separation, water purification, bulky drug delivery and heterogeneous catalysis.

In Chapter 3, an acid etching strategy that was shown to effectively create a defect formation in some water stable MOFs (such as MIL-100(Fe) or UiO-66) was explored for MOFs that are typically not stable in water (here HKUST-1 was used as an example). This method was shown to effectively create macroporous defect formation without compromising on the bulk crystallinity in this MOF. By using phosphoric acid as an etching agent and a mixture of DMSO and MeOH as a dilute solvent, etched and defective HKUST-1 with extra interconnected hexagonal macropores with diameter ~0.5 μm could be produced. The extent of this etching effect depended on both pH and etching time. It was shown that the greater the concentration of phosphoric acid (up to pH 2.6 in this study) the more macropores in HKUST-1 were observed. As the etching is due to the presence of H_3PO_4, it can be predicted that increasing the solution volume with the same pH (*i.e.* same concentration of H_3PO_4, but increasing the number of moles of H_3PO_4 available) could be expected to lead to a greater extent of etching (similar to the effect of leaving a sample in the SSH solution for longer). HKUST-1 immersed at pH 2.6 over 10 days showed the greatest amount of etching, showing an increased number of macropores and a preserved microporous structure. These findings suggest the optimal conditions (etching time and acidity) to obtain macropores in MOF materials using etching process.

Size-selective acid diffusion was considered as the primary mechanism to form the additional macropores in HKUST-1 MOF, which was in agreement with previous work using a similar approach for MIL-100(Fe) MOF. Within this presumption, phosphoric acid with an appropriate diameter (d ~0.61 nm) was predicted to be able to diffuse through the large micropores of HKUST-1 (d ~0.83 nm) but not smaller secondary pores (d ~0.51 nm), resulting in interconnected macropores appearing over longer etching times and higher acid concentrations while the overall crystallinity, morphology and microporosity of this MOF was still preserved. In terms of future wok, it can be predicted that this approach can be extended to other hydrolytically unstable MOFs with micropores less than 0.61 nm in diameter (to maintain the bulk crystallinity) conjunction of other micropores larger than 0.61 nm (to support the etching mechanism). Testing the elemental composition of solution after the etching process (*eg. via*

^{31}P and ^{1}H NMR to confirm if BTC^{3-} linkers or Cu^{2+} dissolved in the acid solution) might provide insight into the etching mechanism. In addition, varying etching agents can also be investigated to understand the effect of acid molecules (size and acidity) on macropore formation (size, shape and connectivity).

In the second preparation method studied in this thesis, $scCO_2$ was introduced to HKUST-1 precursor solution containing Cu^{2+}, BTC^{3-} and DMSO. As proven in Chapter 4, the HKUST-1 synthesis in $scCO_2$ showed a very positive effect on greatly reducing the amount of MeOH solvent needed for MOF crystallisation while a similar yield to the conventional method was produced. This MOF was also formed rapidly in the presence of $scCO_2$ (after 4 minutes), which is significantly faster than the crystallisation time (24 h) reported in the normal synthesis using DMSO or DMF. This finding suggests a new scalable MOF synthetic approach in which a significant amount of solvent used for the crystallisation and the desolvation can be replaced with $scCO_2$.

In this method, the morphology of the formed HKUST-1 was further controlled by adjustment of CO_2 pressure and time. It was shown that the CO_2 expansion technique allowed tight control (by changing pressure) over crystallite size of the resulting MOF. More importantly, etching this MOF in $scCO_2$ for over 24 h showed additional macroporosity which had not previously been seen in previous reports using compressed CO_2. There are some suggestions to improve this work in the future. Firstly, the mechanism of the formation of the macropores in HKUST-1 over CO_2 pressure and time needs to be studied in more depth. The assembly of HKUST-1 framework building blocks using expanded volumes in a CO_2/solvent system was considered as a possible mechanism (as already proposed by Peng *et al.*[307]). However, additional acidity which was introduced by CO_2 ageing could also lead to a high level of macroporosity in this MOF (similar in mechanism to the acid etching method studied earlier). In the view-cell experiment, it was shown that HKUST-1 crystallites without macropores were formed after a few minutes. In addition, it was demonstrated by Toews *et al.*[29] that in the presence of $scCO_2$, the pH of water and alcohols can drop to ~2.8 which is similar to the value that produced a great number of macropores in HKUST-1 via acid etching process. Further experiments (small-angle X-ray scattering analysis for example, which can allow rapid sampling and therefore *in situ* analysis of particle sizes in a high-pressure cell with diamond windows which are

compatible with X-ray analyses) need to be carried out to gain insight into the experimental conditions under which the MOF is formed and under which this additional porosity is introduced. Secondly, in this thesis, the presence of hierarchical porous structures in HKUST-1 synthesised by both methods ($scCO_2$ and acid etching) were mainly confirmed by SEM due to the limitations of N_2 sorption in testing macroporous MOFs. Other methods such as mercury porosimetry or electron beam computed tomography on these materials are recommended, in order to calculate more precisely the macropore volume in these MOFs, providing the correlation between this value and an increase of activity using this MOF in catalysis. Despite incomplete understanding of this mechanism, the findings on the macropores in this MOF suggests a novel controllable approach to obtain hierarchical structures using $scCO_2$.

As a further step, in Chapter 5, the method involving $scCO_2$ was extended to other MOF systems using precursor type I and type II complexes, including MOF-74(Zn), UiO-66, Zn-BTC (in DMSO) and $[Cu_{24}(OH\text{-}m BDC)_{24}]_n$, showing some substantial evidence that $scCO_2$ had an effect on surface texturing and crystal growth in these MOFs. In the MOF-74(Zn) synthesis, introducing $scCO_2$ showed an etching effect with some features on the crystal faces and enhanced surface area while the crystallinity remained unchanged. Surface measurement with atomic force microscopy is recommended to measure the roughness of these samples. In the synthesis of $[Cu_{24}(OH\text{-}m BDC)_{24}]_n$, the sample synthesised in the presence of MeOH and $scCO_2$ had a larger crystal size and some distortion in crystallinity in comparison to the sample synthesised without $scCO_2$. Zn-BTC could not be formed using a mixture of DMSO and MeOH as a solvent instead of DMF, so introducing $scCO_2$ into this system did not lead to the formation of Zn-BTC as in HKUST-1. In the formation of MOF-74(Zn) and $[Cu_{24}(OH\text{-}m BDC)_{24}]_n$ using $scCO_2$, there was no evidence showing that additional porosity appeared in these MOFs in the presence of $scCO_2$. The difference in effect of $scCO_2$ on these MOFs compared to HKUST-1 might be due to the different chemistry between those systems. This finding raises the need to fully understand the mechanism of the formation of macropores in HKUST-1 using $scCO_2$ before generalising this method in other MOF systems.

Finally, in Chapter 6, HKUST-1 samples synthesised via both methods ($scCO_2$ and acid etching) were tested for catalytic activity in methanolysis of styrene oxide and CO oxidation, showing that the hierarchical porous platforms obtained from the two synthesis methods

studied in this thesis have a beneficial effect on the kinetics of the catalytic reaction, making them better catalysts compared to microporous HKUST-1. This result evidences the success of acid etching and use of $scCO_2$ methods in synthesising hierarchical porous HKUST-1, as a way of substantially improving the performance of this MOF. It can be also noted that macroporous structures in HKUST-1 MOF have a slightly greater effect in improving the catalytic performance in liquid phase (where a bulkier molecule was involved) than in the gas phase reaction (~65% compared to 55%). While more catalytic testing is required to support this hypothesis, the findings in this thesis suggest that macropores are of greatest benefit when there are diffusional limitations in the reactions that have to be overcome. For the liquid phase reactions, it is recommended that the diffusion limitations and stability of the macroporous MOF catalysts is further investigated by carrying out experiments at higher stirring speed, for more cycles or with bulkier reagents. For the gas phase reactions (*e.g.* using HKUST-1 for CO oxidation reaction in this thesis), an X-ray Photoelectron Spectroscopy (XPS) measurement needs to be carried out to confirm the oxidation state of catalytic sites, which is important to study the mechanism of these reactions. Chemical reactions involving a catalyst occur on the surface of the catalyst, thus the surface area of a catalyst likely does affect the rate of reaction. In general, by increasing the surface area of the catalyst, by using finer powdered particulates, there is a greater probability of collisions of the reactants on the catalyst and thus the reaction will proceed at a faster rate. It is recommended to perform reactions using a MOF sample with similar nature (same number of catalytic sites and porosity) but different particle size to investigate this factor on catalytic activity.

References

1 H. Li, M. Eddaoudi, M. O'Keeffe and O. M. Yaghi, *Nature*, 1999, **402**, 276–279.

2 Y. Kinoshita, I. Matsubara, T. Higuchi and Y. Saito, *Bull. Chem. Soc. Jpn.*, 1959, **32**, 1221–1226.

3 P. Z. Moghadam, A. Li, S. B. Wiggin, A. Tao, A. G. P. Maloney, P. A. Wood, S. C. Ward and D. Fairen-Jimenez, *Chem. Mater.*, 2017, **29**, 2618–2625.

4 Cambridge Structural Database (CSD), https://www.ccdc.cam.ac.uk/structures/?, (accessed 16 August 2019).

5 S. S. Y. Chui, S. M. F. Lo, J. P. H. Charmant, A. G. Orpen and I. D. Williams, *Science (80-.).*, 1999, **283**, 1148–1150.

6 J. H. Cavka, S. Jakobsen, U. Olsbye, N. Guillou, C. Lamberti, S. Bordiga and K. P. Lillerud, *J. Am. Chem. Soc.*, 2008, **130**, 13850–13851.

7 N. L. Rosi, J. Kim, M. Eddaoudi, B. Chen, M. O'Keeffe and O. M. Yaghi, *J. Am. Chem. Soc.*, 2005, **127**, 1504–1518.

8 K. S. Park, Z. Ni, A. P. Cote, J. Y. Choi, R. Huang, F. J. Uribe-Romo, H. K. Chae, M. O'Keeffe and O. M. Yaghi, *Proc. Natl. Acad. Sci.*, 2006, **103**, 10186–10191.

9 H. Furukawa, K. E. Cordova, M. O'Keeffe and O. M. Yaghi, *Science (80-.).*, 2013, **341**, 1230444.

10 D. A. Gómez-Gualdrón, Y. J. Colón, X. Zhang, T. C. Wang, Y. S. Chen, J. T. Hupp, T. Yildirim, O. K. Farha, J. Zhang and R. Q. Snurr, *Energy Environ. Sci.*, 2016, **9**, 3279–3289.

11 J. A. Mason, J. Oktawiec, M. K. Taylor, M. R. Hudson, J. Rodriguez, J. E. Bachman, M. I. Gonzalez, A. Cervellino, A. Guagliardi, C. M. Brown, P. L. Llewellyn, N. Masciocchi and J. R. Long, *Nature*, 2015, **527**, 357–361.

12 L. Zou and H. C. Zhou, *Nanostructured Mater. Next-Generation Energy Storage Convers. Hydrog. Prod. Storage, Util.*, 2017, **112**, 143–170.

13 J. Liu, L. Chen, H. Cui, J. Zhang, L. Zhang and C. Y. Su, *Chem. Soc. Rev.*, 2014, **43**, 6011–6061.

14 C. De Wu, *Sel. Nanocatalysts Nanosci. Concepts Heterog. Homog. Catal.*, 2011, **110**,

271–298.

15 J. Liu, G. Jiang, Y. Liu, J. Di, Y. Wang, Z. Zhao, Q. Sun, C. Xu, J. Gao, A. Duan, J. Liu, Y. Wei, Y. Zhao and L. Jiang, *Sci. Rep.*, 2014, **4**, 7276.

16 X. Dong, S. Shaikh, J. R. Vittenet, J. Wang, Z. Liu, K. D. Bhatte, O. Ali, W. Xu, I. Osorio, Y. Saih, J. M. Basset, S. A. Ali and Y. Han, *ACS Sustain. Chem. Eng.*, 2018, **6**, 15832–15840.

17 H. Deng, S. Grunder, K. E. Cordova, C. Valente, H. Furukawa, M. Hmadeh, F. Gándara, A. C. Whalley, Z. Liu, S. Asahina, H. Kazumori, M. O'Keeffe, O. Terasaki, J. F. Stoddart and O. M. Yaghi, *Science (80-.).*, 2012, **336**, 1018–1023.

18 O. K. Farha, I. Eryazici, N. C. Jeong, B. G. Hauser, C. E. Wilmer, A. A. Sarjeant, R. Q. Snurr, S. T. Nguyen, A. Ö. Yazaydin and J. T. Hupp, *J. Am. Chem. Soc.*, 2012, **134**, 15016–15021.

19 R. Ameloot, E. Cobechiya, H. Uji-i, J. A. Martens, J. Hofkens, L. Alaerts, B. F. Sels and D. E. De Vos, *Adv. Mater.*, 2010, **22**, 2685–2688.

20 P. G. Jessop and B. Subramaniam, *Chem. Rev.*, 2007, **107**, 2666–2694.

21 A. I. Cooper, *Adv. Mater.*, 2003, **15**, 1049–1059.

22 F. G. Denardin, S. A. B. Vieira De Melo, R. Mammucari and N. R. Foster, *Chem. Eng. Trans.*, 2013, **32**, 529–534.

23 A. Kordikowski, A. P. Schenk, R. M. Van Nielen and C. J. Peters, *J. Supercrit. Fluids*, 1995, **8**, 205–216.

24 V. T. Wyatt, D. Bush, J. Lu, J. P. Hallett, C. L. Liotta and C. A. Eckert, *J. Supercrit. Fluids*, 2005, **36**, 16–22.

25 S. G. Kazarian, N. Sakellarios and C. M. Gordon, *Chem. Commun.*, 2002, **2**, 1314–1315.

26 Y. T. Shieh and H. S. Yang, *J. Supercrit. Fluids*, 2005, **33**, 183–192.

27 P. R. Sassiat, P. Mourier, M. H. Caude and R. H. Rosset, *Measurement of Diffusion Coefficients in Supercritical Carbon Dioxide and Correlation with the Equation of Wilke and Chang*, 1987, vol. 59.

28 T. Umecky, M. Kanakubo, T. Makino, T. Aizawa and A. Suzuki, *Fluid Phase Equilib.*,

2013, **357**, 76–79.

29 K. L. Toews, R. M. Shroll, C. M. Wai and N. G. Smart, *Anal. Chem.*, 1995, **67**, 4040–4043.

30 S. E. Hunter and P. E. Savage, *Ind. Eng. Chem. Res.*, 2003, **42**, 290–294.

31 K. N. West, C. Wheeler, J. P. McCarney, K. N. Griffith, D. Bush, C. L. Liotta and C. A. Eckert, *J. Phys. Chem. A*, 2007, **105**, 3947–3948.

32 S. P. Nalawade, F. Picchioni and L. P. B. M. Janssen, *Prog. Polym. Sci.*, 2006, **31**, 19–43.

33 Z. Liu, W. Wu, B. Han, Z. Dong, G. Zhao, J. Wang, T. Jiang and G. Yang, *Chem. - A Eur. J.*, 2003, **9**, 3897–3903.

34 K. Liu, F. Schuch and E. Kiran, *J. Supercrit. Fluids*, 2006, **39**, 89–101.

35 A. F. Lagalante, R. L. Hall and T. J. Bruno, *Kamlet−Taft Solvatochromic Parameters of the Sub- and Supercritical Fluorinated Ethane Solvents*, 2002, vol. 102.

36 E. Kiran, *J. Supercrit. Fluids*, 2016, **110**, 126–153.

37 A. M. López-Periago and C. Domingo, *J. Supercrit. Fluids*, 2018, **134**, 204–213.

38 M. Sihvonen, E. Järvenpää, V. Hietaniemi and R. Huopalahti, *Trends Food Sci. Technol.*, 1999, **10**, 217–222.

39 V. J. Krukonis, P. M. Gallapher and M. P. Coffey, *US Pat. 5,360,478*.

40 G. Luna-Bárcenas, S. K. Kanakia, I. C. Sanchez and K. P. Johnston, *Polymer (Guildf).*, 1995, **36**, 3173–3182.

41 N. Ventosa, S. Sala and J. Veciana, *J. Supercrit. Fluids*, 2003, **26**, 33–45.

42 N. Ventosa, S. Sala, J. Veciana, J. Torres and J. Llibre, *Cryst. Growth Des.*, 2001, **1**, 299–303.

43 M. C. McLeod, M. Anand, C. L. Kitchens and C. B. Roberts, *Nano Lett.*, 2005, **5**, 461–465.

44 M. C. McLeod, C. L. Kitchens and C. B. Roberts, *Langmuir*, 2005, **21**, 2414–2418.

45 H. Xu and D. M. Rudkevich, *Chem. - A Eur. J.*, 2004, **10**, 5432–5442.

46 Q. Zhang, N. S. Oztekin, J. Barrault, K. De Oliveira Vigier and F. Jérôme,

ChemSusChem, 2013, **6**, 593–596.

47 J. E. Mondloch, O. Karagiaridi, O. K. Farha and J. T. Hupp, *CrystEngComm*, 2013, **15**, 9258.

48 U. Hintermair, C. Roosen, M. Kaever, H. Kronenberg, R. Thelen, S. Aey, W. Leitner and L. Greiner, *Org. Process Res. Dev.*, 2011, **15**, 1275–1280.

49 S. Sun, H. Li and Z. J. Xu, *Joule*, 2018, **2**, 1024–1027.

50 N. Laosiripojana and S. Assabumrungrat, *Chem. Eng. Sci.*, 2006, **61**, 2540–2549.

51 C. Gregor, M. Hermanek, D. Jancik, J. Pechousek, J. Filip, J. Hrbac and R. Zboril, *Eur. J. Inorg. Chem.*, 2010, **2010**, 2343–2351.

52 O. P. Mills and W. I. Rose, *Geosphere*, 2010, **6**, 805–811.

53 K. Omote, Y. Ito and S. Kawamura, *Appl. Phys. Lett.*, 2003, **82**, 544–546.

54 T. Düren, Y. S. Bae and R. Q. Snurr, *Chem. Soc. Rev.*, 2009, **38**, 1237–1247.

55 T. Duren, F. Millange, G. Ferey, K. S. Walton and R. Snurr, *J. Phys. Chem. C*, 2007, **111**, 15350–15356.

56 K. S. Walton and R. Q. Snurr, *J. Am. Chem. Soc.*, 2007, **129**, 8552–8556.

57 H. Swenson and N. P. Stadie, *Langmuir*, 2019, **35**, 5409–5426.

58 G. Fagerlund, *Matériaux Constr.*, 1973, **6**, 239–245.

59 J. Rouquerol, P. Llewellyn and F. Rouquerol, 2007, **160**, 49–56.

60 M. Thommes, K. Kaneko, A. V. Neimark, J. P. Olivier, F. Rodriguez-Reinoso, J. Rouquerol and K. S. W. Sing, *Pure Appl. Chem.*, , DOI:10.1515/pac-2014-1117.

61 K. S. Walton, R. Q. Snurr, K. S. W. and and R. Q. Snurr*, *J. Am. Chem. Soc.*, 2007, **129**, 8552–8556.

62 P. Nugent, E. G. Giannopoulou, S. D. Burd, O. Elemento, E. G. Giannopoulou, K. Forrest, T. Pham, S. Ma, B. Space, L. Wojtas, M. Eddaoudi and M. J. Zaworotko, *Nature*, 2013, **495**, 80–84.

63 D. E. Jiang, V. R. Cooper and S. Dai, *Nano Lett.*, 2009, **9**, 4019–4024.

64 K. M. Steel and W. J. Koros, *Carbon N. Y.*, 2003, **41**, 253–266.

65 Q. Min Wang, D. Shen, M. Bülow, M. Ling Lau, S. Deng, F. R. Fitch, N. O. Lemcoff

and J. Semanscin, *Microporous Mesoporous Mater.*, 2002, **55**, 217–230.

66 S. Rashidi, J. A. Esfahani and N. Karimi, *Renew. Sustain. Energy Rev.*, 2018, **91**, 229–247.

67 C. Vix-Guterl, E. Frackowiak, K. Jurewicz, M. Friebe, J. Parmentier and F. Béguin, *Carbon N. Y.*, 2005, **43**, 1293–1302.

68 Y. Li, Z. Y. Fu and B. L. Su, *Adv. Funct. Mater.*, 2012, **22**, 4634–4667.

69 S. Han, D. Wu, S. Li, F. Zhang and X. Feng, *Adv. Mater.*, 2014, **26**, 849–864.

70 S. Wang, *Microporous Mesoporous Mater.*, 2009, **117**, 1–9.

71 P. Horcajada, C. Serre, M. Vallet-Regí, M. Sebban, F. Taulelle and G. Férey, *Angew. Chemie - Int. Ed.*, 2006, **45**, 5974–5978.

72 P. Horcajada, T. Chalati, C. Serre, B. Gillet, C. Sebrie, T. Baati, J. F. Eubank, D. Heurtaux, P. Clayette, C. Kreuz, J. S. Chang, Y. K. Hwang, V. Marsaud, P. N. Bories, L. Cynober, S. Gil, G. Férey, P. Couvreur and R. Gref, *Nat. Mater.*, 2010, **9**, 172–178.

73 P. Horcajada, C. Serre, G. Maurin, N. A. Ramsahye, F. Balas, M. Vallet-Regí, M. Sebban, F. Taulelle and G. Férey, *J. Am. Chem. Soc.*, 2008, **130**, 6774–6780.

74 C. Perego and R. Millini, *Chem. Soc. Rev.*, 2013, **42**, 3956–3976.

75 J. Lee, O. K. Farha, J. Roberts, K. A. Scheidt, S. T. Nguyen and J. T. Hupp, *Chem. Soc. Rev.*, 2009, **38**, 1450–1459.

76 C. M. A. Parlett, K. Wilson and A. F. Lee, *Chem. Soc. Rev.*, 2013, **42**, 3876–3893.

77 A. Taguchi and F. Schüth, *Microporous Mesoporous Mater.*, 2005, **77**, 1–45.

78 J. Rouquerol, D. Avnir, C. W. Fairbridge, D. H. Everett, J. M. Haynes, N. Pernicone, J. D. F. Ramsay, K. S. W. Sing and K. K. Unger, *Recommendations for the characterization of porous solids (Technical Report)*, 1994, vol. 66.

79 K. S. W. Sing, *Pure Appl. Chem.*, 2007, **57**, 603–619.

80 W. Schwieger, A. G. Machoke, T. Weissenberger, A. Inayat, T. Selvam, M. Klumpp and A. Inayat, *Chem. Soc. Rev.*, 2016, **45**, 3353–3376.

81 U. Betke and A. Lieb, *Adv. Eng. Mater.*, 2018, **20**, 1800252.

82 X. Y. Yang, L. H. Chen, Y. Li, J. C. Rooke, C. Sanchez and B. L. Su, *Chem. Soc. Rev.*, 2017, **46**, 481–558.

83 J. M. Holcroft, K. J. Hartlieb, P. Z. Moghadam, J. G. Bell, G. Barin, D. P. Ferris, E. D. Bloch, M. M. Algaradah, M. S. Nassar, Y. Y. Botros, K. M. Thomas, J. R. Long, R. Q. Snurr and J. F. Stoddart, *J. Am. Chem. Soc.*, 2015, **137**, 5706–5719.

84 J. R. Li, R. J. Kuppler and H. C. Zhou, *Chem. Soc. Rev.*, 2009, **38**, 1477–1504.

85 J. B. DeCoste and G. W. Peterson, *Chem. Rev.*, 2014, **114**, 5695–5727.

86 X. Zhao, Y. Wang, D. S. Li, X. Bu and P. Feng, *Adv. Mater.*, 2018, **30**, 869–932.

87 K. Sumida, D. L. Rogow, J. A. Mason, T. M. McDonald, E. D. Bloch, Z. R. Herm, T.-H. Bae and J. R. Long, *Chem. Rev.*, 2012, **112**, 724–781.

88 T. M. McDonald, J. A. Mason, X. Kong, E. D. Bloch, D. Gygi, A. Dani, V. Crocellà, F. Giordanino, S. O. Odoh, W. S. Drisdell, B. Vlaisavljevich, A. L. Dzubak, R. Poloni, S. K. Schnell, N. Planas, K. Lee, T. Pascal, L. F. Wan, D. Prendergast, J. B. Neaton, B. Smit, J. B. Kortright, L. Gagliardi, S. Bordiga, J. A. Reimer and J. R. Long, *Nature*, 2015, **519**, 303–308.

89 A. Ö. Yazaydin, R. Q. Snurr, T. H. Park, K. Koh, J. Liu, M. D. LeVan, A. I. Benin, P. Jakubczak, M. Lanuza, D. B. Galloway, J. J. Low and R. R. Willis, *J. Am. Chem. Soc.*, 2009, **131**, 18198–18199.

90 G. Férey, *Chem. Soc. Rev.*, 2008, **37**, 191–214.

91 D. Sheberla, L. Sun, M. A. Blood-Forsythe, S. Er, C. R. Wade, C. K. Brozek, A. Aspuru-Guzik and M. Dincă, *J. Am. Chem. Soc.*, 2014, **136**, 8859–8862.

92 H. Y. Guan, R. J. LeBlanc, S. Y. Xie and Y. Yue, *Coord. Chem. Rev.*, 2018, **369**, 76–90.

93 D. Liu, D. Zou, H. Zhu and J. Zhang, *Small*, 2018, **14**, 1801454.

94 K. Wang, Y. Zhang, J. Zhao, C. Yan, Y. Wei, M. Meng, X. Dai, C. Li and Y. Yan, *New J. Chem.*, 2018, **42**, 18084–18095.

95 Q. XIANG and J. YU, *Chinese J. Catal.*, 2011, **32**, 525–531.

96 G. Xi, B. Yue, J. Cao and J. Ye, *Chem. - A Eur. J.*, 2011, **17**, 5145–5154.

97 L. Feng, S. Yuan, J. L. Li, K. Y. Wang, G. S. Day, P. Zhang, Y. Wang and H. C. Zhou, *ACS Cent. Sci.*, 2018, **4**, 1719–1726.

98 S. Brunauer, P. H. Emmett and E. Teller, *J. Am. Chem. Soc.*, 1938, **60**, 309–319.

99 P. Klobes, M. Klaus and R. G. Munro, *NIST - Natl. Inst. Stand. Technol.*, 2006, **Special Pu**, 1–89.

100 E. P. Barrett, L. G. Joyner and P. P. Halenda, *J. Am. Chem. Soc.*, 1951, **73**, 373–380.

101 L. G. Joyner, E. P. Barrett and R. Skold, *J. Am. Chem. Soc.*, 1951, **73**, 3155–3158.

102 L. A. Feigin and D. I. Svergun, *Structure Analysis by Small-Angle X-Ray and Neutron Scattering*, Springer US, Boston, MA, 1987.

103 J. Rouquerol, G. V. Baron, R. Denoyel, H. Giesche, J. Groen, P. Klobes, P. Levitz, A. V. Neimark, S. Rigby, R. Skudas, K. Sing, M. Thommes and K. Unger, *Microporous Mesoporous Mater.*, 2012, **154**, 2–6.

104 A. . Radlinski, M. Mastalerz, A. . Hinde, M. Hainbuchner, H. Rauch, M. Baron, J. . Lin, L. Fan and P. Thiyagarajan, *Int. J. Coal Geol.*, 2004, **59**, 245–271.

105 V. P. Ting, A. J. Ramirez-Cuesta, N. Bimbo, J. E. Sharpe, A. Noguera-Diaz, V. Presser, S. Rudic and T. J. Mays, *ACS Nano*, 2015, **9**, 8249–8254.

106 Y. Wang, F. De Carlo, D. C. Mancini, I. McNulty, B. Tieman, J. Bresnahan, I. Foster, J. Insley, P. Lane, G. Von Laszewski, C. Kesselman, M. H. Su and M. Thiebaux, *Rev. Sci. Instrum.*, 2001, **72**, 2062–2068.

107 A. Taguchi, J. H. Smätt and M. Lindén, *Adv. Mater.*, 2003, **15**, 1209–1211.

108 C. Xue, B. Tu and D. Zhao, *Nano Res.*, 2009, **2**, 242–253.

109 J. H. Smått, S. Schunk and M. Lindén, *Chem. Mater.*, 2003, **15**, 2354–2361.

110 C. M. Yang, J. H. Smått, B. Zibrowius and M. Lindén, *New J. Chem.*, 2004, **28**, 1520–1525.

111 A. M. Nardes, R. A. J. Janssen and M. Kemerink, *Adv. Funct. Mater.*, 2008, **18**, 865–871.

112 F. Sandra, M. Depardieu, Z. Mouline, G. L. Vignoles, Y. Iwamoto, P. Miele, R. Backov and S. Bernard, *Chem. - A Eur. J.*, 2016, **22**, 8346–8357.

113 J. Ren, T. Segakweng, H. W. Langmi, B. C. North and M. Mathe, *J. Alloys Compd.*, 2015, **645**, S170–S173.

114 T. Granato, F. Testa and R. Olivo, *Microporous Mesoporous Mater.*, 2012, **153**, 236–246.

115 Y. Xie, Y. Song, Y. Zhang, L. Xu, L. Miao, C. Peng and L. Wang, *J. Alloys Compd.*, 2018, **757**, 105–111.

116 U. Betke, S. Proemmel, J. G. Eggebrecht, S. Rannabauer, A. Lieb, M. Scheffler and F. Scheffler, *Chemie-Ingenieur-Technik*, 2016, **88**, 264–273.

117 U. Betke, S. Proemmel, S. Rannabauer, A. Lieb, M. Scheffler and F. Scheffler, *Microporous Mesoporous Mater.*, 2017, **239**, 209–220.

118 U. Betke, M. Klaus, J. G. Eggebrecht, M. Scheffler and A. Lieb, *Microporous Mesoporous Mater.*, 2018, **265**, 43–56.

119 Y. Hu, H. Lian, L. Zhou and G. Li, *Anal. Chem.*, 2015, **87**, 406–412.

120 Y. Sun, F. Yang, Q. Wei, N. Wang, X. Qin, S. Zhang, B. Wang, Z. Nie, S. Ji, H. Yan and J. R. Li, *Adv. Mater.*, 2016, **28**, 2374–2381.

121 H. Wang, Z. G. Qu, W. Zhang and L. Q. Zhang, *RSC Adv.*, 2016, **6**, 52888–52897.

122 K. Shen, L. Zhang, X. Chen, L. Liu, D. Zhang, Y. Han, J. Chen, J. Long, R. Luque, Y. Li and B. Chen, *Science (80-.).*, 2018, **359**, 206–210.

123 C. Duan, H. Zhang, M. Yang, F. Li, Y. Yu, J. Xiao and H. Xi, *Nanoscale Adv.*, 2019, **1**, 1062–1069.

124 M. L. Pinto, S. Dias and J. Pires, *ACS Appl. Mater. Interfaces*, 2013, **5**, 2360–2363.

125 K. Y. Andrew Lin and H. A. Chang, *J. Mater. Chem. A*, 2015, **3**, 20060–20064.

126 S. Cao, G. Gody, W. Zhao, S. Perrier, X. Peng, C. Ducati, D. Zhao and A. K. Cheetham, *Chem. Sci.*, 2013, **4**, 3573–3577.

127 S. Bo, W. Ren, C. Lei, Y. Xie, Y. Cai, S. Wang, J. Gao, Q. Ni and J. Yao, *J. Solid State Chem.*, 2018, **262**, 135–141.

128 W. Ren, J. Gao, C. Lei, Y. Xie, Y. Cai, Q. Ni and J. Yao, *Chem. Eng. J.*, 2018, **349**, 766–774.

129 Y. Yuan, D. Yang, G. Mei, X. Hong, J. Wu, J. Zheng, J. Pang and Z. Yan, *Colloids Surfaces A Physicochem. Eng. Asp.*, 2018, **544**, 187–195.

130 J. Mao, M. Ge, J. Huang, Y. Lai, C. Lin, K. Zhang, K. Meng and Y. Tang, *J. Mater. Chem. A*, 2017, **5**, 11873–11881.

131 N. Huang, H. Drake, J. Li, J. Pang, Y. Wang, S. Yuan, Q. Wang, P. Cai, J. Qin and H.

C. Zhou, *Angew. Chemie - Int. Ed.*, 2018, **57**, 8916–8920.

132 N. Moitra, S. Fukumoto, J. Reboul, K. Sumida, Y. Zhu, K. Nakanishi, S. Furukawa, S. Kitagawa and K. Kanamori, *Chem. Commun.*, 2015, **51**, 3511–3514.

133 F. Xu, S. Xian, Q. Xia, Y. Li and Z. Li, *Adsorpt. Sci. Technol.*, 2013, **31**, 325–339.

134 F. J. Ma, S. X. Liu, D. D. Liang, G. J. Ren, F. Wei, Y. G. Chen and Z. M. Su, *J. Solid State Chem.*, 2011, **184**, 3034–3039.

135 J. H. Kim, S. J. Lee, M. B. Kim, J. J. Lee and C. H. Lee, *Ind. Eng. Chem. Res.*, 2007, **46**, 4584–4594.

136 C. Y. Huang, M. Song, Z. Y. Gu, H. F. Wang and X. P. Yan, *Environ. Sci. Technol.*, 2011, **45**, 4490–4496.

137 Y. Lu, *Chem. Mater.*, 1999, **11**, 1223–1229.

138 S. Hitz and R. Prins, *J. Catal.*, 1997, **168**, 194–206.

139 R. A. Pai, R. Humayun, M. T. Schulberg, A. Sengupta, J. N. Sun and J. J. Watkins, *Science (80-.).*, 2004, **303**, 507–510.

140 C. J. Kepert and M. J. Rosseinsky, *Chem. Commun.*, 1999, **0**, 375–376.

141 S. Yuan, L. Zou, J. S. Qin, J. Li, L. Huang, L. Feng, X. Wang, M. Bosch, A. Alsalme, T. Cagin and H. C. Zhou, *Nat. Commun.*, 2017, **8**, 15356.

142 S. Y. Kim, A. R. Kim, J. W. Yoon, H. J. Kim and Y. S. Bae, *Chem. Eng. J.*, 2018, **335**, 94–100.

143 H. Huang, J. R. Li, K. Wang, T. Han, M. Tong, L. Li, Y. Xie, Q. Yang, D. Liu and C. Zhong, *Nat. Commun.*, 2015, **6**, 8847.

144 L. G. Qiu, T. Xu, Z. Q. Li, W. Wang, Y. Wu, X. Jiang, X. Y. Tian and L. De Zhang, *Angew. Chemie - Int. Ed.*, 2008, **47**, 9487–9491.

145 K. M. Choi, H. J. Jeon, J. K. Kang and O. M. Yaghi, *J. Am. Chem. Soc.*, 2011, **133**, 11920–11923.

146 G. Cai and H. L. Jiang, *Angew. Chemie - Int. Ed.*, 2017, **56**, 563–567.

147 J. Koo, I. C. Hwang, X. Yu, S. Saha, Y. Kim and K. Kim, *Chem. Sci.*, 2017, **8**, 6799–6803.

148 A. Ahmed, N. Hodgson, M. Barrow, R. Clowes, C. M. Robertson, A. Steiner, P.

McKeown, D. Bradshaw, P. Myers and H. Zhang, *J. Mater. Chem. A*, 2014, **2**, 9085–9090.

149 H. V. Doan, A. Sartbaeva, J.-C. Eloi, S. Davis and V. P. Ting, *Sci. Rep.*, 2019, **9**, 10887.

150 F. Vermoortele, B. Bueken, G. Le Bars, B. Van De Voorde, M. Vandichel, K. Houthoofd, A. Vimont, M. Daturi, M. Waroquier, V. Van Speybroeck, C. Kirschhock and D. E. De Vos, *J. Am. Chem. Soc.*, 2013, **135**, 11465–11468.

151 M. Hu, Y. Ju, K. Liang, T. Suma, J. Cui and F. Caruso, *Adv. Funct. Mater.*, 2016, **26**, 5827–5834.

152 Y. Yoo and H. K. Jeong, *Chem. Eng. J.*, 2012, **181**–**182**, 740–745.

153 C. Liu, B. Zhang, J. Zhang, L. Peng, X. Kang, B. Han, T. Wu, X. Sang and X. Ma, *Chem. Commun.*, 2015, **51**, 11445–11448.

154 A. López-Periago, P. López-Domínguez, J. Pérez Barrio, G. Tobias and C. Domingo, *Microporous Mesoporous Mater.*, 2016, **234**, 155–161.

155 N. Portolés-Gil, A. Lanza, N. Aliaga-Alcalde, J. A. Ayllón, M. Gemmi, E. Mugnaioli, A. M. López-Periago and C. Domingo, *ACS Sustain. Chem. Eng.*, 2018, **6**, 12309–12319.

156 E. Weidner, *J. Supercrit. Fluids*, 2018, **134**, 220–227.

157 Y. Zhao, J. Zhang, J. Song, J. Li, J. Liu, T. Wu, P. Zhang and B. Han, *Green Chem.*, 2011, **13**, 2078–2082.

158 A. I. Cooper and M. J. Rosseinsky, *Nat. Chem.*, 2009, **1**, 26–27.

159 A. P. Nelson, O. K. Farha, K. L. Mulfort and J. T. Hupp, *J. Am. Chem. Soc.*, 2009, **131**, 458–460.

160 O. K. Farha and J. T. Hupp, *Acc. Chem. Res.*, 2010, **43**, 1166–1175.

161 R. A. Dodson, A. G. Wong-Foy and A. J. Matzger, *Chem. Mater.*, 2018, **30**, 6559–6565.

162 B. Zhang, J. Zhang, C. Liu, L. Peng, X. Sang, B. Han, X. Ma, T. Luo, X. Tan and G. Yang, *Sci. Rep.*, 2016, **6**, 21401.

163 Sigmaaldrich,

https://www.sigmaaldrich.com/catalog/product/aldrich/688614?lang=en&region=GB, (accessed 16 August 2019).

164 L. Li, S. Xiang, S. Cao, J. Zhang, G. Ouyang, L. Chen and C. Y. Su, *Nat. Commun.*, 2013, **4**, 1774.

165 N. Hüsing and U. Schubert, *Angew. Chemie Int. Ed.*, 2005, **37**, 22–45.

166 A. C. Pierre and G. M. Pajonk, *Chem. Rev.*, 2002, **102**, 4243–4265.

167 L. Peng, J. Zhang, J. Li, B. Han, Z. Xue, B. Zhang, J. Shi and G. Yang, *J. Colloid Interface Sci.*, 2014, **416**, 198–204.

168 L. Peng, J. Zhang, Z. Xue, B. Han, X. Sang, C. Liu and G. Yang, *Nat. Commun.*, 2014, **5**, 933–969.

169 H. Yu, D. Xu and Q. Xu, *Chem. Commun.*, 2015, **51**, 13197–13200.

170 Y. Zhao, J. Zhang, B. Han, J. Song, J. Li and Q. Wang, *Angew. Chemie - Int. Ed.*, 2011, **50**, 636–639.

171 P. López-Domínguez, A. M. López-Periago, F. J. Fernández-Porras, J. Fraile, G. Tobias and C. Domingo, *J. CO_2 Util.*, 2017, **18**, 147–155.

172 A. M. López-Periago, N. Portoles-Gil, P. López-Domínguez, J. Fraile, J. Saurina, N. Aliaga-Alcalde, G. Tobias, J. A. Ayllón and C. Domingo, *Cryst. Growth Des.*, 2017, **17**, 2864–2872.

173 N. Portolés-Gil, S. Gowing, O. Vallcorba, C. Domingo, A. M. López-Periago and J. A. Ayllón, *J. CO_2 Util.*, 2018, **24**, 444–453.

174 H. V. Doan, Y. Fang, B. Yao, Z. Dong, T. J. White, A. Sartbaeva, U. Hintermair and V. P. Ting, *ACS Sustain. Chem. Eng.*, 2017, **5**, 7887–7893.

175 K. S. Lin, A. K. Adhikari, C. N. Ku, C. L. Chiang and H. Kuo, *Int. J. Hydrogen Energy*, 2012, **37**, 13865–13871.

176 Y. Suehiro, M. Nakajima, K. Yamada and M. Uematsu, *J. Chem. Thermodyn.*, 1996, **28**, 1153–1164.

177 J. Ren, N. M. Musyoka, H. W. Langmi, A. Swartbooi, B. C. North and M. Mathe, *Int. J. Hydrogen Energy*, 2015, **40**, 4617–4622.

178 C. Zhou, L. Longley, A. Krajnc, G. J. Smales, A. Qiao, I. Erucar, C. M. Doherty, A.

W. Thornton, A. J. Hill, C. W. Ashling, O. T. Qazvini, S. J. Lee, P. A. Chater, N. J. Terrill, A. J. Smith, Y. Yue, G. Mali, D. A. Keen, S. G. Telfer and T. D. Bennett, *Nat. Commun.*, 2018, **9**, 5042.

179 T. D. Bennett, J. C. Tan, Y. Yue, E. Baxter, C. Ducati, N. J. Terrill, H. H. M. Yeung, Z. Zhou, W. Chen, S. Henke, A. K. Cheetham and G. N. Greaves, *Nat. Commun.*, 2015, **6**, 8079.

180 J. M. Tuffnell, C. W. Ashling, J. Hou, S. Li, L. Longley, M. L. Ríos Gómez and T. D. Bennett, *Chem. Commun.*, , DOI:10.1039/c9cc01468c.

181 Y. Chen, X. Huang, S. Zhang, S. Li, S. Cao, X. Pei, J. Zhou, X. Feng and B. Wang, *J. Am. Chem. Soc.*, 2016, **138**, 10810–10813.

182 M. C. Mulakkal, R. S. Trask, V. P. Ting and A. M. Seddon, *Mater. Des.*, 2018, **160**, 108–118.

183 C. Zhu, T. Y. J. Han, E. B. Duoss, A. M. Golobic, J. D. Kuntz, C. M. Spadaccini and M. A. Worsley, *Nat. Commun.*, 2015, **6**, 6962.

184 J. C. Ruiz-Morales, A. Tarancón, J. Canales-Vázquez, J. Méndez-Ramos, L. Hernández-Afonso, P. Acosta-Mora, J. R. Marín Rueda and R. Fernández-González, *Energy Environ. Sci.*, 2017, **10**, 846–859.

185 X. Zhou and C. J. Liu, *Adv. Funct. Mater.*, 2017, **27**, 1701134.

186 I. Buj-Corral, A. Bagheri and O. Petit-Rojo, *Materials (Basel).*, 2018, **11**, 1532.

187 T. Femmer, A. J. C. Kuehne, J. Torres-Rendon, A. Walther and M. Wessling, *J. Memb. Sci.*, 2015, **478**, 12–18.

188 S. Badalov and C. J. Arnusch, *J. Memb. Sci.*, 2016, **515**, 79–85.

189 Z. X. Low, Y. T. Chua, B. M. Ray, D. Mattia, I. S. Metcalfe and D. A. Patterson, *J. Memb. Sci.*, 2017, **523**, 596–613.

190 C. R. Rambo, N. Travitzky and P. Greil, *J. Compos. Mater.*, 2015, **49**, 1971–1976.

191 H. Thakkar, S. Eastman, A. Hajari, A. A. Rownaghi, J. C. Knox and F. Rezaei, *ACS Appl. Mater. Interfaces*, 2016, **8**, 27753–27761.

192 S. Couck, J. Lefevere, S. Mullens, L. Protasova, V. Meynen, G. Desmet, G. V. Baron and J. F. M. Denayer, *Chem. Eng. J.*, 2017, **308**, 719–726.

193 S. Couck, J. Cousin-Saint-Remi, S. Van der Perre, G. V. Baron, C. Minas, P. Ruch and J. F. M. Denayer, *Microporous Mesoporous Mater.*, 2018, **255**, 185–191.

194 H. Thakkar, S. Eastman, A. Al-Mamoori, A. Hajari, A. A. Rownaghi and F. Rezaei, *ACS Appl. Mater. Interfaces*, 2017, **9**, 7489–7498.

195 C. R. Tubío, J. Azuaje, L. Escalante, A. Coelho, F. Guitián, E. Sotelo and A. Gil, *J. Catal.*, 2016, **334**, 110–115.

196 O. Shekhah, H. Wang, M. Paradinas, C. Ocal, B. Schüpbach, A. Terfort, D. Zacher, R. A. Fischer and C. Wöll, *Nat. Mater.*, 2009, **8**, 481–484.

197 L. E. Kreno, K. Leong, O. K. Farha, M. Allendorf, R. P. Van Duyne and J. T. Hupp, *Chem. Rev.*, 2012, **112**, 1105–1125.

198 T. Kitao, Y. Zhang, S. Kitagawa, B. Wang and T. Uemura, *Chem. Soc. Rev.*, 2017, **46**, 3108–3133.

199 H. Thakkar, S. Eastman, Q. Al-Naddaf, A. A. Rownaghi and F. Rezaei, *ACS Appl. Mater. Interfaces*, 2017, **9**, 35908–35916.

200 R. Semino, J. C. Moreton, N. A. Ramsahye, S. M. Cohen and G. Maurin, *Chem. Sci.*, 2018, **9**, 315–324.

201 A. J. Young, R. Guillet-Nicolas, E. S. Marshall, F. Kleitz, A. J. Goodhand, L. B. L. Glanville, M. R. Reithofer and J. M. Chin, *Chem. Commun.*, 2019, **55**, 2190–2193.

202 S. Sultan, H. N. Abdelhamid, X. Zou and A. P. Mathew, *Adv. Funct. Mater.*, 2019, **29**, 1805372.

203 J. L. Zhuang, D. Ar, X. J. Yu, J. X. Liu and A. Terfort, *Adv. Mater.*, 2013, **25**, 4631–4635.

204 Z. Shi, C. Xu, F. Chen, Y. Wang, L. Li, Q. Meng and R. Zhang, *RSC Adv.*, 2017, **7**, 49947–49952.

205 M. C. Kreider, M. Sefa, J. A. Fedchak, J. Scherschligt, M. Bible, B. Natarajan, N. N. Klimov, A. E. Miller, Z. Ahmed and M. R. Hartings, *Polym. Adv. Technol.*, 2018, **29**, 867–873.

206 M. Bible, M. Sefa, J. A. Fedchak, J. Scherschligt, B. Natarajan, Z. Ahmed and M. R. Hartings, *3D Print. Addit. Manuf.*, 2018, **5**, 63–72.

207 X. Li, L. Lachmanski, S. Safi, S. Sene, C. Serre, J. M. Grenèche, J. Zhang and R. Gref, *Sci. Rep.*, 2017, **7**, 13142.

208 I. Bezverkhyy, G. Weber and J. P. Bellat, *Microporous Mesoporous Mater.*, 2016, **219**, 117–124.

209 C. Baerlocher and L. McCusker, Database Zeolite Struct. http//www.iza-structure.org/databases/, http://www.iza-structure.org/databases/, (accessed 3 September 2019).

210 D. A. Gómez-Gualdrón, P. Z. Moghadam, J. T. Hupp, O. K. Farha and R. Q. Snurr, *J. Am. Chem. Soc.*, 2016, **138**, 215–24.

211 O. K. Farha, A. Ö. Yazaydin, I. Eryazici, C. D. Malliakas, B. G. Hauser, M. G. Kanatzidis, S. T. Nguyen, R. Q. Snurr and J. T. Hupp, *Nat. Chem.*, 2010, **2**, 944–948.

212 H. Furukawa, N. Ko, Y. B. Go, N. Aratani, S. B. Choi, E. Choi, A. Ö. Yazaydin, R. Q. Snurr, M. O'Keeffe, J. Kim and O. M. Yaghi, *Science (80-.).*, 2010, **329**, 424–428.

213 K. Matsuyama, *J. Supercrit. Fluids*, 2018, **134**, 197–203.

214 M. Rubio-Martinez, C. Avci-Camur, A. W. Thornton, I. Imaz, D. Maspoch and M. R. Hill, *Chem. Soc. Rev.*, 2017, **46**, 3453–3480.

215 C. Duan, F. Li, S. Luo, J. Xiao, L. Li and H. Xi, *Chem. Eng. J.*, 2018, **334**, 1477–1483.

216 C. Duan, F. Li, H. Zhang, J. Li, X. Wang and H. Xi, *RSC Adv.*, 2017, **7**, 52245–52251.

217 N. S. Bobbitt, M. L. Mendonca, A. J. Howarth, T. Islamoglu, J. T. Hupp, O. K. Farha and R. Q. Snurr, *Chem. Soc. Rev.*, 2017, **46**, 3357–3385.

218 S. M. J. Rogge, A. Bavykina, J. Hajek, H. Garcia, A. I. Olivos-Suarez, A. Sepúlveda-Escribano, A. Vimont, G. Clet, P. Bazin, F. Kapteijn, M. Daturi, E. V. Ramos-Fernandez, F. X. I. Llabrés Xamena, V. Van Speybroeck and J. Gascon, *Chem. Soc. Rev.*, 2017, **46**, 3134–3184.

219 K. Adil, Y. Belmabkhout, R. S. Pillai, A. Cadiau, P. M. Bhatt, A. H. Assen, G. Maurin and M. Eddaoudi, *Chem. Soc. Rev.*, 2017, **46**, 3402–3430.

220 X. Lian, Y. Fang, E. Joseph, Q. Wang, J. Li, S. Banerjee, C. Lollar, X. Wang and H. C. Zhou, *Chem. Soc. Rev.*, 2017, **46**, 3386–3401.

221 W. P. Lustig, S. Mukherjee, N. D. Rudd, A. V. Desai, J. Li and S. K. Ghosh, *Chem.*

Soc. Rev., 2017, **46**, 3242–3285.

222 C. Duan, H. Zhang, A. Peng, F. Li, J. Xiao, J. F. Zou, S. Luo and H. Xi, *ChemistrySelect*, 2018, **3**, 5313–5320.

223 X. Yang, S. Wu, P. Wang and L. Yang, *J. Solid State Chem.*, 2018, **258**, 220–224.

224 J. Park, Z. U. Wang, L. B. Sun, Y. P. Chen and H. C. Zhou, *J. Am. Chem. Soc.*, 2012, **134**, 20110–20116.

225 W. Zhang, M. Kauer, P. Guo, S. Kunze, S. Cwik, M. Muhler, Y. Wang, K. Epp, G. Kieslich and R. A. Fischer, *Eur. J. Inorg. Chem.*, 2017, **2017**, 925–931.

226 S. El-Hankari, J. Huo, A. Ahmed, H. Zhang and D. Bradshaw, *J. Mater. Chem. A*, 2014, **2**, 13479–13485.

227 A. J. Howarth, Y. Liu, P. Li, Z. Li, T. C. Wang, J. T. Hupp and O. K. Farha, *Nat. Rev. Mater.*, 2016, **1**, 15018.

228 N. C. Burtch, H. Jasuja and K. S. Walton, *Chem. Rev.*, 2014, **114**, 10575–10612.

229 N. Al-Janabi, P. Hill, L. Torrente-Murciano, A. Garforth, P. Gorgojo, F. Siperstein and X. Fan, *Chem. Eng. J.*, 2015, **281**, 669–677.

230 S. Hindocha, *"The Chemistry of Metal-Organic Frameworks: Synthesis, Characterization, and Applications"*, Wiley-VCH Verlag GmbH & Co. KGaA, Weinheim, Germany, 2017, vol. 61.

231 H.-C. Zhou, J. R. Long and O. M. Yaghi, *Chem. Rev.*, 2012, **112**, 673–674.

232 H. Wu, Q. Gong, D. H. Olson and J. Li, *Chem. Rev.*, 2012, **112**, 836–868.

233 A. Bétard and R. A. Fischer, *Chem. Rev.*, 2012, **112**, 1055–1083.

234 M. Yoon, R. Srirambalaji and K. Kim, *Chem. Rev.*, 2012, **112**, 1196–1231.

235 P. Horcajada, R. Gref, T. Baati, P. K. Allan, G. Maurin, P. Couvreur, G. Férey, R. E. Morris and C. Serre, *Chem. Rev.*, 2012, **112**, 1232–1268.

236 M. Shöâeè, J. R. Agger, M. W. Anderson and M. P. Attfield, *CrystEngComm*, 2008, **10**, 646–648.

237 J. Gascon, S. Aguado and F. Kapteijn, *Microporous Mesoporous Mater.*, 2008, **113**, 132–138.

238 S. Hermes, F. Schröder, R. Chelmowski, C. Wöll and R. A. Fischer, *J. Am. Chem.*

Soc., 2005, **127**, 13744–13745.

239 J. L. Zhuang, D. Ceglarek, S. Pethuraj and A. Terfort, *Adv. Funct. Mater.*, 2011, **21**, 1442–1447.

240 J. A. Darr and M. Poliakoff, *Chem. Rev.*, 2002, **99**, 495–542.

241 C. A. Eckert, B. L. Knutson and P. G. Debenedetti, *Nature*, 1996, **383**, 313–318.

242 L. A. Blanchard, D. Hancu, E. J. Beckman and J. F. Brennecke, *Nature*, 1999, **399**, 28–29.

243 D. Crawford, J. Casaban, R. Haydon, N. Giri, T. McNally and S. L. James, *Chem. Sci.*, 2015, **6**, 1645–1649.

244 K. B. Lausund and O. Nilsen, *Nat. Commun.*, 2016, **7**, 13578.

245 B. Alinče, *Colloid Polym. Sci. Kolloid Zeitschrift Zeitschrift für Polym.*, 1975, **253**, 720–729.

246 M. Hartmann and W. Schwieger, *Chem. Soc. Rev.*, 2016, **45**, 3311–3312.

247 B. L. Su, C. Sanchez and X. Y. Yang, in *Hierarchically Structured Porous Materials: From Nanoscience to Catalysis, Separation, Optics, Energy, and Life Science*, eds. B.-L. Su, C. Sanchez and X.-Y. Yang, Wiley-VCH Verlag GmbH & Co. KGaA, Weinheim, Germany, 2011, pp. 1–27.

248 U. Hintermair, W. Leitner and P. Jessop, in *Handbook of Green Chemistry*, Wiley-VCH Verlag GmbH & Co. KGaA, Weinheim, Germany, 2010.

249 S. Bernès, G. Hernández, R. Portillo and R. Gutiérrez, *Acta Crystallogr. Sect. E. Struct. Rep. Online*, 2008, **64**, o1366.

250 I. Persson, *Pure Appl. Chem.*, 2007, **58**, 1153–1161.

251 A. P. Abbott, E. G. Hope, R. Mistry and A. M. Stuart, *Green Chem.*, 2009, **11**, 1530–1535.

252 C. Prieto, L. Calvo and C. M. M. Duarte, *J. Supercrit. Fluids*, 2017, **124**, 72–79.

253 Y. Ge, H. Yan, B. Hui, Y. Ni, S. Wang and T. Cai, *J. Agric. Food Chem.*, 2002, **50**, 685–9.

254 A. Capuzzo, M. E. Maffei and A. Occhipinti, *Molecules*, 2013, 18, 7194–7238.

255 M. Budich and G. Brunner, *J. Supercrit. Fluids*, 2003, **25**, 45–55.

256 I. Medina and J. L. Martínez, *J. Chem. Technol. Biotechnol.*, 1997, **68**, 14–18.

257 M. J. E. Van Roosmalen, M. Van Diggelen, G. F. Woerlee and G. J. Witkamp, *J. Supercrit. Fluids*, 2003, **27**, 97–108.

258 M. A. McHugh and V. J. Krukonis, *Supercritical fluid extraction: principles and practice, Butterworth – Heinemann series in chemical engineering*, Butterworth-Heinemann, 1996.

259 H. V. Doan, H. Amer Hamzah, P. Karikkethu Prabhakaran, C. Petrillo and V. P. Ting, *Nano-Micro Lett.*, 2019, **11**, 54.

260 Y. Zhang, J. Cai, D. Zhang, X. Ke and L. Zhang, *Chem. Commun.*, 2018, **54**, 3775–3778.

261 K. A. Evans, Z. C. Kennedy, B. W. Arey, J. F. Christ, H. T. Schaef, S. K. Nune and R. L. Erikson, *ACS Appl. Mater. Interfaces*, 2018, **10**, 15112–15121.

262 D. J. Tranchemontagne, J. R. Hunt and O. M. Yaghi, *Tetrahedron*, 2008, **64**, 8553–8557.

263 J. Lee, J. H. Kwak and W. Choe, *Nat. Commun.*, 2017, **8**, 14070.

264 T. Grant Glover, G. W. Peterson, B. J. Schindler, D. Britt and O. Yaghi, *Chem. Eng. Sci.*, 2011, **66**, 163–170.

265 J. L. C. Rowsell and O. M. Yaghi, *J. Am. Chem. Soc.*, 2006, **128**, 1304–1315.

266 L. Garzón-Tovar, A. Carné-Sánchez, C. Carbonell, I. Imaz and D. Maspoch, *J. Mater. Chem. A*, 2015, **3**, 20819–20826.

267 K. Egeblad, C. H. Christensen, M. Kustova and C. H. Christensen, *Chem. Mater.*, 2008, **20**, 946–960.

268 Y. Wei, T. E. Parmentier, K. P. De Jong and J. Zečević, *Chem. Soc. Rev.*, 2015, **44**, 7234–7261.

269 Q. Sun, Z. Dai, X. Meng and F. S. Xiao, *Chem. Soc. Rev.*, 2015, **44**, 6018–6034.

270 C. M. A. Parlett, D. W. Bruce, N. S. Hondow, A. F. Lee and K. Wilson, *ACS Catal.*, 2011, **1**, 636–640.

271 C. Pirez, J. M. Caderon, J. P. Dacquin, A. F. Lee and K. Wilson, *ACS Catal.*, 2012, **2**, 1607–1614.

272 G. Collins, M. Blömker, M. Osiak, J. D. Holmes, M. Bredol and C. O'Dwyer, *Chem. Mater.*, 2013, **25**, 4312–4320.

273 Y. Z. Chen, G. Cai, Y. Wang, Q. Xu, S. H. Yu and H. L. Jiang, *Green Chem.*, 2016, **18**, 1212–1217.

274 X. Li, B. Zhang, Y. Fang, W. Sun, Z. Qi, Y. Pei, S. Qi, P. Yuan, X. Luan, T. W. Goh and W. Huang, *Chem. - A Eur. J.*, 2017, **23**, 4266–4270.

275 C. Zhu, T. Ding, W. Gao, K. Ma, Y. Tian and X. Li, *Int. J. Hydrogen Energy*, 2017, **42**, 17457–17465.

276 T. A. Wezendonk, V. P. Santos, M. A. Nasalevich, Q. S. E. Warringa, A. I. Dugulan, A. Chojecki, A. C. J. Koeken, M. Ruitenbeek, G. Meima, H. U. Islam, G. Sankar, M. Makkee, F. Kapteijn and J. Gascon, *ACS Catal.*, 2016, **6**, 3236–3247.

277 Y. F. Zhang, L. G. Qiu, Y. P. Yuan, Y. J. Zhu, X. Jiang and J. D. Xiao, *Appl. Catal. B Environ.*, 2014, **144**, 863–869.

278 K. E. Dekrafft, C. Wang and W. Lin, *Adv. Mater.*, 2012, **24**, 2014–2018.

279 S. Dissegna, K. Epp, W. R. Heinz, G. Kieslich and R. A. Fischer, *Adv. Mater.*, 2018, **30**, 1704501.

280 G. Barin, V. Krungleviciute, O. Gutov, J. T. Hupp, T. Yildirim and O. K. Farha, *Inorg. Chem.*, 2014, **53**, 6914–6919.

281 A. K. Cheetham, T. D. Bennett, F. X. Coudert and A. L. Goodwin, *Dalt. Trans.*, 2016, 45, 4113–4126.

282 H. Kim, M. Oh, D. Kim, J. Park, J. Seong, S. K. Kwak and M. S. Lah, *Chem. Commun. Chem. Commun*, 2015, **3678**, 3678–3681.

283 Q. L. Zhu and Q. Xu, *Chem. Soc. Rev.*, 2014, **43**, 5468–5512.

284 H. Wang, T. Yu, X. Tan, H. Zhang, P. Li, H. Liu, L. Shi, X. Li and J. Ye, *Ind. Eng. Chem. Res.*, 2016, **55**, 8096–8103.

285 T. Liu, Y. Liu, L. Yao, W. Yang, L. Tian, H. Liu, D. Liu and C. Wang, *Nanoscale*, 2018, **10**, 13194–13201.

286 A. Dhakshinamoorthy, M. Alvaro and H. Garcia, *Chem. - A Eur. J.*, 2010, **16**, 8530–8536.

287 A. S. Münch and F. O. R. L. Mertens, *CrystEngComm*, 2015, **17**, 438–447.

288 J. Jiang and O. M. Yaghi, *Chem. Rev.*, 2015, **115**, 6966–6997.

289 M. Opanasenko, A. Dhakshinamoorthy, M. Shamzhy, P. Nachtigall, M. Horáček, H. Garcia and J. Čejka, *Catal. Sci. Technol.*, 2013, **3**, 500–507.

290 X. Zhang, Z. Zhan, Z. Li and L. Di, *Catalysts*, 2017, **7**, 106.

291 W. Qiu, Y. Wang, C. Li, Z. Zhan, X. Zi, G. Zhang, R. Wang and H. He, *Chinese J. Catal.*, 2012, **33**, 986–992.

292 J. Y. Ye and C. J. Liu, *Chem. Commun.*, 2011, **47**, 2167–2169.

293 H. Noei, S. Amirjalayer, M. Müller, X. Zhang, R. Schmid, M. Muhler, R. A. Fischer and Y. Wang, *ChemCatChem*, 2012, **4**, 709–709.

294 Y. Zhao, C. Zhong and C. J. Liu, *Catal. Commun.*, 2013, **38**, 74–76.

295 Y. Chen, X. Mu, E. Lester and T. Wu, *Prog. Nat. Sci. Mater. Int.*, 2018, **28**, 584–589.

296 N. An, X. Yuan, B. Pan, Q. Li, S. Li and W. Zhang, *RSC Adv.*, 2014, **4**, 38250.

297 Y. Ji, H. Yang and W. Yan, *Catalysts*, 2017, **7**, 367.

298 A. Galarneau, H. Cambon, F. Di Renzo and F. Fajula, *Langmuir*, 2001, **17**, 8328–8335.

299 S. Dissegna, P. Vervoorts, C. L. Hobday, T. Düren, D. Daisenberger, A. J. Smith, R. A. Fischer and G. Kieslich, *J. Am. Chem. Soc.*, 2018, **140**, 11581–11584.

300 L. H. Wee, M. R. Lohe, N. Janssens, S. Kaskel and J. A. Martens, *J. Mater. Chem.*, 2012, **22**, 13742–13746.

301 L. H. Wee, F. Bonino, C. Lamberti, S. Bordiga and J. A. Martens, *Green Chem.*, 2014, **16**, 1351–1357.

302 D. D. Zu, L. Lu, X. Q. Liu, D. Y. Zhang and L. B. Sun, *J. Phys. Chem. C*, 2014, **118**, 19910–19917.

303 V. V. Costa, K. A. Da Silva Rocha, I. V. Kozhevnikov and E. V. Gusevskaya, *Appl. Catal. A Gen.*, 2010, **383**, 217–220.

304 J. Szanyi, M. Daturi, G. Clet, D. R. Baer and C. H. F. Peden, *Phys. Chem. Chem. Phys.*, 2012, **14**, 4383.

305 M. R. Sovizi, S. S. Hajimirsadeghi and B. Naderizadeh, *J. Hazard. Mater.*, 2009, **168**, 1134–1139.

306 A. Ahmed, E. A. Afolabi, M. U. Garba, U. Musa, M. Alhassan and K. Ishaq, *Chem. Eng. Commun.*, 2019, **206**, 1228–1240.

307 L. Peng, J. Zhang, Z. Xue, B. Han, X. Sang, C. Liu and G. Yang, *Nat. Commun.*, 2014, **5**, 933–969.

308 X-Ray Diffraction - an overview | ScienceDirect Topics, https://www.sciencedirect.com/topics/materials-science/x-ray-diffraction, (accessed 4 September 2019).

309 W. H. Bragg and W. L. Bragg, *Proc. R. Soc. A Math. Phys. Eng. Sci.*, 1913, **88**, 428–438.

310 H. P. (Harold P. Klug and L. E. (Leroy E. Alexander, *X-ray diffraction procedures for polycrystalline and amorphous materials*, .

311 B. E. (Bertram E. Warren, *X-ray diffraction*, Dover Publications, 1990.

312 C. R. Wie, T. A. Tombrello and T. Vreeland, *J. Appl. Phys.*, 1986, **59**, 3743–3746.

313 Applications of XRD, https://myscope.training/legacy/xrd/applications/, (accessed 3 September 2019).

314 What is the difference between physisorption and chemisorption?, http://www.saralstudy.com/study-eschool-ncertsolution/chemistry/surface-chemistry/1852-what-is-the-difference-between-physisorption-and-c, (accessed 4 September 2019).

315 Basic operating principles of the Sorptomatic 1990, http://saf-files.chem.ox.ac.uk/Instruments/BET/sorpoptprin.html, (accessed 4 September 2019).

316 Quantachrome Instruments, http://www.quantachrome.com/application/catalysts.html, (accessed 4 September 2019).

317 H. Tsunoyama, H. Sakurai and T. Tsukuda, *Chem. Phys. Lett.*, 2006, **429**, 528–532.

318 Microscopy training, https://myscope.training/#/SEMlevel_2_10, (accessed 3 September 2019).

319 A. Nanakoudis, Spot size in scanning electron microscopy (SEM): why it matters!,

https://blog.phenom-world.com/spot-size-sem, (accessed 3 September 2019).

320 Applications and uses of SEM, https://myscope.training/#/SEMlevel_3_2, (accessed 3 September 2019).

321 JoVE Science Education Database, https://www.jove.com/science-education/5500/using-a-ph-meter, (accessed 3 September 2019).

322 A. C. Warden, M. Warren, M. T. W. Hearn and L. Spiccia, *Inorg. Chem.*, 2004, **43**, 6936–6943.

323 N. Greeves, ChemTube3D, http://www.chemtube3d.com/solidstate/MOF-HKUST-1.html, (accessed 23 January 2019).

324 M. Taddei, *Coord. Chem. Rev.*, 2017, **343**, 1–24.

325 T. Tian, Z. Zeng, D. Vulpe, M. E. Casco, G. Divitini, P. A. Midgley, J. Silvestre-Albero, J. C. Tan, P. Z. Moghadam and D. Fairen-Jimenez, *Nat. Mater.*, 2018, **17**, 174–179.

326 M. R. DeStefano, T. Islamoglu, S. J. Garibay, J. T. Hupp and O. K. Farha, *Chem. Mater.*, 2017, **29**, 1357–1361.

APPENDIX A

Supplementary Information for the characterisation techniques (power X-ray diffraction, gas sorption, and scanning electron microscopy) used in this thesis. This section gives additional information on the general experimental procedure, a concise discussion of theory, and applications of these techniques. Details of all characterisation experiments (sample preparation, sample size, and analysis method) are given in the subsequent appendix.

A1. Powder X-ray diffraction

Powder X-ray diffraction (PXRD) is used to study the crystalline phases of solid materials by measuring the diffraction angles of X-rays diffracted through the atomic planes of a material. In an X-ray diffraction experiment (as illustrated in Figure 9 in Chapter 1), a beam of mono chromatic X-rays irradiates the sample placed in the centre of the X-ray instrument. The intensity of diffracted X-rays is recorded using a scintillation counter generating a diffraction pattern. The diffraction angles and intensities of the X-rays are associated with the atomic structure of the sample. In all crystalline materials, such as MOFs, atoms are arranged at regularly spaced intervals. On irradiation of the sample, X-rays are scattered by the dense cloud of electrons around each atom in the crystalline lattice (this process is called elastic scattering[308]). The angle between the incident and the scattered X-ray beam is called 2 theta. The wavelength of an X-ray (most commonly from copper source with wavelength of 1.5418 Å) is chosen to be similar to the distance between atoms in a crystal; thus interference between scattered X-rays can occur. Depending on the alignment of the waves, the signal can be amplified (so-called constructive interference) or destroyed (so-called destructive interference), see Figure S1a. This interference effect is reflected by the peak position and intensity in PXRD patterns and can be used to measure the distance between atoms. The relationship between the diffraction angle and the spacing between the atoms can be determined by applying the function of sinθ (see Equation S1), where d is a distance between the atomic planes and λ is a wavelength. This equation is commonly known as Bragg's law (see Equation 1.1 in Chapter 1) and is named after William Henry Bragg and Lawrence Bragg,[309] who solved the first crystal structure of zinc sulphide by X-ray diffraction.

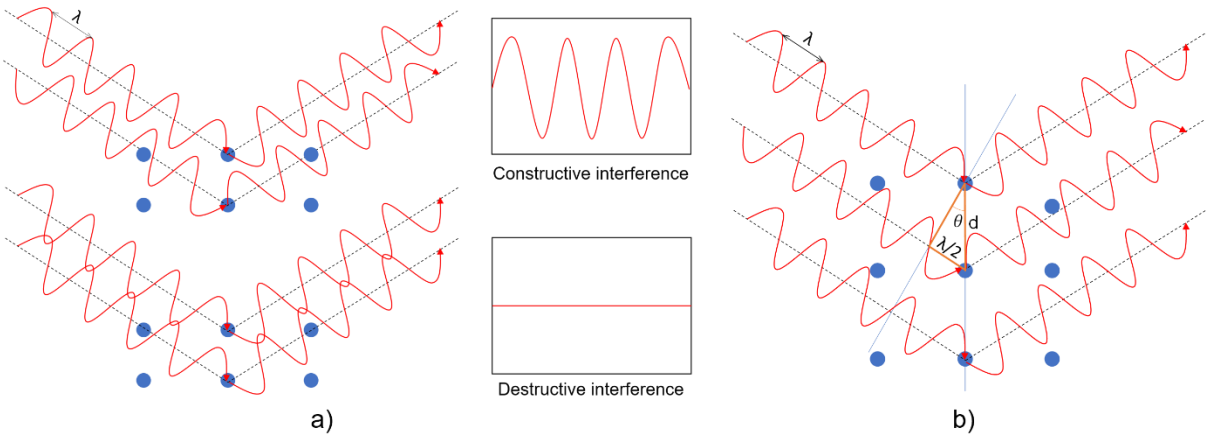

Figure S1. Schematic of PXRD technique depicting wave interference (a) and parameters in Bragg's law (b)

$$\sin\theta = \frac{\lambda}{2d} \quad \text{(Equation S1)}$$

This technique of X-ray diffraction is used today for a wide variety of materials ranging from powders, thin films, and moderately rough surfaces (*e.g.* composite fibre mats) to highly oriented samples (*e.g.* clays) and Fe and Mn bearing minerals.[310–312] In addition, determination of unknown solids is critical to studies in geology, environmental science, material science, engineering and biology.[313]

A2. Gas sorption analysis

Gas sorption analysis is a technique used to characterise material texture, including surface area and porosity, which are important physical properties that directly reflect the practicability of many porous materials. In a typical gas sorption experiment, a sample is prepared by degassing to remove weakly adsorbed molecules using either evacuation or an inert gas purge while heating the sample (typically to 120 ^{o}C). The analysis is typically performed using nitrogen at 77 K and are attracted to the sample surface by intrinsic surface energy. In porous materials, the number of molecules adsorbed increases as a function of increasing pressure. The attraction between the individual gas molecules and the atoms or ions in the sample (which defines a gas adsorption isotherm) is characterised as physical (or Van der Waals) adsorption. This physical interaction requires a low enthalpy (20-40 kJ mol^{-1}, compared to 40-400 kJ mol^{-1} in chemisorption[314]). Therefore, the adsorbed gas molecules can be easily removed by reducing the pressure (which defines a gas desorption isotherm). The shape of the completed adsorption and desorption isotherms can provide crucial information on the surface area, total pore volume, and pore size distribution of a material,[315] see Figure 12 and Figure 13 in Chapter 1 for IUPAC classifications of adsorption isotherms and hysteresis loops. In most gas sorption isotherms, quantity adsorbed per unit mass of solid is plotted against relative pressure, which is the ratio of the absolute pressure to the saturation pressure. The relative pressure used in a typical sorption isotherm ranges between 0 and 1 for the most commonly used gases such as nitrogen and argon. Surface area and pore size distribution of all MOF samples studied in this thesis were measured on a 3-Flex volumetric gas adsorption system. A schematic of the instrument is shown in Figure S2. This machine can be connected to a wide range of gases (inert and corrosive for different applications. A powerful turbomolecular vacuum pump is used to generate a dynamic high vacuum over the sample of 10^{-6} mbar, which is used for degassing the sample surface in order to perform reliable and reproducible measurements. A

precise pressure is maintained in stainless steel pipes with high vacuum fittings, starting from high vacuum and increasing step by step to the saturation pressure. Two pressure sensors are connected to the sample tube to measure absolute pressure during the analysis. Once the experiment is started, the instrument controls the injection pressure and volume *via* a feedback loop of sample adsorption rate and hence can optimise the number of equilibrium points that are collected. In the 3-Flex, 3 samples can be pre-treated and analysed simultaneously. The gas sorption method performed on this machine can be used to evaluate surface area and pore size distribution of microporous and mesoporous materials with highly accurate and reliable results produced but long analysis time required.

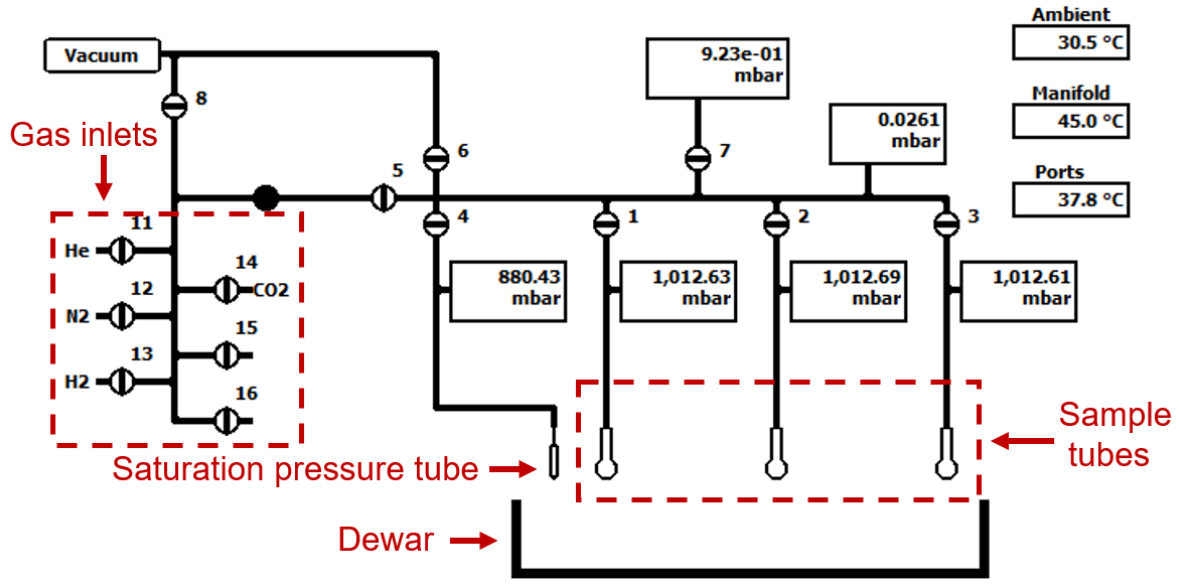

Figure S2. A schematic of a 3-Flex volumetric gas adsorption system, captured from the 3-Flex software

Gas sorption is a useful technique to evaluate the performance characteristics of porous materials such as activated carbons, zeolites, and MOFs. It provides highly beneficial information in various application areas such as catalysis, gas storage, energy storage and pharmaceutical industry. Differences in the surface area and porosity of materials that otherwise have the same physical dimensions can significantly influence the performance of these materials.[316] For example, a higher reaction rate can be achieved by increasing the surface area of gold clusters used as catalysts for aerobic oxidation of p-hydroxybenzyl alcohol.[317]

A3. Scanning electron microscopy

Scanning electron microscopy (SEM) is a technique which uses electrons as a substitute of visible light in an optical microscope to create a magnified image of a sample. In this technique, a focussed beam of electrons is scanned in a regular pattern across the surface of the sample, and the electrons scattered from the sample are used for various types of imaging. In many SEMs, the electrons are emitted from a tungsten filament which is heated by high currents in a process called thermionic emission. These electrons are accelerated by an applied voltage and travel down to the sample by means of electromagnetic fields and lenses in the microscope, which is held under vacuum. The voltage in SEMs can be variable (up to around 30 kV in a typical SEM) depending on different experiments. For example, the accelerated voltage should be reduced (*eg.* to 5 kV) to avoid charging while it must be increased (*eg.* 20 kV) for the emission of X-rays for chemical identification. After acceleration, the electron beam passes through a magnetic lens (commonly called condenser lens) which concentrates the beam to make it smaller and forms it into a spot. The beam then passes through a scanning coil (also called objective lens) which bends the beam to focus the spot on the sample, see Figure 14 in Chapter 1. On interacting with the sample electrons can be absorbed, reflected off the surface (generating high energy backscattered electrons), excite surface molecules and release electrons (low energy secondary electrons), and remove a core-shell electron (those cloest to the nucelus) to emit a characteristic x-ray. A typical SEM can be equipped with different detectors including backscattered electron detector (BSED), secondary electron detector (SED), and X-ray detector to collect various signals. SEM images with topographical information are priimarily collected from secondary electron detectors while elemental composition (from energy-dispersive X-ray spectroscopy) are collected using X-ray detectors. In a typical SEM, signals generated from the sample are collected by an electron detector, converted to photons via a scintillator, amplified in a photomultiplier, converted to electrical signals and used to modulate the intensity of the image on the viewing screen. To improve the number of secondary electrons scattered to the detector the sample is usually coated with a thin layer of a heavy metal such as gold, platinum, or silver (~10 nm). This can be also useful to reduce surface charging effects, which can either block the secondary electrons or distort beam signals in non-conductive samples.[318] In most cases, adjusting the spot size during the SEM experiment is extremely important to obtain high-resolution images with accurate information. This can be achieved by changing the accelerating voltage, the convergence angle of the

electron-beam cone, the beam current that hits the sample, and the diameter of the final beam spot on the sample, see *Figure S3*.[319]

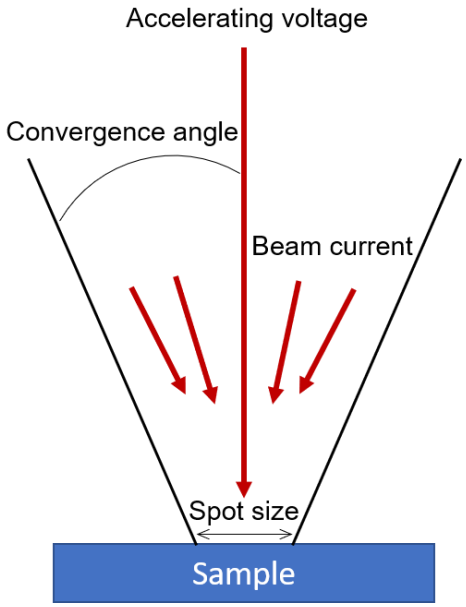

Figure S3. The four major parameters of the electron beam in a SEM: accelerating voltage, convergence angle, beam current and spot size.

As a remarkably versatile technique, SEM is used as one of the most common techniques to image morphology of samples (*e.g.* view bulk material, coatings, sectioned material) as well as to analyse X-rays from samples for microanalysis. The SEM has many advantages over traditional light microscopopy, such as better resolution at high-magnification (the best resolution possible in a light microscope is about 200 nm whereas those in a typical SEM can be 10 nm or below) and greater topographical details (SEM has more than 300 times the depth of field compared to a light microscope). Due to the fact that SEM makes use of electromagnets, the degree of magnification is controlled more proficiently in this technique. SEM is widely used in materials science, biological science, geology, and forensic science.[320]

APPENDIX B

Supplementary Information for

Defective hierarchical porous copper-based metal-organic frameworks synthesised via a facile acid etching strategy

B1. Experimental

Table S1. Chemicals used.

No.	Name and supplier	Purity	Formula
1	Methanol (Sigma-Aldrich)	99.9%	CH_3OH
2	Dimethyl sulfoxide (DMSO) (Sigma-Aldrich)	99.9%	$(CH_3)_2SO$
3	Orthophosphoric acid (Honeywell)	85-90%	H_3PO_4
4	Basolite® C 300 (HKUST-1) (Sigma-Aldrich)	NA	$C_{18}H_6Cu_3O_{12}$
5	Deuterium chloride (Sigma-Aldrich)	99 atom% D	DCl
6	Dimethyl sulfoxide-d_6 (Sigma-Aldrich)	99.9 atom% D	$(CD_3)_2SO$

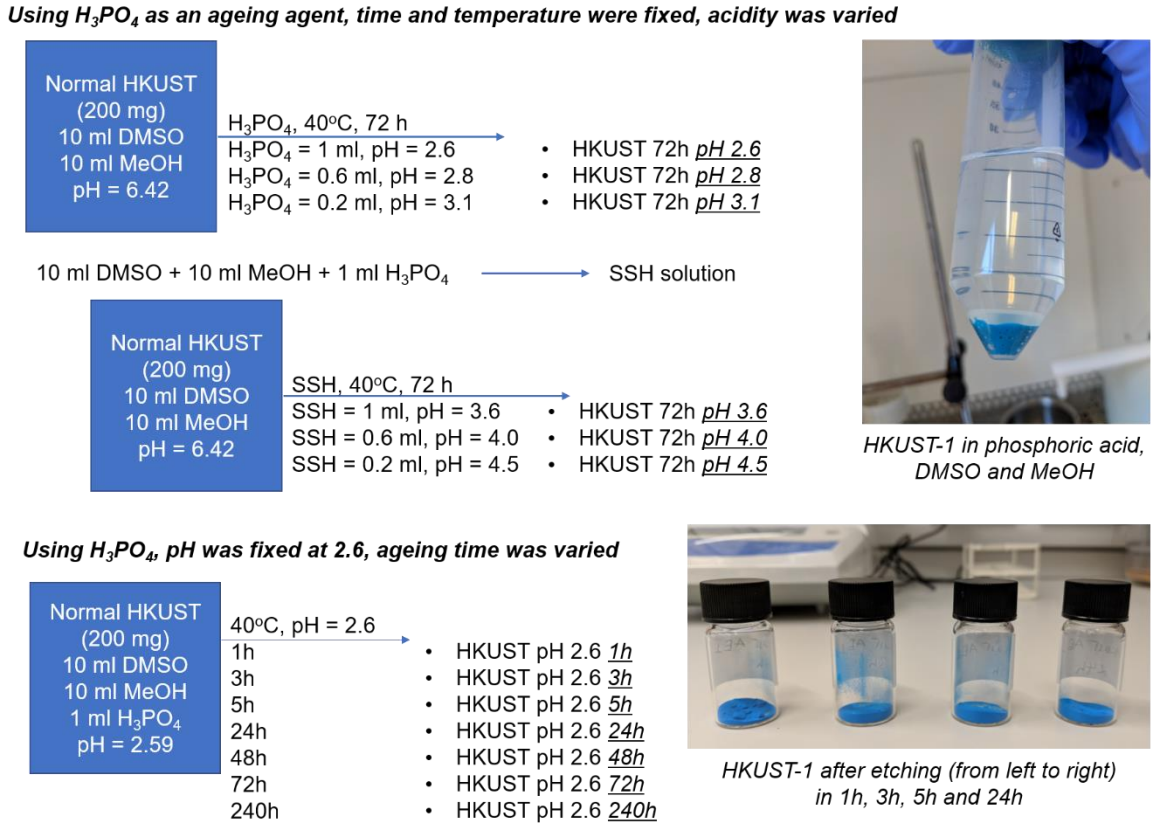

Figure S4. Experimental details of HKUST-1 etching in phosphoric acid using DMSO and MeOH as dilute solvents.

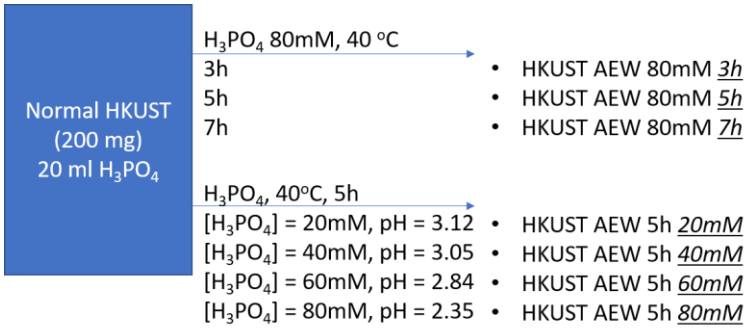

Figure S5. Experimental details of HKUST-1 etching in phosphoric acid using water as a dilute solvent (HKUST AEW)

At the highest concentration investigated in this study (200 mg HKUST etching in 20 mL phosphoric solution at pH 2.6), 0.15 mmol H^+ from the phosphoric acid was available to interact with 1 mmol copper cation in HKUST-1. As the etching is due to the presence of H_3PO_4, increasing the solution volume with the same pH (*i.e.* same concentration of H^+, but increasing the number of moles of H^+ available) could be expected to lead to a greater extent of etching (similar to the effect of leaving a sample in the SSH solution for longer).

B2. Characterisation techniques

The pH of a solution was determined by electrochemical measurements with a calibrated Jenway 3510 pH meter with a glass proton-sensitive electrode (see Figure S6) in contact with the solution. The difference in the potentials of the pH and reference electrodes provides a millivolt (mV) signal to measure pH by using Equation S2.[321] In the pH meter used in this work, a built-in reference electrode was combined in the glass electrode. This reference electrode was used to maintain a constant potential at any given temperature, and serves to complete the pH measuring circuit within the solution. The pH sensor in Jenway 3510 can be used to measure pH between -2.000 and 19.999 with an accuracy of ±0.003.

$$E = E_0 + 2.303\left(\frac{RT}{F}\right) log a_{H^+} = E_0 - 2.303\left(\frac{RT}{F}\right) pH \qquad \text{(Equation S2)}$$

where E is a measured potential, E_0 is the standard electrode potential at a_{H^+}= 1 mol L^{-1}, R is the gas constant, T is the temperature in Kelvin, F is the Faraday constant.

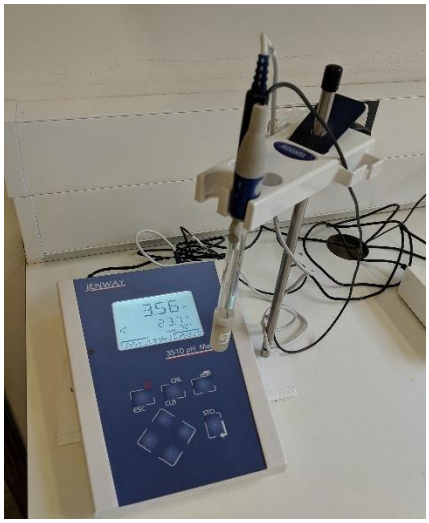

Figure S6. Jenway 3510 pH meter used for pH measurement

Powder X-ray diffraction analyses were performed on a BRUKER AXS D8-Advance instrument with Vantec-1 detector using Cu Kα (λ = 1.5418 Å) as the source of X-ray radiation, in flat plate geometry, spinner speed 15 rpm, at 21 ºC. The two theta range, between 2 and 60 degrees, was used with a 0.02 degree interval for collection and 20 minute scans.

Gas sorption isotherms were determined using nitrogen sorption at 77 K with a Micromeritics 3-Flex volumetric gas sorption analysis system. Samples were degassed at 120 °C under dynamic high vacuum (10^{-6} mbar) over 6 hours prior to analysis. The total pore volume was taken at the end of the filling of the pore. Surface area was determined by the BET method according to British Standards, with relative pressure (P/P_o) selected considering the Rouquerol consistency criterion between values of 0 and 0.3.

Scanning electron microscopy (SEM) analysis was performed on a JSM-IT300 (JEOL, Japan) at 5 kV with a 10.8 mm working distance and magnifications from 350 to 40,000 times. The samples were sputtered with a thin layer of silver (10 nm) and imaged with a secondary electron detector.

Thermogravimetric analysis (TGA) was carried out in a thermogravimetric analyser (TGAQ500, TA-instruments) at the Material and Chemical Characterisation Facility, University of Bath. The temperature ramping was 5 °C min^{-1} from room temperature to 600 °C in 100 mL min^{-1} of air.

^{31}P nuclear magnetic resonance (NMR) spectra were recorded at 298 K on a Bruker Advance 300 MHz Ultrashield NMR spectrometer at the Department of Chemistry, University of Bristol. ^{1}H NMR spectra were referenced to the residual *protio* peaks at δ 2.50 ppm for DMSO-

d6. The samples were digested in 0.1 mL deuterium chloride (DCl, 99 atom% D) and 3 mL anhydrous dimethyl sulfoxide-d_6 (DMSO-d_6, 99 atom% D) before carrying out the experiment.

B3. Additional characterisation data and discussion

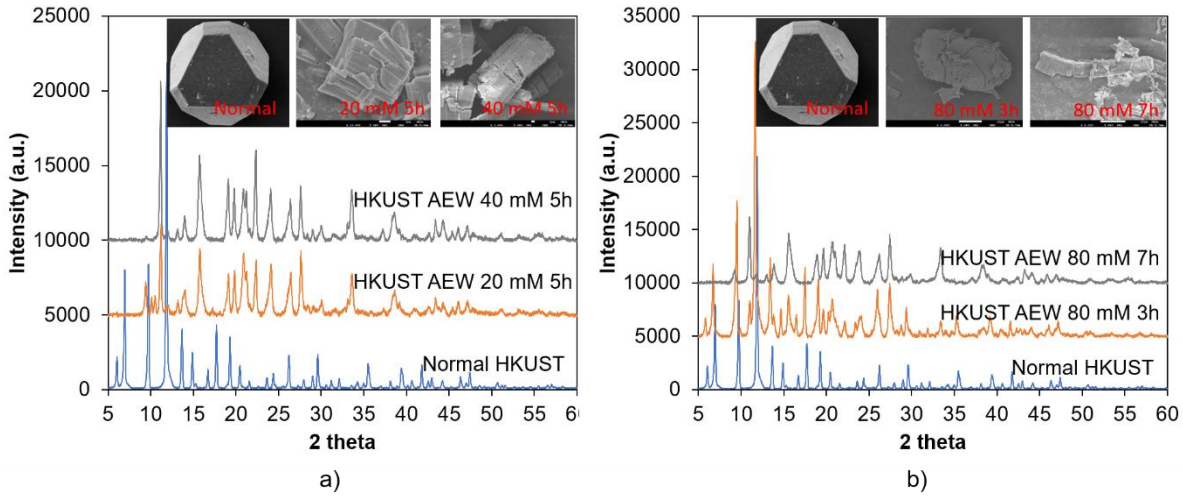

Figure S7. PXRD and SEM results of HKUST-1 etching in phosphoric acid using water as a dilute solvent (HKUST AEW in different concentrations (a) and times (b).

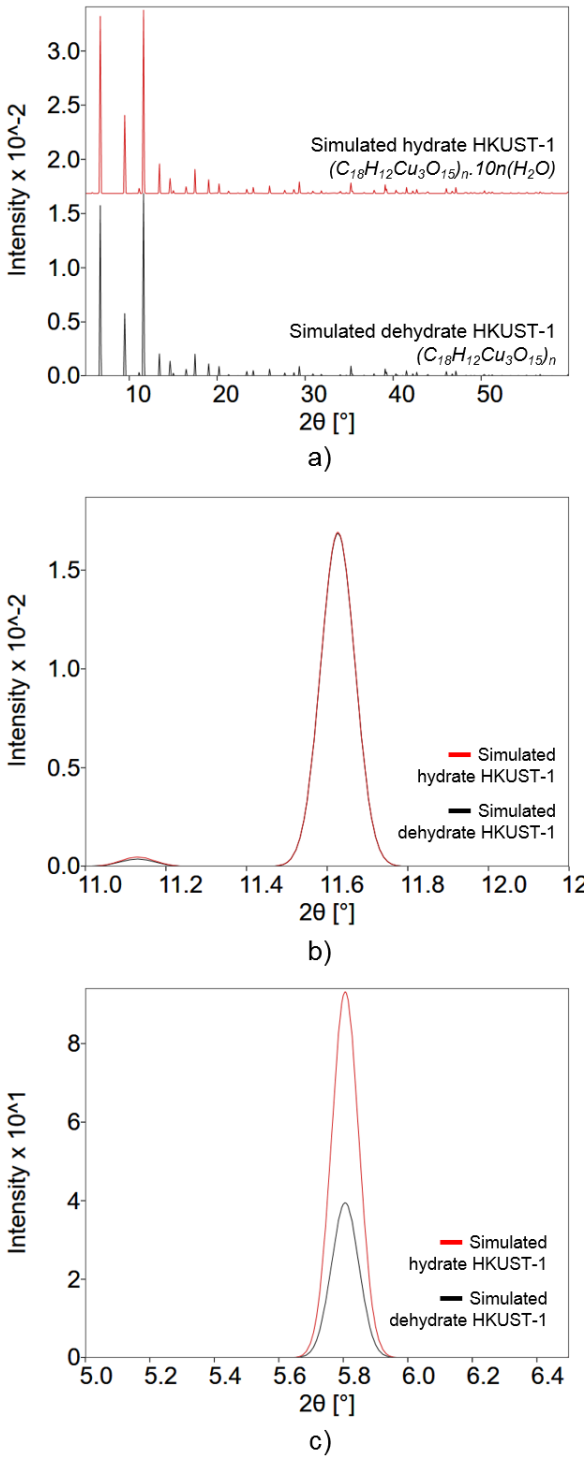

Figure S8. PXRD results of simulated hydrate and dehydrate HKUST-1 generated by CrystalMaker and CrystalDiffract, normalised to the height of the peak at 11.6 degrees 2θ. a) PXRD of both samples in 5-60 degrees 2θ. b) Peaks at 11.6 degrees 2θ in both patterns are identical. c) Peak at 5.8 degrees 2θ shown in hydrate HKUST-1 has much higher intensity than the dehydrated state.

Table S2. BET surface areas of HKUST-1 (measured via N_2 sorption at 77 K) etching in phosphoric acid using water as a dilute solvent (HKUST AEW) at different concentrations.

	Normal HKUST	HKUST AEW 5h 20mM	HKUST AEW 5h 40mM	HKUST AEW 5h 60mM	HKUST AEW 5h 80mM
BET surface area (m^2 g^{-1})	2208.04 ± 1.62	993.54 ± 0.65	17.64 ± 0.44	25.27 ± 0.89	17.06 ± 0.55

Table S3. BET surface areas of HKUST-1 (measured via N_2 sorption at 77 K) etching in phosphoric acid using water as a dilute solvent (HKUST AEW) in different times.

	Normal HKUST	HKUST AEW 80mM 3h	HKUST AEW 80mM 5h	HKUST AEW 80mM 7h
BET surface area (m^2 g^{-1})	2208.04 ± 1.62	33.44 ± 1.06	17.06 ± 0.55	33.47 ± 1.26

Table S4. Gas sorption results of HKUST-1 etching in phosphoric acid using DMSO and MeOH as dilute solvents at different concentrations and times.

	BET surface area (m^2 g^{-1})	Total pore volume (cm^3 g^{-1})
For different concentrations		
Normal HKUST	2208	0.899
HKUST 72 h pH 6.4	2088	0.913
HKUST 72h pH 4.5	1743	0.737
HKUST 72h pH 4.0	1730	0.715
HKUST 72h pH 3.6	1538	0.701
HKUST 72h pH 3.1	1525	0.625
HKUST 72h pH 2.8	1523	0.623
HKUST 72h pH 2.6	1455	0.585
Over different times		
HKUST pH 2.6 1h	1523	0.665
HKUST pH 2.6 3h	1623	0.702
HKUST pH 2.6 5h	1616	0.689
HKUST pH 2.6 48h	1578	0.640
HKUST pH 2.6 72h	1455	0.585
HKUST pH 2.6 240h	1117	0.520

It was previously shown that phosphoric acid with molecular diameter of 0.61 nm[322] is a very promising diffusing agent in some water stable MOFs for example MIL-100(Fe)[147] to create a hollowed out structure via selective acid etching. HKUST-1 MOF, which has larger primary pores (d ~ 0.83 nm - 1.26 nm) and smaller secondary pores (d ~ 0.51 nm) (Figure S9) could be a very promising candidate to employ this process. Regrettably, this MOF degrades in water under standard aqueous acid etching conditions. In this research, a mixture of DMSO and MeOH was systematically employed to control the concentration of H_3PO_4, enabling the mechanism of selective acid etching to be applied to MOFs with limited water stability.

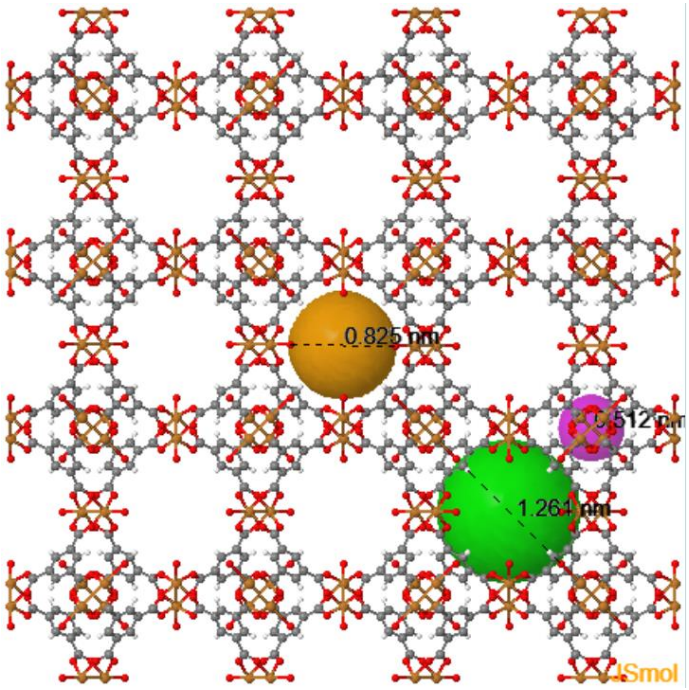

Figure S9. Structure of HKUST-1 visualised using ChemTube3D.[323] *The spheres represent the pore sizes within the framework. The smaller secondary pore is represented by the purple sphere (0.512 nm, measured from two C atoms in the benzene rings) and the larger primary pores can be represented by either the orange sphere (0.825 nm, measured from O to O atoms in the two Cu paddlewheels) or the green sphere (1.261 nm, measured between the carbons of the two benzene rings)*

In this study, thermogravimetric analysis (TGA) was used to determine linkers or clusters missing in defect formation. This method was employed previously to study defect-engineered MOFs such as HKUST-1[142,225,236,280], UiO-66[324], NU-125[280] and PCN-125[224]. For example, Taddei *et al.* observed that defected UiO-66 had smaller weight loss between 300 and 450 ^{o}C, indicating the existence of missing-linker defects in the framework.[324] Inspired by this research, TGA spectra of all HKUST-1 samples were collected and normalised to the weight loss at 600

^{o}C, allowing us to see the differences of linkers which might have been removed in the region between 250 and 300 ^{o}C. From Figure S10, it can be seen that most etched samples possess missing-linker defects demonstrated by less weight loss than the normal HKUST-1, however, there is no obvious evidence to show that the number of linkers and clusters missing in HKUST acid etching depends on time or acidity. In addition, there was no peak for phosphorous compounds appearing in ^{31}P NMR of samples etched in phosphoric acid using DMSO and MeOH as dilute solvents (Figure S11), indicating that there were no linker vacancies or partial linker decoordination by PO_4^{3-}. The phosphate anions were removed after washing out the sample 3 times with MeOH.

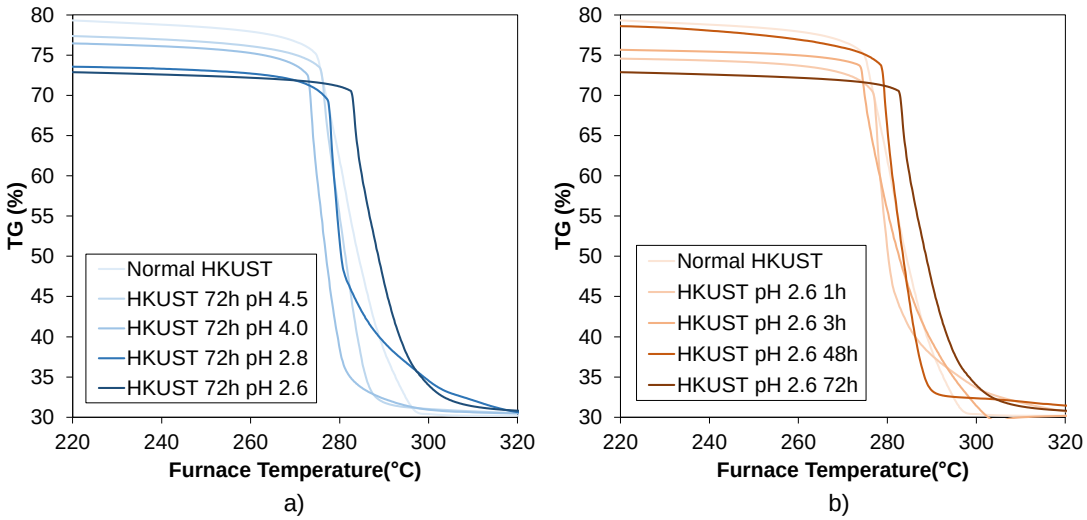

Figure S10. TGA results of HKUST-1 etching in phosphoric acid using DMSO and MeOH as dilute solvents at different concentrations (a) and times (b). Increasing time and decreasing pH are illustrated by the colours from lightest to darkest.

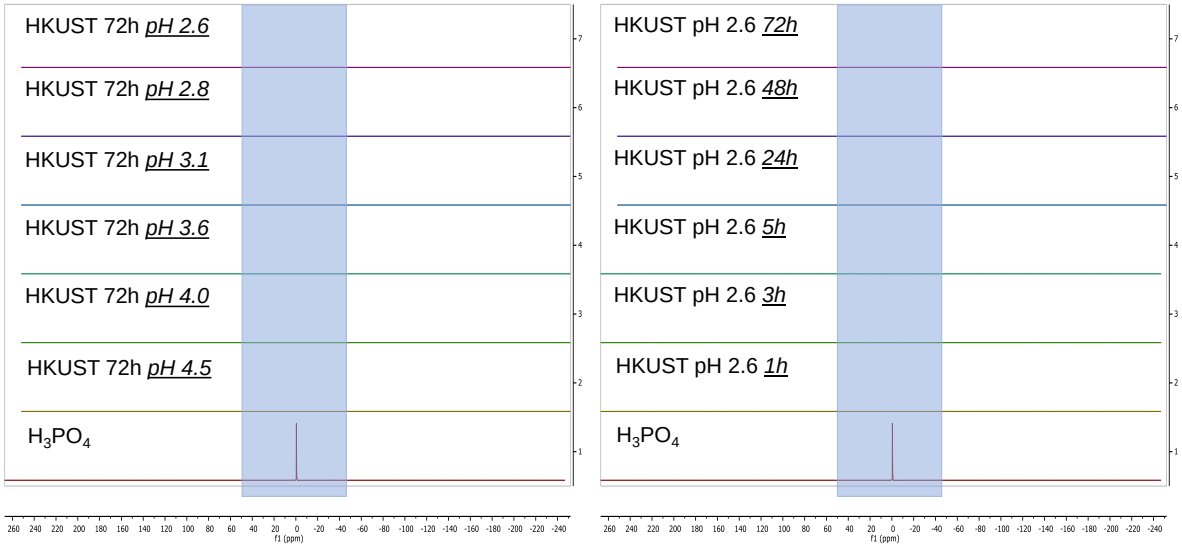

a) b)

Figure S11. ^{31}P NMR of HKUST-1 etching in phosphoric acid using DMSO and MeOH as dilute solvents at different concentrations (a) and etching times (b).

Table S5. Sample mass loss of HKUST 72h pH 2.6 repeated 5 times.

HKUST 72h pH 2.6 sample	**Empty tube (g)**	**Tube + sample (before) (g)**	**Sample (before) (g)**	**Tube + sample (after) (g)**	**Sample (after) (g)**	**Sample mass lost (g)**	**Delta R (g)**
Batch 1	14.3037	14.5080	0.2043	14.4576	0.1539	0.0504	0.0020
Batch 2	14.2790	14.4993	0.2203	14.4466	0.1676	0.0527	0.0043
Batch 3	14.3551	14.5715	0.2164	14.5261	0.1710	0.0454	0.0030
Batch 4	14.3073	14.5111	0.2038	14.4654	0.1581	0.0457	0.0027
Batch 5	14.3274	14.5268	0.1994	14.4791	0.1517	0.0477	0.0007
						0.0484	***0.0030***

APPENDIX C

Supplementary Information for

Controlled formation of hierarchical metal-organic frameworks using CO_2 expanded solvent systems

C1. Characterisation techniques

Powder X-ray diffraction analyses were performed on a BRUKER AXS D8-Advance instrument with Vantec-1 detector using Cu Kα (λ = 1.5418Å) as the source of X-ray radiation, in flat plate geometry, spinner speed 15 rpm, at 21 ºC. The two theta range, between 2 and 60 degrees, was used with a 0.02 degree interval for collection and 20 minute scans.

Gas sorption isotherms were determined using nitrogen sorption at 77 K with a Micromeritics 3-Flex volumetric gas sorption analysis system (nitrogen with purity of 99.9999% was purchased from Air Products). Samples were degassed at 180 °C under dynamic high vacuum (10^{-6} mbar) over 6 hours prior to analysis. The total pore volume was taken at the end of the filling of the pore. Surface area was determined by the BET method according to British Standards, with relative pressure (P/P_o) selected considering the Rouquerol consistency criterion between values of 0 and 0.3.

High-resolution micrographs were taken using JEOL FESEM 6340F and 7600F field emission scanning electron microscopes at University of Bristol and Nanyang Technological University. Source: cold cathode UHV field emission conical anode gun, accelerating voltage: 5-10 kV, Specimen stage: Eucentric Type I, X = 70 mm, Y = 50 mm, Z = 38.5 mm (WD: 6 to 10 mm), T = -5 to 70°, R = 360°, magnifications from 10,000 times to 85,000 times. The high-resolution TEM experiment was performed on a JEOL 2100F instrument at 200 kV with UHR configuration at Nanyang Technological University.

Particle size distribution was determined using dynamic light scattering with a Malvern Zetasizer Nano S instrument. Samples were dispersed in methanol (concentration ~100 ppm) and placed in a 12 mm glass cuvette (PCS8501). The particle size distribution data were obtained by using Zetasizer software with parameters as following: refractive index: 1.475; absorption: 0.01; temperature: 25 ºC, equilibration time: 120 s and number of measurements: 3.

C2. Experimental

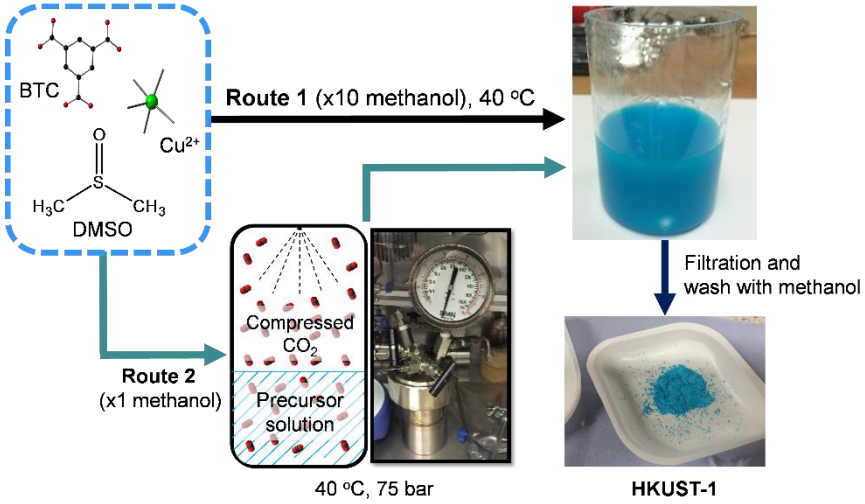

Figure S12. Synthesis procedures of HKUST-1 using conventional solvothermal synthesis (route 1) and the method employing supercritical CO_2 (route 2)

Table S6. Chemicals used

No.	Name and supplier	Purity	Formula
1	Methanol (Sigma-Aldrich)	99.9%	CH_3OH
2	Copper(II) nitrate hemipentahydrate (Sigma-Aldrich)	99.9%	$Cu(NO_3)_2.2.5H_2O$
3	Benzene-1,3,5-tricarboxylic acid (Trimesic acid/BTC) (Sigma-Aldrich)	95%	$C_6H_3(CO_2H)_3$
4	Dimethyl sulfoxide (DMSO) (Sigma-Aldrich)	99.9%	$(CH_3)_2SO$
5	Methanol (Sigma-Aldrich)	99.9%	CH_3OH

Table S7. Description and yields of HKUST-1 samples synthesised in different conditions.

Conditions		**Sample name**	**Description**	**Yields (wt.%)**
Without CO_2, synthesised by a conventional method		HKUST CO_2 free	10 mL stock solution + 100 mL methanol, 40 °C	8.6
Ageing in DMSO and methanol		HKUST ageing	0.2 g HKUST CO_2 free + 40 mL DMSO + 40 mL methanol, 40 °C, 48 h	N.D.
Pressure varied, 40 °C, 24 h, flow rate 5 mL min^{-1}	40 bar	HKUST 60 bar	30 mL stock solution + 30 mL methanol, 40 °C, 24 h	2.8
	60 bar	HKUST 60 bar	30 mL stock solution + 30 mL methanol, 40 °C, 24 h	9.3
	70 bar	HKUST 70 bar	30 mL stock solution + 30 mL methanol, 40 °C, 24 h	7.4
	80 bar	HKUST 80 bar	30 mL stock solution + 30 mL methanol, 40 °C, 24 h	2.7
Ageing time varied, 40 °C, 75 bar CO_2, flow rate 5 mL min^{-1}	4 min	HKUST VC	1.5 mL stock solution + 1.5 mL methanol in a view cell, 40 °C, 75 bar	6.3
	1 h	HKUST 1 h	40 mL stock solution + 40 mL methanol, 40 °C, 60 bar	4.5
	24 h	HKUST 24 h	40 mL stock solution + 40 mL methanol, 40 °C, 75 bar	5.6
	48 h	HKUST 48 h	40 mL stock solution + 40 mL methanol, 40 °C, 75 bar	9.9
	72 h	HKUST 72 h	40 mL stock solution + 40 mL methanol, 40 °C, 75 bar	7.2
Cycling, 24 h cycled 3 times		HKUST 24 h x 3	40 mL stock solution + 40 mL methanol, 40 °C, 75 bar, cycled pressurise every 24 h 3 times	9.9
Slow CO_2 pressurisation, pressurisation rate 0.1 bar min^{-1}		HKUST SP 72 h	40 mL stock solution + 40 mL methanol, 40 °C, 75 bar, pressurisation rate 0.1 bar min^{-1}, 72 h	6.9

VC: view cell. SP: slow pressurisation. N.D: not determined

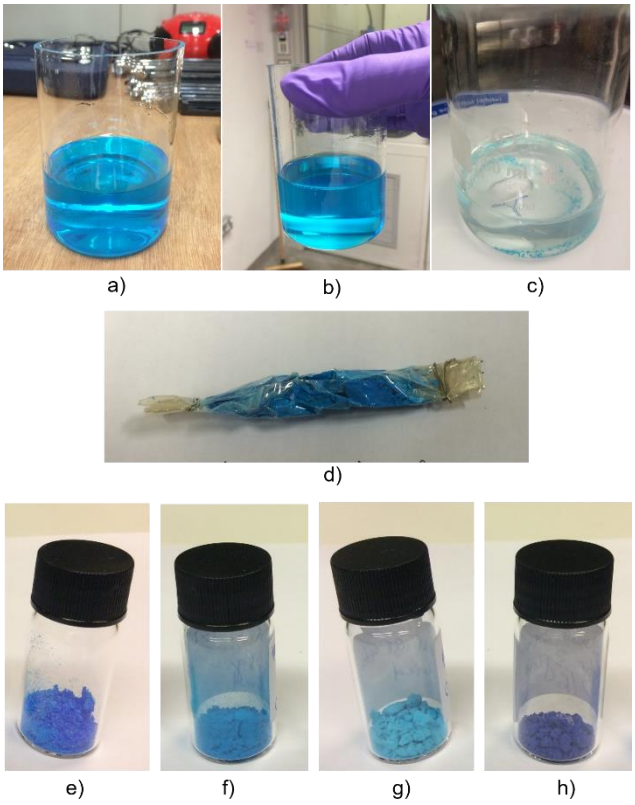

Figure S13. a) 1:1 DMSO/MeOH precursor solution after 10 minutes. b) 1:1 DMSO/MeOH precursor after 30 days. c) Conventional HKUST-1 ageing in methanol and DMSO at 40 °C for 48 hours. d) HKUST-1 sample in dialysis tubing prepared for scCO₂ drying. e-h) Sample color change after different drying treatments. From left to right: $Cu(NO_3)_2.2.5H_2O$, HKUST-1 after air drying, HKUST-1 after CO_2 drying, HKUST-1 after vacuum heating to 200 °C.

C3. Additional characterisation data and information

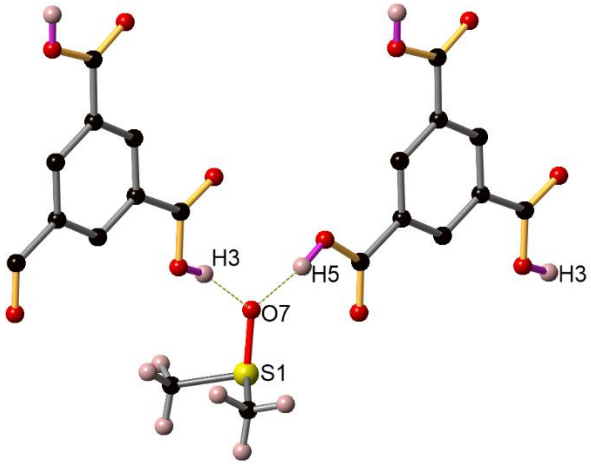

Figure S14. Hydrogen bonds formed between trimesic acid and DMSO. C atoms are represented by back spheres. O atoms are represented by red spheres. H atoms are represented by pink spheres. S atoms are represented by yellow spheres.

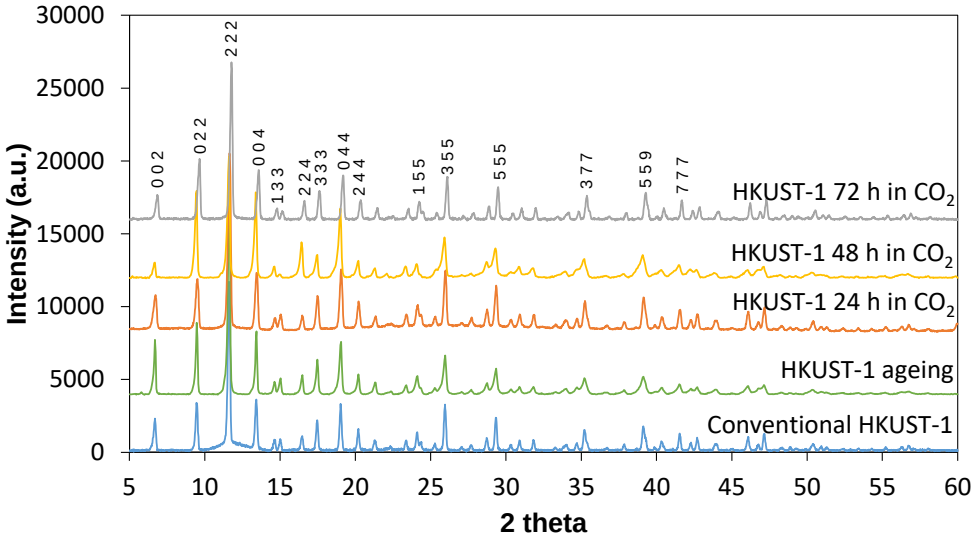

Figure S15. PXRD data of various HKUST-1 samples

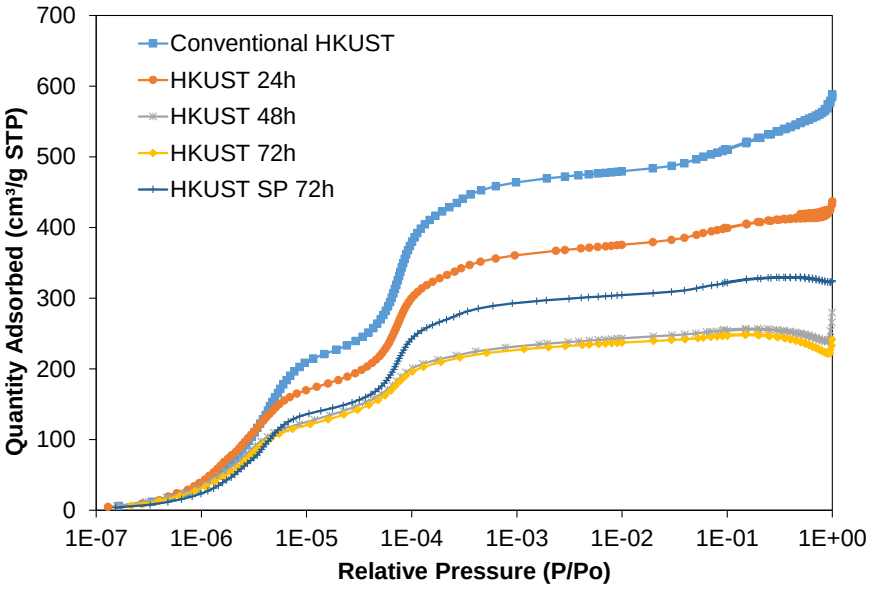

Figure S16. Nitrogen isotherms of various HKUST-1 samples.

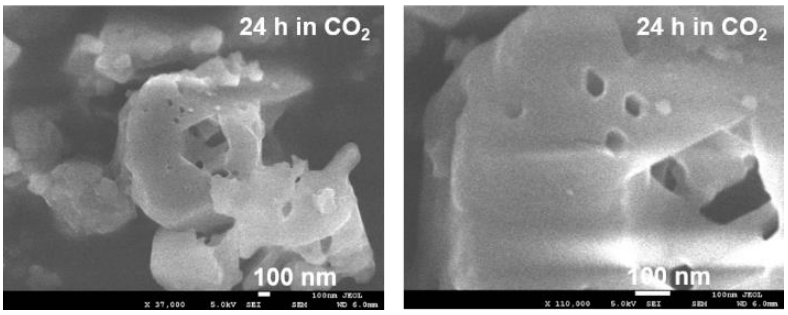

a)

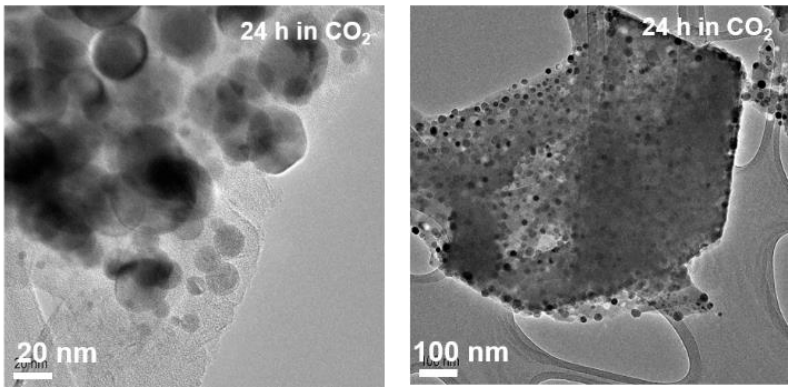

b)

Figure S17. Images of HKUST-1 24 h in CO_2. a) SEM. b) TEM

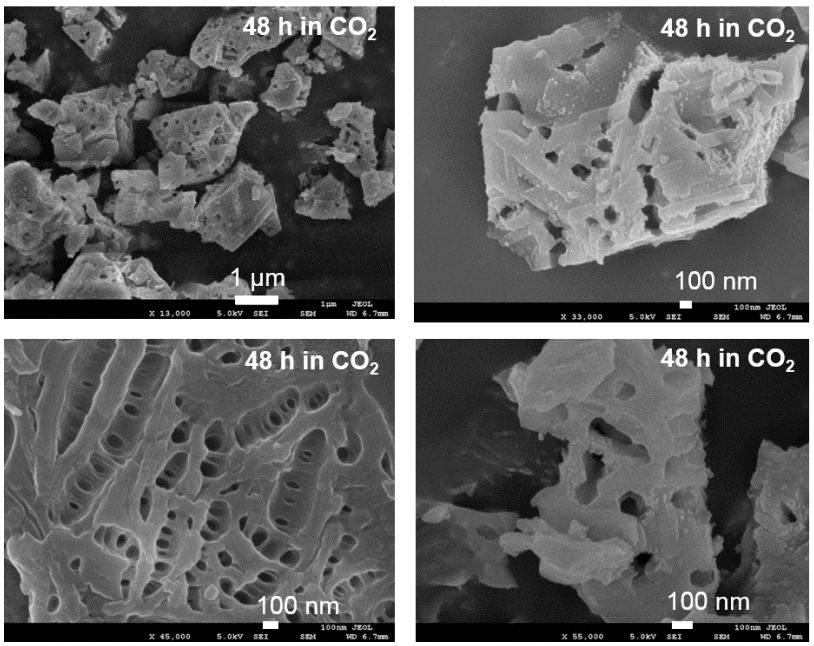

Figure S18. SEM images of HKUST-1 48 h in CO_2.

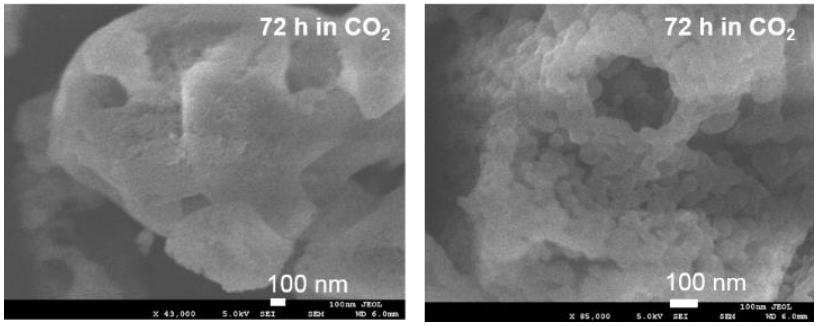

a)

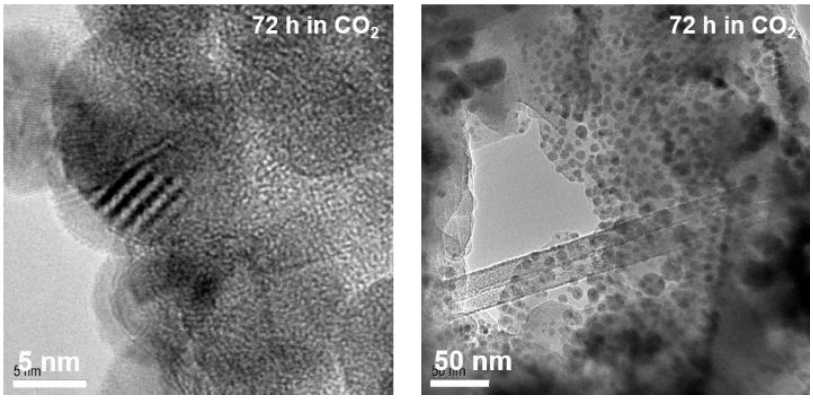

b)

Figure S19. Images of HKUST-1 72 h in CO_2. a) SEM. b) TEM.

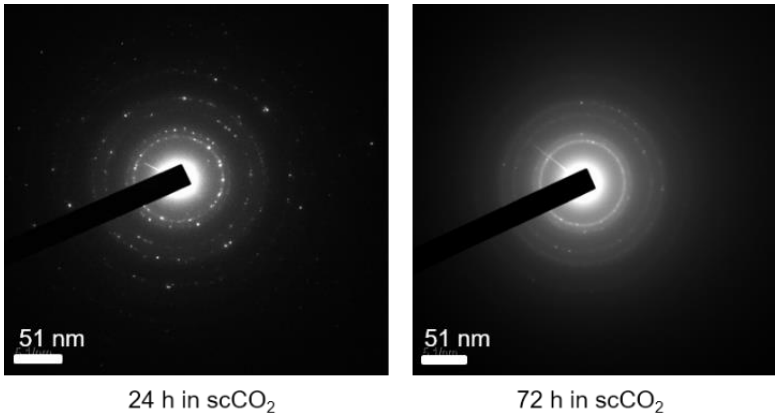

Figure S20. EDX-TEM results of HKUST-1 24 h and 72 h in CO_2.

APPENDIX D

Supplementary Information for

Using supercritical CO_2 in the preparation of metal-organic frameworks: investigating effects on crystallisation

D1. Characterisation methods

Materials after synthesis were tested by powder X-ray diffraction (PXRD) on a BRUKER AXS D8-Advance instrument with Vantec-1 detector using Cu Kα (λ = 1.5418Å) as the source of X-ray radiation, in flat plate geometry, spinner speed 15 rpm, at 21 ^{o}C. The two theta range, between 2 and 60 degrees, was used with a 0.02 degree interval for collection and 20 minute scans.

Scanning electron microscopy (SEM) images were taken using JEOL IT300 SEM with a SED detector at School of Chemistry, University of Bristol with the following settings, objective aperture: 1, acceleration voltage: 5kV, probe current: 10.3 m, working distance: 10.8 mm and magnifications from 350 to 40,000 times. The samples were coated with 15 nm silver before conducting the experiment.

Gas sorption isotherms were determined using nitrogen sorption at 77 K with a Micromeritics 3-Flex volumetric gas sorption analysis system (nitrogen with purity of 99.9999% was purchased from Air Products). Samples were degassed at 120 °C under dynamic high vacuum (10^{-6} mbar) over 6 hours prior to analysis. The total pore volume was taken at the end of the filling of the pore. Surface area was determined by the BET method according to British Standards, with relative pressure (P/P_o) selected considering the Rouquerol consistency criterion between values of 0 and 0.3.

D2. Additional characterisation data and discussion

D2.1. Synthesis of $[Cu_{24}(OH\text{-}mBDC)_{24}]_n$ in DMSO and MeOH

Figure S21. A mixture of 1.6 g $Cu(OAc)_2.H_2O$ and 1.5 g OH-mBDC in 100 mL DMSO after 2 hours, showing a precipitation had occurred in the $[Cu_{24}(OH\text{-}mBDC)_{24}]_n$ stock solution.

D2.2. Synthesis of Zn-BTC in DMSO and MeOH

With previous success in creation of macroporous HKUST-1 (or Cu-BTC) in $scCO_2$,[174] Zn-BTC synthesis was repeated in the same manner. In a typical experiment, 3.1 mg $Zn(NO_3)_2.6H_2O$ (10 mmol) and 1.5 mg BTC (5 mmol) were dissolved in 100 mL DMSO, resulting in a clear precursor solution. As demonstrated previously,[19] H-bonding between DMSO and BTC dominated the metal-ligand coordination forces and hindered the aggregation process, resulting in a stable stock solution. This solution (1-5 mL) was added in MeOH at volume ratios varied between 1:1 and 1:10, and left for up to 10 days at 40 ^oC. However, no precipitation was observed, consistent with the precursor solution of HKUST-1[174]. A mixture of 4 mL stock solution and 40 mL MeOH was pressurised with CO_2 at 40 ^oC and 75 bar, however, no solid was formed after 3 days. This might be due to the metal-ligand coordination forces between Zn and BTC not being able to overcome the H-bonding even in the presence of CO_2-expanded MeOH as an antisolvent at 40 ^oC.

Figure S22. Stock solution of $Zn(NO_3)_2.6H_2O$ (10 mmol), BTC (5 mmol) and DMSO in MeOH at different volume ratios. Stock solution/MeOH volume ratio (from left to right) is 1:1, 1:2, 1:4, 1:6, 1:8 and 1:10.

D2.3. Synthesis of UiO-66 in DMF at low temperature

Normal UiO-66 was synthesised by dissolving 3.18 g $ZrCl_4$ (0.014 mol) and 2.04 g benzene-1,4-dicarboxylic acid (H_2BDC) (0.014 mol) in 80 mL anhydrous dimethylformamide (DMF) at room temperature. The reaction of this step is given in Scheme S1. The reaction mixture was heated in an autoclave at 120 ^oC for 24 hours. After cooling in air to room temperature the white solid was separated by filtration, repeatedly washed with DMF and dried at room temperature. In the modified synthetic procedure, the autoclave was heated at 40 ^oC instead of 120 ^oC, all other steps were maintained the same. In the synthesis with $scCO_2$, the stock solution was added in a glass vial and placed in a 250 mL cylindrical steel reactor pressure vessel and

heated to 40 °C in an oven. The vessel was connected to a $scCO_2$ rig equipped with a flow controllable liquid pump. The vessel was pressurised to 75 bar at a flowrate of 5 g min^{-1} for 24 h. After that, the reactor was depressurised slowly to atmospheric pressure. The white solid was separated by filtration, repeatedly washed with DMF and dried at room temperature.

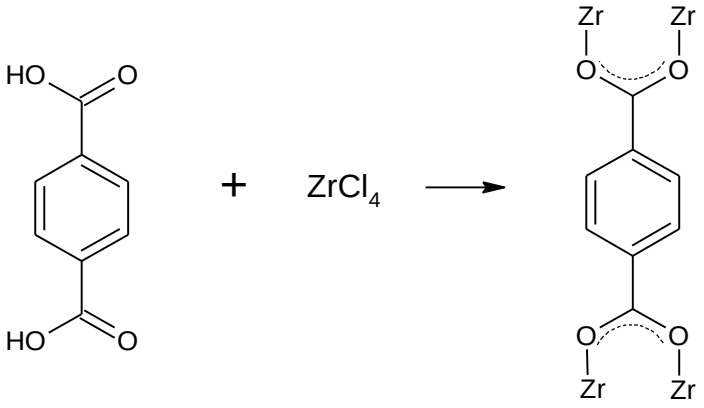

Scheme S1. Synthesis of UiO-66

The sample synthesised at 40 °C and dried at room temperature appeared to be gel-like light yellow crystals which are very different from the solids in the sample synthesised at 120 °C. Tian *et al.* also reported that a gel like UiO-66 monolith could be formed by a sol-gel process and mild drying conditions.[325] In the PXRD results, it can be seen that the low temperature synthesised sample has preserved peaks at 7, 12, 22, 26, 31, 43 and 50 degrees 2θ (see Figure S23), confirming the UiO-66 structure in this sample. However, these peaks appeared much broader than the peaks in normal UiO-66, showing that the sample synthesised at 40 °C has smaller crystal size than those synthesised at 120 °C. It has been demonstrated that UiO-66 obtained by room-temperature synthesis had defect sites with the maximal number achieved (~1.3 missing linker per SBU) at a temperature of 45 °C.[326] In this study, highly-crystalline MOFs were the principal focus. The $scCO_2$ experiment was applied in this MOF synthesis, however, the PXRD patterns of both samples synthesised at 40 °C are almost identical, showing that $scCO_2$ did not enhance the crystallite size in this MOF.

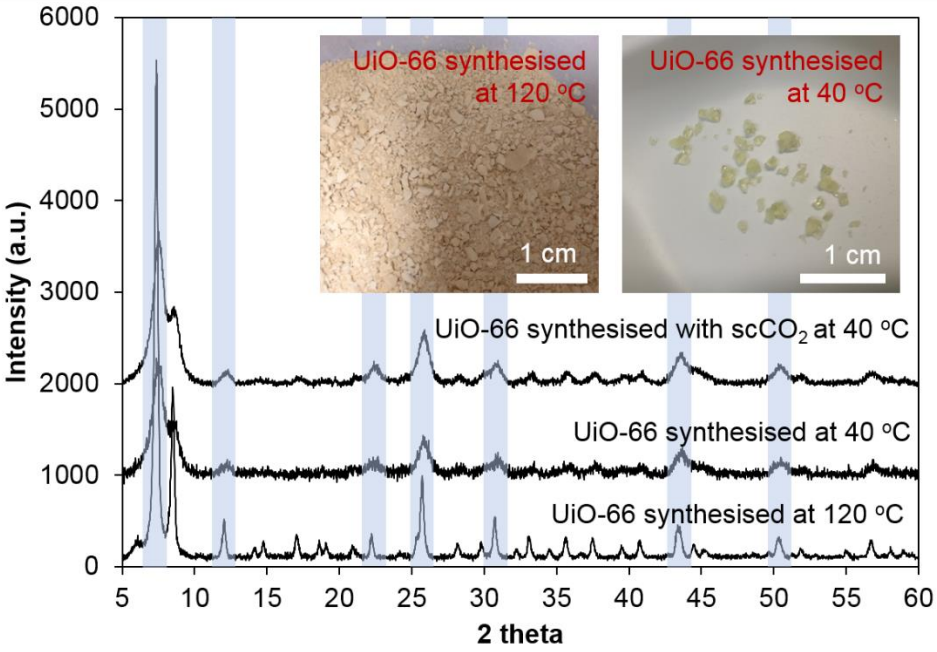

Figure S23. UiO-66 synthesised at 40 °C (with and without $scCO_2$) and 120 °C. These results show that UiO-66 synthesised at 40 °C has significant bigger crystal size than via the normal method (120 °C).

APPENDIX E

Supplementary Information for

Novel hierarchical copper-based metal-organic frameworks for improved catalytic performance

E1. Experimental

All chemicals were sourced from commercial suppliers and used without further purification.

E1.1. Synthesis of HKUST AE

First, 10 mL DMSO and 10 mL methanol were mixed and magnetically stirred at room temperature for 10 minutes to obtain a stock solution (SS) with pH = 6.4. Subsequently, 1 mL of 90% phosphoric acid was added to this stock solution, with continuous stirring at room temperature for another 10 minutes (pH = 2.6). In the etching process, 20 mL of the prepared solution was added to 50 mL centrifuge tubes containing 200 mg of normal HKUST, and was agitated strongly before being placed in an oven at 40 ^{o}C for 72 h. After etching, the solid was isolated by centrifugation (10,000 rpm for 10 minutes), washed with pure methanol, re-centrifuged and re-washed three times and dried at 60 ^{o}C overnight to obtain HKUST AE.

E1.2. Synthesis of HKUST CO_2

HKUST CO_2 was synthesised following the method stated in literature.[174] First, 9.8 g copper(II) nitrate hemipentahydrate ($Cu(NO_3)_2 \times 2.5H_2O$) (4.22 mmol) and 4.7 g benzene-1,3,5-tricarboxylic acid (trimesic acid/BTC) (2.22 mmol) were dissolved in a 220 mL glass vial containing 40 mL dry DMSO and 40 mL methanol, resulting in a clear blue precursor solution (Figure S24a). This vial was placed and sealed inside a 250 mL cylindrical steel reactor pressure vessel, magnetically stirrer at 200 rpm and heated to 40 ^{o}C in an oven. The vessel was connected to a $scCO_2$ rig equipped with a flow controllable liquid pump. The vessel was pressurised to 75 bar at a flowrate of 5 g min^{-1} and left the reaction for 72 h. After that, the reactor was then depressurised slowly to atmospheric pressure. A cloudy dark blue solution which can be seen in Figure S24b was observed in the vessel. This solution was centrifuged (10,000 rpm for 10 minutes), washed 3 times with methanol and dried in air at room temperature to obtain a solid product. The residual solvent in the product was extracted by continuous-flow $scCO_2$ (flowrate 2 g min^{-1}) overnight at 40 ^{o}C and 120 bar.

Figure S24. Precursor HKUST-1 solution before (a) and after (b) being pressurised with $scCO_2$

E2. Characterisation techniques

Catalysts after the reaction were tested by powder X-ray diffraction (PXRD) on a BRUKER AXS D8-Advance instrument with Vantec-1 detector using Cu Kα (λ = 1.5418Å) as the source of X-ray radiation, in flat plate geometry, spinner speed 15 rpm, at 21 ºC. The two theta range, between 2 and 60 degrees, was used with a 0.02 degree interval for collection and 20 minute scans.

Scanning electron microscopy (SEM) experiments were taken using JEOL IT300 SEM with a SED detector at School of Chemistry, University of Bristol with following settings, objective aperture: 1, acceleration voltage: 5kV, probe current: 10.3 m, working distance: 10.8 mm and magnifications from 350 to 40,000 times. The samples were coated with 15 nm silver before conducting the experiment. EDX data were acquired using an Oxford INCA X-ray analyser attached to the microscope.

Thermogravimetric analysis (TGA) was carried out in a thermogravimetric analyser (TGAQ500, TA-instruments) at the Material and Chemical Characterisation Facility, University of Bath. The temperature ramping was 5 °C min^{-1} from room temperature to 600 °C in 100 mL min^{-1} of air.

Gas sorption isotherms were determined using nitrogen sorption at 77 K with a Micromeritics 3-Flex volumetric gas sorption analysis system. Samples were degassed at 120 °C under dynamic high vacuum (10^{-6} mbar) over 6 hours prior to analysis. The total pore volume was taken at the end of the filling of the pore. Surface area was determined by the BET method according to British Standards, with relative pressure (P/P_o) selected considering the Rouquerol

consistency criterion between values of 0 and 0.3. Error bars mentioned in the BET surface area were from the calculation.

E3. Testing HKUST AE and HKUST CO_2 samples in methanolysis of styrene oxide

E3.1. EDX results of normal HKUST, HKUST AE and HKUST CO_2

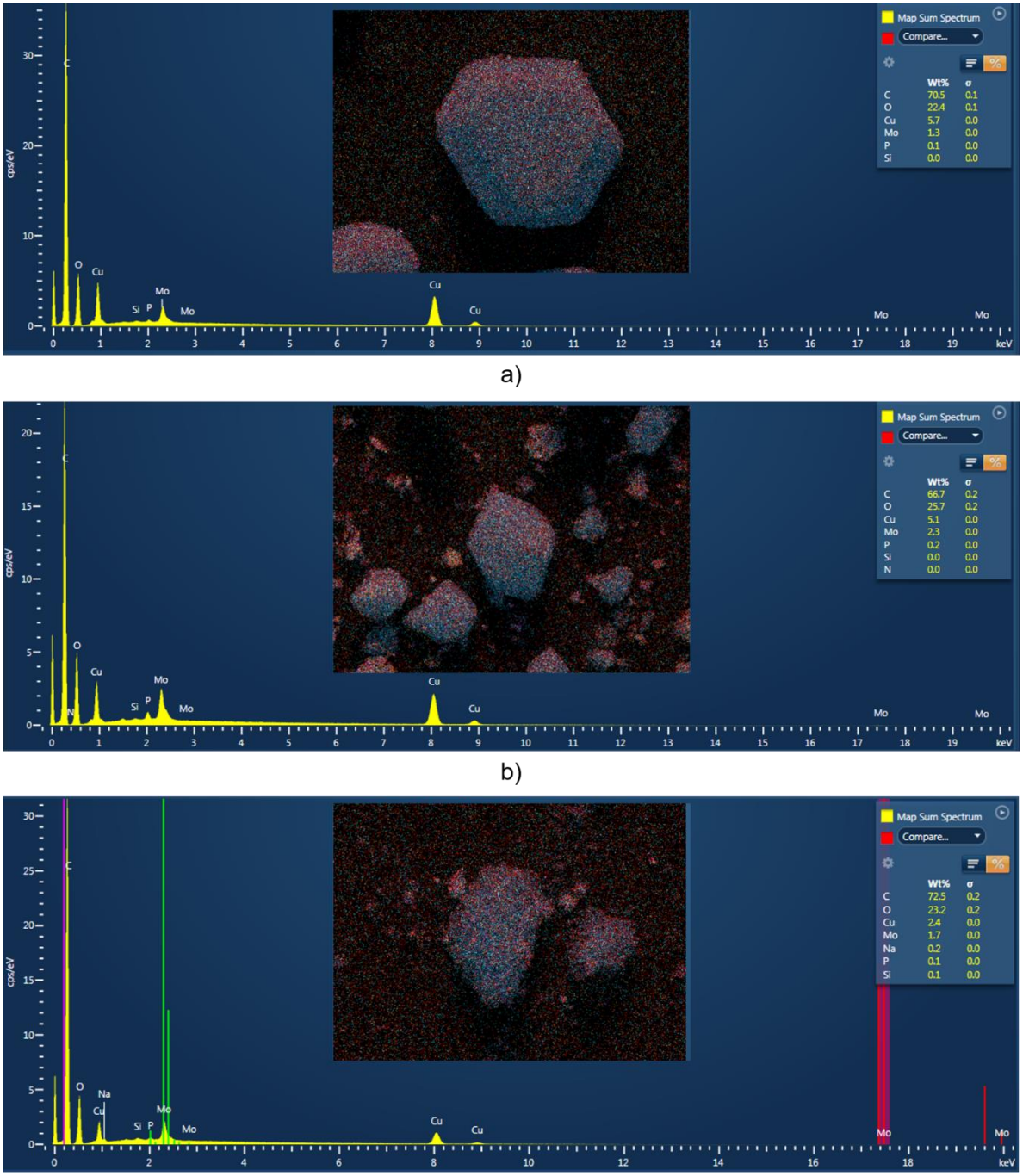

Figure S25. EDX scan images and spectra of HPMo/normal HKUST, HPMo/HKUST AE and HPMo/HKUST CO_2

Table S8. EDX elemental composition of HPMo/normal HKUST, HPMo/HKUST AE and HPMo/HKUST CO_2

Samples	Elemental composition (wt.%)			
	C	O	Cu	Mo
HPMo/normal HKUST	70.5	22.4	5.7	1.3
HPMo/HKUST AE	66.7	25.7	5.1	2.3
HPMo/HKUST CO_2	72.5	23.2	2.4	1.7

E3.2. Reaction mechanisms of methanolysis of styrene oxide

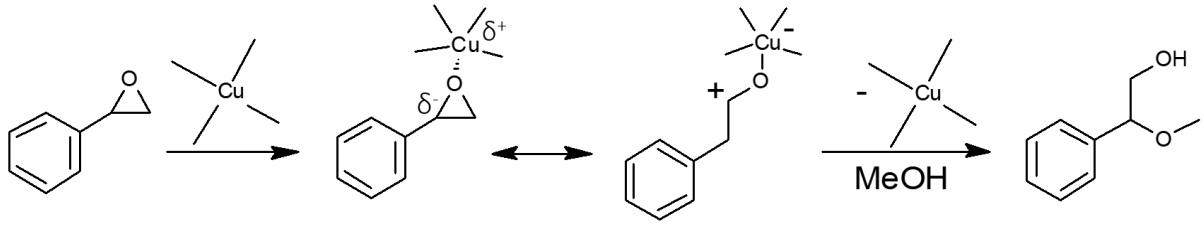

Figure S26. The ring opening of styrene oxide with MeOH catalysed by Lewis site in HKUST-1

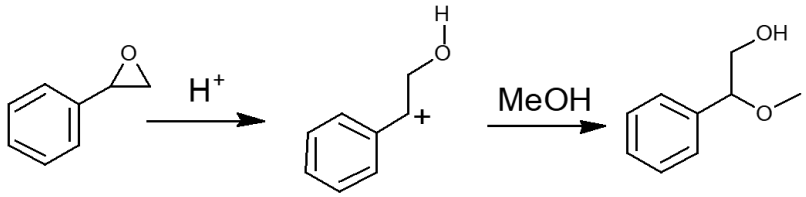

Figure S27. The ring opening of styrene oxide with MeOH catalysed by Brønsted site in heteropoly acid

E3.3. GC results of methanolysis of styrene oxide testing

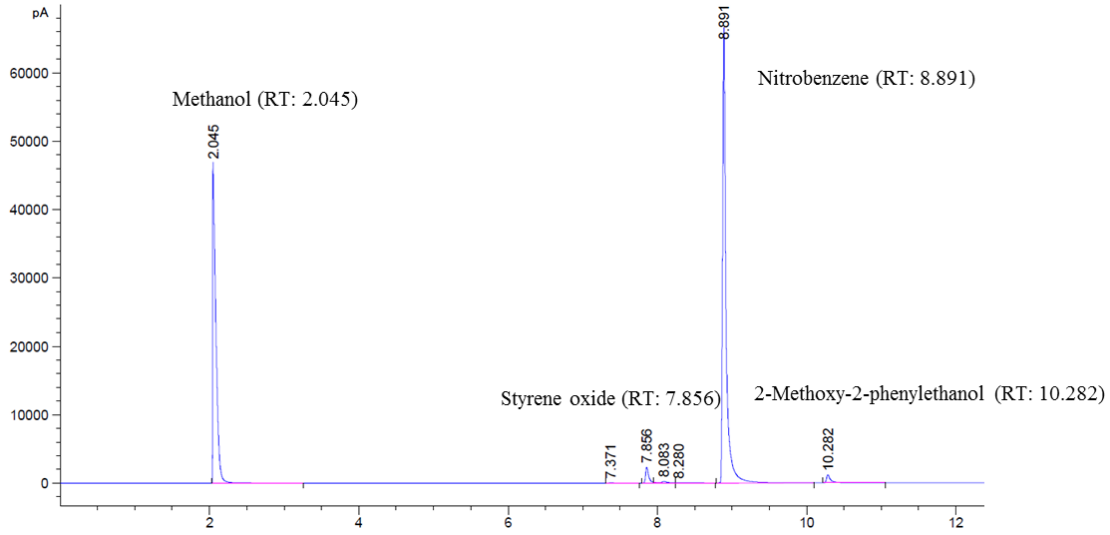

Figure S28. GC spectra of methanolysis reaction using HPMo/HKUST AE as a catalyst

Table S9. GC peak position and area of methanolysis reaction using HPMo/HKUST AE as a catalyst

Peak #	**RetTime [min]**	**Area [pA*s]**
1	2.045	1.37E+05
2	7.371	77.15365
3	7.856	6960.341
4	8.083	1257.001
5	8.280	317.6672
6	8.891	2.15E+05
7	10.282	4781.975

E3.4. PXRD results of samples after methanolysis of styrene oxide

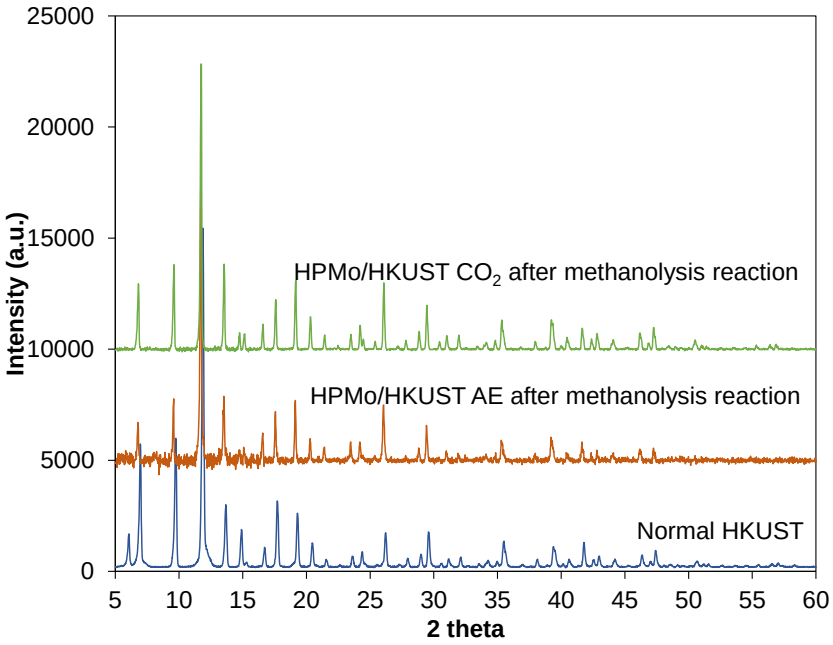

Figure S29. XRD results of HKUST AE and HKUST CO_2 after methanolysis of styrene oxide compared to normal HKUST. PXRD spectra are offset in intensity, for clarity.

E4. Testing HKUST CO_2 sample in CO oxidation

E4.1. EDX results of normal HKUST and HKUST CO_2

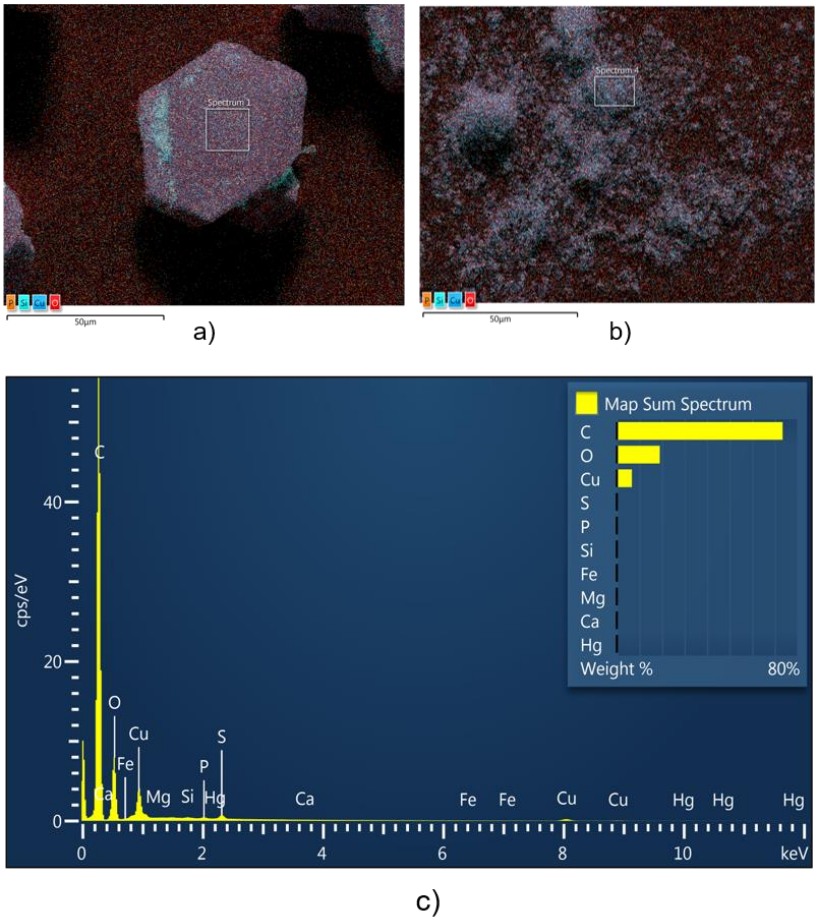

Figure S30. EDX scan images of normal HKUST (a) and HKUST CO_2 (b) and representative EDX spectrum of normal HKUST (c)

Table S10. EDX elemental composition of normal HKUST and HKUST CO_2

Samples	**Elemental composition (wt.%)**		
	C	O	Cu
Normal HKUST	60.1	32.2	7.2
HKUST CO_2	67.2	26.7	5.9

E4.2. CO_2 sorption isotherm of normal HKUST and HKUST CO_2

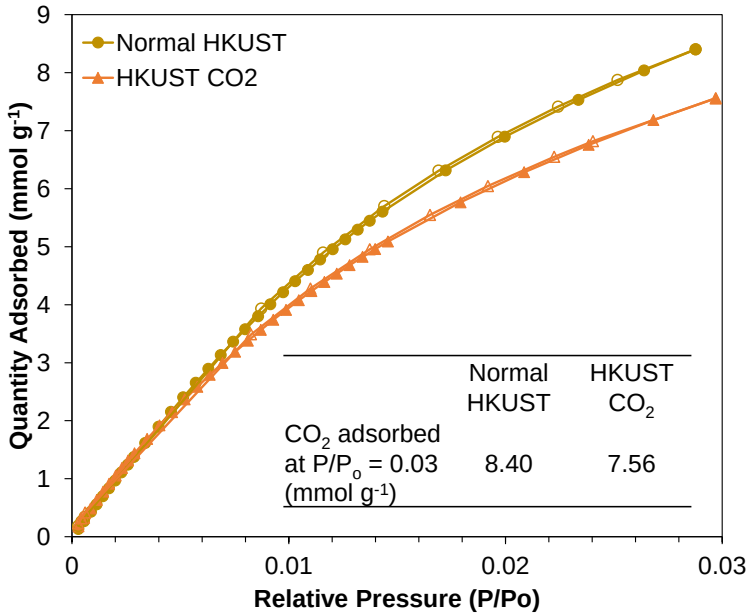

Figure S31. CO_2 isotherm at 273 K of normal HKUST and HKUST CO_2. Adsorbed CO_2 isotherms were represented by filled markers and desorbed nitrogen isotherm were represented by unfilled markers.

E4.3. GC results of CO oxidation testing

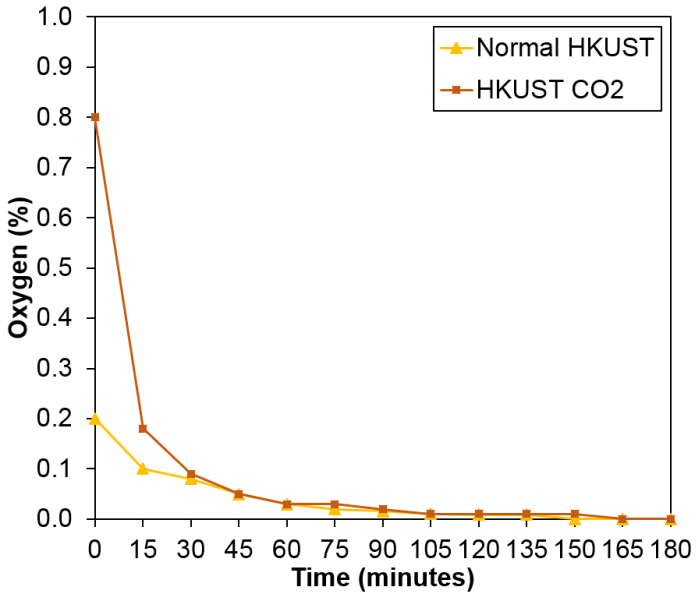

Figure S32. Oxygen released from normal HKUST and HKUST CO_2 during CO activation. The y-axis shows the percentage of oxygen in the outlet gas containing CO, oxygen and argon.

E4.4. PXRD results of samples after CO oxidation

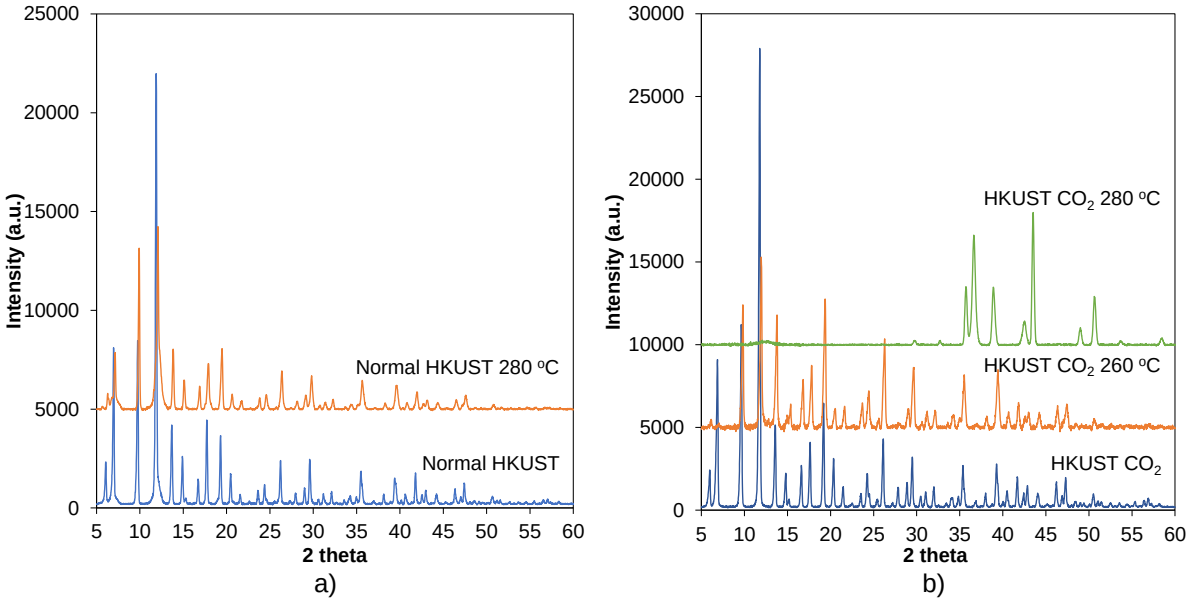

Figure S33. PXRD results of (a) normal HKUST before and after reaction at 280 °C and (b) HKUST CO_2 before reaction and after reaction at 260 and 280 °C. PXRD spectra are offset in intensity, for clarity.

E4.5. TGA results of normal HKUST and HKUST CO_2

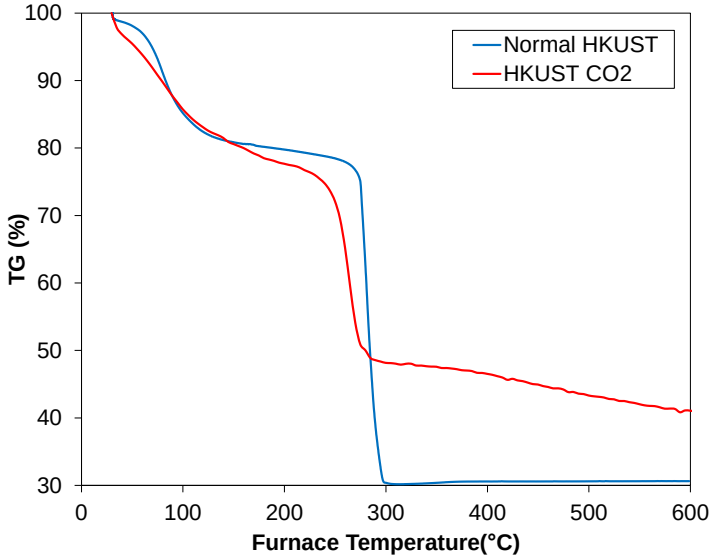

Figure S34. TGA results of normal HKUST and HKUST CO_2